Development of a standardless miniature XRF setup for the analysis of actinides : coupling MC methods with fundamental parameters

Tetiana Sokoltsova

université PARIS-SACLAY

Développement d'un système XRF miniaturisé standardless pour l'analyse des actinides: couplage modélisation MC et paramètres fondamentaux

Development of a standardless miniature XRF setup for the analysis of actinides: coupling MC methods with fundamental parameters

Thèse de doctorat de l'université Paris-Saclay

École doctorale n°576 : particules hadrons énergie et noyau : instrumentation, image, cosmos et simulation (PHENIICS)
Spécialité de doctorat : aval du cycle nucléaire, radioprotection et radiochimie
Unité de recherche : Université Paris-Saclay, CEA, Institut LIST, 91191, Gif-sur-Yvette, France
Référent : Faculté des sciences d'Orsay

Thèse présentée et soutenue à Marcoule, le 18 mars 2021, par

Tetiana SOKOLTSOVA

Composition du Jury

Anne LAFOSSE Professeur, Université Paris-Sud/Paris-Saclay	Présidente du jury
Jean-Emmanuel GROETZ Maître de Conférences (HDR), Université de Franche-Comté	Rapporteur & Examinateur
Philippe JONNARD Directeur de Recherche, CNRS Sorbonne Université	Rapporteur & Examinateur
Burkhard BECKHOFF Docteur, Physikalisch-Technische Bundesanstalt (PTB), Berlin	Examinateur
Emmanuelle BRACKX Ingénieure, CEA Marcoule	Examinatrice
Mme Marie-Christine LÉPY Directrice de Recherche, CEA Saclay (LNHB)	Directrice de thèse
Mr Eric ESBELIN Ingénieur de Recherche, CEA Marcoule	Encadrant

Thèse de doctorat

NNT : 2021UPASP018

« Dans la vie, rien n'est à craindre, tout est à comprendre. »

— Marie Skłodowska-Curie (1867-1934)

Remerciements

Je tiens tout d'abord à remercier Marie-Christine Lépy de m'avoir dirigé tout au long de la réalisation de ce travail. Je lui suis reconnaissante pour son soutien, son aide, ses conseils avisés qui ont beaucoup contribué à ma réflexion, pour la relecture méticuleuse du manuscrit, même le week-end. J'ai été extrêmement sensible à ses qualités humaines d'écoute et de compréhension. Marie-Christine, merci pour l'amitié et un réel impact positif que tu as eu sur mon parcours professionnel et personnel. Je suis heureuse qu'aujourd'hui tu fasses ainsi partie des gens qui ont marqué ma vie. Enfin, merci pour l'opportunité de participer à la formation organisée par EXSA !

Je remercie tout particulièrement Eric Esbelin d'avoir encadré cette thèse, de m'avoir guidé dans le monde de la recherche et de sa présence à tout instant sur le terrain. Grâce à ses qualités scientifiques et pédagogiques, j'ai beaucoup appris et il m'a donné l'envie d'aller plus loin et de connaître la richesse du métier de chercheur. Eric, merci pour le temps que tu m'as accordé, ta patience, nos discussions fructueuses, et de maints conseils que je n'oublierai jamais. Merci pour un grand respect de ma personnalité.

Marie-Christine, Eric, je ne pense pas qu'il y ait suffisamment de mots pour vous exprimer toute ma gratitude. Grâce à vous j'ai pu réaliser ce travail doctoral.

Je souhaite exprimer ma profonde reconnaissance à Philippe Jonnard, directeur de recherche au CNRS Sorbonne Université, et Jean-Emanuel Groetz, maître de conférences à l'Université de Franche-Comté, pour l'honneur qu'ils ont fait en acceptant d'être rapporteurs de ce travail et pour leur relecture scrupuleuse du manuscrit. Ils ont contribué par leurs suggestions et remarques à améliorer la qualité de ce mémoire. Je voudrais adresser tous mes remerciements à Anna Lafosse, professeur à l'Université Paris-Saclay, pour avoir présidé le jury de cette thèse. Je remercie profondément Emmanuelle Brackx, ingénieure au CEA Centre de Marcoule, ainsi que Burkhard Beckhoff, docteur au Physikalisch-Technische Bundesanstalt, pour m'avoir fait l'honneur de participer au jury de soutenance.

Je tiens à remercier Cédric Rivier pour m'avoir accueilli au sein de son laboratoire et pour m'avoir fourni un environnement de travail. Je lui suis reconnaissante pour l'intérêt qu'il avait porté à ce travail. Je remercie également toute l'équipe du laboratoire LAAT pour leur bienveillance, leur gentillesse et leur bonne humeur. Ils m'ont aidée à m'intégrer dans la société.

Je remercie l'ensemble des personnes du LNHB pour leur accueil chaleureux permanent. Je tiens à remercier particulièrement Yves Ménésguen de son aide apporté à l'étalonnage du rendement du détecteur.

Je remercie les thésards Sara, Eleonora, Hanan et Sasha pour leur amitié et tous les bons moments passés ensemble.

J'exprime toute ma gratitude à Yaroslava pour le temps qu'elle m'a consacré et pour avoir enrichi mes connaissances. Merci pour tout ce que vous avez fait !

Enfin, un très grand MERCI à ma famille qui a su me soutenir, me supporter, m'encourager pendant toute la durée de ma thèse.

Table of contents

List of abbreviations V

Introduction 1

References 4

Chapter 1 X-Ray Fluorescence 5

1. Electron configuration of the atom 6
2. X-ray radiation 6
   - 2.1. Production of X-rays 7
     - 2.1.1 Continuous spectrum 8
     - 2.1.2 Characteristic lines 9
3. Interaction of X-rays with matter 12
   - 3.1. Photoabsorption 13
   - 3.2. Scattering 14
   - 3.3. Emission of fluorescent X-rays 16
4. XRF quantitative analysis 17
   - 4.1 Components of the XRF spectrum 17
   - 4.2 Theoretical equations 18
5. Matrix effects 21
   - 5.1. Fundamental parameters method 21
   - 5.2. Influence coefficient algorithm 22
6. Conclusions 22

References 23

Chapter 2 Diffraction 25

1. Geometrical optics 26
2. Crystal structure 27
   - 2.1. General structure of crystals 27
   - 2.2. Mosaic crystals 29
3. X-ray diffraction 30
   - 3.1. Electromagnetic waves 31
   - 3.2. Diffraction and interference 31
   - 3.3. Bragg diffraction 33
   - 3.4. X-ray diffraction in crystals 34
     - 3.4.1. Reflectivity of perfect crystals 34
     - 3.4.2. Reflectivity of real crystals 36
4. General diffraction properties of HOPG crystal 38
5. Conclusions 39

References 40

Chapter 3 Miniature XRF setup design and characteristics 42

1. Nuclearized EDXRF setup for actinide analysis 43

2. Miniature XRF setup....46
2.1. X-ray tube....49
2.2. Sample holder....51
2.3. Detection System....52
2.4. Detection efficiency calibration....55
2.4.1. Experimental efficiency calibration....56
2.4.2. Spectrum processing with the COLEGRAM software....57
2.5. Highly oriented pyrolytic graphite (HOPG) monochromator....61
3. Conclusions....62
References....63

Chapter 4 Numerical solutions for the experimental setup....65

1. Monte Carlo simulation of X-ray fluorescence setup....66
1.1. Monte Carlo basic principles....66
1.2. Monte Carlo packages....68
1.2.1. GEANT4....69
1.2.2. MCNP....69
1.2.3. PENELOPE....69
1.3. Monte Carlo simulation of the experimental setup....70
2. Ray tracing simulation for HOPG optics....71
2.1. Ray tracing model....71
2.2. Ray tracing packages....74
2.2.1. SHADOW-XOP....74
2.2.2. RAY....74
2.2.3. XRT (XRayTracer)....75
2.3. Simulation of the HOPG optics with the ray tracing method....75
3. Conclusions....76
References....76

Chapter 5 Monte Carlo simulation of the experimental setup....78

1. Simulation of the spectrum emitted by the X-ray tube....79
1.1. Simulation with the PENELOPE code....79
1.2. Comparison of the spectra calculated with the PENELOPE and theoretical models....82
2. Simulation of the first channel of the experimental setup....84
2.1. Comparison of X-ray fluorescence spectra with unfiltered primary radiation....86
2.2. Comparison of X-ray fluorescence spectra with filtered primary radiation....88
3. Simulation of the second channel....89
4. Conclusions....91
References....91

Chapter 6 Modelling of the optical system with a ray-tracing method....93

1. Investigation of the optical system by ray-tracing....94
1.1. Reflection of a monochromatic beam from a point source....96
1.2. Diffraction of a beam with several discrete energies....98
1.3. Diffraction of a polychromatic beam for a point source....101
2. Investigation of the optical performance of the system....103
2.1. Influence of the source size on the reflection profile....105
2.2. Influence of the focused and defocused geometry on the reflection profile....107
2.3. Calculation of the second order reflection of the HOPG crystal....110
3. Simulations using the experimental spectrum as input data....112

4. Ray-tracing simulations with PENELOPE results as input data 118
5. Conclusions 119
References 120

Chapter 7 Implementation of the transfer function into the fundamental parameters algorithm 121

1. Spectrum processing 122
2. Spectrum processing with FP-based package 127
   2.1. XRF analysis with PyMCA 127
   2.2. Definition of the transfer function 135
3. Conclusions 140
References 141

Conclusions & recommendations for future work 142

Résumé en Français 149

Appendices 155

A. Experimental data 155
B. PENELOPE simulations of the miniature XRF setup 160
C. Ray-tracing simulations 165

Abstract 172

List of abbreviations

ATALANTE	ATelier Alpha et Laboratoires pour ANalyses, Transuraniens et Études de retraitement
CEA	Alternative Energies and Atomic Energy Commission (French: Commissariat à l'énergie atomique et aux énergies alternatives)
CP	Crystal to image plane (distance)
DCS	Differential cross section
EDXRF	Energy dispersive X-ray fluorescence
ESRF	European Synchrotron Radiation Facility
FEPE	Full-energy peak efficiency
FP	Fundamental parameters
FWHM	Full width at half maximum
GEANT4	GEometry ANd Tracking
HAPG	Highly annealed pyrolytic graphite
HOPG	Highly oriented pyrolytic graphite
HPGe	High purity germanium
ICP-AES	Inductively coupled plasma atomic emission spectroscopy
ICP-MS	Inductively coupled plasma mass spectrometry
IUPAC	International Union of Pure and Applied Chemistry
LAAT	Laboratoire d'analyses d'Atalante
LNHB	Laboratoire National Henri Becquerel
MC	Monte Carlo
MCA	Multichannel analyser
MCNP	Monte Carlo N-Particle
MLC	Multilayer collimator
PDF	Probability distribution functions

PENELOPE	PENenetration and Energy LOss of Positrons and Electrons
ROI	Region of interest
SDD	Silicon drift detector
SNIP	Statistical nonlinear iterative peak clipping
SP	Source to crystal (distance)
WDXRF	Wavelength dispersive X-ray fluorescence
XRD	X-ray diffraction
XRF	X-ray fluorescence
XRS	X-ray spectroscopy
XRT	X-ray tracer

Introduction

ATALANTE (ATelier Alpha et Laboratoires pour ANalyses, Transuraniens et Études de retraitement) is a nuclear facility of great importance to the French alternative energies and Atomic Energy Commission (CEA). Located on the Marcoule nuclear site, it is dedicated to research into spent nuclear fuel reprocessing and management of high-level long-lived radioactive wastes. Basic and applied research experiments on many stages of the fuel cycle take place, in particular concerning the back end. Within ATALANTE, the LAAT analysis laboratory (Laboratoire d'analyses d'Atalante) particularly focuses on actinides, for numerous studies carried out in glove boxes (intermediate activity) or in hot cells (high activity). It has different analytical devices available for the identification and quantification of actinides in liquid phase (aqueous or organic) samples. The following techniques can be used for the actinide analyses:

- *ICP-AES (Inductively Coupled Plasma - Atomic Emission Spectrometry) or ICP-MS (Inductively Coupled Plasma - Mass Spectrometry)*. The methods are destructive and time-consuming.
- *α- and γ-spectrometry*. These methods are implemented to measure the activity of certain actinide isotopes (^{239}Pu and ^{240}Pu using α-spectrometry, or ^{241}Am in γ-spectrometry). The methods require knowledge of the isotopic composition of the Pu or Am samples in order to estimate the total concentration of these elements. In addition, α-spectrometry requires special preparation of the sample.
- *Chemical analysis* as an electrochemical process (redox titration). This method is destructive and requires chemical reagents.
- *Spectrophotometry.* This is used to measure the absorption band of Pu(VI) or Am(III). Some redox reagents are necessary to convert the element to be analysed into the correct redox state, and can be considered as destructive.
- *X-ray spectrometry (XRS) (fluorescence and absorption).* Use of these methods is preferred because they are non-destructive and easy to implement. Details regarding XRS are given below.

X-ray fluorescence (XRF) analysis is a well-established technique for qualitative and quantitative elemental analyses. It is based on using a beam of primary X-rays to excite an analyte and to induce the emission of X-ray fluorescence from the sample. The method is non-destructive, suitable for the analysis of a wide range of elements, and can be used with solid, liquid, or powder samples. Furthermore, X-ray fluorescence analysis requires little sample preparation and measurements can be performed in a relatively short time.

Quantitative XRF analysis is based on the measurement of the X-ray intensity from an element in a sample, which enables its concentration to be derived. This task is not straightforward, because the X-ray intensity observed depends on: i) the sample (preparation

conditions, size, matrix composition, concentration of the element(s) of interest), ii) the experimental setup (source of the primary X-ray radiation, detection system, geometrical conditions), and iii) the measurement conditions (tube characteristics and operating conditions, acquisition time). To derive quantitative information taking into account these parameters, either theoretical or empirical approaches are applied. The first approach is based on mathematical equations involving basic physical parameters, whereas an empirical approach requires a large number of standard samples with similar chemical and physical properties to those of the unknown sample.

In the analysis laboratory hot cells, a nuclearized system was designed and manufactured to perform X-ray fluorescence analyses of radioactive samples containing actinides, mainly U and Pu, based on their intense L X-ray lines [1]. This large device had to be lead-shielded, since the measurements are on high-activity samples, inducing very high dose rates. The principal components of the system are: i) an Rh anode X-ray tube, ii) a cylindrical highly oriented pyrolytic graphite (HOPG) monochromator, and iii) a high purity germanium (HPGe) detector. The setup has the HOPG crystal positioned between the sample and the detector. In this geometry, the HOPG crystal acts as a bandpass filter, which modifies the spectral distribution of the fluorescence radiation emitted by the analysed sample. The HOPG focusing optics allows optimization of the recorded fluorescence spectrum over a certain energy range. Thus, it is possible to reduce the detector loads from any parasitic radiation outside the energy range of interest, and improve analytical efficiency.

The experimental setup was adjusted to favour the fluorescence of lines of interest. The monochromator covers the energy window from 12 keV to 17 keV, which allows X-ray line recording of several elements (actinides L lines such as Th, U, Np, Pu, Am, Cm, but also the K lines of Rb, Pb, Sr, Y, Zr). A spectrum obtained with this experimental setup is shown in Figure 1. It can be seen that the region covered by the HOPG crystal is more intense compared to the lower-energy part of the spectrum and to the higher energy region, which includes peaks due to the emissions of the Rh tube.

The use of the HOPG crystal in this setup permits the detection of actinides in concentrations between 0.5 mg L^{-1} and 5 g L^{-1}.

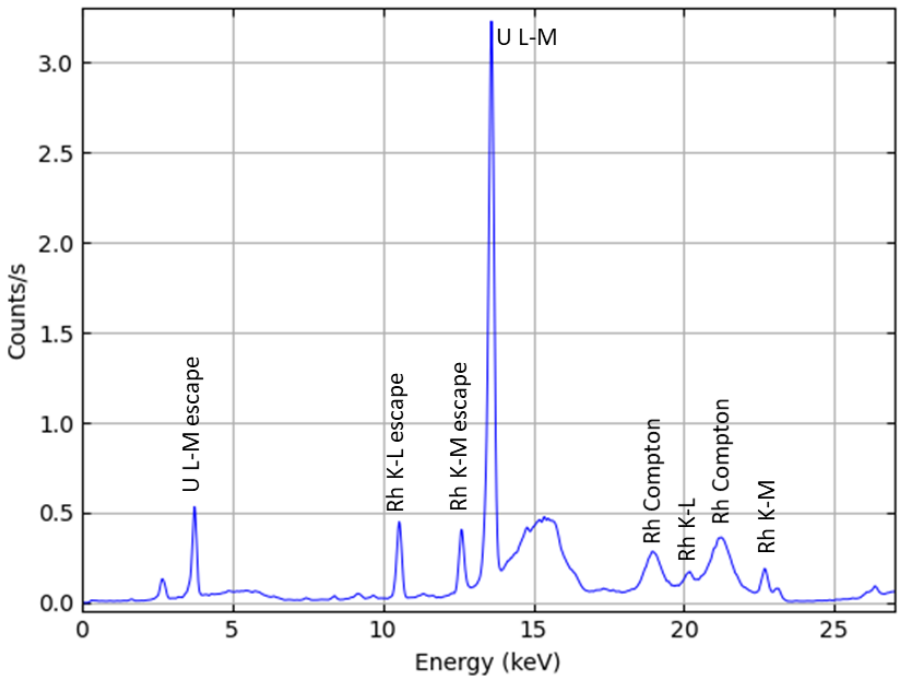

Figure 1. Spectrum collected from U at a concentration of 50 mg L^{-1} in HNO_3 3M with the LAAT nuclearized device. The X-ray tube operated at 50 kV high voltage and 30 mA current. Acquisition time was 800 s.

X-ray spectra obtained with the nuclearized setup are analysed with a processing software developed in the laboratory [1]. It includes a library of standard spectra. A calibration is performed for each standard element, establishing a nonlinear relationship between peak intensity and concentration. However, the calibration is time-consuming and has to be checked regularly in order to ensure its validity.

For the analysis of intermediate activity levels, it was highly desirable to design a new miniaturised XRF device able to be installed in a glove box and flexible to use. Objectives included obtaining the same performance as that of the existing nuclearized system. Furthermore, repeated calibrations of the instrument were to be avoided if possible.

A prototype of the miniature setup was built, taking into account size constraints imposed by the space available inside the glove box. It includes an Ag-anode X-ray tube and two detection channels equipped with silicon drift detectors (SDD). The X-ray tube, manufactured by Amptek (USA), is designed for a compact application in XRF analysis and does not require a cooling system, unlike the hot cell device. The first detection channel is a conventional energy-dispersive X-ray fluorescence (EDXRF) analysis system allowing full spectrum recording. The second detection channel was copied from the nuclearized device. It is equipped with a compact HOPG crystal, manufactured by Optigraph (Germany). It is possible to move the HOPG monochromator and the SDD independently along the sample-detection axis, thereby adjusting the appropriate energy window (bandpass of the monochromator). The prototype device is able to cover the energy range from 10 keV to 18 keV. While this possibility is also available on the nuclearized device, it was never used because i) a calibration would have to be performed for each new position, ii) it requires a lot of handling, and iii) the position accuracy is not sufficiently reproducible. To avoid time-

consuming calibrations, a standardless approach with the miniature device is of great interest.

The spectra measured with the classical XRF channel can be successfully processed using software based on the fundamental parameters (FP) algorithm, i.e. without the need for standards. However, the same algorithm is not able to analyze the spectra collected with the second channel, as the HOPG crystal modifies the spectral distribution. To process spectra recorded with the second channel with an FP-based software, it is necessary to determine the transmission function of X-rays through the HOPG monochromator and to include this in the processing algorithm. During this study, the miniature setup was tested in a non-nuclear laboratory using samples with medium-Z elements (Rb, Sr, Y, etc.) whose K X-ray emission lines are in the same energy range as the actinide L X-ray emission lines.

The manuscript has seven chapters. Chapter 1 starts with a review of the interactions of X-rays with matter, and the emission of characteristic and continuous radiations. The relationships between the intensities of characteristic X-rays and elemental concentrations are also presented. Chapter 2 focuses on geometric optics and elements of X-ray diffraction. The crystal structure and its diffraction properties are discussed, with special emphasis on HOPG crystals. The design of the miniature XRF setup and the nuclearized device are described in detail in Chapter 3. All the principal components of the new XRF setup are presented. Chapter 4 gives a review of the digital tools used to model the miniature setup, and pays particular attention to the tools to be used in the thesis.

The investigation of the miniature setup and of the phenomena involved, utilizing the Monte Carlo method for the radiation transport, are presented in Chapter 5. The simulation model comprises the X-ray tube and both detection channels, but without HOPG optics since this radiation transport code does not include simulation of crystal diffraction. Comparisons of simulated XRF spectra with measurements are provided.

A large part of the thesis is devoted to the characterisation of the cylindrical HOPG crystal performance. The development of the optical model using a ray-tracing algorithm is extensively presented in Chapter 6. It starts with the investigation of the properties of a single HOPG crystal and the influence of different parameters, such as source size, source to crystal distance, etc., on the crystal reflectivity. The chapter continues with the development of an optical model mimicking the optical part of the experimental setup.

Chapter 7 presents all the processing of the experimental data with the FP-based algorithms. It demonstrates the capabilities of the processing tool for measurements from both channels. The implementation of the HOPG crystal transfer function in the analysis algorithm is presented in detail, as well as the validation examples.

The concluding Chapter summarizes the XRF analysis capabilities of the miniature setup, and discusses the promising perspectives for the setup design and its further use.

References

[1] E. Esbelin, "Graphite monochromator for actinide L-line energy dispersive X-ray fluorescence analysis in liquid sample", *X-Ray Spectrom.*, 43, 198–208, 2014

Chapter 1

X-Ray Fluorescence

The discovery of X-rays in 1895 by Röntgen was followed by vigorous growth in the development of a wide variety of applications. In particular, X-ray fluorescence (XRF) has opened up the analysis of materials in a broad range of fields. This analytical technique is widely applied for the determination of the elemental composition of materials, both qualitatively and quantitatively, by measuring the energies and intensities of characteristic X-rays. The method can be used to characterize a wide range of elements at different weight fractions in a given sample. XRF analysis is based on the excitation of the atom of an analyte element by a primary X-ray beam. Passing through the matter, the X-ray beam is either scattered from its initial direction or absorbed within the matter and, as a result, the initial X-ray beam intensity is reduced. X-rays can be scattered with no energy change or they can give up some energy to atomic electrons. In the absorption process (photoabsorption), the atom is left in an ionised state and the rearrangement of electronic shells is accompanied by the emission of secondary X-rays, called characteristic X-rays. The measured analyte peak provides information as to its nature. The intensity of the characteristic X-ray line depends on the elemental concentration, but the relationship is not direct. The characteristic X-rays emitted can be absorbed by other elements in the sample with a resulting reduction in their intensity.

In this chapter, the electronic structure of the atom, and the production of X-rays and their properties are respectively presented in sections 1 and 2. The basics of the interaction of X-rays with matter and the principles of X-ray fluorescence are discussed in section 3. XRF analysis consists in the conversion of the measured peak intensity of an analyte to its concentration. The net peak intensity observed is not only a function of the concentration of an element of interest, but also depends on other elements. The matrix effects are presented in section 5: they can lead to errors in XRF analysis and must not be neglected.

The end of this chapter discusses the theoretical and empirical methods applied to take them into account for quantitative analysis.

1. Electron configuration of the atom

The atom is conventionally described as a dense, central nucleus surrounded by electrons. These occupy discrete energies and spin levels in electronic shells, which are "located" at certain distances from the nucleus, increasing in size as they get further away from the nucleus. Each electron has an amount of energy (binding energy) due to its position in a certain shell, which is specified by four parameters or quantum numbers n, ℓ, s, m [1]. n (n=1, 2, 3, 4…) is the principal quantum number or when labelled alphabetically, K, L, M, N…, respectively. The K-shell (n=1) is the closest to the nucleus, followed by the L-shell (n=2), the M-shell (n=3), and so on. Each shell has a number of subshells, i.e. the K-shell has one subshell, the L-shell is split into three subshells, called L_I, L_{II} and L_{III}, the M-shell consists of five subshells, M_I, M_{II}, M_{III}, M_{IV} and M_V, etc. ℓ is the angular momentum quantum number that defines the shape of the atomic orbital and takes values from 0 to (n-1). The magnetic quantum number m has integer values between $-\ell$ and $+\ell$, including 0. The spin quantum number s describes the angular momentum of the electron and can only take one of the two possible values, +1/2 and -1/2 [2].
The energy levels are different and unique for each chemical element. The Pauli exclusion principle states that there can be no more than one electron occupying the same quantum state in an atom, i.e. two electrons cannot have the identical set of quantum numbers [1], [2], [3]. Thus, there are only two electrons in the first subshell for which n=1, for n=2 eight combinations exist, for n=3 eighteen, etc. In general, there can be $2 \cdot n^2$ combinations. The total angular momentum quantum number J is expressed by the sum $\vec{J} = \vec{\ell} + \vec{s}$ of the angular momentum and the spin quantum numbers s and ℓ, respectively.

2. X-ray radiation

Electromagnetic radiation is a flow of energy, in the form of wave packets with energy stored in electric and magnetic fields, which propagates through space. It can be defined in terms of wavelength λ, frequency ν, or equivalent energy E, covering a large spectrum (see Figure 1.1).

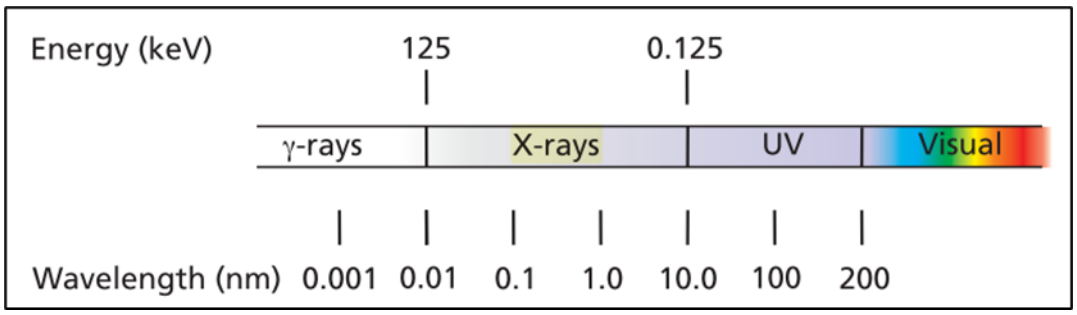

Figure 1.1. Electromagnetic radiation spectrum [4].

The energy of the radiation is inversely related to the wavelength as:

$$E = hc/\lambda \tag{1.1}$$

where h is Planck's constant (4.135×10^{-15} eV s), and c is the velocity of light (3×10^{8} m s^{-1}). The X-ray region of the electromagnetic spectrum is defined between ultraviolet and gamma radiation and spans the energy range from about 0.125 keV to 125 keV, which corresponds to the wavelength range from 0.01 to 10 nm [4].
Like all types of radiation, X-rays have a dualistic nature, exhibiting both particle and wave properties. X-rays are invisible and are also undetectable by the other human senses (hearing, taste, smell, feel). They can pass through matter of different thicknesses, densities, and elemental compositions, being scattered and absorbed differently depending on the matter involved. They have enough energy to ionize atoms and disturb molecular bonds [3].

2.1. Production of X-rays

There are two mechanisms responsible for the production of X-rays:

1. When the trajectory of a charged particle is changed, i.e., if the particle accelerates, decelerates, or if its trajectory is bent, this results in the emission of a continuous spectrum of X-rays.
2. When electrons in the lower orbits of an atom are rearranged, X-rays are emitted with energies that are characteristic of the emitting atom (atomic relaxation).

X-ray tubes are one of the most widely employed sources of X-rays. In these, energetic electrons are accelerated towards an anode target (very pure metal) by the application of a high voltage. They interact with the target material and lose their energies, which induces X-rays depending on the two production mechanisms. The spectrum emitted from an X-ray tube, known as an exciting primary X-rays, consists of characteristic lines produced by the target material, superimposed upon a continuous spectrum known as bremsstrahlung radiation (see Figure 1.2).

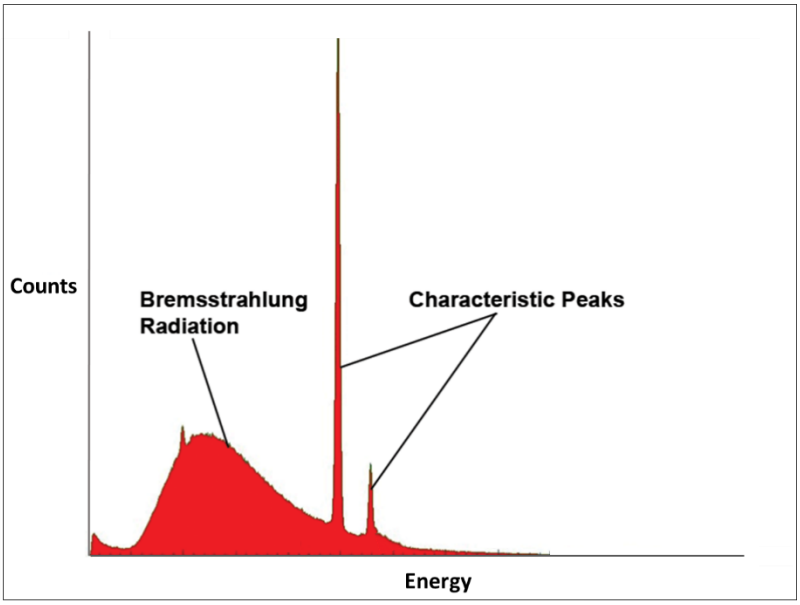

Figure 1.2. Typical spectrum from an X-ray tube [5].

Synchrotrons are another kind of powerful X-ray radiation sources. X-rays are emitted when charged particles are accelerated to extremely high speeds and their trajectories are bent when a magnetic field is applied [6], [7]. The radiation emitted is called synchrotron radiation. In X-ray spectroscopy (XRS), bremsstrahlung and synchrotron radiation are used as sources of continuous X-ray radiation.

2.1.1 Continuous spectrum

Bremsstrahlung radiation is emitted when an energetic electron (or other charged particle) is incident upon the material and undergoes deflection from its initial direction due to the strong electric field of an atomic nucleus. In the interaction process, the electron loses its kinetic energy, which is released in the form of radiation. The closer high-speed electrons pass by nuclei, the greater the energy of the resulting bremsstrahlung radiation (see Figure 1.3).
The intensity of the continuous radiation *I(E)* in the energy range from *E* to *E+dE* is expressed by Kramer's equation:

$$\mathrm{I(E)dE} = \mathrm{K\,Z}\left(\frac{\mathrm{E_0}}{\mathrm{E}} - 1\right)\mathrm{dE} \tag{1.2}$$

K is an empirical constant, Z is the atomic number of material, and E_0 is the energy of the incident electrons [8], [9].

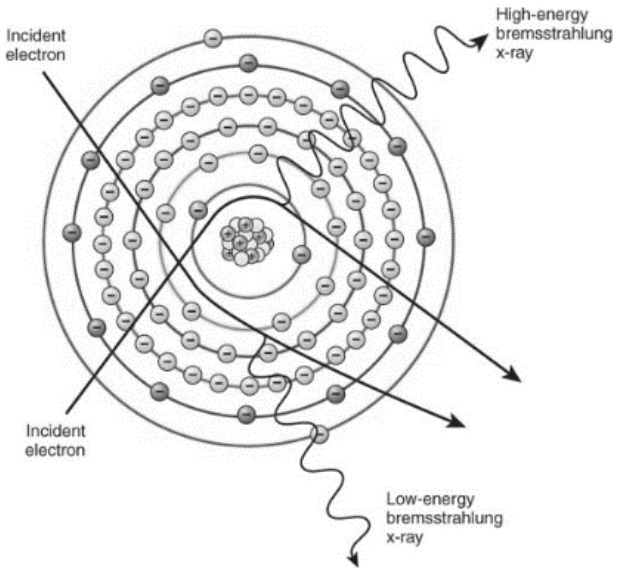

Figure 1.3. Emission of bremsstrahlung radiation.

2.1.2 Characteristic lines

When an incoming particle strikes an atom, it can eject an atomic electron from one of its inner shells if the binding energy of the electron shell is lower than that of the incident particle. The binding energy is the energy required to remove an electron from its shell. As a result, the atom is left in an ionized state due to the vacancy created in the internal shell. To return to its stable state, the initial vacancy must be filled by an outer electron. One of the possible consequences is the emission of a characteristic X-ray (see Figure 1.4). The energy of the latter is equal to the difference between the electron energies of the initial and final states. The emitted X-rays are called "*characteristic*" because their energies are different and unique to each element.

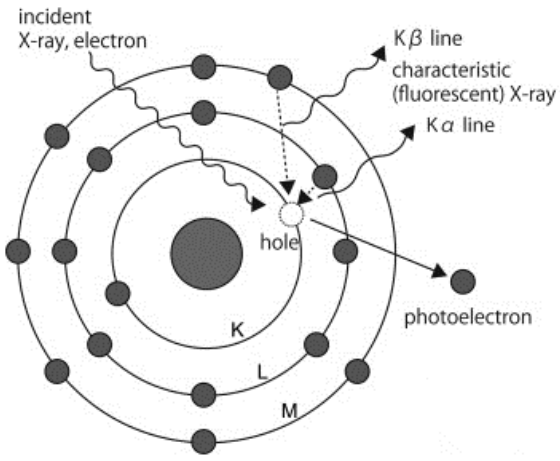

Figure 1.4. XRF generation diagram.

In XRS, two nomenclature systems are used to describe the characteristic X-ray lines. The

commonly used nomenclature was introduced by Siegbahn: it is based on the relative intensities of lines from different series. The X-ray line is named depending on the shell in which the vacancy was created, and includes the chemical symbol for the element, the series symbol (K, L, M) and a line within the series ($\alpha_{1,2}$, $\beta_{1,3}$, etc.). Officially, the Siegbahn notation has been replaced by the International Union of Pure and Applied Chemistry (IUPAC) nomenclature [3], [6].
The IUPAC notation is more systematic. It includes the levels of the initial and final states of the electron. However in practice, the Siegbahn notation is still used [3]. Both the Siegbahn and the IUPAC notations for some X-ray spectral lines are listed in Table 1.1.

Table 1.1. Correspondence between the Siegbahn and IUPAC notations for some X-ray spectral lines.

K Series		L Series		M Series	
Siegbahn	IUPAC	Siegbahn	IUPAC	Siegbahn	IUPAC
$K\alpha_{1,2}$	$K\text{-}L_{2,3}$	$L\alpha_1$	$L_3\text{-}M_5$	$M\alpha_{1,2}$	$M_5\text{-}N_{6,7}$
$K\alpha_1$	$K\text{-}L_3$	$L\alpha_2$	$L_3\text{-}M_4$	$M\beta$	$M_4\text{-}N_6$
$K\alpha_2$	$K\text{-}L_2$	$L\beta_1$	$L_2\text{-}M_4$		
$K\beta_1$	$K\text{-}M_3$	$L\beta_2$	$L_3\text{-}N_5$		
$K\beta_{1,3}$	$K\text{-}M_{2,3}$	$L\Upsilon_1$	$L_2\text{-}N_4$		

Moseley's Law establishes the relationship between the energy of a characteristic X-ray and the atomic number Z:

$$E = C_1(Z - C_2)^2 \tag{1.3}$$

where E is the energy of the characteristic X-ray, and C_1 and C_2 are constants for a given line type [2]. According to Moseley's Law, the energy of any particular line increases with the atomic number of the emitting atom (see Figure 1.5).

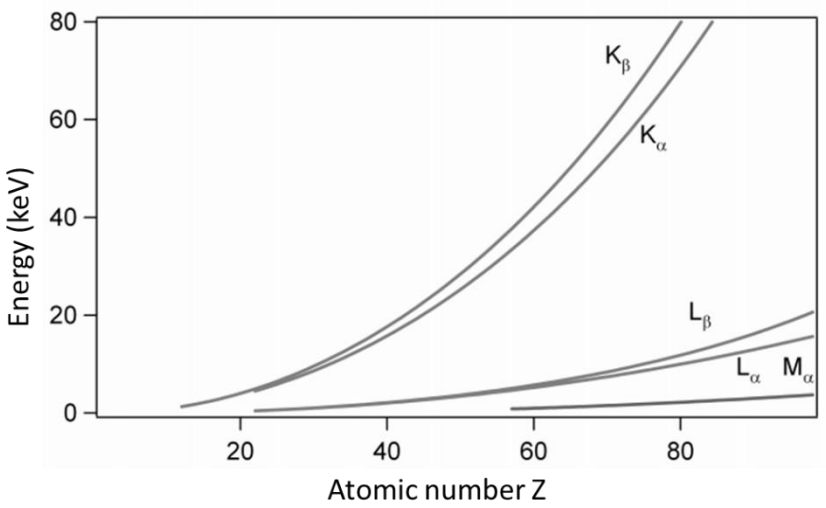

Figure 1.5. Moseley's relationship between energy and atomic number.

The number of electron transitions from any higher to any lower energy level is limited. The

transitions are defined by the quantum-mechanical selection rules for dipolar transitions as:

- $\Delta n \geq 1$
- $\Delta \ell = \pm 1$
- $\Delta J = 0$ or ± 1

where n, ℓ, J are the quantum numbers (see § 1).
The vacancy initially created in the K-shell can be filled by an electron from one of the higher shells (e.g., L-, M-, or N-shell). According to the selection rules, the electron transitions L_2->K, L_3->K, M_3->K, etc. are allowed, whereas the transitions M_5->K, N_5->K are forbidden (see Figure 1.6) [1], [10].

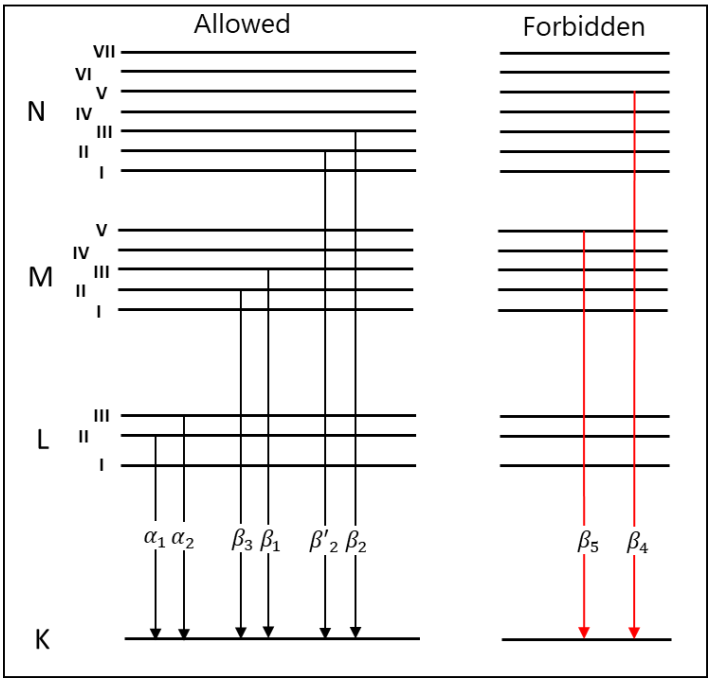

Figure 1.6. Major transitions following a K-vacancy [10].

Let us consider that an electron from a tungsten atom (W) is ejected by an incident X-ray. The atom is in K^+ state or in L^+ state depending on whether the electron was expelled from the K shell or from the L shell, respectively. It requires 69.525 keV to create a vacancy in the K-shell and only 10.207 keV for the L_{III} subshell. Thus, tungsten is in an ionized state with a 69.525 keV excess of energy if an electron was removed from the K-shell. The ionized atom reverts back to the stable electron configuration by filling the vacancy with an electron from an outer shell, one of which could be from the L_{III} level, resulting in the emission of the W K-L_3 (W-Kα_1, see Table 1.1) X-ray line [3].
The emission of the characteristic spectral line is given by:
K^+ state $\rightarrow$ L_{III}^+ state + K-L_3
which corresponds to:
E (K-L_3) = E (K) – E (L_3) = 69.525 keV - 10.207 keV = 59.318 keV
59.318 keV is the energy of the W K-L_3 X-ray line.

3. Interaction of X-rays with matter

Different interaction processes can occur when X-rays strike a material. On reaching it, some X-rays will be absorbed inside, giving up all their energy to electrons (photoabsorption), and a fraction of X-rays will be scattered (coherently and incoherently) away from their initial directions. These interaction processes are illustrated in Figure 1.7.

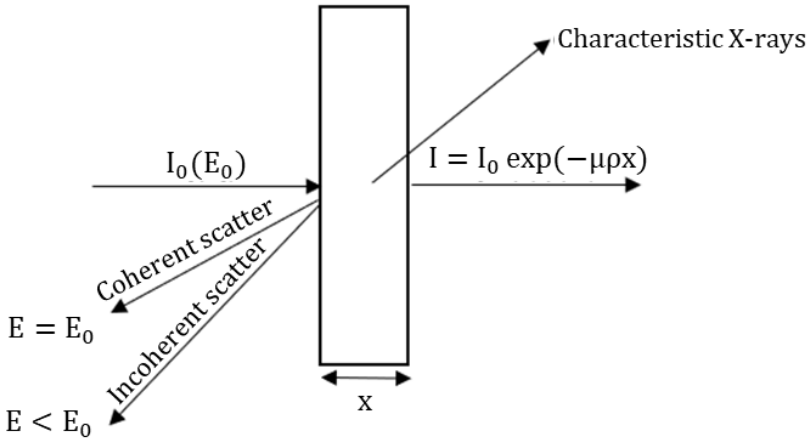

Figure 1.7. Illustration of the interaction of X-rays with matter [10].

Penetrating a layer of material of thickness x and density ρ upon normal incidence, the intensity of the incident X-ray beam $I_0\,(E)$ decreases according to the Lambert-Beer Law:

$$I\,(E) = I_0\,(E)\exp\,(-\mu\rho x) \tag{1.4}$$

where μ is the mass attenuation coefficient of the material, which is dependent on the energy of the incident radiation and the atomic number of the material. It is expressed in $cm^2\ g^{-1}$. The negative sign indicates a decrease in intensity [2]. Extensive tabulations of mass attenuation coefficients for atoms from Z = 1 (hydrogen) to Z = 92 (uranium) are available in [11], [12].

The mass attenuation coefficient of an element is related to the total interaction cross-section by:

$$\mu = \frac{N_A}{A}\sigma_{tot} \tag{1.5}$$

where N_A is Avogadro's number, and A is the atomic mass number of the corresponding element.

The total cross-section σ_{tot} can be expressed as the sum of the contributions of each interaction process:

$$\sigma_{tot} = \tau + \sigma_{Coh} + \sigma_{Incoh} \tag{1.6}$$

where τ is the photoabsorption cross-section, and σ_{Coh} and σ_{Incoh} are the coherent and incoherent scattering cross-section, respectively [10]. The interaction processes of X-rays

with an atom of the material will decrease its intensity by decreasing the number of X-rays. The total mass attenuation coefficient of a material composed of *n* chemical elements (alloys, solutions, etc.), with the mass fraction in the material W_i and the mass attenuation coefficient $\mu_i(E_0)$ for each element *i* in the material, is given by:

$$\mu_{\text{compound}}(E_0) = \sum_{i=1}^{n} \mu_i(E_0) W_i \tag{1.7}$$

The interaction of X-rays with matter and the properties of each interaction process will be discussed in more detail in the following paragraphs.

3.1. Photoabsorption

In the photoabsorption process, the incident X-ray interacts with a bound (internal) electron, which absorbs the incident energy and is consequently ejected. The emitted inner shell electron is called a "*photoelectron*". Photoabsorption takes place when the energy of an incoming X-ray E_X is higher than the binding energy of the electron E_B. Some of the incident X-ray energy is spent overcoming the binding energy of the atomic electron, and the rest is transferred to the electron. Photoelectron kinetic energy E_k is expressed as:

$$E_k = E_X - E_B \tag{1.8}$$

The atom is left in an ionized state, since a "*vacancy*" has been created in one of the inner shells due to the electron ejection. Photoabsorption is followed by atomic relaxation: an electron from one of the outer shells fills the vacancy, resulting in the release of energy in a form of a characteristic X-ray or an Auger electron. The first process is called X-ray fluorescence (XRF) and will be described in § 3.3. In the Auger-transition process, the excess energy is transferred within the atom to a lower-energy electron, which is then emitted from the atom. The expelled electron is known as an Auger electron, and provides chemical information about the emitting atom [2].
Photoabsorption can occur at each energy level of the atom, and the total photoabsorption cross-section τ_i can be written as the sum of each absorption cross-section within an individual (sub)shell:

$$\tau_i = \tau_K + \tau_{L1} + \tau_{L2} + \tau_{L3} + \tau_M \ldots \tag{1.9}$$

The tabulated values of the photoabsorption cross-sections and mass absorption coefficients are available in [12], [13].
The mass photoabsorption coefficient as a function of energy is plotted in Figure 1.8.

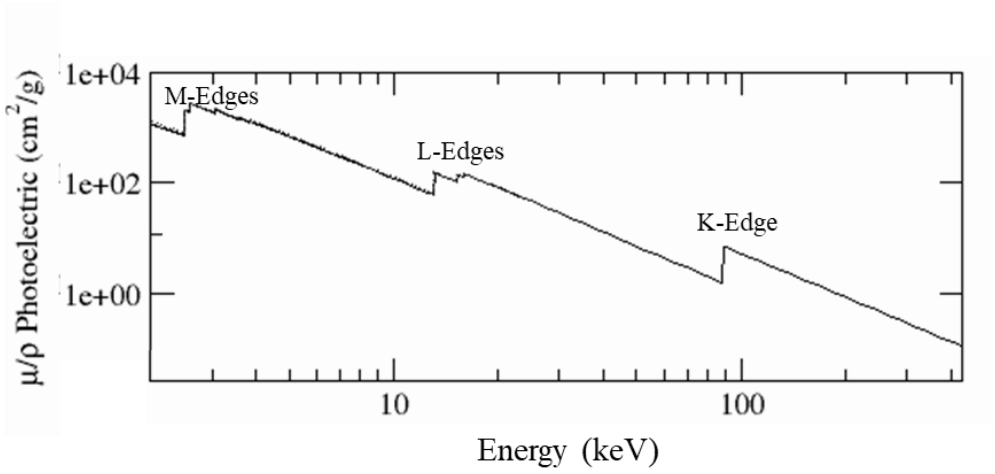

Figure 1.8. Mass photoabsorption coefficient for Pb [14].

In Figure 1.8, the sharp discontinuities observed at specific energies correspond to the binding energies of the electrons in the (sub)shells and are called "*absorption edges*". The absorption cross-section increases with decreasing energy of X-rays. Starting from high energies, and decreasing, if the energy of an incoming X-ray approaches the binding energy of an electron, the probability of absorption increases and reaches its maximum at the binding energy. A sharp drop is followed (K absorption edge) and the probability becomes lower. Afterwards, this is repeated at the L- and M- shells. The number of absorption edges of each element corresponds to the number of electron (sub)shells, and each edge is denoted with the name of the electron shell.
The probability that the absorbed X-ray will expel an electron from the K shell rather than from L or M shells is given by the absorption jump ratio. As an example, the K-shell absorption jump ratio is expressed by:

$$J_k = (r_k - 1)/r_k \tag{1.10}$$

where r_k is the K-shell absorption jump which is defined as the ratio of τ_{max} just above an absorption edge and τ_{min} below that edge [10], [15], [16]:

$$r_k = \tau_{max}/\tau_{min} \tag{1.11}$$

3.2. Scattering

In the scattering processes, an X-ray collides with one of the electrons of an element, which causes a change in the X-ray direction. The electromagnetic theory describes coherent and incoherent scatterings.
Coherent or Rayleigh scattering is the process in which an X-ray is scattered by bound atomic electrons without ionization of the atom during the collision, i.e., without energy loss. The energy of the X-ray remains unchanged after the scattering, and only its direction is affected [17].
The total atomic cross-section for Rayleigh scattering is given by [18]:

$$\sigma_R = \pi r_e^2 \int_{-1}^{1} (1 + \cos^2\theta)[F(x,Z)]^2 d(\cos\theta) \tag{1.12}$$

where r_e is the classical electron radius and θ is the scattering angle.
The atomic form factor $[F(x,Z)]$ is expressed by:

$$F(x,Z) = \int_0^{\infty} \rho(r) 4\pi r \frac{\sin[(2\pi/\lambda)rs]}{(2\pi/\lambda)rs} dr \tag{1.13}$$

where ρ(r) is the total density, r is the distance to the nucleus, and s=2sin(θ/2). Detailed tabulation of the atomic form factors can be found in [19].
In another collision process, the incident X-ray gives up part of its energy and momentum to a weakly bound atomic electron. This is referred to as Compton or incoherent scattering. As a consequence of the energy transfer, the electron leaves the atomic shell and the X-ray itself is deflected by an angle θ compared to its initial direction, and with lower energy (see Figure 1.9) [2], [20].

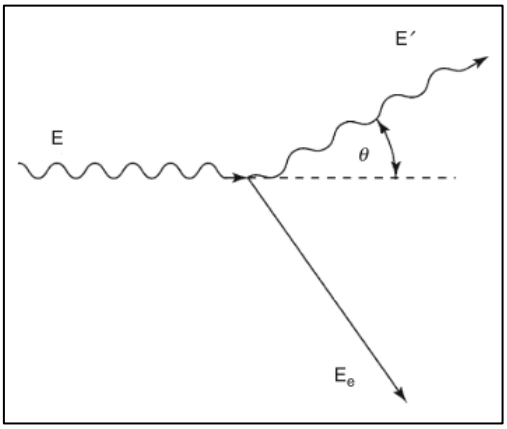

Figure 1.9. Illustration of the process of Compton scattering.

The energy of the scattered X-ray E' is given by the Compton equation:

$$E' = \frac{E}{1 + \frac{E}{m_0 \cdot c^2}(1 - \cos\theta)} \tag{1.14}$$

where E is the initial energy of the X-ray, m_0c^2 is the rest-mass energy of an electron which is equal to 510.996 keV, and θ is the scattering angle. From Eq. (1.14), it follows that the energy of the scattered X-ray depends on the energy of the incident X-ray and the scattering angle, but it is independent of the atomic number *Z*.
The probability that an X-ray will be scattered into a solid angle *dΩ* is expressed by the differential cross-section. The incoherent differential cross-section is given by the Klein-Nishina formula:

$$\frac{d\sigma_{Co}^{KN}}{d\Omega} = \frac{r_e^2}{2}\left(\frac{E_C}{E}\right)^2\left(\frac{E_C}{E} + \frac{E}{E_C} - \sin^2\theta\right) \quad (1.15)$$

3.3. Emission of fluorescent X-rays

X-ray fluorescence is based on the ionization of the atoms with X-rays. An incident X-ray can be completely absorbed by the atom, causing the ejection of an inner shell electron (see § 3.1). The atom is left in an ionised state due to the hole created in the orbit. As described above, the ionisation of an atom can be followed by the emission of either a fluorescence X-ray or an Auger electron. The probability that energy will be released through radiative transition rather than non-radiative or Auger-effect transition is called the fluorescence yield. This value is determined as the ratio of the total number of characteristic X-rays emitted to the total number the vacancies in an electronic shell. For example, the fluorescence yield of the K shell is given by:

$$\omega_k = I_k/n_k \quad (1.16)$$

where I_k is the total number of the K-fluorescent X-rays emitted and n_k is the number of primary K shell vacancies [21]. The fluorescence yield increases with the atomic number Z. It is approximated by:

$$\omega = Z^4/(A + Z^4) \quad (1.17)$$

where A is 10^6 for K X-rays and 10^8 for L X-rays [22].
The fluorescence yield of atomic shells above the K shell is a more complicated value to determine, since higher shells consist of several subshells and radiationless transitions between subshells can take place. These processes are known as Coster-Kronig transitions [15], [21]. The fluorescence yields of K and L shells of some medium-Z elements and high-Z element are listed in Table 1.2

Table 1.2. Fluorescence yields of some elements [23].

Element	Shell	ω
Sr	K	0.690
Y	K	0.710
Zr	K	0.730
U	L3	0.489
Pu	L3	0.514

4. XRF quantitative analysis

The goal of quantitative XRF analysis is to convert the measured X-ray fluorescence intensity into the concentration of an analyte element. The observed net X-ray intensity of the element of interest, besides its concentration, is also dependent on the matrix effects (absorption and enhancement), sample type and method of preparation, the flux and distribution of a primary X-rays, parameters of the detection system, etc. [24].

XRF quantitative analysis is divided into two steps: spectrum processing and matrix corrections. The objective of spectrum processing is to extract the net peak area of the fluorescent line of the analyte. This task refers to mathematical procedures such as digital filters (smoothing filters) to reduce noise, background estimation to eliminate the continuum, and fitting to derive the analytically important information from the measured spectrum. The characteristic peaks are predominantly described by Gaussian function; however, in some cases they may be fitted with Voigt or Hypermet functions or a combination of several (Gaussians including tail and step functions, etc.). The fitting of the peak profile obtained with a semiconductor detector involves a Voigt profile. This represents the convolution of the Gaussian detector response function with the Lorentzian function which is linked to the width of electronic subshells. The X-ray spectrum evaluation procedures and some examples will be presented in detail in Chapter 7.

After spectrum processing, the net intensity of a fluorescent line is determined and quantification can be accomplished using matrix correction approaches. These determine the relationship between the measured X-ray intensities and the concentrations of the matrix elements. In quantitative XRF analysis, theoretical or empirical correction methods are employed to do this. The theoretical methods are based on mathematical equations to describe the relationship. Another way to correct the effect of the matrix elements on the intensity emitted by an analyte is to use empirical methods, which involve influence coefficients.

It is necessary to understand all the phenomena that contribute to the appearance of the resulting spectrum in order to accurately interpret the results obtained. The following paragraphs will present the main parts of a typical XRF spectrum and discuss theoretical and some empirical approaches.

4.1 Components of the XRF spectrum

The phenomena discussed in § 3 contribute to the final appearance of the XRF spectrum. This spectrum shows the intensity of X-rays (in counts or counting rate) as a function of energy (in eV or keV). An energy-dispersive XRF spectrum of the sample solution irradiated by the Ag anode X-ray tube is shown in Figure 1.10. It contains characteristic peaks, Rayleigh and Compton scattering peaks from the tube target material, and background continuum.

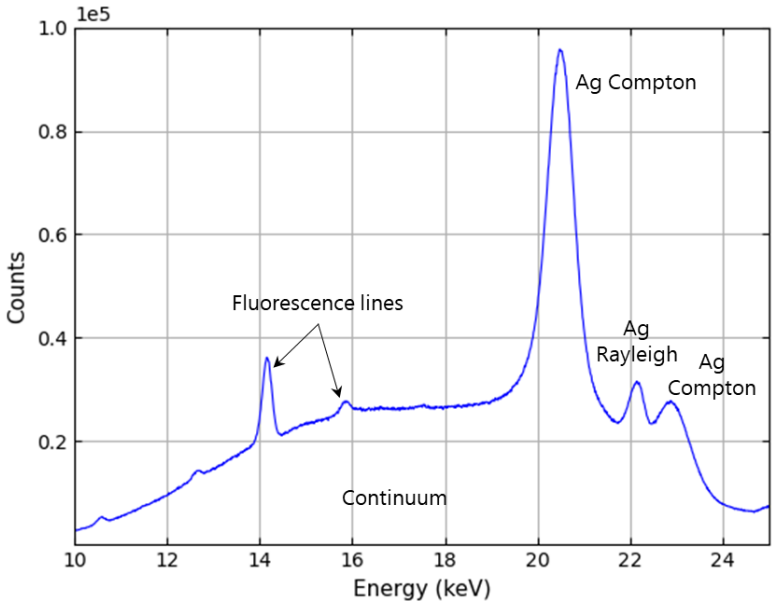

Figure 1.10. Typical XRF spectrum from a liquid sample irradiated with the Ag-anode X-ray tube.

The fluorescence lines of the analyte element (strontium (Sr) in this example) are superimposed on the background and are the key components in the XRF spectrum. X-rays deposit their full energies after being completely absorbed within the active volume of the detector, and appear as the full-energy peaks (FEP). The intensity of a fluorescence peak of an element is proportional to the total number of X-rays recorded in the detector.

The shape of the background depends on the sample composition and the shape of the primary spectrum. *The background continuum* observed is due to the coherent and incoherent scattering of primary radiation (Bremsstrahlung and characteristic lines) by the sample, and consists of a broad range of energies. The interaction of radiation with setup elements and the detector also contribute to the spectral background. Figure 1.10 illustrates the case of a liquid sample.

Rayleigh-scattered peaks in the fluorescence spectrum appear exactly at the energies of the fluorescence lines of the tube target material (Ag K-L_3 and Ag K-M_3 in this case). The spectrum of a denser sample shows lower Rayleigh peaks because of the increased absorption of the primary X-rays.

Compton-scattered peaks of the tube anode material result from incoherent scattering. They are observed at energies shifted toward lower values, which depend on the incident angle and the energy according to the Compton equation (see Eq. (1.14)).

In the EDXRF spectrum, apart from the peaks discussed above, other peaks may appear, such as sum and escape peaks, and characteristic peaks of other elements from the surroundings of the experimental setup (e.g., setup housing, filter material, etc.) can occur.

4.2 Theoretical equations

The intensity of the fluorescence line in a spectrum is related to the concentration of a

corresponding element in a sample. The mathematical derivation of this relationship was established by Sherman. He proposed a mathematical formula to calculate the X-ray intensities emitted by an analyte in a sample of known composition [25].
Let us suppose that the monochromatic beam with energy E_0 and intensity I_0 (E_0) is incident on a sample of density ρ_s at an angle ψ' compared to the sample surface (see Figure 1.11).

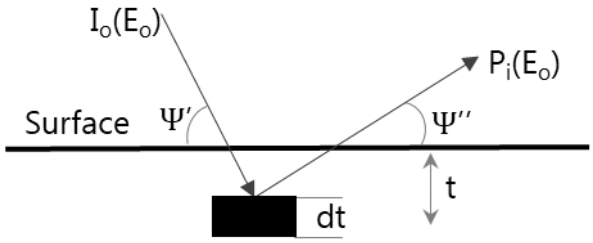

Figure 1.11. Geometry of primary fluorescence emission.

The radiation is attenuated by the sample at depth t below the surface. According to the Lambert-Beer Law, the intensity $I_t(E_0)$ is given by:

$$\mathrm{I_t(E_0) = I_0(E_0)exp[-\mu_s(E_0)\rho_s t\,(csc\,\psi')]} \tag{1.18}$$

where $\mu_s(E_0)$ is the mass attenuation coefficient of the sample for X-rays with energy E_0; $csc\,\psi' = \frac{1}{sin\,\psi'}$
The value of $\mu_s(E_0)$ is the total mass attenuation coefficient of a material of n chemical elements.
The characteristic X-rays are emitted isotropically in all directions and only some of the X-rays are emitted towards the detection system into the solid angle Ω (in units of steradians). The X-rays leaving the sample are detected at an angle ψ'' compared to the sample surface. The intensity $P_i(E_0)$ of element i, excited by incident X-rays with energy E_0, is given by:

$$\mathrm{P_i(E_0) = I_0(E_0)\mu_i(E_0)W_iQ_i(E_0,E_i)(csc\,\psi')\,\frac{\Omega}{4\pi}\,exp\,[-(\mu_s(E_0)\,csc\,\psi' + \mu_s(E_i)\,csc\,\psi'')\rho_s t]\rho_s dt} \tag{1.19}$$

where $Q_i(E_0, E_i)$ represents the factor whose expression for K-L characteristic lines is given by:

$$\mathrm{Q_i(E_0,E_i) = \omega_i\,\frac{r_{Ki}-1}{r_{Ki}}\,f_{iK\alpha}} \tag{1.20}$$

The fraction of absorbed X-rays, that creates vacancies in the K shell in element i, is given by $\frac{r_{Ki}-1}{r_{Ki}}$, where r_{Ki} is the absorption jump ratio of the K shell (see § 3.1). The probability that the vacancy produced by photoabsorption in the K shell will be filled by an electron from the L shell is expressed by the transition probability $f_{iK\alpha}$.
The contributions from all layers of the sample have to be taken into account by integrating the Eq. (1.19) over dt. If the thickness of the sample is considered as infinite, the expression

becomes:

$$P_i(E_0) = I_0(E_0)\mu_i(E_0)W_i(\csc\psi')\,Q_i(E_0,E)\,\frac{\Omega}{4\pi}\int_0^{\infty}\exp\left[-(\mu_s(E_0)\csc\psi' + \mu_s(E_i)\csc\psi'')\rho_s t\right]\rho_s dt \quad (1.21)$$

Leading to a simpler expression for the primary fluorescence:

$$P_i(E_0) = K_i I_0(E_0)\frac{\mu_i(E_0)}{\mu_s(E_0) + G\mu_s(E_i)}W_i \quad (1.22)$$

where $K_i = \frac{\Omega}{4\pi}Q_i(E_0,E_i)$ and $G=\csc\psi''/\csc\psi' = \sin\psi'/\sin\psi''$

In addition, other elements in the sample can be excited by the primary fluorescence radiation if the latter has sufficient energy. The interaction results in the emission of the secondary fluorescence X-rays. Thus, the intensity of the primary element is attenuated, whereas the intensity of the secondary element is enhanced. After some integrations, the intensity of the secondary fluorescence of the analyte *i* induced by characteristic X-rays of energy E_j for an infinitely thick sample becomes:

$$S_{ij}(\mathbf{E}_0,\mathbf{E}_j) = \frac{I_0(\mathbf{E}_0)\mu_j(\mathbf{E}_0)W_j(\csc\psi')\,Q_j(\mathbf{E}_0,\mathbf{E}_j)\,\mu_i(\mathbf{E}_j)W_iQ_i(\mathbf{E}_j,\mathbf{E}_i)\frac{\Omega}{4\pi}}{2(\mu_s(\mathbf{E}_0)\csc\psi' + \mu_s(\mathbf{E}_i)\csc\psi'')} \times\left(\frac{\csc\psi'}{\mu_s(\mathbf{E}_0)}\ln\left[1+\frac{\mu_s(\mathbf{E}_0)}{\mu_s(\mathbf{E}_j)\sin\psi'}\right] + \frac{\sin\psi''}{\mu_s(\mathbf{E}_j)}\ln\left[1+\frac{\mu_s(\mathbf{E}_j)}{\mu_s(\mathbf{E}_j)\sin\psi''}\right]\right) \quad (1.23)$$

The total intensity is given by the sum of primary (see Eq. (1.22)) and secondary (see Eq. (1.23)) fluorescence:

$$I_i(E_0) = P_i(E_0) + \sum_j S_{ij}(E_0,E_j) \quad (1.24)$$

In the case of an incident polychromatic beam, the total intensity I_{total} must be considered for each energy:

$$I_{total} = \int_{E_{min}}^{E_{edge,i}} I_i(J(E))dE = \int_{E_{min}}^{E_{edge,i}} [P_i(E) + \sum_j S_{ij}(E_0,E_j)]dE \quad (1.25)$$

where $E_{edge,i}$ is the energy of the absorption edge of the analyte *i*, $J(E)$ is the function which represents the tube spectrum [15].

Sherman's equation is very important for XRF analysis and plays a key role in the development of other methods for the correction of matrix effects.

5. Matrix effects

The relationship between the intensity of a fluorescence line and the concentration of an analyte must be established taking into account any inter-element interaction within a sample. The effects of each matrix element on the analyte intensity are called *matrix effects*, and can cause the absorption (primary and secondary) and enhancement of X-rays in a sample.
The matrix elements absorb the fluorescent X-rays of the analyte in an amount relative to the value of the attenuation coefficient. The strongest enhancement effect occurs when a matrix element emits fluorescent X-rays with the energy just above the absorption edge of the analyte element.
Matrix effects include elemental interactions (absorption and enhancement) and also physical effects (particle size, surface effects and effects due to physical states) [2].
Physical effects can have a considerable effect on the X-ray intensities, since the radiation measured depends upon the effective penetration depth of the measured energy. A sample can be solid, liquid, or powder, and its preparation is a very important step [26]. For example, metals have to be polished at the surface; powdered samples must be prepared as a very fine powder in order to obtain a homogeneous sample and avoid particle-size effects. Liquid samples also require special preparations because different problems can arise, such as bubbles forming in the liquid, evaporation, and precipitations during irradiation, etc.. The major difficulty in the analysis of liquid samples is the background radiation produced, which limits the analysis of low-concentration elements.

5.1. Fundamental parameters method

The fundamental parameters (FP) method is widely used for the correction of matrix effects in order to convert measured XRF intensities into elemental concentrations [26] - [32]. These methods are based on Sherman's equation. Eq. (1.25) allows determination of the intensity of the characteristic radiation of an analyte originating from a sample of known composition, and takes into consideration the primary and secondary fluorescence.
The intensities measured depend on:

- Matrix composition,
- Thickness of the analysed sample,
- Geometry of the experimental setup,
- Flux and spectral distribution of the excitation source,
- Efficiency and resolution of the detection system.

The X-ray tube spectrum requires special attention, and can be calculated using existing theoretical algorithms (e.g. [9]). The analysis of light elements differs from that of intermediate and high Z-elements, due to the lower fluorescence yield. The excitation of low-Z elements by an X-ray tube is very low since there is no anode material of an X-ray tube in the energy range of the absorption edges of light elements and because their fluorescence yields are weak.

Compared with the empirical coefficient method, which will be described in the next paragraph, the FP method assumes only that the sample is homogeneous and has a flat surface. The FP method is considered as the state-of-the-art method for matrix effect corrections.

5.2. Influence coefficient algorithm

The empirical methods can be used as another solution in correcting for matrix effects. These methods determine the relationship between the intensity of characteristic radiation and the analyte concentration by means of influence coefficients. The latter are numerical coefficients and can be determined from theory (using FP equations) or from experimental data. Consequently, algorithms are classified in two categories: theoretical and empirical [32]. The quantification procedure can be limited to a certain range of concentrations, and requires carefully prepared sets of standard samples similar to the unknown ones.
A number of influence coefficient algorithms are available [15], [24], [26], [30]. In the influence coefficient models, the total matrix effect M_i is expressed as:

$$\mathrm{M_i} = 1 + \sum_{\mathrm{j}} \alpha_{\mathrm{ij}}\ \mathrm{W_j} \tag{1.26}$$

where α_{ij} is the influence coefficient which expresses the influence of the matrix element *j* on the analyte *i*, and W_j is the weight fraction of a matrix element *j*.
The weight fraction of the analyte W_i can be written in terms of the relative radiation intensity, R_i:

$$\mathrm{W_i} = \mathrm{R_i M_i} \tag{1.27}$$

This relationship can be derived by combining Eq. (1.26) and Eq. (1.27):

$$\mathrm{W_i} = \mathrm{R_i}\left[1 + \sum_{\mathrm{j}} \alpha_{\mathrm{ij}}\ \mathrm{W_j}\right] \tag{1.28}$$

A number of influence coefficient algorithms are obtained using general expression (1.28). One of the algorithms was proposed by Lachance and Traill, where the influence coefficients can be obtained from multiple regression analysis using reference materials or from the relative radiation intensity [30].
Rousseau presented the fundamental algorithm which combines the fundamental parameters method and the influence coefficient concept, and can be applied to calculate the composition of any sample type [27], [28], [30] - [32].

6. Conclusions

X-rays are one of the forms of electromagnetic radiation, and have an energy range from the ultraviolet and the γ-ray radiation. X-rays can be emitted in continuous radiation or

characteristic radiation with discrete energies, as discussed in the first section of this chapter. X-rays can be absorbed or scattered in the interaction process with the matter. The absorption process gives rise to the emission of fluorescence lines with energies characteristic of the emitting atom. This property of X-rays is applied to extract the quantitative and qualitative information on a sample. The purpose of quantitative XRF analysis is to convert fluorescence intensities into elemental concentrations. However, the issue is complex because the measured intensities, besides the concentrations, are dependent on the matrix, the spectral distribution of the X-ray source, the measurement conditions, the efficiency of the detection system, etc. For accurate quantitative analysis, theoretical and empirical approaches are applied. In this chapter, the theoretical method based on mathematical equations and some empirical methods have been presented. Chapter 3 will discuss the nuclearized system and the miniature XRF setup, in which quantitative analysis is based on the empirical approach and FP method, respectively.

References

[1] R. Jenkins. *X-Ray Fluorescence Spectrometry Second Edition*. Wiley, 1999.

[2] E. P. Bertin. *Introduction to X-Ray Spectrometric Analysis*. Springer Science, 1978.

[3] A. R. Duncan, J. P. Willis. *Understanding XRF Spectrometry Volume 1*. PANalytical, 2008.

[4] P. Brouwer. *Theory of XRF Third Edition*. PANalytical, 2010.

[5] "Typical X-ray Spectra by Anode Material - X-Ray Technology Learning Centre- Oxford Instruments". (available at https://xray.oxinst.com/learning/view/article/typical-x-ray-spectra-by-anode-material).

[6] R. Jenkins, R. Manne, R. Robin, and C. Senemaud. "Nomenclature system for X-ray spectroscopy", *Pure Appl. Chem.*, 63, 735–746, 1991.

[7] "What is a synchrotron?". (available at https://www.esrf.eu/about/synchrotron-science/synchrotron).

[8] M. Haschke. *Micro-X-Ray Fluorescence Spectroscopy Instrumentation and Application.* Springer, 2014.

[9] H. Ebel. "X-ray Tube Spectra", *X-Ray Spectrom.*, 28, 255–266, 1999.

[10] K. Janssens. "*Chapter 4. X-ray based methods of analysis" in Comprehensive Analytical Chemistry.* Elsevier, 129-226, 2004.

[11] J. H. Hubbell, S. M. Seltzer. "Tables of X-ray mass attenuation coefficients and mass energy-absorption coefficients", *NIST Res. Inf.*, 1–111, 1995.

[12] C. T. Chantler. "Theoretical Form Factor, Attenuation and Scattering Tabulation for Z=1-92 from E=1-10 eV to E=0.4-1.0 MeV", *J. Phys. Chem.*, 24, 71, 1995.

[13] B. L. Henke, E. M. Gullikson, J. C. Davis. "X-ray interactions: photoabsorption, scattering, transmission, and reflection at E = 50-30, 000 eV, Z = 1-92", *At. Data Nucl. Data Tables*, 54, 181–342, 1993.

[14] "X-Ray Form Factor, Attenuation, and Scattering Tables | NIST". (available at https://www.nist.gov/pml/x-ray-form-factor-attenuation-and-scattering-tables).

[15] R. E. Van Grieken, A. A. Markowicz. *Handbook of X-ray Spectrometry Second edition*. Marcel Dekker, Inc., 2001.

[16] V. Thomsen. "Basic Fundamental Parameters in X-Ray fluorescence", *Spectroscopy*, 22, 46–50, 2007.

[17] L. Méray, E. Házi. "Effect of scattered photons on the intensities of X-ray characteristic lines", *Acta Phys. Hungarica*, 63, 171–176, 1988.

[18] F. Salvat, J. Fernández-Varea, J. Sempau. *PENELOPE-2014: A Code System for Monte Carlo Simulation of Electron and Photon Transport.* OECD/NEA Data Bank, 2014.

[19] J. H. Hubbell, W. J. Veigele, E. A. Briggs, R. T. Brown, D. T. Cromer, R. J. Howerton. "Atomic form factors, incoherent scattering functions, and photon scattering cross sections", *J. Phys. Chem. Ref. Data*, 4, 471–538, 1975.

[20] M. Van Gysel, P. Lemberge, P. Van Espen. "Description of Compton peaks in energy-dispersive x-ray fluorescence spectra", *X-Ray Spectrom.*, 32, 139–147, 2003.

[21] W. Bambynek, B. Crasemann, et al. "X-Ray fluorescence yields, Auger, and Coster-Kroning transition probabilities. Rewiews of Modern Physics", *Rev. Mod. Phys.*, 44, 716–813, 1972.

[22] M. C. Miller. "*Chapter 10. X-Ray Fluorescence" in Passive Nondestructive Assay of Nuclear Materials*. Los Alamos National Laboratory, 313-335, 1991.

[23] M. O. Krause, "Atomic radiative and radiationless yields for K and L shells", *J. Phys. Chem.*, 8, 307–327, 1979.

[24] Sitko, B. Zawisz. "*Chapter 8. Quantification in X-Ray Fluorescence Spectrometry" in X-Ray Spectroscopy*. InTech, 137-162, 2012.

[25] J. Sherman. "The theoretical derivation of fluorescent X-ray intensities from mixtures.", *Spectrochim. Acta*, 7, 283–306, 1955.

[26] B. Beckhoff B. Kanngießer N. Langhoff R. Wedell H. Wolff (Eds.). *Handbook of Practical X-Ray Fluorescence Analysis*. Springer, 2006.

[27] R. M. Rousseau, J. A. Boivin. "The fundamental algorithm: A natural extension of the Sherman equation Part 1: Theory", *Rigaku J.*, 15, 13–28, 1998.

[28] R. Rousseau. "Fundamental Algorithm between concentration and itensity in XRF analysis 1-Theory", *X-Ray Spectrom.*, 13, 115, 1984.

[29] J. W. Criss, L. S. Birks. "Calculation Methods for Fluorescent X-Ray Spectrometry: Empirical Coefficients vs. Fundamental Parameters", *Anal. Chem.*, 40, 1080–1086, 1968.

[30] R. M. Rousseau. "Corrections for matrix effects in X-ray fluorescence analysis-A tutorial", *Spectrochim. Acta - Part B*, 61, 759–777, 2006.

[31] R. M. Rousseau. "The Quest for a Fundamental Algorithm in X-Ray Fluorescence Analysis and Calibration", *Open Spectrosc. J.*, 3, 31–42, 2009.

[32] R. M. Rousseau. "Concept of the Influence Coefficient", *Rigaku J.*, 18, 8–21, 2001.

Chapter 2

Diffraction

The research on X-ray diffraction by Max von Laue in 1912 showed that crystals are able to diffract X-rays in a characteristic manner. In experiments, he investigated whether the interplanar spacing of the crystals can be defined when X-rays with known wavelengths are impinging on a crystal or conversely, whether the wavelength of the X-rays can be determined if the interatomic distances in the crystal are known. The experimental results confirmed the wave properties of X-rays. The investigation of X-ray diffraction (XRD) by crystals gave the opportunity to study the structure of crystal materials precisely and to develop new technical applications.

Based on the research of XRD by von Laue, W. H. Bragg presented the geometrical interpretation of X-ray diffraction that is analogous to those used in classical optics. Nowadays, XRD based techniques have become very powerful tools in materials science: they are used for structure determination, studies of crystal surfaces, the measurement of particle sizes, the determination of the orientation of the crystal lattice, etc. [1] - [4]. The diffraction patterns obtained contain information about the sample features. The application of X-ray optical elements in experimental setups may fulfil the requirements to obtain monochromatic and concentrated X-ray beams. X-ray optical elements enable a setup to focus, monochromatize, or reflect X-rays [4].

This chapter presents the fundamentals of geometrical optics, the wave properties of X-rays, and the phenomenon of X-ray diffraction that is the interaction of both. The basics of the crystal structure and some characteristic parameters will be presented. The specific structure of mosaic crystals and their diffraction properties will be described. X-ray analysis setups using mosaic crystals are widely implemented in many domains. Such optical elements can be used as monochromators or dispersion filters, and permit the recording of a spectrum in the desired energy range. Modern optical elements applied in elemental analysis will be

presented.

1. Geometrical optics

X-rays, like other forms of electromagnetic radiation, exhibit wave-particle duality. In the previous chapter, the interaction of X-rays with matter has been explained in terms of particles (corpuscles) having discrete energies. X-ray radiation also demonstrates wave properties characterised by wavelength and frequency. The principles of the interaction of X-rays with matter can be explained within the framework of classical optics by means of refraction index *n*. Let us consider an X-ray beam of wavelength λ incident at an angle α_0 at a plane interface (see Figure 2.1).

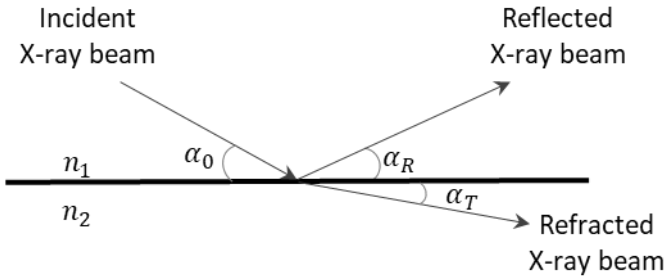

Figure 2.1. Reflection and refraction of an X-ray beam at the interface between two media.

The interface is the geometrical plane separating two homogeneous media of different optical densities having the refraction indices n_1 and n_2, respectively, where $n_1 > n_2$. The incident X-ray is partly reflected and partly refracted (transmitted) at this interface. The angle of reflection α_R is equal to the angle of the incident beam α_0. Considering absorption and scattering processes in the medium, the refraction index can be expressed as:

$$\mathrm{n} = 1 - \delta - \mathrm{i}\beta \tag{2.1}$$

with

$$\delta = \frac{\lambda^2 \, \mathrm{r_0} \, \rho \, \mathrm{N_A} \mathrm{f_1}(\lambda)}{2 \, \pi \, \mathrm{A}} \tag{2.2}$$

The imaginary part of the refraction index is related to the attenuation coefficient through the following expression:

$$\beta = \frac{\lambda^2 \, \mathrm{r_0} \, \rho \mathrm{N_A} \mathrm{f_2}(\lambda)}{2 \, \pi \, \mathrm{A}} = \frac{\lambda \, \mu_\mathrm{m}}{4 \, \pi} \tag{2.3}$$

where r_0 is the classical electron radius, ρ is the density of the medium, N_A is Avogadro's number, A is the atomic mass, $f_1(\lambda)$ and $f_2(\lambda)$ are atomic scattering factors, and μ_m is the mass attenuation coefficient. The values of δ and β can be calculated for different wavelengths using atomic scattering factors tabulated in [5], [6].
The refraction index can also be written in terms of the scattering factors as:

$$n = 1 - \frac{\lambda^2 r_0 \rho N_A}{2 \pi A}\{f_1(\lambda) + i f_2(\lambda)\} \tag{2.4}$$

While passing to a medium with another optical density, the X-ray beam is refracted from the interface of the two media. According to Snell's law, the incident and refraction angles are related to the refraction indices of the two media through:

$$\frac{n_1}{n_2} = \frac{\cos \alpha_T}{\cos \alpha_0} \tag{2.5}$$

where α_0 and α_T are the incident and refraction angles, respectively.
In the wavelength range of X-rays (from 0.01 nm to 10 nm), the real part of the refraction index in Eq. (2.1) is slightly smaller than unity for any medium, while for a vacuum (or air) the value of n is equal to 1. If the X-ray beam is incident below a certain critical angle α_C (where $\alpha_T = 0°$), it travels along the boundary. In accordance with Snell's law, the critical angle is defined as:

$$\cos \alpha_c = \frac{n_2}{n_1} \tag{2.6}$$

The value is related to δ through the following equation:

$$\alpha_C \approx \sqrt{2\,\delta} \tag{2.7}$$

At angles below α_C (the so-called grazing incident angles), the X-ray beam undergoes total external reflection [7], [8].

2. Crystal structure

The X-rays incident on a crystal are diffracted in a characteristic manner. It is necessary to have knowledge about its structure, because this determines how X-rays are diffracted. This paragraph discusses the basics of crystal structure and some characteristic parameters. A special emphasis is placed on the structure and features of mosaic crystals, and in particular on the highly oriented pyrolytic graphite (HOPG) crystal as the latter is of particular interest for this thesis.

2.1. General structure of crystals

A crystal is a solid material composed of atoms or molecules arranged in ordered structures. Atoms in a crystal may be regarded as an array of intersection points of the lines of a framework, called a space lattice, in three-dimensional space (see Figure 2.2, left panel). In turn, the points in the space lattice are called lattice points and they are arranged so that each one has identical surroundings. Each space lattice can be described by a unit cell, which corresponds to the smallest unit volume (fundamental unit) of the space lattice (see Figure 2.2, right panel).

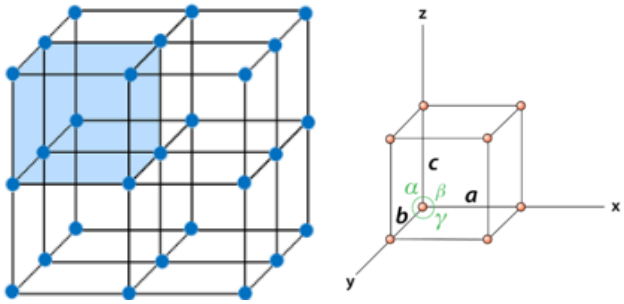

Figure 2.2. Illustration of a space lattice (left panel) and a unit cell (right panel).

The shape and dimensions of a unit cell are specified by three lattice vectors ($\vec{a}, \vec{b}, \vec{c}$) which present the crystallographic axes of the cell. They can also be specified by lengths (a, b, c) and by angles between these (α, β, γ). These sets of values are termed the lattice parameters [1]. The structures of all crystals are classified in crystal systems depending on the symmetry of the unit cells. The latter can be determined by assigning the specific values of lattice parameters to a unit cell. There are seven crystal systems: Triclinic, Monoclinic, Orthorhombic, Tetragonal, Trigonal, Hexagonal, and Cubic. Another very important characteristic of a crystal is the Bravais lattice. The crystal systems have repeating variations of the unit cells that can be described by 14 Bravais lattices. Detailed descriptions and illustrations of the crystal systems and Bravais lattices can be found in [1] and [9].
The orientation of planes (or family of planes) in crystal lattices are identified with Miller indices. These are the inverse of the intercepts of planes along the lattice vector with crystallographic axes and are denoted *(h k l)*. The Miller indices of lattice planes are illustrated in Figure 2.3.

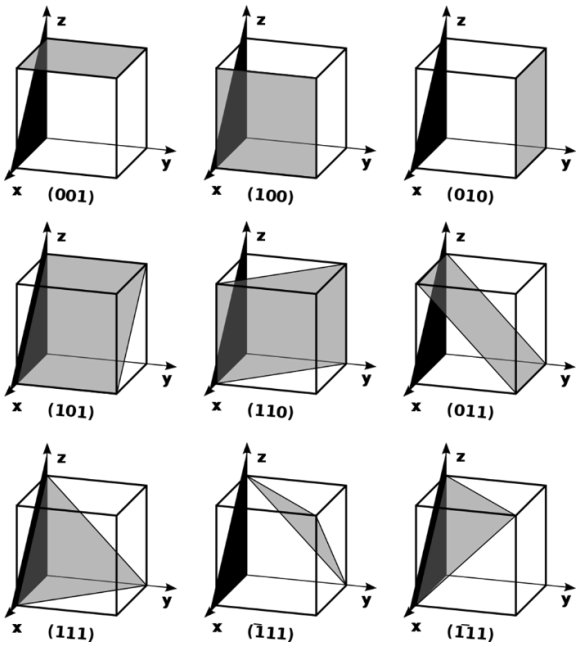

Figure 2.3. Miller indices of lattice planes (in grey).

The distance between two successive planes of a family of planes is constant and is called interplanar spacing (or d-spacing) d_{hkl}. The d-spacing is a function of the lattice parameters (a, b, c, α, β, ϒ) and plane indices (h k l). The exact value of d_{hkl} depends on the crystal system and, as an example, the interplanar spacing for the hexagonal system is given by:

$$\frac{1}{d^2} = \frac{4}{3}\left(\frac{h^2 + hk + k^2}{a^2}\right) + \frac{l^2}{c^2} \tag{2.8}$$

The interplanar spacing for different crystal systems is presented in [1].

2.2. Mosaic crystals

HOPG is an artificial graphite crystal with a mosaic structure. Graphite is built from hexagonal planes of carbon atoms, which in turn are stacked in close-packed planes in an *ABABAB...* sequence (see Figure 2.4). Unlike a simple hexagonal structure where the hexagonal layers are stacked directly one on top of the other, in graphite each *B* layer is generally placed above the voids of each *A* layer [9].

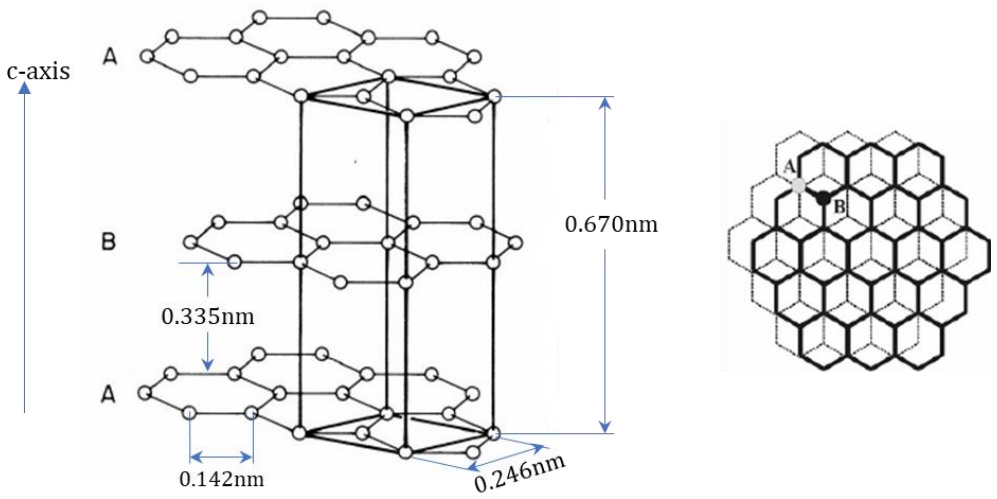

Figure 2.4. Illustration of the hexagonal crystal structure of graphite - c-axis (left panel), and top view (right panel).

The graphite layers lie parallel to the basal plane of the crystal and perpendicular to the *c*-axis. The interplanar distance of crystal d is equal to 0.335 nm; the plane indices (h k l) are (0 0 2). The lattice parameters are listed in Table 2.1.

Table 2.1. Lattice parameters of hexagonal graphite [1].

Lattice parameters	
a	0.245 nm
b	0.245 nm
c	0.670 nm
α	90°
β	90°
γ	120°

An HOPG crystal is built with a large number of mosaic blocks, which in turn consist of graphite crystallites of microscopic size (see Figure 2.5). The angular distribution of the crystallites to the normal axis to the crystal surface is termed the mosaic spread (or mosaicity), and lies in the range from 0.2° to 1.2° [10]. The mosaic blocks are, in turn, slightly misoriented relative to one another, which contributes to the overall mosaic spread [11], [12].

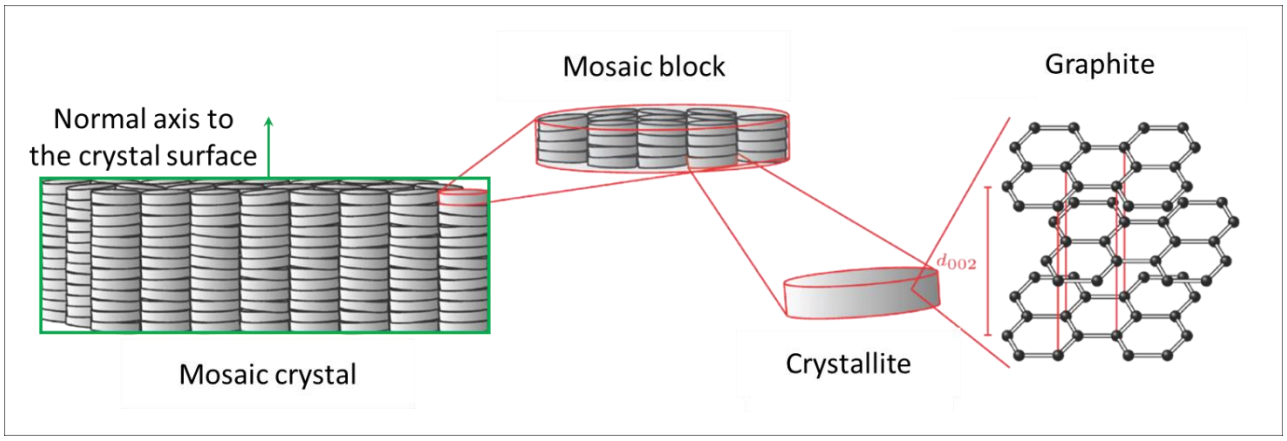

Figure 2.5. Structure of mosaic crystal [13].

HOPG crystals can be mounted on a mould of any desired shape in varying thicknesses, even on a cylindrically shaped element. The diffraction properties of HOPG crystal will be presented in detail in § 4
Another kind of graphite films exists - Highly Annealed Pyrolytic Graphite (HAPG). It has much lower mosaicity (typically <0.1°) than HOPG [14]. Descriptions of the physical properties and applications of both HOPG and HAPG crystals can be found on the web sites of the three original manufacturers in the world: Momentive Performance Materials (USA) [15], Optigraph GmbH (Germany) [16] and Panasonic (Japan) [17].

3. X-ray diffraction

Diffraction phenomenon refers to the processes that take place when the path of an electromagnetic wave encounters an obstacle or an aperture with a size close the wavelength. A change in the wave properties by the limiting its propagation by an obstacle, leads to a redistribution of the emitting intensity in preferred directions. When the X-ray

beam is incident on the crystal, it is diffracted in a characteristic manner due to the periodic atomic planes of the crystal. Therefore, the resulting wave functions are superposed, and constructive and/or destructive interferences are observed. This paragraph discusses the properties and behaviour of electromagnetic waves as well as the geometrical interpretation of X-ray diffraction by crystals and, in particular, by mosaic crystals.

3.1. Electromagnetic waves

Electromagnetic radiation can be regarded as a motion of waves propagating in space which are time-varying electric and magnetic fields, as described by Maxwell. It follows that electric and magnetic fields in an electromagnetic wave are perpendicular to one another, and to the direction of propagation [18]. The electric field E_x and the magnetic field B_y are along the x-axis and the y-axis, respectively, varying sinusoidally with the z-axis:

$$\mathrm{E_x} = \mathrm{E_0}\ \sin\left(\mathrm{kz} - \omega \mathrm{t}\right) \tag{2.9}$$

$$\mathrm{B_y} = \mathrm{B_0}\ \sin\left(\mathrm{kz} - \omega \mathrm{t}\right) \tag{2.10}$$

where λ is the wavelength, ω is the angular frequency and k is the wave number which relates to the wavelength as:

$$\mathrm{k} = 2\pi/\lambda \tag{2.11}$$

Electromagnetic radiation carries energy and is characterised by its intensity, i.e. the fl of the radiation energy which passes through a unit surface perpendicular to the direction of the wave motion per unit of time.

3.2. Diffraction and interference

X-ray diffraction by matter is the result of two different processes: coherent scattering by individual atoms, and interference of the diffracted waves. Coherent scattering takes place when no wavelength (energy) loss is involved in the scattering process, as discussed in Chapter 1. For example, Figure 2.6 illustrates two beams incident upon the periodically ordered array of atoms at an angle α_0.

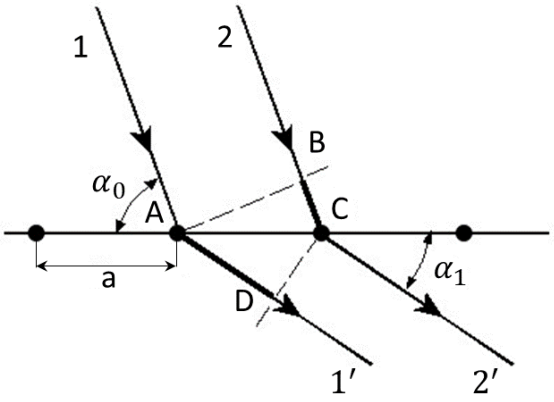

Figure 2.6. Scattering of waves at a row of atoms separated by distance *a*.

Beam 2 reaches the atom with a path difference $BC = a\,cos\,\alpha_0$ relative to beam 1. Both beams are scattered from the row under an angle α_1 but beam 2 travels farther from beam 1 at path difference $AD = a\,cos\,\alpha_1$. The difference in path length between the two beams is equal to (AD-BC), and in order to observe constructive interference this value must be an integer multiple of the wavelength. The relationship is given by:

$$(\mathrm{AD} - \mathrm{BC}) = \mathrm{a}(\cos\alpha_1 - \cos\alpha_0) = \mathrm{n}\,\lambda \tag{2.12}$$

n is an integer and takes the values 0, 1, 2,...

The repeating distance *a* can be regarded as the distance between atoms in a crystal. If an X-ray beam is incident on a space lattice with cell parameters $(\vec{a}, \vec{b}, \vec{c})$, it will be diffracted along these directions satisfying the Laue conditions:

$$\begin{cases} \mathrm{a}(\cos\alpha - \cos\alpha_0) = \mathrm{h}\,\lambda \\ \mathrm{b}(\cos\beta - \cos\beta_0) = \mathrm{k}\,\lambda \\ \mathrm{c}(\cos\gamma - \cos\gamma_0) = \mathrm{l}\,\lambda \end{cases} \tag{2.13}$$

where $(\alpha_0, \beta_0, \gamma_0)$ and (α, β, γ) are incident and diffracted angles, respectively. Thus, the angles are defined by the wavelength of the radiation and the length of a unit cell. X-rays are diffracted by a crystal if the X-ray wavelength is the same order of magnitude as the cell lengths in the crystal.

In the case of constructive interference two waves travel in phase, i.e., their electric field vectors are of the same magnitude, and the direction at any point in space along their motion is the same. If we add the amplitudes of each wave, the resulting value will be greater than the individual results (see Figure 2.7, left panels). When two X-rays are completely out of phase, they undergo destructive interference, or in other words, the waves cancel each other out (see Figure 2.7, right panels).

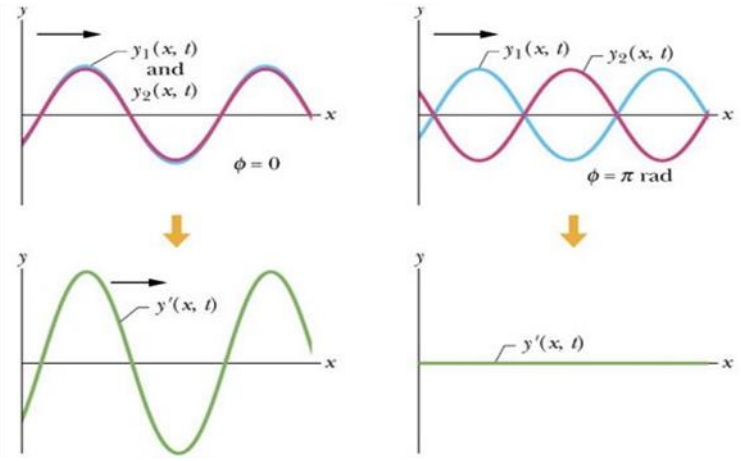

Figure 2.7. Effect of constructive (left panels) and destructive (right panels) interference of waves.

3.3. Bragg diffraction

Based on Laue's equations, Bragg determined the necessary geometrical condition for diffraction, referring to classical optics. The incoming X-rays of wavelength λ strike the crystal planes with an interplanar spacing *d* at an angle *θ* and are reflected at the same angle (see Figure 2.8), as in the geometrical optics presented in § 1.

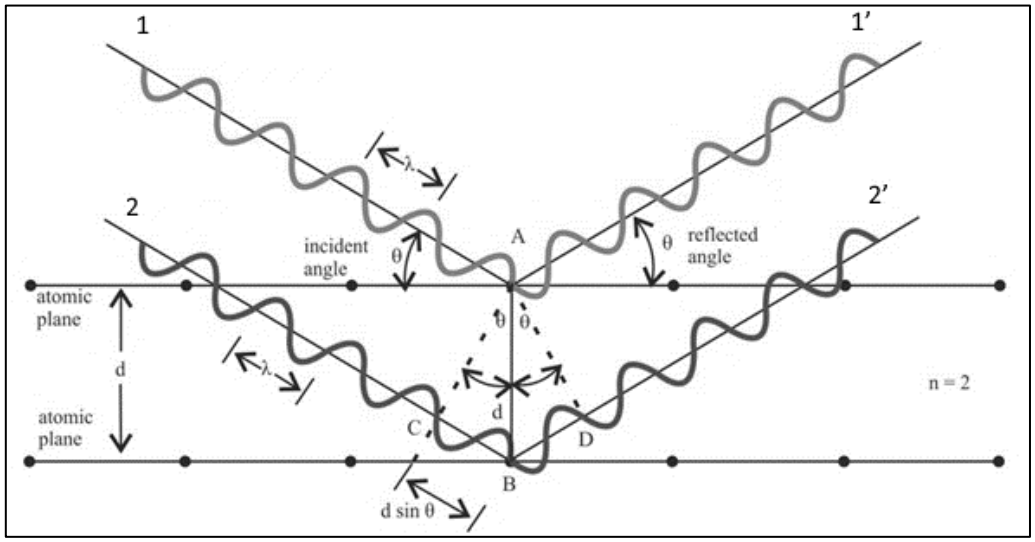

Figure 2.8. Diffraction by a crystal and the derivation of Bragg's law.

Incoming X-ray beam 2 travels farther than beam 1 at a distance (CB+BD), and is reflected at the next crystal plane. The path difference between rays 1A1′ and 2B2′ is given by:

$$\mathrm{CBD} = (\mathrm{CB} + \mathrm{BD}) = 2\,\mathrm{AB}\sin\Theta \tag{2.14}$$

Diffracted rays 1′ and 2′ are completely in phase if their path difference (CBD) is equal to an integer number of λ:

$$n \cdot \lambda = 2 \cdot d \cdot \sin\theta_B \tag{2.15}$$

where n is the order of reflection and corresponds to n=1, 2, 3..., and θ_B is the Bragg angle. This is known as *Bragg's Law*. As mentioned earlier, when rays diffracted by a crystal are in phase, they will reinforce one another, resulting in a constructive interference; other out of phase diffracted rays undergo destructive interference. The first order diffraction (n=1) is the strongest and the intensity of diffracted rays decreases with an increase of n.
Bragg's relationship is very important in XRD, since it offers different possibilities for material investigations. For example, if the d-spacing in the crystal is known, then the wavelength of the X-rays can be measured, and vice versa.

3.4. X-ray diffraction in crystals

Geometrical and dynamic theories are two approaches that can account for X-ray diffraction in crystals. Geometrical theory describes the amplitudes of the scattered rays from each volume element of the crystal as an independent element. The total amplitude is defined as the sum of individual diffracted amplitudes from each volume element, considering the phase differences between them and ignoring the interaction of X-rays within the crystal material [19]. The dynamic theory of diffraction describes the diffracted amplitudes, taking into account all ray interactions within the crystal volume elements. It provides a correct expression for the reflected intensities. The dynamic theory has to be used in the case of X-ray diffraction by perfect crystals with a non-negligible thickness or even by thin imperfect crystals where multiple reflections and interference take place [19]. The theory of diffraction in mosaic crystals is described by Zachariasen [3], [20].

3.4.1. Reflectivity of perfect crystals

Let us consider that the radiation is incident on a small thin-volume element of a perfect crystal δV that can reflect only a single beam. The reflected intensity can be expressed as:

$$I(\lambda) = \delta V \cdot Q(\lambda) \tag{2.16}$$

where

$$Q(\lambda) = \frac{\lambda^3 N^2}{\sin 2\theta_B} K F^2 \tag{2.17}$$

λ is the wavelength, N is the reciprocal of the unit cell volume, θ_B is the Bragg angle, and K represents the polarisation factor, equal to $\frac{1}{2}(1 + cos^2 2\theta_B)$ for X-rays [20].
The reflected intensity is proportional to the square of the crystal structure factor *F*. This is a complex number, which contains information regarding the atom arrangement within a unit cell, given by the relative atomic position *xyz*. The structure factor for *n* atoms in a unit cell is expressed as:

$$F_{hkl} = \sum_{j=1}^{n} \frac{e^2}{mc^2} \cdot f_j \cdot \exp\left(2\pi i\left(h\,x_j + k\,y_j + l\,z_j\right)\right) \tag{2.18}$$

e is the elementary charge, m is the mass of an electron, c is the velocity of light, f_j is the atomic scattering factor of j-th atom, and hkl are the Miller indices. The tabulated values of the atomic scattering factors are available in [5], [6]. The structure factor is a very important quantity because it enables calculation of the intensity reflected from a unit cell with given atomic positions.

It follows that the total intensity reflected by a single unit cell is obtained by adding together all the intensities reflected by the individual atoms [1], [2].

In this thesis, the ray tracing code XRT [21], [22] was used for the crystal reflection simulation. The features of the code and the simulation results will be presented in detail in Chapter 4 and Chapter 6. The equations presented above are implemented in the XRT code, and enable us to reach a better understanding of the reflection behaviour of perfect crystals.

The reflectivity of rays with an energy of E=10 keV by a perfect graphite (002) crystal was calculated. As illustrated in Figure 2.9, the reflectivity is non-zero in a narrow angular range.

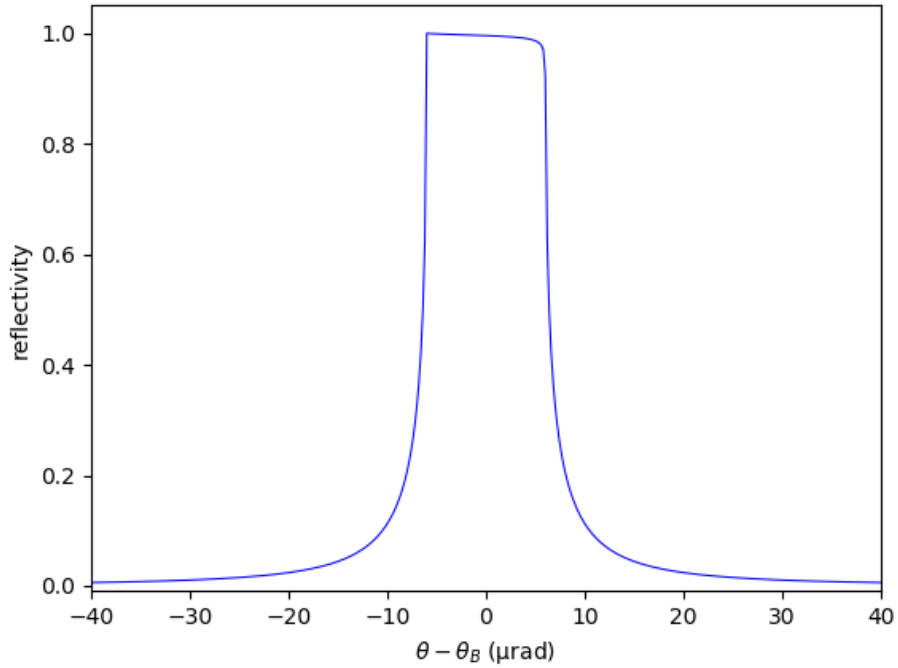

Figure 2.9. Reflectivity curve for a perfect graphite (002) crystal as a function of $(\theta - \theta_B)$ at 10 keV ray energy. The calculations were performed with the XRT code.

Perfect crystals produce an intense diffracted beam within the scattering plane, and enable high energy resolution to be obtained. For this reason, perfect crystals are used in wavelength dispersive spectrometers (WDS) as dispersive and focusing elements to resolve X-ray lines. Hence, they have narrow angular acceptance.

When an X-ray beam penetrates deeper within the crystal, its intensity is reduced due to absorption [23]. Thus, the deeper layers of the crystal contribute less to the reflection than the upper ones. For this reason, Eq. (2.16) cannot be applied to calculate the integrated reflectivity (area under the profile) for a crystal with the thickness *t*, since the incident beam intensity decreases as it penetrates. The decrease in the incident intensity is called *extinction.* Extinction in the ordered structure of a perfect crystal is called *primary*.

3.4.2. Reflectivity of real crystals

All real crystals are imperfect and have a mosaic structure. As was described in § 2, mosaic crystals are assumed to be formed by a large number of crystallites with small deviations of their normals from the normal to the crystal surface [24]. The fraction of the crystallites with the angular distribution $W(\Delta)d\Delta$ have their normals in the range of angles from Δ to Δ+$d\Delta$ to the normal of the crystal surface. The disorientation of mosaic blocks is described by a Gaussian distribution law, which is given by:

$$W(\Delta) = \frac{1}{\eta\sqrt{2\pi}} \exp\left(-\Delta^2/2\eta^2\right) \tag{2.19}$$

where η represents the standard deviation of the distribution. The full width at half maximum of this distribution is $\gamma = 2\sqrt{2ln2} \cdot \eta$.
The reflecting power of a layer of mosaic blocks of thickness dt is:

$$\sigma(\lambda) = \frac{Q(\lambda)}{\gamma_0} W(\theta - \theta_B) \tag{2.20}$$

where γ_0 is the direction cosines of the incident beam relative to the normal of the crystal surface, and is equal to $\sin\theta_B$ in the case of symmetrical reflection [20], [23]. Θ is the glancing angle relative to the mean lattice plane.
Considering that P_0 and P_H are the power of the incident and diffracted beams, respectively, then:

$$\left.\begin{aligned} dP_0 &= P_H\sigma dt - P_0\sigma dt - \mu_0 P_0 \frac{dt}{\sin\theta_{in}} \\ dP_H &= P_H\sigma dt - P_0\sigma dt + \mu_0 P_H \frac{dt}{\sin\theta_{diff}} \end{aligned}\right\} \tag{2.21}$$

μ_0 is the linear attenuation coefficient, θ_{in} is the incidence angle, θ_{diff} is the diffraction angle. This system of equations can be solved considering the boundary conditions: $P_0(t=0)$ is known, where t is the crystal depth, and no diffracted beam enters the back face of the crystal, and the power of a diffracted beam is $P_H(t=t_0)=0$, where t_0 is the crystal thickness. Thus:

$$P_0(t) = P_0(0)\frac{1 + \sigma(t_0 - t)}{1 + \sigma t_0} \tag{2.22}$$

Then the reflecting power is the following:

$$\frac{P_H(0)}{P_0(0)} = \frac{\sigma t_0}{1 + \sigma t_0} \tag{2.23}$$

According to Eq. (2.20) and Eq. (2.23), integrated reflecting power R_0 over Δ is:

$$R_0 = \int_{-\infty}^{\infty} \left[Q\frac{t_0}{\gamma_0} W(\Delta) \Big/ \left\{ 1 + Q\frac{t_0}{\gamma_0} W(\Delta) \right\} \right] d\Delta \tag{2.24}$$

As it was pointed out in [23], the integrated reflectivity from Eq. (2.24) tends to infinity when crystal thickness increases. In this case, the crystal is called non-absorbing.
In the case of an absorbing crystal, the integrated reflectivity is given by:

$$R^{\theta} = \int_{-\infty}^{\infty} \frac{a d\Delta}{(1+a) + \sqrt{(1+2a)}\coth\left[A\sqrt{(1+2a)}\right]} \tag{2.25}$$

where $A = \frac{\mu_0 t_0}{\gamma_0}$, and $a = \frac{Q}{\mu_0} W = \frac{Q}{\mu_0} \frac{1}{\eta\sqrt{2\pi}} \exp\left(-\Delta^2 / 2\eta^2\right)$;
With the increase of the ratio $\frac{Qt_0}{\gamma_0}$, the integrated reflectivity also increases according to Eq. (2.16). Then the value diminishes under the influence of absorption and secondary extinction, which is the attenuation of the X-ray beam due to diffraction by mosaic crystals. The reflectivity of a mosaic crystal primarily depends on the angular spread of mosaic blocks, since the crystal mosaicity is responsible for the increase in integrated reflectivity. This is in contrast with the perfect crystal.
With the help of the XRT package, the reflectivity of X-rays with an energy of E=10 keV by mosaic crystals with a mosaic spread of 0.2° and 0.4° was calculated (see Figure 2.10).

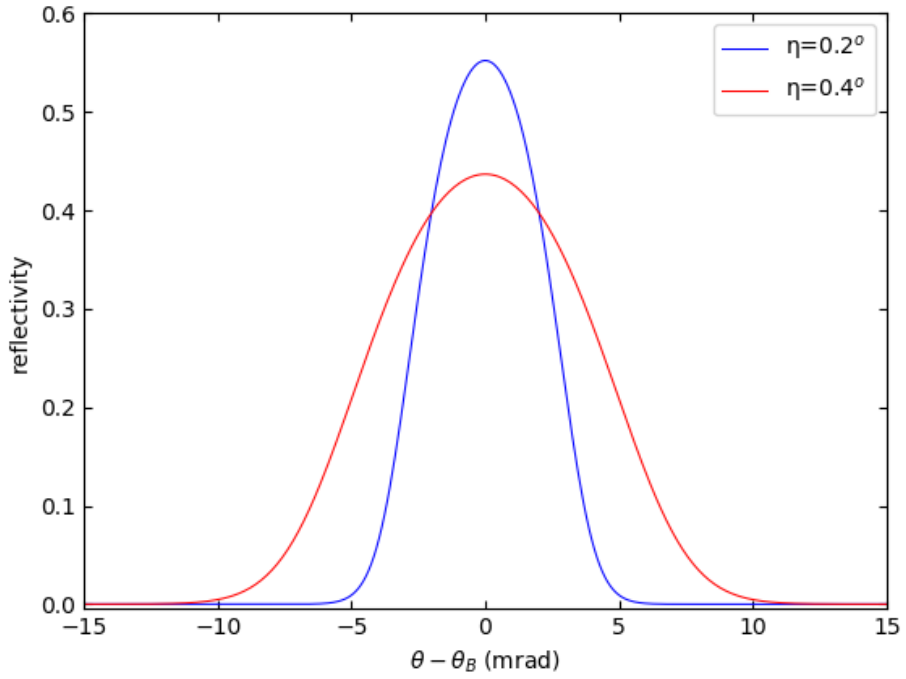

Figure 2.10. Reflectivity curves for a mosaic graphite crystal (002) with 0.2° (blue line) and 0.4° (red line) mosaic spread as a function of $(\theta - \theta_B)$ at 10 keV ray energy. The calculations were performed utilizing the XRT code.

Due to their crystallite misorientation, mosaic crystals provide a wide divergence of the diffracted beam and reduced energy resolution. They possess higher integrated reflectivity

and a wide angular acceptance compared to a perfect crystal. This enables them to reflect rays in a broad energy range.
The misorientation of the crystallites contributes to enhancing the number of diffracted rays in a given direction and consequently increases the integrated reflectivity. In fact, as it penetrates deeper into the mosaic crystal, each ray finds properly oriented crystallites to be diffracted according to Bragg's Law. This means that the effective depth (i.e., the depth at which diffraction occurs) in the mosaic crystal thickness is greater than in perfect crystals and depends on the incident energy. The effective penetration depth increases with increasing X-ray energy (see Figure 2.11).

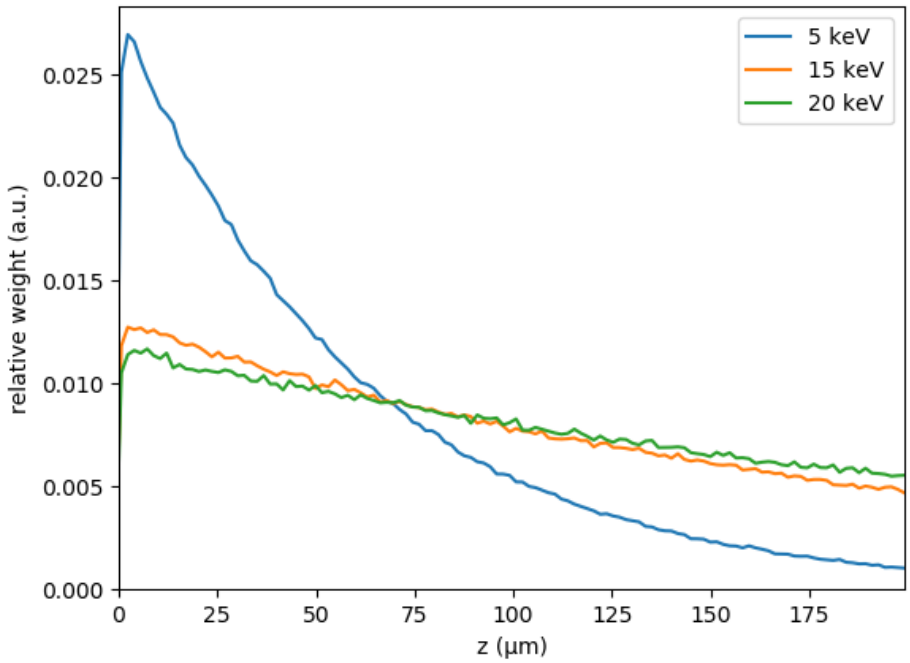

Figure 2.11. Penetration of rays into the depth of the graphite mosaic crystal, calculated with the XRT code.

4. General diffraction properties of HOPG crystal

When choosing a crystal material, the d-spacing plays a very important role since, according to Bragg's Law, the value of the diffracted wavelength and relative Bragg angle are defined by the appropriate value of d-spacing. The special structure of HOPG crystals enables efficient diffraction of rays in the energy range from 2 keV up to several tens of keV [25]. According to Eq. (2.15), in the first order of reflection (n=1), HOPG can be applied down to the K binding energy of phosphorus (E=2.014 keV). However, the value of d is too small for lighter elements [26].
The mosaic spread is responsible for broadband reflection, and integral reflectivity. It also influences the energy resolution. The mosaic crystallites produce a parafocusing effect (see Figure 2.12) of the X-ray beam in the diffraction plane, and the effect takes place in 1:1 magnification geometry. It means that the point source-to-crystal and crystal-to-image plane distances F should be equal. In addition, this geometry allows the best energy

resolution to be reached. This concept could be applied to rays with different energies, but they would be focused on different points because the Bragg angle is different for different wavelengths (energies). With a polychromatic X-ray source, the image spots are smeared. The position of spots in the image plane depends on the Bragg angle, producing different spatial positions for different photon energies.

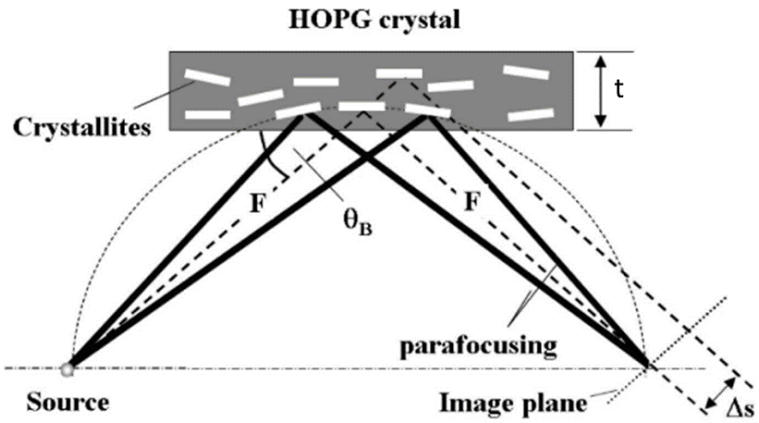

Figure 2.12. Diffraction properties of HOPG crystals (side view) [25].

Figure 2.13 presents the defocusing effects of mosaic crystals, and it is shown that the beam divergence increases to $2\,\tau\,sin\theta_B$ in the perpendicular plane due to the mosaic spread τ. The large mosaic spread of HOPG leads to high integrated reflectivity.

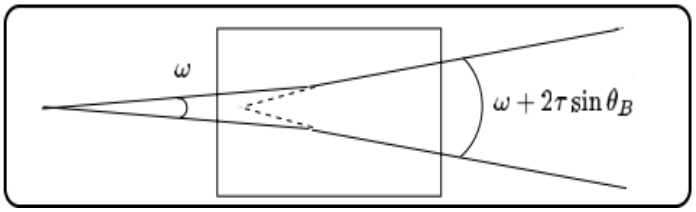

Figure 2.13. Defocusing effect of mosaic crystals in the plane perpendicular to the diffraction plane (top view) [27].

The reflectivity of HOPG also depends on the thickness t of the reflecting crystal because the absorption in carbon is low and, for thicker crystals, the scattering volume increases.

5. Conclusions

This chapter recalls basic optical rules and the crystal diffraction properties required to characterize the optical elements of an experimental setup. The first section of this chapter discussed the basics of geometrical optics and the equations involved. The interaction of X-rays with matter was presented in terms of the refraction index. The crystal structure and structural parameters involved were described in section 2. The reflection behaviours of perfect and mosaic crystals were presented and compared. The XRT ray tracing code was

used to calculate the reflection profiles of perfect and mosaic crystals. It was demonstrated that with an increase in crystal misorientation, a crystal provides larger divergence of the diffracted beam and reduced energy resolution. Throughout this chapter, particular emphasis was placed on the HOPG crystal structure and reflection properties, since it has considerable interest for this thesis.

References

[1] B. D. Cullity. *Elements of X-ray Diffraction Second Edition*. Addison-Wesley Publishing Company, 1978.

[2] J. Epp. "*Chapter 4. X-Ray diffraction (XRD) techniques for materials characterization" in Materials Characterization Using Nondestructive Evaluation (NDE) Methods*. Elsevier Ltd, 81-124, 2016.

[3] W. H. Zachariasen. *Theory of X-ray Diffraction in Crystals*. Dover Publications, 1967.

[4] B. Beckhoff B. Kanngießer N. Langhoff R. Wedell H. Wolff (Eds.). *Handbook of Practical X-Ray Fluorescence Analysis*. Springer, 2006.

[5] B. L. Henke, E. M. Gullikson, J. C. Davis. "X-ray interactions: photoabsorption, scattering, transmission, and reflection at E = 50-30, 000 eV, Z = 1-92", *At. Data Nucl. Data Tables*, 54, 181–342, 1993.

[6] C. T. Chantler. "Theoretical Form Factor, Attenuation and Scattering Tabulation for Z=1-92 from E=1-10 eV to E=0.4-1.0 MeV", *J. Phys. Chem.*, 24, 71, 1995.

[7] J. Als-Nielsen, D. McMorrow. *Elements of modern X-ray physics Second Edition.* Wiley, 2011.

[8] Y. Kayser, J. Szlachetko, J. Sà. "Scanning-free grazing emission x-ray fluorescence by means of an angular dispersive arrangement with a two-dimensional position-sensitive area detector", *Rev. Sci. Instrum.*, 84, 123102, 2013.

[9] C. Hammond. *The basics of crystolography and diffraction Thirt Edition*. Oxford University Press, 2009.

[10] I. G. Grigorieva, A. A. Antonov. "HOPG as powerful x-ray optics", *X-Ray Spectrom.*, 32, 64–68, 2003.

[11] M. Ohler, J. Baruchel, A. W. Moore, P. Galez, A. Freund. "Direct observation of mosaic blocks in highly oriented pyrolytic graphite", *Nucl. Instruments Methods Phys. Res. B*, 129, 257–260, 1997.

[12] M. Ohler, M. Sanchez Del Rio, A. Tuffanelli, M. Gambaccini, A. Taibi, A. Fantini, G. Pareschi. "X-ray topographic determination of the granular structure in a graphite mosaic crystal: A three-dimensional reconstruction", *J. Appl. Crystallogr.*, 33, 1023–1030, 2000.

[13] "AG Kanngießer: AG Kanngießer". (available at https://www.axp.tu-berlin.de/ag_kanngiesser/).

[14] M. Gerlach, L. Anklamm, A. Antonov, I. Grigorieva, I. Holfelder, B. Kanngießer, H. Legall, W. Malzer, C. Schlesiger, B. Beckhoff. "Characterization of HAPG mosaic crystals using synchrotron radiation", *J. Appl. Crystallogr.*, 48, 1381–1390, 2015.

[15] "Silicone & Specialty Chemicals | Momentive". (available at https://www.momentive.com/en-us).

[16] "Optigraph". (available at http://www.optigraph.eu/).

[17] "Industrial Devices & Solutions - Panasonic". (available at https://industrial.panasonic.com/ww).

[18] L. D. Landau, E. M. Lifshitz. *Theory of Fields*. Pergamon Press, 1971.

[19] A. Authier. "Dynamical theory of X-ray diffraction", *Mater. Today*, 7, 51, 2004.

[20] W. H. Zachariasen. "A general theory of X-ray diffraction in crystals", *Acta Crystallogr.*, 23, 558–564, 1967.

[21] K. Klementiev, R. Chernikov. in Powerful scriptable ray tracing package xrt. *Proc. of SPIE* Vol. 9209 92090A-1 2014.

[22] "xrt (XRayTracer)". (available at https://xrt.readthedocs.io/).

[23] G. E. Bacon, R. D. Lowde. "Secondary Extinction and Neutron Crystallography", *Actq Cryst.*, 303–314, 1948.

[24] A. Guinier. X-Ray Diffraction in Crystals, Imperfect Crystals, and Amorphous Bodies. W. H. Freeman and Company, 1963.

[25] H. Legall, H. Stiel, V. Arkadiev. in A new generation of X-ray optics based on pylopytic garphite, *Proceedings of FEL*, 798–80, 2006.

[26] M. Haschke. Micro-X-Ray Fluorescence Spectroscopy Instrumentation and Application. Springer, 2014.

[27] M. Sanchez del Rio, M. Gambaccini, G. Pareschi, A. Taibi, A. Tuffanelli, A. K. Freund. "Focusing properties of mosaic crystals", *Proc. SPIE*, 246–255, 1998.

Chapter 3

Miniature XRF setup design and characteristics

XRF instruments are widely used for material investigations in industry, research institutes, analytical laboratories, public services, etc. XRF spectrometers fall into two main classes: wavelength-dispersive XRF (WDXRF) and energy-dispersive XRF (EDXRF) spectrometers. The principal components of a classical XRF instrument are a primary X-ray source, a detection system (detector and analyser), and X-ray optics, which are most frequently used in WDXRF spectrometers. Additionally, a setup can include collimators and filters of various materials.
WDXRF spectrometers are based on Bragg diffraction, where the X-rays emitted from a sample are incident on a wavelength dispersive device, and split into narrow wavelength bands to be measured individually at a specific reflection angle. These kinds of spectrometers can be equipped with different X-ray optical elements (crystal monochromators, multilayer crystals, mirrors, lenses, etc.) with different diffraction and reflection properties, depending on the energy range of interest and the energy resolution required for the measurements needed.
In EDXRF spectrometers, the characteristic X-rays emitted by a sample are directly measured by an energy-dispersive detector. This is connected to a multichannel analyser (MCA) that delivers an energy spectrum. The detectors in EDXRF are capable of storing a wide energy spectrum where the radiations of all elements present are recorded simultaneously. This type of spectrometer is more compact compared to WDXRF, has low power consumption, and is able to perform simultaneous elemental analyses.
The commercial systems currently available are not always able to meet the particular requirements of customers. To improve the analytical performance of XRF systems in terms

of increasing intensity, minimising background, polarisation adjustment, the capability to analyse small samples, and the determination of elements at low concentrations, it is necessary to develop specific advanced laboratory instruments. Some needs in particular require the use of an appropriate optical element intended to monochromatize, reflect, or focus X-rays.

The Atalante facility analysis laboratory at Marcoule has a nuclearized X-ray fluorescence setup dedicated to the analysis of actinides via their L X-ray lines. The device is widely used for U and Pu measurements on highly radioactive samples [1]. The instrument has an EDXRF system equipped with a cylindrical HOPG crystal between the sample and the detection system. The characteristic X-rays emitted by the sample are diffracted by the HOPG crystal, and only those X-rays which satisfy Bragg's Law are measured by the detector. A detailed description of the experimental setup and some features of the processing of the acquired data have been reported in the section 1 of this chapter.

Because of the need for an XRF system for work in laboratory glove-boxes (intermediate activity), a new miniature XRF setup was built. This setup includes one X-ray tube and two detection channels. The first channel is a classical EDXRF system, where the fluorescent X-rays originating from a sample are directly recorded by the detector. The channel allows the collection of a wide energy range X-ray emission spectrum (3 keV < E < 30 keV). The second channel was designed and constructed as a copy of the existing nuclearized setup, employing a cylindrical HOPG monochromator in the detection line. The crystal-based channel enables the measurement of K X-ray emission lines from medium-Z elements as well as L X-ray spectra of actinides (10 keV < E < 18 keV).

After the brief description of the original nuclearized system, the main part of this chapter is devoted to the description of the geometrical arrangement and operation principles of the miniature XRF setup. In section 2, the main features of the components used for this new system are presented in detail.

1. Nuclearized EDXRF setup for actinide analysis

The ATALANTE analysis laboratory performs measurements on samples with radionuclides of high levels of radioactivity in a hot cell. The front side of the hot cell contains nine posts (cells) with remote manipulators for handling the radioactive samples behind a thick glass window so that there is no hazard to personal (see Figure 3.1). The samples are carried through a pneumatic transfer line to the EDXRF setup placed in the rear of the analysis hot cell (see Figure 3.2). The analysis setup was constructed in the 1990s to analyse the L X-ray spectra of actinides (U, Np, Pu, Am, and Cm) in the energy range from 12 keV to 17 keV [1], [2] and is shielded with lead to ensure radiation protection. The L X-ray emission energies of the actinides of interest and their radiative emission intensities are listed in Table 3.1.

Figure 3.1. Front zone of the analysis hot cell.

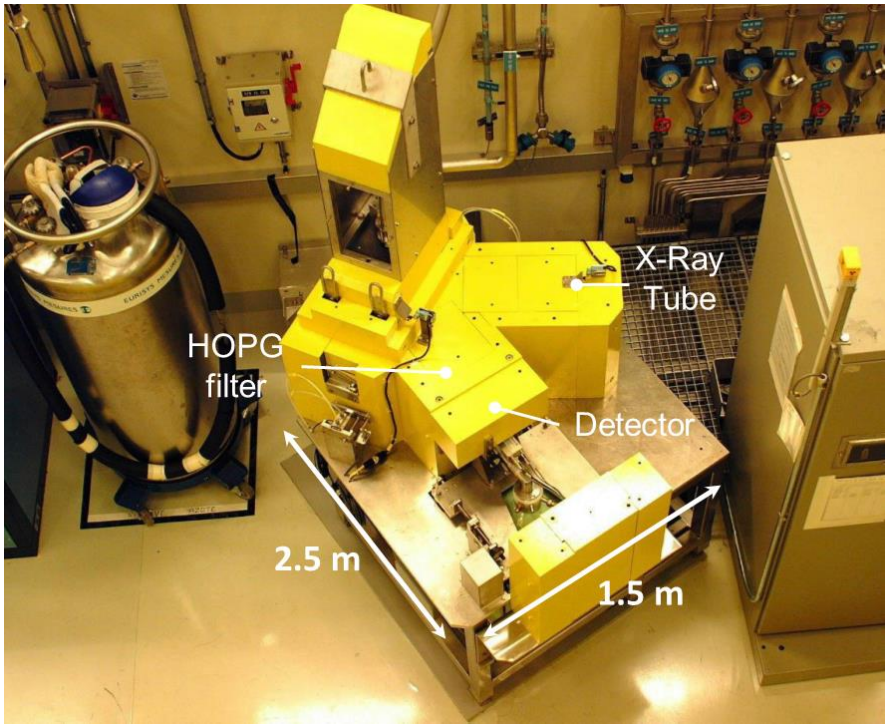

Figure 3.2. Nuclearized EDXRF setup in a hot cell.

Table 3.1. L X-ray energies and relative emission intensities for some actinides [3].

Element	Line L_2-M_4 keV	Relative emission intensity	Line L_3-M_5 keV	Relative emission intensity
U	17.222	0.762	13.618	0.672
Np	17.751	0.760	13.946	0.670
Pu	18.296	0.758	14.282	0.669
Am	18.856	0.756	14.620	0.666
Cm	19.427	0.753	14.961	0.664

The setup includes an X-ray tube, a pneumatic transfer line, a cylindrical crystal monochromator, and a HPGe detector (see Figure 3.3). The samples to be analysed are in an aqueous or organic liquid phase, contained in a 5 mL vial.

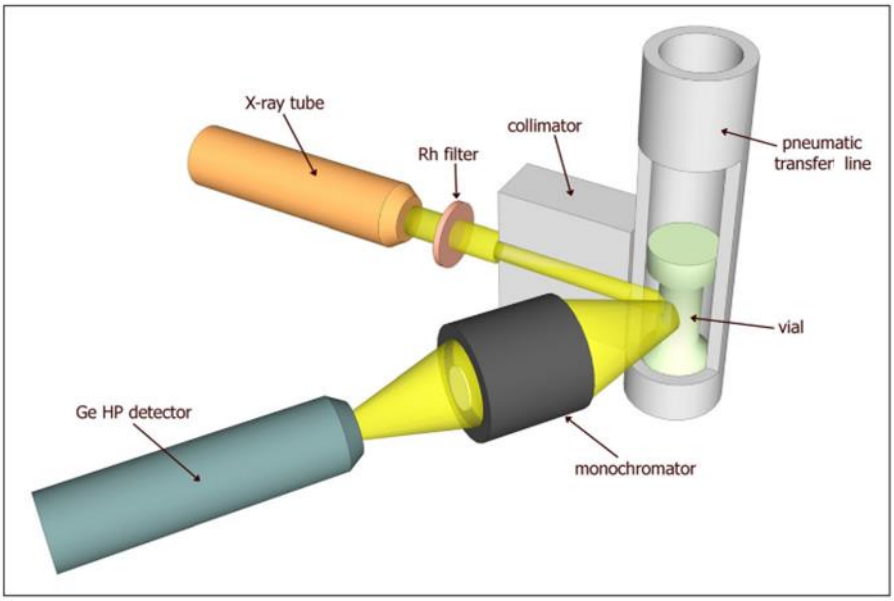

Figure 3.3. Illustration of the nuclearized EDXRF setup equipped with a cylindrical crystal monochromator [1].

The X-ray tube with a rhodium anode (3 kW, 75 µm), manufactured by PANanalytical, is mostly operated at an excitation potential of 50 kV and a current intensity of 30 mA. The X-ray beam filtered by the Rh filter irradiates the sample in the vial, transported to the measurement point via a stainless-steel pneumatic transfer tube. The HOPG monochromator inserted between the sample and the detection system acts as a broadband filter. It enables the collection of fluorescence spectra within the energy range of elements of interest and eliminates undesirable parts of the spectrum. Thus, the dead time of the detector is reduced and the power of the X-ray tube can be increased. The monochromator is custom manufactured, made of a thin graphite lamella (300 µm thick) with a mosaic spread of 0.8°. The X-rays are diffracted by the crystal and reach the detector positioned on the axis of the HOPG cylinder. The HPGe detector has an active area of 30 mm^2 and is cooled with liquid nitrogen. Measurements with the setup can be performed at actinide concentrations down

to 0.5 mg L^{-1}.
A classical XRF analysis software cannot process the spectra obtained with the nuclearized XRF setup. In fact, the built-in crystal monochromator modifies the spectral distribution of the fluorescence X-rays, which classical spectra processing cannot take into account. A specific data processing software was therefore developed [2] using the free science and engineering development language Python [4]. Besides, this algorithm requires a library of standard spectra. Calibration is performed for each standard element for every channel of the spectrum, establishing a nonlinear relationship between intensity and concentration. The calibration is checked regularly in order to ensure its validity and avoid result deviations.
Correction for the matrix effects is based on the Lachance-Traill approach [5] which was mentioned in Chapter 1. The processing requires an accurate description of the sample matrix composition. The software uses the XCOM database to estimate mass attenuation coefficients [2]. This approach, based on calibration using reference samples, has been validated and is used in the laboratory to analyse actinides in solution. However, the establishment of the calibration file is time-consuming and it is difficult to obtain standards such as Np, Am, and Cm at a high concentration[1] and purity.

2. Miniature XRF setup

The new miniature XRF setup was custom-built, and can be regarded as a copy of the nuclearized system. Its advantage over the latter is the ability to perform measurements with two detection channels. The setup comprises an X-ray tube, a sample holder, a cylindrical HOPG monochromator, and two SDD, one on each measurement channel. Throughout this manuscript, the detectors on the first and the second channels are marked SDD-1 and SDD-2, respectively.
In this new setup, the X-ray tube and the sample holder are common to both channels (see Figure 3.4, Figure 3.5 and Figure 3.7). The X-ray tube is at an angle of 22° to the sample holder axis, and at a distance of 16.3 mm from it. The fluorescent X-rays from the sample material reach the SDD of each measurement channel in different ways.

[1] Commercial gamma spectrometry standards are not concentrated enough

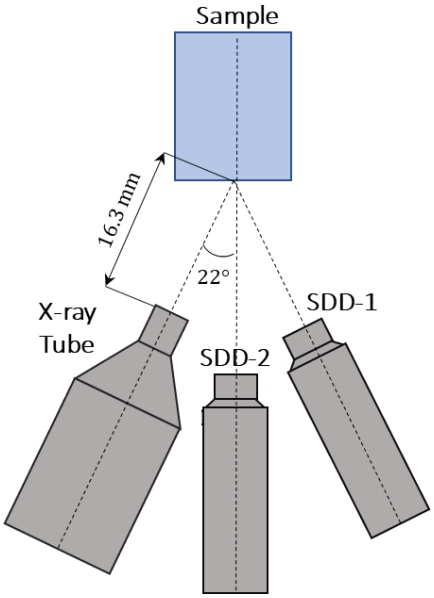

Figure 3.4. Illustration of the miniature XRF setup.

The first channel is a classical XRF system where the X-ray fluorescence is directly detected by SDD-1 (see Figure 3.5). The detector and the X-ray tube are coplanar (see Figure 3.6). The detector is positioned at a distance of 17.9 mm from the sample center and at an angle of 23°. Thus, the angle between the X-ray tube and the detector axes is 45°.
This first channel enables recording of an X-ray spectrum in the energy range from 3 keV to 30 keV at a short acquisition time compared to the second channel, because SDD-1 is closer to the sample.

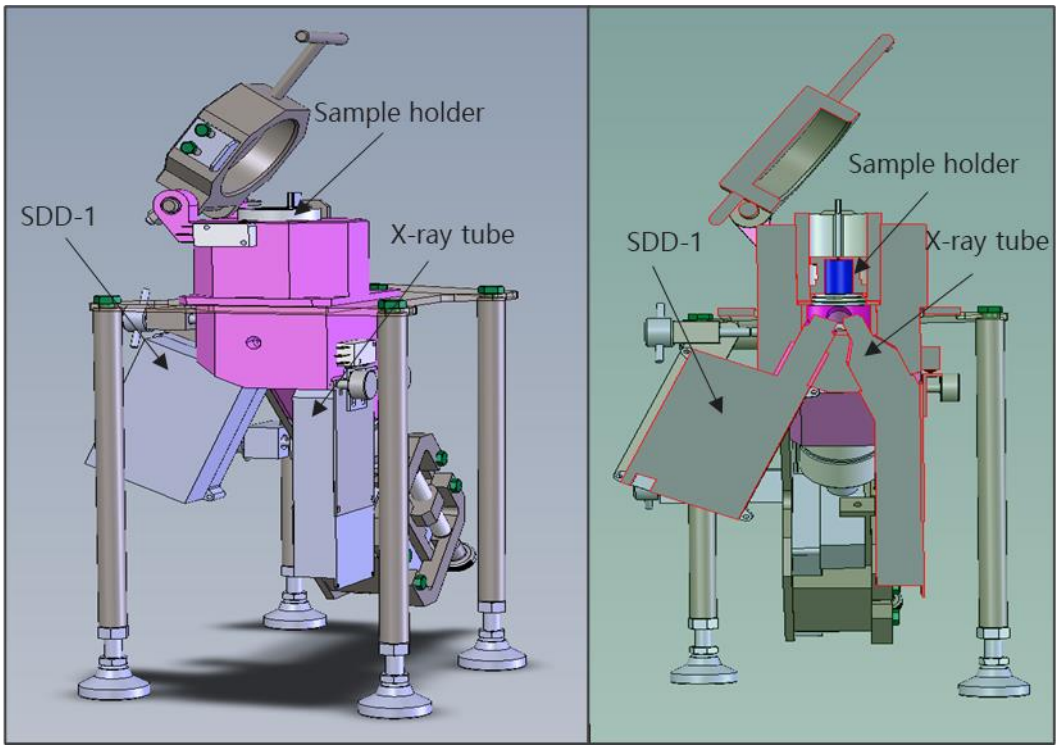

Figure 3.5. Drawing of the first channel (classical XRF channel) of the miniature setup - inside view (right panel) and cutaway view (left panel).

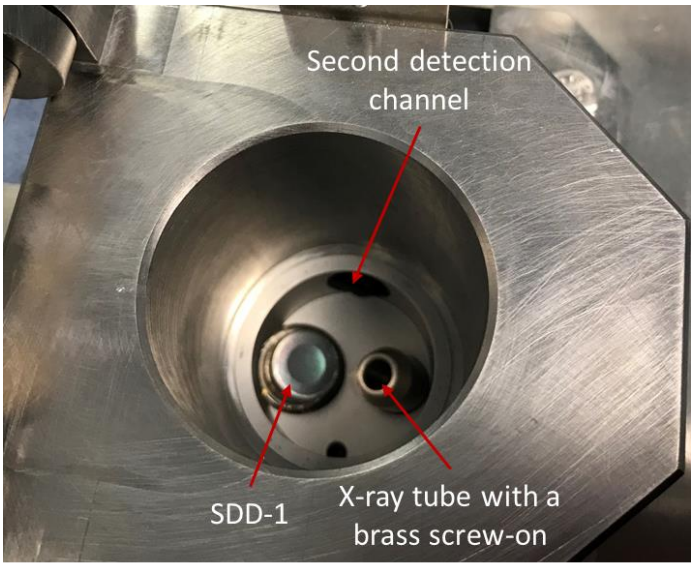

Figure 3.6. Top view of the experimental setup with the sample holder removed.

The second channel has an additional built-in optical element - *the cylindrical HOPG monochromator* - between the sample holder and SDD-2. SDD-2 is placed on the cylinder axis of the monochromator, which is in the plane perpendicular to that of the X-ray tube (see Figure 3.7). The monochromator cylinder axis is tilted by an angle of 46° relative to the sample holder axis.

The advantage of this channel is that the HOPG monochromator and SDD-2 can be moved

separately along their common axis. The choice of the position of the optical element with respect to the sample and SDD-2 determines the range of the energy window. The HOPG monochromator enables measurements between 10 keV and 18 keV, and eliminates any undesirable part of the spectrum. Thus, the second detection channel, like the nuclearized device, allows measurement of the K X-ray emission lines of medium-Z elements and the L X-ray lines of actinides.
To provide radiation shielding, the instruments are enclosed in a stainless-steel housing, with an aluminium (Al) insert which minimizes the contribution of fluorescence radiation from the stainless-steel elements. The whole XRF assembly is mounted on supporting legs.

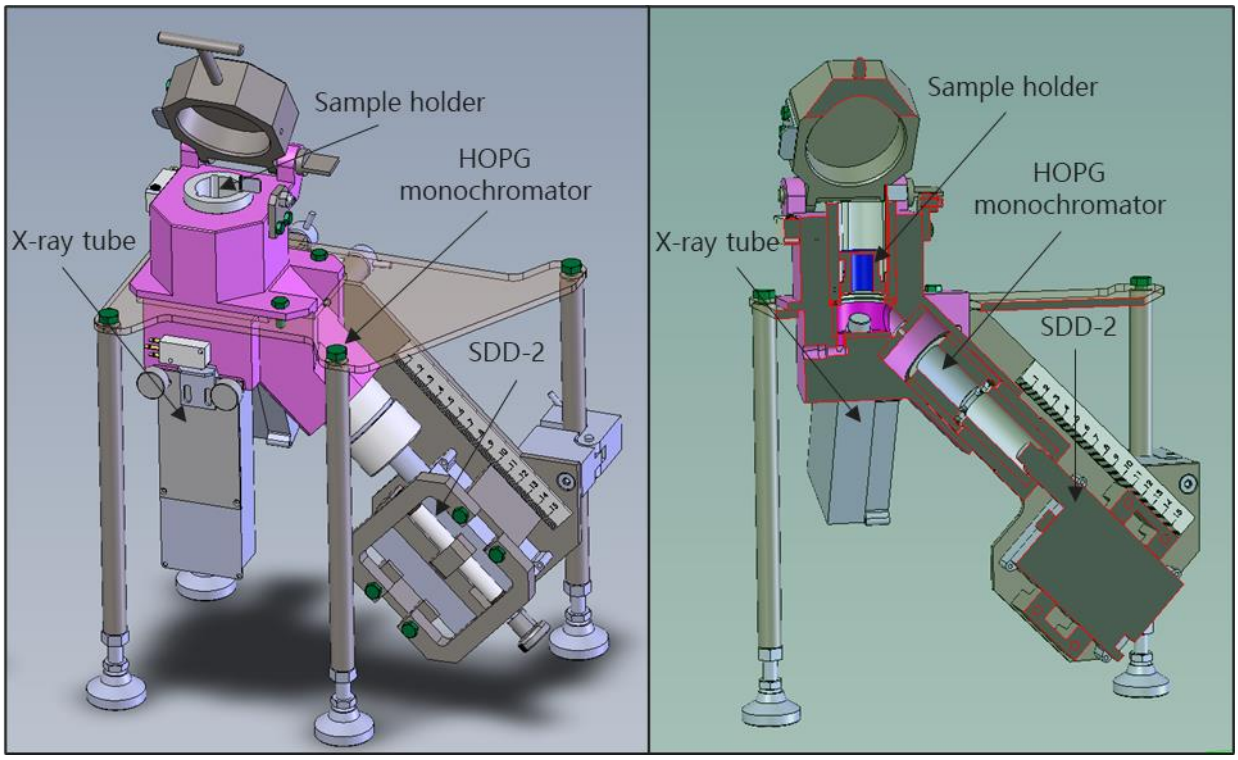

Figure 3.7. Drawing of the second detection channel equipped with the HOPG monochromator in side view (right panel) and cutaway view (left panel).

In Figure 3.7, it can be seen that the geometrical arrangement of the second channel and nuclearized XRF setup (see Figure 3.3) are very similar.

2.1. X-ray tube

The primary radiation delivered by the X-ray tube is used to excite the fluorescent X-rays of the elements in a sample. The principles of X-ray generation in an X-ray tube were presented previously in Chapter 1. The miniature XRF setup is equipped with a transmission-anode X-ray tube. There, a thin layer of the target material is deposited directly on the inner side of the exit window, and in this arrangement, the anode is bombarded by the electron beam under normal incidence. X-rays generated in the anode pass through the tube window in the same direction [6] – [9].

The "Mini-X" X-ray tube system was designed and manufactured by the technology company Amptek [10]. The instrument includes an X-ray tube, a power supply, and USB control of current and voltage. The X-ray tube is equipped with an Ag anode and a beryllium (Be) window, and can deliver a maximum power of 4 W. The tube is operated via connections with a USB cable and an AC adaptor. All the Mini-X specifications are listed in Table 3.2.

Table 3.2. Mini-X X-ray tube specifications [10].

Target material	Silver (Ag)
Target thickness	0.75 μm (±0.1 μm)
Tube voltage	10 to 50 kV
Tube current	Min 5 μA and max 200 μA
Maximum power	4 W
Window material	Beryllium (Be)
Window thickness	127 μm
Focal spot size	About 2 mm
Operating temperature range	-10 °C to +50 °C

The emission spectrum of the X-ray tube contains the continuous bremsstrahlung and the characteristic X-rays of the anode material (see Figure 3.8).

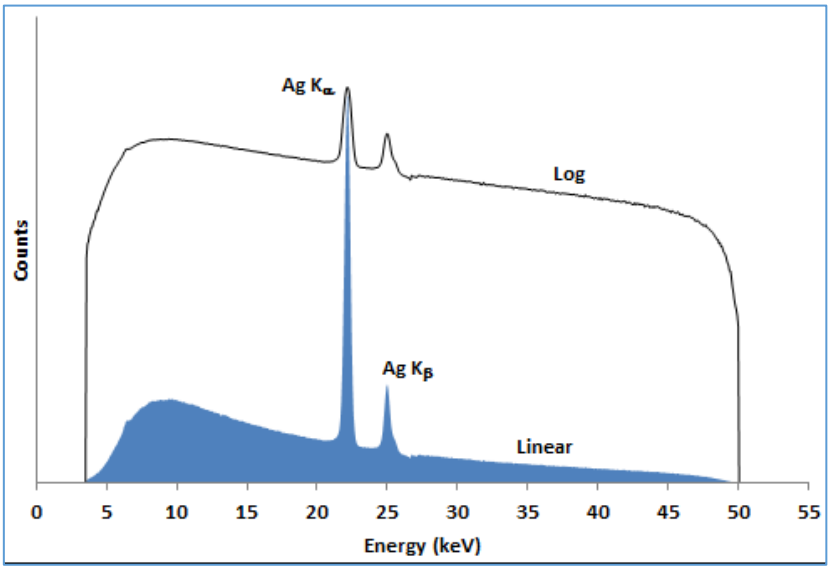

Figure 3.8. X-ray tube emission spectrum at 50 kV [10].

The X-ray tube comes with filters of various materials (see Table 3.3) and two cylindrical collimators (see Figure 3.9). In the experiments, filters were placed between the X-ray tube and the sample to improve the peak-to-background count rate ratio for a given element

and to decrease the characteristic X-ray intensity from the anode material. Suitable choices for the high voltage of the tube, the filter material, and the thickness are very important, since these permit optimisation of the important parts of the spectrum and improve the detection limits for the elements of interest [8].

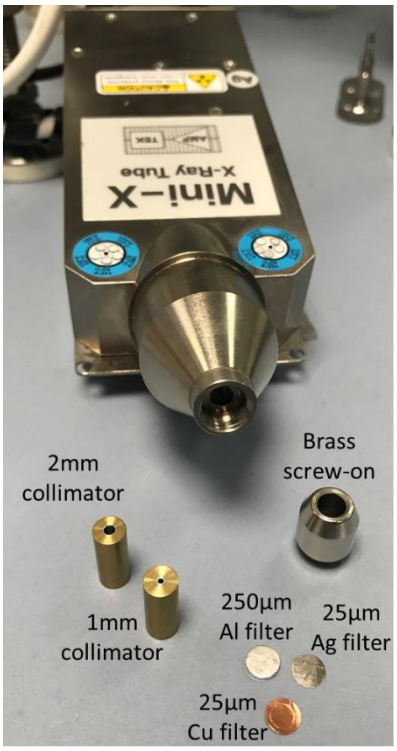

Figure 3.9. Mini X-ray tube with filters and collimators.

Table 3.3. Filters provided with the Mini-X X-ray tube.

Material	Thickness, µm
Al	1000
Al	250
Cu	25
Mo	25
Ag	25
W	25

The application of the X-ray tube can be optimized by using collimators. The 15 mm brass collimators with thin aluminium (Al) inserts have 1 mm and 2 mm diameter holes. X-rays are emitted from the tube in a 120° cone which is limited by the tube shielding, and using the 2 mm collimator, the output cone angle is reduced to 5°.

2.2. Sample holder

During this study, liquid samples were analysed. The samples were placed in a sample cup

manufactured by Chemplex Industries, Inc., USA [12] which in turn was positioned in the aluminium sample holder. The sample cup, marked № 3115, is assembled from a vented snap-on cap, a cell, and a collar (see Figure 3.10).

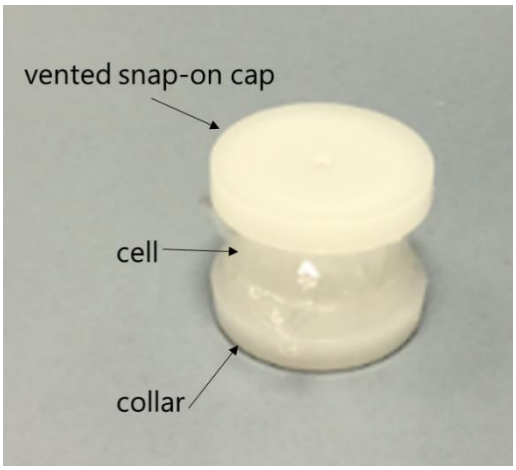

Figure 3.10. XRF sample cup.

The vented cap is manufactured with a small hole in order to stabilize pressure differences within the cell. The collar covers the bottom of the cell with a Mylar® thin-film for sample support. Both the vented cap and the collar have external diameters of 30.5 mm. The cell has a conical shape, which facilitates the sample placing. It is 25.1 mm high, and the radii of the top and bottom are 20 mm and 15 mm, respectively. To maintain the sample substance, a thin-film support fabricated by Chemplex Industries, Inc, is used. These circular films are 63.5 mm in diameter and 2.5 μm in thick. The thin film provides a very high degree of transmittance that is a great advantage for the measurement of elements in low concentrations and low-energy photons [12]. The sample cup with secured thin-film can be used for powder, solid, or liquid sample substances.
The size of the XRF sample cup was determined by the size of the sample holder. The latter is cylindrical, and its bottom is also covered with thin-film in order to avoid contamination of the experimental setup with the sample solution should the sample cup film be damaged. The holder has inner and outer radii of 31 mm and 45 mm, respectively, and is 63.5 mm high.

2.3. Detection System

Silicon drift detectors are widely used for XRF analysis. They are equipped with a thermoelectric cooler, which reduces the electric noise in the detector and operates like a room temperature system. This type of detector has a low electronic noise contribution and provides good energy resolution (down to 125 eV for Mn K-M line) [10]. A typical instrument comprises an active region of fully depleted high-resistivity Si, a collecting anode, and a radiation entrance window. The incoming X-rays are absorbed by the active region on the entrance window, producing electron-hole pairs. The holes are collected by the p+ electrode arrays, whereas the electrons are directed between drift rings toward a collecting anode by an additional electric field added to the surface of the silicon wafer (see Figure 3.11). The

charge collected by the anode is proportional to the energy of the incident radiation [13], [14].

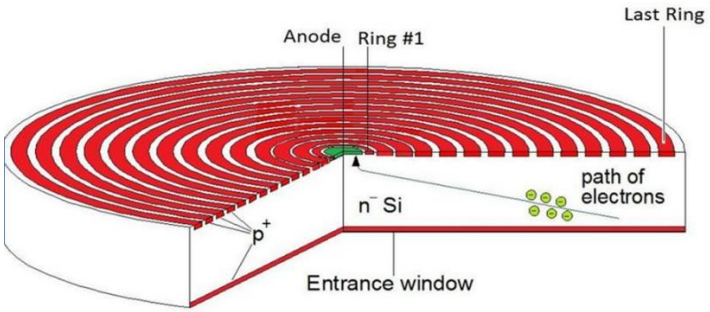

Figure 3.11. Illustration of the SDD design [14].

Both the experimental setup measurement channels were equipped with detection systems provided by Amptek [10]. The X-123 X-ray spectrometer includes the X-123SDD silicon drift detector, a preamplifier, a digital pulse processor (DPP), a multichannel analyser (MCA), a power supply, and a software interface. This high-performance instrument is small and easy to operate.

The DPPMCA application software provided by Amptek configures the X-123SDD, and controls the spectrum acquisition and its computer display (see Figure 3.12).

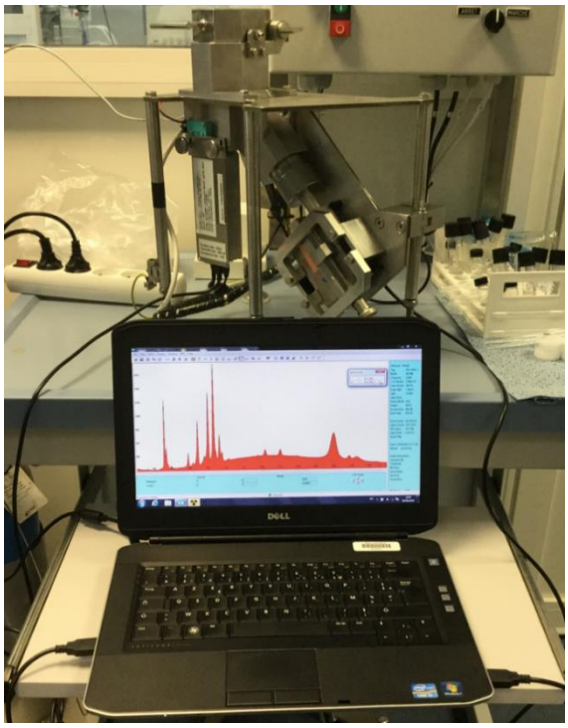

Figure 3.12. Acquisition of an XRF spectrum with DPPMCA application software.

The system is housed in a protective aluminium box (see Figure 3.13), dimensions 7×10×2.5 cm. The detector is mounted on a 4.5 cm long extender.

Figure 3.13. 123-SDD X-ray spectrometer [10].

The hermetically sealed X-123SDD has an entrance Be window to maintain vacuum integrity. The SDD and its characteristics are presented in Figure 3.14 and Table 3.4, respectively.

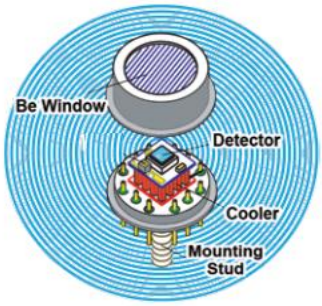

Figure 3.14. Detail of the SDD mounting [10].

Table 3.4. Silicon drift detector specifications.

Detector area	25 mm^2
Detector thickness	500 µm
Detector window	Beryllium (Be)
Window thickness	12.5 µm
Collimator	Multilayer

The SDD is manufactured with an internal collimator – a multilayer collimator (MLC) - between the Be window and the detector. The MLC consists of four layers: the first (base) layer is tungsten (W) of 100 µm thick, the second layer is 35 µm of chromium (Cr), the third layer is 15 µm of titanium (Ti) and the last layer is 75 µm of aluminium (Al). The interaction of X-rays near the edge of the active volume of the detector can result in poor charge collection. To avoid this effect, the MLC was used to restrict the X-rays to the active volume where the full charge collection is produced. The SDD and its mechanical dimensions are presented in Figure 3.15 and Table 3.5, respectively [10].

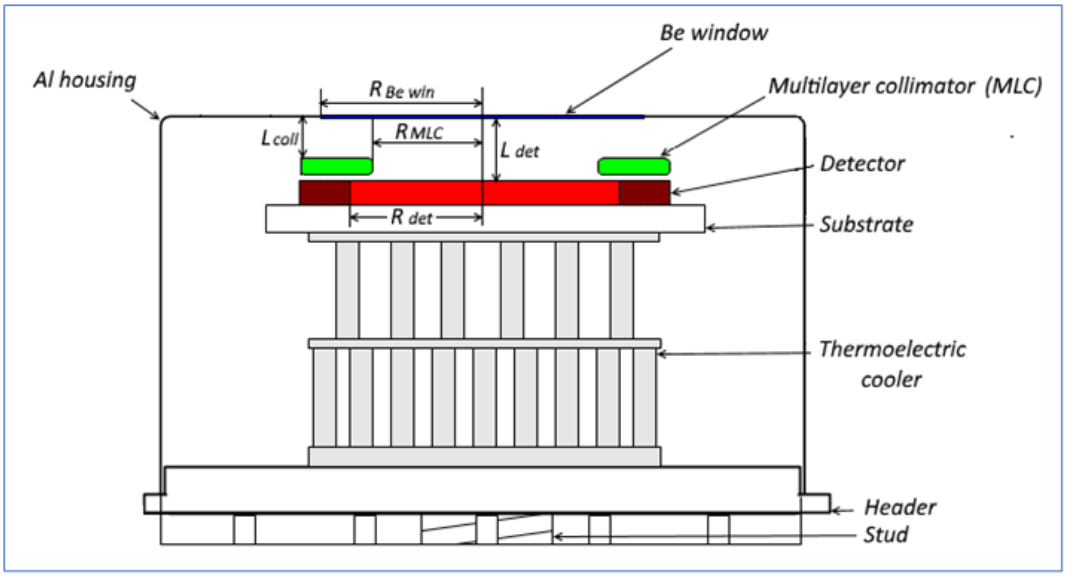

Figure 3.15. Drawing of the silicon drift detector.

Table 3.5. Mechanical dimensions of SDD.

(all values are in mm)

$R_{Be\ win}$	3
R_{MLC}	2.33
R_{det}	2.82
L_{coll}	0.9
L_{det}	1.4

The ability of the detector to resolve characteristic X-rays with close energies, i.e. to separate adjacent energy peaks, is due to the energy resolution. It is determined as the full width at half-maximum (FWHM) of the observed full-energy peak. This value is one indicator of the detector system quality. According to the information provided by the manufacturer, the SDD energy resolution is specified as FWHM=125 eV at 5.9 keV (Mn K-L line (^{55}Fe)).

2.4. Detection efficiency calibration

Detection efficiency (full-energy peak efficiency, FEPE) is a very important characteristic of the detector, and is defined as the ratio of X-rays which interact in the detector and are completely absorbed compared to the total number of X-rays emitted by the source. This value is dependent on the energy of the incident X-rays, and is limited by the source-detector geometry and the active area and thickness of the detector [6]. FEPE $\varepsilon_p(E)$ can be expressed by the intrinsic efficiency $\varepsilon_I(E)$ and the source-detector geometrical arrangement ε_G, as a function of the energy [15]:

$$\varepsilon_P(E) = \varepsilon_G\, \varepsilon_I(E) \tag{3.1}$$

The geometrical efficiency ε_G is defined as the fraction of the X-rays emitted by a point-source which enter the detector within the solid angle Ω:

$$\varepsilon_G = \frac{\Omega}{4\pi} \tag{3.2}$$

where Ω is the solid angle defined by the source-detector distance *d* and the area of the active volume of the detector. For a point source, the value is given by:

$$\Omega = 2\pi\left(1 - \frac{d}{\sqrt{d^2 + r^2}}\right) \tag{3.3}$$

where *r* is the detector active radius.
The intrinsic efficiency is the fraction of the number of X-rays which is totally absorbed within the sensitive volume of the detector [16]. It can be estimated as a product of the interaction probability and the full-energy absorption probability in the detector.

$$\varepsilon_I(E) = \eta_i(E)P_P(E) \tag{3.4}$$

The interaction probability η_i is expressed as:

$$\eta_i(E) = 1 - \exp(-\mu_d(E)\rho_d x) \tag{3.5}$$

where μ_d is the total mass attenuation coefficient at a given X-ray energy, and ρ_d and x are the density and the thickness of the detector material, respectively.

The probability of full-energy absorption in the detector can be approximated in the low energy range as:

$$P_P(E) \approx \frac{\tau_d(E)}{\mu_d(E)} \tag{3.6}$$

where τ_d is the photoelectric mass absorption coefficient for the detector material.
The experimental FEPE calibration can be performed using standard radionuclides with standardized activity, and can be derived as:

$$\varepsilon_p(E) = \frac{N_p(E)}{A \cdot I_X(E)} \tag{3.7}$$

where $N_p(E)$ is the peak net area, and *A* is the standardized activity (Bq) with emission intensity I_X of the X- (or gamma-) ray line with energy *E*.

2.4.1. Experimental efficiency calibration

The experimental efficiency calibration of detector SDD-1 was performed at the Laboratoire National Henri Becquerel (LNHB), a facility dedicated to the preparation of standard radioactive sources [17]. In the experiment, each standard point source was positioned at the same well-defined axial distance (D = 61.2 mm) from the detector entrance window, utilizing a laboratory-made holder which was firmly fixed on the detector external cylinder. A "point source" is obtained by the deposition of a few milligrams of a weighed standard radioactive solution on a Mylar® film, which is then dried and sandwiched with

terphane (see Figure 3.16).

Figure 3.16. Standard point source at the LNHB [17].

Different radioactive sources with standardized activity and with well-known X-ray emission intensities were used in the experiments to cover the energy range from 6.4 keV to 35.5 keV. The radionuclides for calibration sources and their activities at the reference date, with their uncertainties and half-lives, are listed in Table 3.6.

Table 3.6. Radionuclides used in the experimental efficiency calibration.

Radionuclide	Activity on the reference date (Bq)	Uncertainty (%)	Reference date	Half-life
^{57}Co	35 685	0.30	12/06/2017	271.80(5) d
^{109}Cd	32 294	0.70	24/06/2013	461.4(12) d
^{129}I	1 407	0.18	24/06/2013	$16.1(7)\times10^{6}$ y
^{133}Ba	34 359	0.43	01/10/2011	1.0540(6) y
^{241}Am	23 879	0.15	01/04/2011	432.6(6) y

The spectra were successively acquired for each reference source with DPPMCA software. The solid angle of detection was limited by the internal MLC (R_{MLC} =2.33 mm) of the detector. Under these measurement conditions, the geometrical efficiency can be estimated according to Eq. (3.2) (where $d=D+L_{det}$). The value obtained using the standard sources is $\varepsilon_G = 3.45 \times 10^{-4}$.

2.4.2. Spectrum processing with the COLEGRAM software

The information in the measured spectrum can be converted into a more accessible form using mathematical fitting functions. Spectrum processing was therefore performed with the dedicated COLEGRAM software, developed in the LNHB for applications in gamma-ray and X-ray spectrometry [18]. The software enables direct reading of the spectra obtained by the acquisition software and permits an estimation of the energy (position) and area of each peak of interest. COLEGRAM uses the non-linear least-squares method to fit mathematical functions to the experimental data [19].

As an example, let us consider COLEGRAM processing of the spectrum from a ^{241}Am-point source, step by step. Americium-241 decays to ^{237}Np by alpha transitions, emitting some gamma-rays (among them that at 26.35 keV in the range of interest) and the L X-rays (11.89 keV<E<21.16 keV) of the daughter nuclide (neptunium). Firstly, it was necessary to calibrate the energy scale of the spectrum (see Figure 3.17), using reference peak positions.

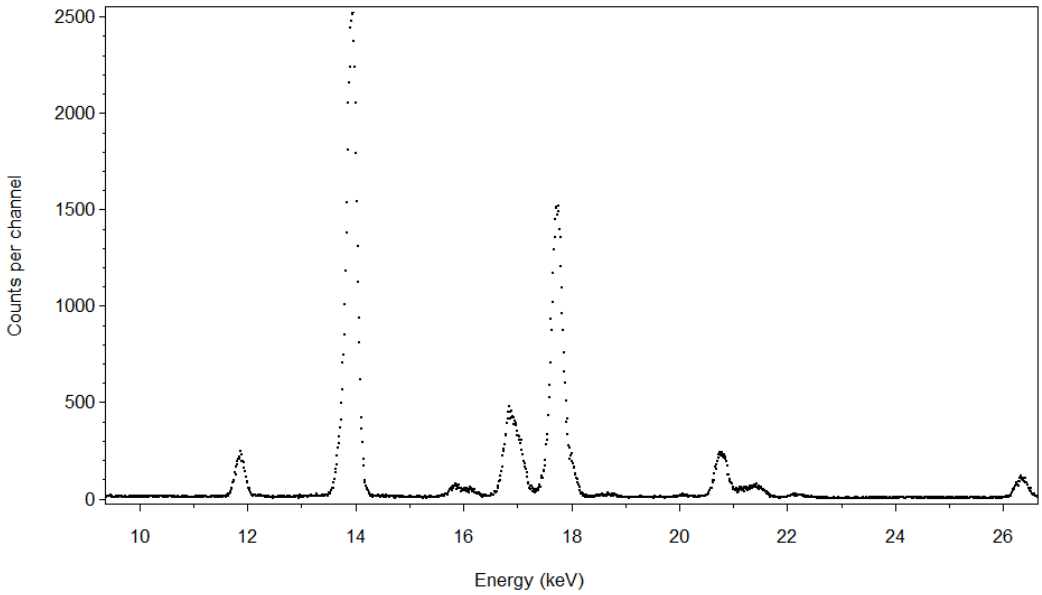

Figure 3.17. Display of the experimental spectrum obtained from ^{241}Am.

Afterwards, the spectrum was separated into regions of interest (ROIs) with respect to the ɣ-ray emission and each of the L X-ray groups (L_α (13.761 keV<E<13.946 keV), L_β (16.109 keV<E<17.751 keV), L_γ (20.784 keV<E<21.491 keV), L_l (11.871 keV)). The ROIs were established manually, and afterwards the background of each region was defined and removed.

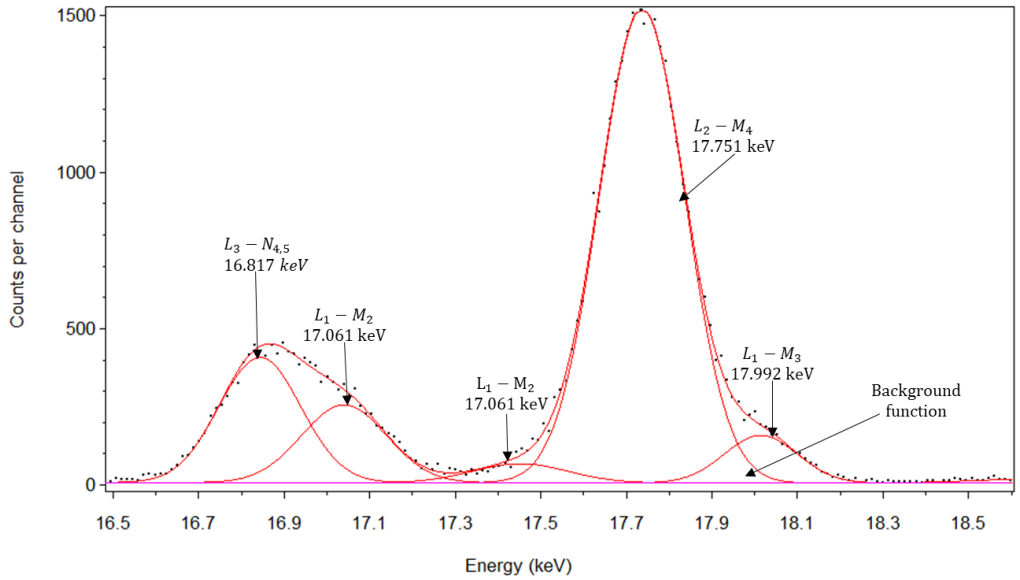

Figure 3.18. Processing of the ^{237}Np L_β region.

The components of each ROI were identified and individually fitted with a Gaussian function. The amplitude, position, and width of each Gaussian were adjusted by the minimization algorithm to find the best fit for the experimental spectrum. Figure 3.18 shows the result of the processing of the experimental spectrum in the L_β region.

The net peak area of each ROI was derived from the fitting procedure. Using Eq. (3.7) and data given in Table 3.6, the experimental FEPE $\varepsilon_p(E)$ for the SDD corresponding to each group of the radionuclides were calculated, and are reported in Table 3.7.

Table 3.7. Full-energy peak efficiencies.

Radionuclide	Group	Energy (keV)	Emission intensity (%)	FEP efficiency
^{57}Co	K_α	6.40	50.0	2.83 × 10^{-4}
^{57}Co	K_β	7.08	7.10	2.85 × 10^{-4}
^{57}Co	ɣ	14.41	9.15	2.52 × 10^{-4}
^{109}Cd	K_α	22.10	83.70	1.06 × 10^{-4}
^{109}Cd	K_β	25.07	17.79	7.69 × 10^{-5}
^{129}I	K_α	29.6	57.30	1.57 × 10^{-5}
^{133}Ba	K_α	30.7	96.80	1.19 × 10^{-5}
^{133}Ba	K_β	35.5	22.80	3.58 × 10^{-6}
^{241}Am	L_l	11.89	0.844	3.01 × 10^{-4}
^{241}Am	L_α	13.93	13.02	2.59 × 10^{-4}
^{241}Am	L_β	17.50	19.01	1.77 × 10^{-4}
^{241}Am	L_γ	21.01	4.84	1.17 × 10^{-4}
^{241}Am	ɣ	26.34	2.31	6.09 × 10^{-5}

Thus, the intrinsic efficiency of the SDD can be derived from the relationship (3.1), and the efficiency values of each radionuclide as a function of the energy are plotted in Figure 3.19. The value of the associated uncertainty is less than 4.1%.

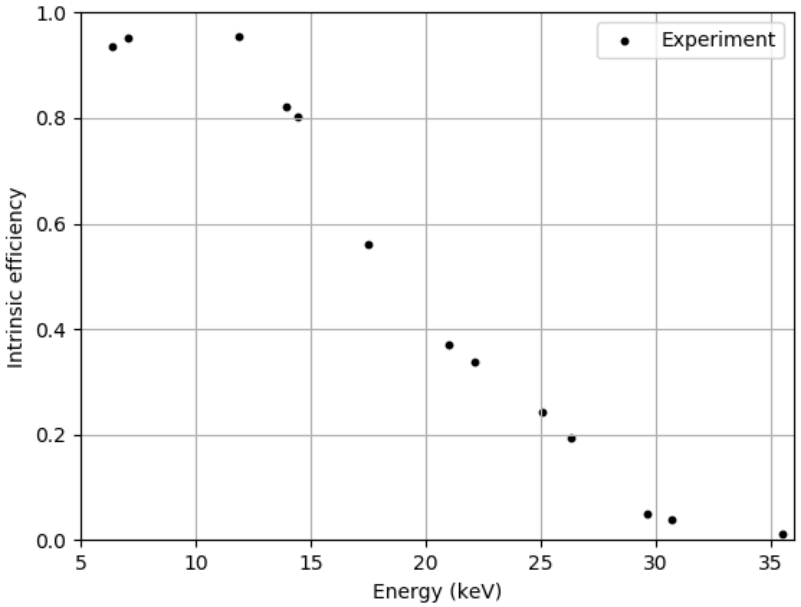

Figure 3.19. Intrinsic efficiency calibration for SDD-1.

The relationship between the efficiency and the energy can be determined by means of an appropriate mathematical function. Thus, to join the data points smoothly, fitting was performed with a polynomial function with a degree of 4. In the fitting procedure with a polynomial, the polynomial degree *n* is limited and it must be adjusted depending on the number of the data point (p): n<<p [16]. The efficiency calibration is plotted in Figure 3.20.

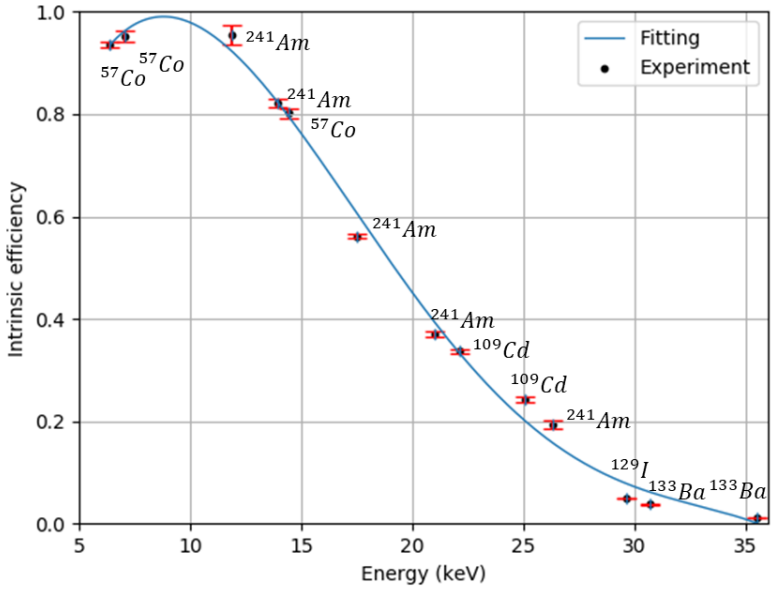

Figure 3.20. Mathematical fitting of the experimental data by a fourth-degree polynomial.

A gap can be observed between 7.08 keV and 11.89 keV. This can be fulfilled by performing Monte Carlo (MC) simulations using the PENELOPE code for electron and photon transport. The MC method is widely applied for the calculation of detector efficiency [15], [20], [21]. The features of the code are out of the scope of this chapter, and will be presented in more

detail in Chapter 4 and Chapter 5. Here, the aim is to demonstrate the calculated intrinsic efficiency.
In the simulation, the experimental geometry for efficiency calibration is considered. The dimensions of the crystal correspond to those provided by the manufacturer (listed in Table 3.5). The detector efficiency was calculated for the energy range from 5 keV to 25 keV in order to ensure results calculated through comparison with the experimental calibration. In Figure 3.21, a good agreement can be seen between experimental and calculated efficiencies.

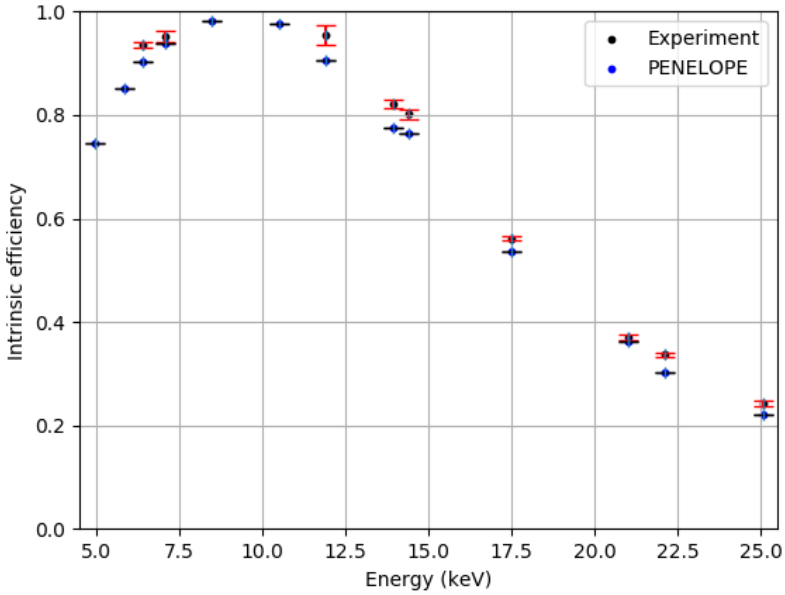

Figure 3.21. Comparison of the experimental and calculated intrinsic efficiency.

It was concluded that efficiency calculated with the PENELOPE code could be used. The framework of the efficiency calibration is experimental and, in this work, the calculated results will be used for the energy region which is not covered by the calibration sources.

2.5. Highly oriented pyrolytic graphite (HOPG) monochromator

The second detection channel is equipped with the HOPG monochromator between the sample holder and SDD-2. In this geometry, the HOPG optics are employed as a broadband filter [6], [22].
As was discussed in Chapter 2, HOPG crystals are artificial mosaic crystals with a particular mosaic spread of the crystallites. Owing to their unique structure, HOPG crystals have large integrated reflectivity [23], and are used as excellent monochromatizing and focalizing devices [24] – [26].
In this thesis, an HOPG monochromator manufactured by Optigraph GmbH, Germany [27], was implemented. The instrument geometry is cylindrical, with an internal radius R of 20.2 mm and length L of 40 mm (see Figure 3.22 and Figure 3.23). The inner surface of the cylinder is covered with a 200 μm thick HOPG layer with a mosaic spread of 0.4°.

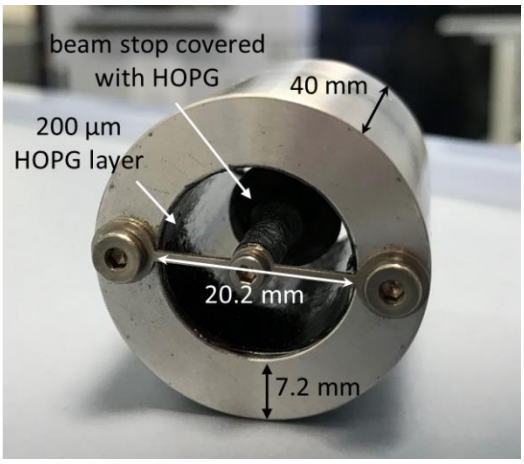

Figure 3.22. HOPG monochromator.

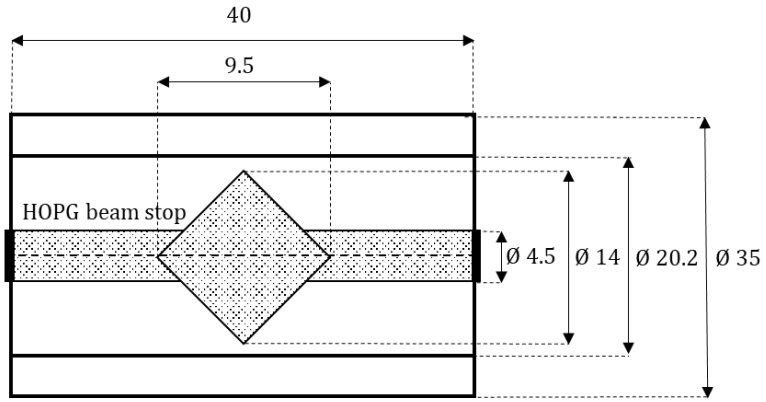

Figure 3.23. HOPG monochromator geometry (all values are in mm).

The monochromator contains an internal beam stop to avoid the direct transmission of the fluorescence radiation from the sample to the detector surface without it being diffracted [24], [28]. The beam stop is covered with a thin HOPG layer as well.
The reflection properties of the HOPG crystal were discussed in Chapter 2. The role of the crystal in the miniature setup is reported in Chapter 6 and Chapter 7.

3. Conclusions

In this chapter, the geometrical arrangements and special features of two EDXRF setups for actinide analysis were reported. Both systems were equipped with HOPG monochromators, which act as broadband filters and modify the spectra distribution of the fluorescence radiation emitted by the sample. Most of the chapter focused on the new miniature system. Its principal components, such as the X-ray tube, the SDDs, and the HOPG monochromator were described in detail. The detector efficiency was determined both experimentally and by calculations with the help of the MC PENELOPE code. The results demonstrated a good agreement. The following chapters are devoted to the study of the miniature XRF setup using numerical tools. Additionally, the experimental results will be extensively presented.

References

[1] E. Esbelin. "Actinide L-line ED-XRF and Hybrid K-edge Densitometer spectra processing", *AIEA Symposium on International Safeguards: Linking Strategy, Implementation and People* , 2014.

[2] E. Esbelin. "Graphite monochromator for actinide L-line energy dispersive X-ray fluorescence analysis in liquid sample", *X-Ray Spectrom.*, 43, 198–208, 2014.

[3] J.H. Scofield. "Relativistic Hartree-Slater Values for K and L X-ray Emission Rates", *Atomic Data and Nuclear Data Tables*, 14, 121-137, 1974.

[4] "Python-xy.GitHub.io by python-xy". (available at http://python-xy.github.io/).

[5] R. M. Rousseau. "Corrections for matrix effects in X-ray fluorescence analysis-A tutorial", *Spectrochim. Acta - Part B*, 61, 759–777, 2006.

[6] B. Beckhoff B. Kanngießer N. Langhoff R. Wedell H. Wolff (Eds.). *Handbook of Practical X-Ray Fluorescence Analysis*. Springer, 2006.

[7] P. Brouwer. *Theory of XRF Third Edition*. PANalytical, 2010.

[8] R. E. Van Grieken, A. A. Markowicz. *Handbook of X-ray Spectrometry Second edition*. Marcel Dekker, Inc., 2001.

[9] L. M. N. Távora, E. J. Morton, W. B. Gilboy. "Design considerations for transmission X-ray tubes operated at diagnostic energies", *J. Phys. D. Appl. Phys.*, 33, 2497–2507, 2000.

[10] "Amptek". (available at https://www.amptek.com/).

[11] "Mini-X2 X-Ray Tube System for XRF – Amptek – X-Ray Detectors and Electronics". (available at https://www.amptek.com/products/x-ray-sources/mini-x2-ray-tube).

[12] "Chemplex Industries Online Store | Chemplex Industries, Inc. Porto - Homepage 7". (available at https://www.chemplex.com/).

[13] L. Strüder, P. Lechner, P. Leutenegger. "Silicon drift detector–the key to new experiments", *Sci. Nat.*, 85, 539–543, 1998.

[14] A. D. Butt. *Silicon Drift Detector arrays for X- and Gamma-ray detection application. PhD Dissertation*, Politecnico di Milano, 2016.

[15] M. C. Lépy, J. Plagnard, L. Ferreux. "Measurement of 241Am L X-ray emission probabilities", *Appl. Radiat. Isot.*, 66, 715–721, 2008.

[16] K. Debertin, R. G. Helmer. *Gamma and X-ray spectrometry with semicondactor detectors*. North-Holland, 1988.

[17] "Laboratoire National Henri Becquerel – Laboratoire national de métrologie dans le domaine des rayonnements ionisants". (available at http://www.lnhb.fr/en/).

[18] M.-C. Lépy. "Presentation of the COLEGRAM software", *Note Technique*, 2004.

[19] "Logiciels spécifiques développés par le LNHB – Laboratoire National Henri Becquerel". (available at http://www.lnhb.fr/activites-recherche-developpement/logiciels-traitement-spectres/).

[20] M. J. Vargas, A. L. Guerra. "Application of PENELOPE code to the efficiency calibration of coaxial germanium detectors", *Applied Radiation and Isotopes,* 64, 1319-1322, 2006.

[21] J. G.Guerra, J. G.Rubiano, G. Winter, A. G.Guerra, H. Alonso, M. A. Arnedo, A. Tejera, P. Martel, J. P. Bolivar. "Modeling of a HPGe well detector using PENELOPE for the calculation of full

energy peak efficiencies for environmental samples", *Nucl. Instruments Methods Phys. Res. Sect. A*, 908, 206–214, 2018.

[22] Y. Kolmogorov, V. Trounova. "Analytical potential of EDXRF using toroidal focusing systems of highly oriented pyrolytic graphite (HOPG)", *X-Ray Spectrom.*, 31, 432–436, 2002.

[23] H. Legall, H. Stiel, I.G. Grigorieva, A.A. Antonov, A. Erko. "Advances in high spectral resolution X-ray Optics based on thin films of Pyrolytic Graphite", *Working paper,* 2016.

[24] A. A. Antonov, V. B. Baryshev, I. G. Grigoryeva, G. N. Kulipanov, N. N. Shchipkov. "Focusing shaped pyrographite monochromators in synchrotron radiation experiments", *Nucl. Inst. Methods Phys. Res. A*, 442–446, 1991.

[25] U. Zastrau, C. R. D. Brown, T. Döppner, S. H. Glenzer, G. Gregori, H. J. Lee, H. Marschner, S. Toleikis, O. Wehrhan, E. Förster. "Focal aberrations of large-aperture HOPG von-Hàmos x-ray spectrometers", *J. Instrum.*, 2012.

[26] T. Döppner, P. Neumayer, F. Girard, N. L. Kugland, O. L. Landen, C. Niemann, S. H. Glenzer. "High order reflectivity of highly oriented pyrolytic graphite crystals for x-ray energies up to 22 keV", *Rev. Sci. Instrum.*, 79, 10–13, 2008.

[27] "Optigraph". (available at http://www.optigraph.eu/).

[28] A. A. Antonov, V. B. Baryshev, I. G. Grigoryeva, G. N. Kulipanov, Y. V Terekhov, N. N. Shipkov. "First results on application of short-focus monochromators from formed pyrolytic graphite for x-ray fluorescent analysis using synchrotron radiation", *Rev. Sci. Instrum.*, 60, 2462, 1989.

Chapter 4

Numerical solutions for the experimental setup

One of the main objectives of this thesis was to investigate the experimental setup and all related physical phenomena using computational tools. Monte Carlo and ray tracing methods can used when a detailed description of an instrument is needed.
The Monte Carlo simulation of radiation transport consists in the numerical generation of random tracks to provide solutions for the equations describing the transport of particles in material. Ray tracing, on the other hand, is based on geometrical considerations, and is a very powerful tool to predict the performance of an optical system and study the properties of individual optical elements. Programs based on these methods are widely used. They can provide useful information on the instrument and predict the outputs.
This chapter focuses on the Monte Carlo and ray tracing methods, and discusses their principles and the validity of their application to the study's experimental conditions. The advantages and limitations of these numerical tools will be presented, and the most appropriate simulation codes will be described in more detail.

1. Monte Carlo simulation of X-ray fluorescence setup

Monte Carlo (MC) is a numerical method based on random sampling, and is widely employed in many fields. The technique is commonly used when it is difficult to solve a certain problem with analytical methods or experimentally, for investigations of the performance of various systems, or for the modelling of systems with complex geometries. In particular, the method has become an essential tool in XRF to gain a better understanding of physical phenomena, for the simulation of XRF experiments [1], [2], for quantitative analysis procedures [3], and for the computation of other practical parameters. MC simulations are able to take into account all the interaction processes of X-rays with matter. For example, the efficiency of a detector can be obtained by MC simulation when the detector geometry and source characteristics are known [4]. As demonstrated in Chapter 3, MC calculations enabled us to compute the detection efficiency when it was difficult to determine it experimentally.

The modelling of an XRF setup using the MC method is attractive for different reasons. The simulations consider generation of fluorescence X-rays, scattering interactions, and enhancement effects of fluorescence radiation which, together, enable the building of a complete spectral response. The simulation results can be verified by comparison with experimental data. An MC modelling allows conditions that are not yet applicable experimentally to be studied and therefore, the geometrical parameters of the existing XRF instrument can be optimised.

1.1. Monte Carlo basic principles

Monte Carlo simulation of radiation transport consists in the numerical generation of random tracks of particles as sequential free flights and interaction processes; these are sampled with probabilities depending on the particle energy and the material composition. In MC radiation transport simulations, an interaction medium is presented as randomly distributed atoms (or molecules) with uniform density. Each interaction event of a particle with an atom or a molecule is described by the differential cross section (DCS). This determines the probability density functions (PDF) of corresponding interaction events. Let us consider that a particle of energy E is incident on a molecule M (see Figure 4.1). In each interaction, the particle undergoes a loss of energy, W, and changes its direction as defined by the polar and azimuthal angles θ and ϕ, respectively. The particle-molecule interaction is described by the double-differential DCS as $\frac{d^2\sigma}{dW\, d\Omega}$, where $d\Omega$ is an element of solid angle in the direction (θ, ϕ).

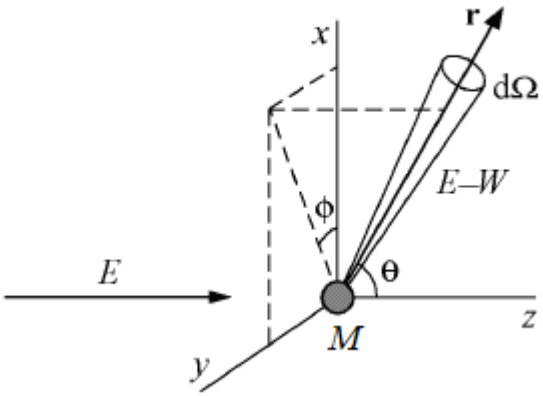

Figure 4.1. Illustration of particle interaction with media [5].

Projectiles crossing a plane surface perpendicular to their initial directions lose their energies and are deflected from their initial trajectory. The total cross section geometrically represents the area of the plane surface crossed by those projectiles [5].
The total cross section σ is the integral of the double-differential DCS over direction and over the energy loss, and is expressed as:

$$\sigma(\mathrm{E}) = \int_0^{\mathrm{E}} \left(\int \frac{\mathrm{d}^2\sigma}{\mathrm{dW}\,\mathrm{d}\Omega} \mathrm{d}\Omega \right) \mathrm{dW} \tag{4.1}$$

Detailed simulation of particle transport can be modelled as a Markov process in which the future interaction event is statistically determined by the present state, and depends only on the event immediately preceding it. Depending on this state, the generation of the particle history can be stopped at any point along the track.
As illustrated in Figure 4.2, the particle moves from material 1 to material 2 with mean free paths $\tau_{T,1}$ and $\tau_{T,2}$, respectively, and does not stop crossing an interface between two materials. The mean free path is defined as the inverse of the interaction cross section $\lambda_T = (N, \sigma)$, where N is the number of molecules per unit volume and σ is the geometrical cross section.

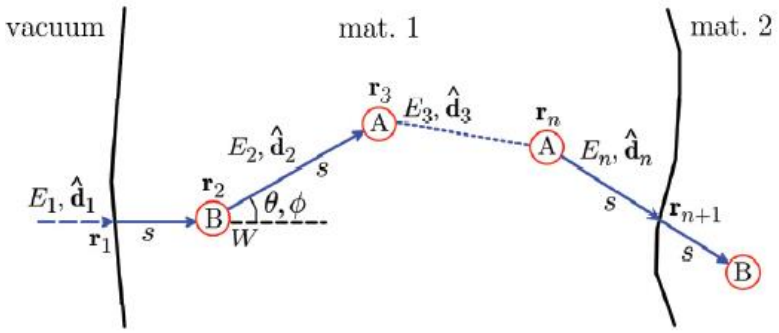

Figure 4.2. Representation of random trajectories of simulated particles.

Each simulated interaction process of the particle is characterised by a set of parameters: the position of n-th interaction event r_n, the energy of the particle after the interaction E_n, and direction cosines after the interaction $\hat{d}_n$. Each following interaction takes place at the position:

$$\mathrm{r_{n+1}} = \mathrm{r_n} + \mathrm{s\hat{d}_n} \tag{4.2}$$

Random values of path length s are generated as:

$$\mathrm{s} = -\lambda_\mathrm{T} \ln \xi \tag{4.3}$$

where ξ is a random number uniformly distributed in the interval (0,1).
The direction cosines of the direction of flight after the interaction $\hat{d}_{n+1}$ ares obtained by rotating $\hat{d}_n$:

$$\mathrm{\hat{d}_{n+1}} = \mathrm{R(\theta, \phi)\hat{d}_n} \tag{4.4}$$

where $R(\theta, \phi)$ is the rotation matrix given by the polar and azimuthal angles θ and ϕ.
After the interaction process, the energy of the particle is reduced to:

$$\mathrm{E_{n+1}} = \mathrm{E_n} - \mathrm{W} \tag{4.5}$$

1.2. Monte Carlo packages

A number of Monte Carlo codes are utilised for simulations in XRF spectrometry, such as MCNP (Monte Carlo N-Particle code) [6], PENELOPE (PENenetration and Energy LOss of Positrons and Electrons) [7], GEANT4 (GEometry ANd Tracking) [8], FLUKA [9], EGS5 (Electron-Gamma Shower) [10], etc. The latter is commonly used for simulations of X-ray tube sources [11]. Most MC codes are supplied with a user interface and provide graphical output. However, the utilization of some codes requires a knowledge of object-oriented programming in order to establish the simulation model. The MC tools include extensions

for different energy ranges and are supplied with up-to-date physical constants.
The interaction process calculations differ for each code. In this section, some free MC codes suitable for this work will be briefly reviewed and their particular features will be discussed.

1.2.1. GEANT4

GEANT4 is an object-oriented simulation toolkit for determining the passage and interaction of particles in matter, and was developed at CERN [8], [12]. The tool is commonly applied in high energy physics (simulation of accelerators and detectors), in medical physics, radiation protection and security, space science, etc. GEANT4 allows the simulation of a wide variety of physical processes that involve particle interactions in energy ranges from 250 eV to the TeV ranges. It allows systems with a great number of elements of different shapes and materials to be built and handled. The toolkit provides the graphical-user interface, through which users can construct an interaction model, and visualise geometries and particle trajectories. Users can develop their own applications using three mandatory and five optional classes. The mandatory class bases include: *DetectorConstruction*, where a user builds a simulation geometry assembling all necessary components; *PhysicsList* enables the definition of all particles and processes, and a production threshold; through the *PrimaryGenerator* class, primary particles are generated. The other classes can be used optionally to define additional elements for any part of the system, to control tracking, visualise desired attributes, or analyse events, etc. GEANT4 is written in C++ programming language, and some knowledge of this language is required to use the code.

1.2.2. MCNP

The general-purpose MCNP code system was developed by Los Alamos National Laboratory, and can be used for neutron, photon, and electron or coupled particle transport covering a wide energy domain from the 1 keV to GeV ranges [6]. It is employed in different fields, such as radiation protection and dosimetry, medical physics, detector design and analysis, nuclear safety, etc. The toolkit is written in Fortran 90 and C programming languages. Users create their own simulation models through the input file with the dedicated structure. This includes the source, materials, geometry definitions, problem parameters, and tally specifications. It may invoke variance reduction techniques and other necessary information related a particular problem. The geometry is built by defining bounded surfaces through polynomials. MCNP involves tallies (data cards) used to specify information on the radiation field (energy, direction, weight, position) which the user wants to obtain. For simulations of X-ray interactions, the tool considers elastic and inelastic scattering, emission of characteristic radiation, and Bremsstrahlung. The latest release is MCNP version 6.2.

1.2.3. PENELOPE

PENELOPE is a code system for the simulation of coupled electron-photon transport developed by Francesc Salvat, José M. Fernández-Varea, Eduardo Acosta, and Josep Sempau of the University of Barcelona [7]. PENELOPE is widely used for experimental simulations of

X-ray tube spectra [13], [14], calculations of the full energy peak efficiency of detectors [15], and simulations of XRF setups [16]. Particle transport can be simulated in the energy range from a few hundred eV to ~1 GeV (in the case of electrons and positrons). Photon transport is simulated by means of a standard simulation method, while electron and positron tracking are simulated by means of combined detailed simulation of hard and soft interactions. The code system consists of a set of packages, which specify the properties of materials, carry out the simulation of interactions, define the geometry, apply variance reduction methods, display interaction properties, etc. The code system includes examples of the main programs: *pencyl* and *penmain*. The difference between these main programs is that *pencyl* performs simulations through cylindrical geometries, whereas *penmain* allows particles to be tracked through a more complex set of bodies limited by quadric surfaces. The PENELOPE subroutine geometry package *PENGEOM* builds the quadric geometries and can be directly linked to the main code. A complex system with a large number of elements, e.g. an experimental setup, can be developed. The code is supplied with various examples, which can be used as a starting point for the development of a model. The code is written in FORTRAN programming language and contains a set of subroutine packages.

1.3. Monte Carlo simulation of the experimental setup

After examination of the Monte Carlo codes, it was necessary to select the most appropriate one, weighing up all the advantages and disadvantages. It should be mentioned that the ranges of energies that needed to be modelled for this thesis were from 1 keV to 50 keV. For example, GEANT4 includes a set of low-energy physics models for electron, positron, and photon transport from the PENELOPE package, and is applicable for the energy domain 100 eV<E<1 GeV. For the sake of simplicity, the PENELOPE code can be directly utilised. Comparing the MCNP and PENELOPE codes, the latter is more flexible for programming and describes the interactions at low energies more accurately [17]. It was therefore decided to use PENELOPE, and in the following section we consider the structure of the package in more detail and emphasize options to be used in this thesis.

The PENELOPE subroutine packages are used for particle transport in materials, meaning for random sampling, for particle tracking through quadric geometries, and for generation of the material data files. They include variance reduction and timing subroutines. The *pengeom* program is used to define the geometrical conditions as a system consisting of homogeneous bodies limited by quadric surfaces, and to provide a geometry file (extension: .geo) that is used as part of the input file (extension: .in) required to run the code. The particle transport is described in a detailed, sequential way with accurate atomic relaxation [18]. Both *pencyl* and *penmain* programs generate an output file with the information needed, such as the number of simulated showers, average deposited energies, simulation speed, the simulation parameters for materials (absorption energies, scattering parameters, energy-loss threshold), parameters for variance reduction techniques, and detector definition. The information from the simulation can be collected with impact and/or energy deposition detectors, which should be defined as an element of the modelled geometry. The user can create up to 25 such detectors. The impact detector contains the

energy distribution of all particles that entered its body. Using the impact detector, the user can generate a phase-space file (containing information about particles, such as type, energy, and direction) which is practical for the simulation of complex models. Here, the modelling was split into several sequential steps, using the output of each previous simulation as an input for the following one. The energy-deposition detector delivers the distribution of fully absorbed energies within the detector body.
Additionally, the implemented variance reduction techniques enabled an increase in the efficiency of the simulation, avoiding time-consuming calculations while reducing the statistical uncertainty. For example, a technique of forcing interaction was applied for the simulation of the primary X-ray radiation.
During the PENELOPE 2019 training course, a new version of the code was presented with a PenGUIn graphical-user interface which simplifies interaction with the code. Through the interface, the user can describe the system parameters or directly load an input file. The materials, tables of executables, and geometry viewer are linked to the interface [19].

2. Ray tracing simulation for HOPG optics

The most widely used numerical approach when studying a geometric optics system is the ray tracing method. Unlike the previously discussed Monte Carlo codes, which are based on particle-matter interactions, the ray tracing method is able to simulate the diffraction process according to Bragg's Law. For more complex studies, most of the ray tracing codes also include a wave propagation algorithm, which, coupled with ray tracing, enables the study of the diffraction for coherent waves, for example. A number of ray tracing programs, such as Ray [20], SHADOW-XOP [21], OSLO [22], McXtrace [23], XRT [24], and the COMSOL platform (Ray Optics Module) [25] have been developed in recent decades. These programs enable studies of an optical system, the propagation of beams through the system, and can obtain detailed information about its performance. They can be used to study the imaging and focussing properties of optical elements. All simulation codes are able to visualise the beam characteristics using graphical tools. The following paragraph primarily discusses the ray tracing approach, and presents several ray-tracing codes suitable for the thesis work.

2.1. Ray tracing model

Let us consider the optical system with the origin in the source centre, as illustrated in Figure 4.3. Each ray emitted by the source is specified by the coordinates $(\mathrm{X},\mathrm{Y},\mathrm{Z})$ (global coordinate system) and the direction cosines (a,b,c). A ray passes through the optical element and then reaches the detection screen referred to as the coordinate systems (X_{OE},Y_{OE},Z_{OE}) (local coordinate system) and $(\mathrm{X},\mathrm{Y},\mathrm{Z})$, respectively; the Z-axis is always upward and the Y-axis is along the beam line.

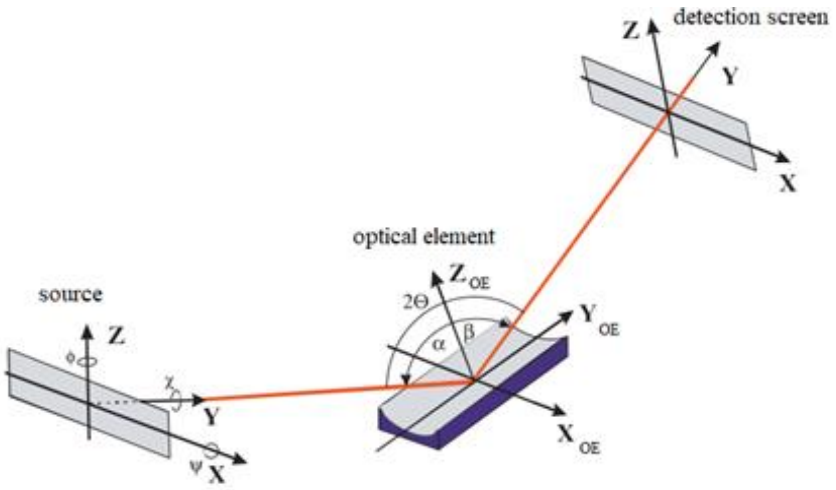

Figure 4.3. Coordinates of the optical system [20].

In the ray tracing procedure, the propagation of the beam through the optical system is computed according to the following sequence:

1. Transform the coordinates $(\mathrm{X},\mathrm{Y},\mathrm{Z})$ and the direction cosines (a,b,c) of each ray to their values in the coordinate system (X_{OE},Y_{OE},Z_{OE});
2. Find the intersection point of the ray with the surface of the optical element;
3. Calculate the new direction according to Snell's Law for reflection and refraction and Bragg's Law for diffraction;
4. Calculate reflectivity or transmissivity;
5. Transform the new beam coordinates and direction cosines back to the coordinate system $(\mathrm{X},\mathrm{Y},\mathrm{Z})$.

After the transformation from a global to a local coordinate system, the intersection point of the ray with the surface of the optical element is determined.

Detailed review of diffraction with mosaic crystals

The tracing model of rays on a mosaic crystal is presented in [26]. In order to describe the focusing properties and defocussing effects of mosaic crystals (see Chapter 2) with ray-tracing, it is necessary to calculate the normals of the individual crystallites diffracting the rays.

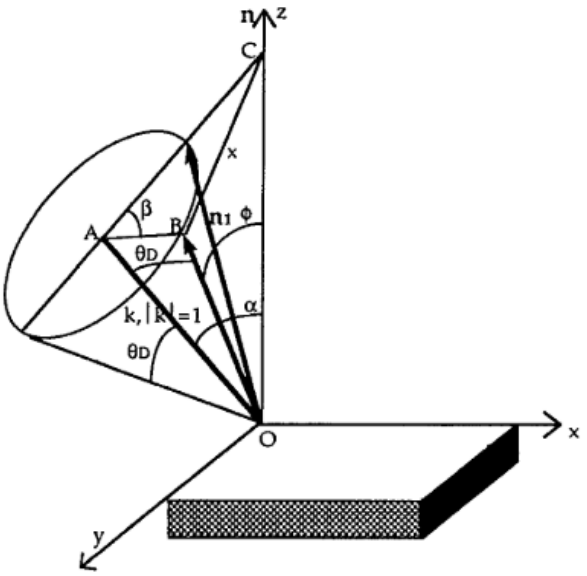

Figure 4.4. Ray tracing on mosaic crystal [26].

The normals of small crystallites are distributed around the crystal normal $\vec{n}$ with respect to a Gaussian distribution law:

$$W(\phi) = \frac{1}{\eta\sqrt{2\pi}} \exp\left(-\phi^2 \Big/ 2\eta^2\right) \tag{4.6}$$

where η is the standard deviation of the distribution and ϕ is the Gaussian distribution angle. The distribution of reflected directions of rays is determined by the distribution of the crystallite normals. As illustrated in Figure 4.4, the diffraction angle θ_D is between the incident ray $\overrightarrow{AO}$ and the crystallite normal $\vec{n}_1$. Rays diffracted by crystallites can be illustrated as vectors which form a cone around the incident ray. In order to perform the reflection, it is necessary to select the values of crystalline normals that satisfy the Bragg Law. The procedure is firstly to calculate the most probable value of the normal $\overrightarrow{n_1}$, which is defined by normal $\vec{n}$ rotated by an angle $(\alpha - \theta_D)$ around an axis perpendicular to $\overrightarrow{AO}$ and $\vec{n}$. Here, α is the angle between the wave vector $\vec{k}$ of the incident ray and $\vec{n}$. Afterwards, the vector $\overrightarrow{n_1}$ is rotated around $\vec{k}$ by angle β, which is defined from ϕ, θ_D and α and considering the relationships established for the ABC and BOC triangles:

$$x^2 = \tan^2\theta_D + \tan^2\alpha - 2\tan\theta_D \tan\alpha \cos\beta \tag{4.7}$$

$$x^2 = \cos^{-2}\theta_D + \cos^{-2}\alpha - 2\cos\phi/(\cos\theta_D \cos\alpha) \tag{4.8}$$

where ϕ lies in interval $(\alpha + \theta_D)$ and $(\alpha - \theta_D)$. To check whether the result is inside the desired interval, an inversion algorithm is used. The probability distribution function is expressed as:

$$d(y) = \int_{-\infty}^{y} W(\phi)\, d\phi \tag{4.9}$$

The detection points lie in the interval between $d_1 = d(\alpha + \theta_D)$ and $d_2 = d(\alpha - \theta_D)$. A selected random value $d_r = d_1 + r(d_2 - d_1)$, where r is a pseudorandom number between 0 and 1. The value ϕ is $\phi = d^{-1}(d_r)$. $\overrightarrow{OB}$ can be obtained by rotation of $\overrightarrow{n_1}$ around $\vec{k}$. The diffracted ray can be characterised by the values $\vec{k}$ and $\overrightarrow{OB}$ with respect to the reflection law.

2.2. Ray tracing packages

The ray tracing programs are increasing in popularity, and are continuing to evolve. They are widely used for modelling synchrotron sources, beamlines, and various optical systems. A ray-tracing program can be chosen depending on the user's particular requirements. The packages include user interfaces, and some codes having implemented colour maps that encode energy and intensity. However, codes have limitations on energy ranges and on the shapes of optical elements. The following sections present some ray tracing packages, describing their particular features.

2.2.1. SHADOW-XOP

SHADOW-XOP is a one of the most widespread ray tracing codes and was developed at the ESRF (European Synchrotron Radiation Facility) for the design of optical systems with different optical elements, such as mirrors, crystals, and gratings. It is mainly intended for synchrotron radiation. The tool is based on a geometrical ray tracing approach and applies phase ray-tracing methods [21]. It performs the tracing of a beam through the optical system, introduced by the collection of various optical elements, and predicts their effects on the output image, transmitted energy, and intensity. SHADOW is written in Fortran programming language and is fully integrated with a recent open source graphical environment, OASYS (OrAnge SYnchrotron Suite), for modelling [27].
SHADOW-XOP allows the simulation of an optical system with mosaic crystals [26]; however there is a limited choice of shapes for the optical elements.

2.2.2. RAY

The ray tracing program RAY was elaborated at BESSY (Berlin Electron Storage Ring Society for Synchrotron Radiation) [28] for optical systems design. It has become a powerful tool for the simulation of synchrotron radiation beamlines and optical systems. RAY creates various types of sources and simulates their tracing through an optical element as governed by the laws of geometric optics [20]. It allows simulation of optical elements such as reflection mirrors of nearly any shape, crystals, zone plates, and gratings, and visualisation of the ray distributions at the source and at the image plane [29]. Focal properties, energy resolution rocking curves, and polarisation characteristics can be calculated. Visualisation of the distribution of the rays at optical elements and onto image planes is possible. The program

is written in Fortran programming language. The features of RAY are similar to those of the SHADOW-XOP program.

2.2.3. XRT (XRayTracer)

The XRT Package is a powerful ray tracing tool developed by Konstantin Klementiev (MAX IV Laboratory) and Roman Chernikov (Canadian Light Source) [24], [30]. It is written in Python programming language. The code can define various sources, optical elements, rectangular and round apertures, screens for beam visualisation, and can specify material properties (absorption coefficients, reflectivity, transmissivity). XRT is provided with many examples and explanations. It has an excellent graphical presentation. Some SHADOW algorithms are used in XRT.

2.3. Simulation of the HOPG optics with the ray tracing method

SHADOW-XOP and RAY codes offer significant opportunities for modelling complex optical instruments, and are more intended to design optical systems for the synchrotron radiation domain. At the beginning of the development of the optical model for this work, no cylindrical optical element had been implemented in either code. Therefore, it was supposed that the XRT package was the most appropriate tool for modelling the optical device. The missing parameters of individual elements of the optical system, and notably the cylindrical HOPG crystal, could be added thanks to the flexibility of the Python programming language. In the XRT code, the user can build an optical system using a well-developed user interface where the physical and geometrical parameters of individual optical elements can be changed. Another feature is that the user can obtain visual information about the properties of rays at any stage of the ray tracing.
The parameters of an optical system are defined through the next modules:

- The *sources* module represents the container class and allows the creation of geometric and synchrotron sources, including bending magnet, wiggler, and planar and elliptic undulators;
- with the *optical elements* module, such elements as flat mirrors, crystals, multilayers, or gratings can be generated and defined in various shapes (so-called parametric surfaces), and any surface of an optical element can be embedded with a crystal;
- the *materials* module allows the definition of atomic and material properties related to x-ray scattering, diffraction, and propagation;
- the *screen* module defines a flat screen for beam visualisation.

The screen intercepts the rays delivering the coloured images, and can accumulate information on the beam. The output file thus generated contains the necessary information on the beam properties.

3. Conclusions

This chapter presented the basic principles of the Monte Carlo and ray tracing methods, which are essential for the detailed description of the miniature setup. The features and limitation of codes based on these two methods were discussed. The miniature system without HOPG optics can be modelled with the Monte Carlo code PENELOPE. The ray tracing code XRT allowed us to study the reflection behaviour of the HOPG monochromator and compute the output of the complex setup. Chapter 5 and Chapter 6 extensively describe the simulation of the entire experimental setup using these two codes.

References

[1] S. Pessanha, M. Manso, V. Antunes, M. L. Carvalho, J. M. Sampaio. "Monte Carlo simulation of portable XRF setup: Non-invasive determination of gold leaf thickness in indo-Portuguese panel paintings", *Spectrochim. Acta - Part B*, 156, 1–6, 2019.

[2] M. Moralles, C. Da Costa Guimarães, E. Okuno. "Monte Carlo simulation of X-ray generation and detection."

[3] K. Rickers, R. Thomas, W. Heinrich. "Trace-element analysis of individual synthetic and natural fluid inclusions with synchrotron radiation XRF using Monte Carlo simulations for quantification", *Eur. J. Mineral.*, 16, 23–35, 2004.

[4] K. Debertin, B. Grosswendt. "Efficiency calibration of semiconductor detectors by primary standard sources ans Monte Carlo calculations", *Nucl. Instruments Methods*, 203, 343, 1982.

[5] F. Salvat, J. Fernández-Varea, J. Sempau. *PENELOPE-2014: A Code System for Monte Carlo Simulation of Electron and Photon Transport*. OECD/NEA Data Bank, 2014.

[6] "Los Alamos National Laboratory: MCNP Home Page". (available at https://mcnp.lanl.gov/).

[7] "NEA archived lists". (available at http://www.oecd-nea.org/lists/penelope.html).

[8] "Overview | geant4.web.cern.ch". (available at http://geant4.web.cern.ch/).

[9] "The official FLUKA site". (available at http://www.fluka.org/fluka.php).

[10] H. Hirayama, Y. Namito, A. F. Bielajew, S. J. Wilderman, W. R. Nelson. "The EGS5 Code System". Available from KEK (High Energy Accelerator Research Organization), 2005

[11] L. M. N. Távora, E. J. Morton, W. B. Gilboy. "Design considerations for transmission X-ray tubes operated at diagnostic energies", *J. Phys. D. Appl. Phys.*, 33, 2497–2507, 2000.

[12] S. Agostinelli, J. Allison, K. Amako, et al.. "Geant4 - a simulation toolkit", Nucl. Instruments *Methods Phys. Res.*, 506, 250–303, 2003.

[13] J. G. Zhou, D. Lockley, A. Vella, A. M. A. Munoz, M. J. F. Healy, D. W. Lane. "A fast and reliable approach to simulating the output from an x-ray tube used for developing security backscatter imaging", *Adv. Comput. Methods X-Ray Opt.* IV, 33, 2017.

[14] D. M. Cunha, A. Tomal, M. E. Poletti, "Monte carlo simulation of X-ray spectra in mammography and contrast-enhanced digital mammography using the code PENELOPE", *IEEE Trans. Nucl. Sci.*, 60, 495–502, 2013.

[15] K. L. Karfopoulos, M. J. Anagnostakis. "Parameters affecting full energy peak efficiency

determination during Monte Carlo simulation", *Appl. Radiat. Isot.*, 68, 1435–1437, 2010.

[16] E. García, J. Jiménez, J. Puimedón. "Dose calculation in patients with PENELOPE/PENGEOM", J. *Phys. Conf. Ser.*, 74,2007.

[17] D. Roet, C. Ceballos, P. Van Espen. "Comparison between MCNP and PENELOPE for the simulation of X-ray spectra in electron microscopy in the keV range", *Nucl. Instruments Methods Phys. Res. B*, 251, 317–325, 2006.

[18] P. J. Sempau, J. M. Fern A Andez-Varea, E. Acosta, F. Salvat. "Experimental benchmarks of the Monte Carlo code PENELOPE", *Nucl. Instruments Methods Phys. Res. B*, 207, 107–123, 2003.

[19] "Penguin". (available at http://www.mcnpvised.com/penguin/penguin.html).

[20] A. Erko, T. Krist, A. G. Michette. *Modern Developments in X-Ray and Neutron Optics*. Springer series in optical sciences, 2008.

[21] M. Sanchez Del Rio, N. Canestrari, F. Jiang, F. Cerrina. "SHADOW3: A new version of the synchrotron X-ray optics modelling package", *J. Synchrotron Radiat.*, 18, 708–716, 2011.

[22] "OSLO is a powerful Optical design program with the scope you need.". (available at https://www.lambdares.com/oslo/).

[23] E. Bergbäck Knudsen, A. Prodi, J. Baltser, et al. "McXtrace: A Monte Carlo software package for simulating X-ray optics, beamlines and experiments", *J. Appl. Crystallogr.*, 46, 679–696, 2013.

[24] "xrt (XRayTracer) — xrt 1.3.3 documentation". (available at https://xrt.readthedocs.io/).

[25] "Modeling Software for Ray Tracing in Optically Large Systems". (available at https://www.comsol.com/ray-optics-module).

[26] M. Sánchez Del Río, S. Bernstorff, A. Savoia, F. Cerrina. "A conceptual model for ray tracing calculations with mosaic crystals", *Rev. Sci. Instrum.*, 63, 932–935, 1992.

[27] M. Sanchez, D. Rio, L. Rebuffi. "OASYS: A software for beamline simulations and synchrotron virtual experiments" in *Proceedings of the 13th International Conference on Synchrotron Radiation Instrumentation – SRI2018*", 2054, 060081, 2019.

[28] "Synchrotron Radiation at BESSY II". (available at https://www.helmholtz-berlin.de/forschung/oe/fg/mi-synchrotron-radiation/synchrotron/photons/bessy_en.html).

[29] B. Beckhoff, B. Kanngießer, N. Langhoff, R. Wedell, H. Wolff (Eds.). *Handbook of Practical X-Ray Fluorescence Analysis*. Springer, 2006.

[30] K. Klementiev, R. Chernikov. in Powerful scriptable ray tracing package xrt. *Proc. of SPIE* Vol. 9209 92090A-1, 2014.

Chapter 5

Monte Carlo simulation of the experimental setup

This chapter focuses on Monte Carlo simulations of the experimental setup. This information is necessary when studying the related physical phenomena, and to gain a better understanding of the instrument. Furthermore, the device modelled in combination with HOPG optics simulation may be used to predict the potential output of the entire device under geometrical arrangements not experimentally feasible today.

The Monte Carlo method and several codes for the simulation of particle interaction with matter have been presented in Chapter 4. After a preliminary review of the simulation tools, the Monte Carlo PENELOPE code was chosen as the most appropriate for this work.

The experimental setup modelling is divided into two parts. Firstly, the simulation of the energy spectrum emitted from an X-ray tube is presented. This comprises the generation of the primary X-rays in a target, absorption in a tube window, and filters. X-rays are generated by mono-energetic electrons interacting with the tube anode material and are recorded by a fictitious detector. By simulating the X-ray tube separately, a library of spectra calculated for a range of different configurations (e.g., different voltages and filtering) can be established. Thus, any desired spectra can be rapidly exploited for subsequent simulations. The second part consists in the simulation of both measurement channels used by the miniature setup. The geometries of each channel are presented in this chapter. The models include a point source, a sample, and a detection body. The calculated X-ray tube spectra are inserted as input data at the position of the point source.

1. Simulation of the spectrum emitted by the X-ray tube

The Monte Carlo method is widely used for the calculation of X-ray radiation. It is intended to help understand X-ray production [1], and has become a powerful tool for the development and optimisation of X-ray imaging systems [2] - [4]. In this work, the estimation of the primary source spectrum constitutes an essential part of the simulation of the spectrum obtained with an entire XRF instrument. This paragraph presents the simulation of the X-ray tube spectrum using PENELOPE, and compares it with the results calculated from a theoretical model.

1.1. Simulation with the PENELOPE code

The transmission type X-ray tube was designed utilizing the geometry subroutine package PENGEOM (for details, see Chapter 4). Since we lacked a detailed description of the tube design from the manufacturer, a simplified X-ray tube geometry was modelled. It just consists of a cathode, an Ag anode, a Be window, and an impact detector, as depicted in Figure 5.1.
The collimators and housing assembly of the real X-ray tube [5] were not taken into consideration in the simulation, because particle tracking through the complete system would require a prohibitive amount of calculation time to obtain a satisfactory statistical uncertainty.

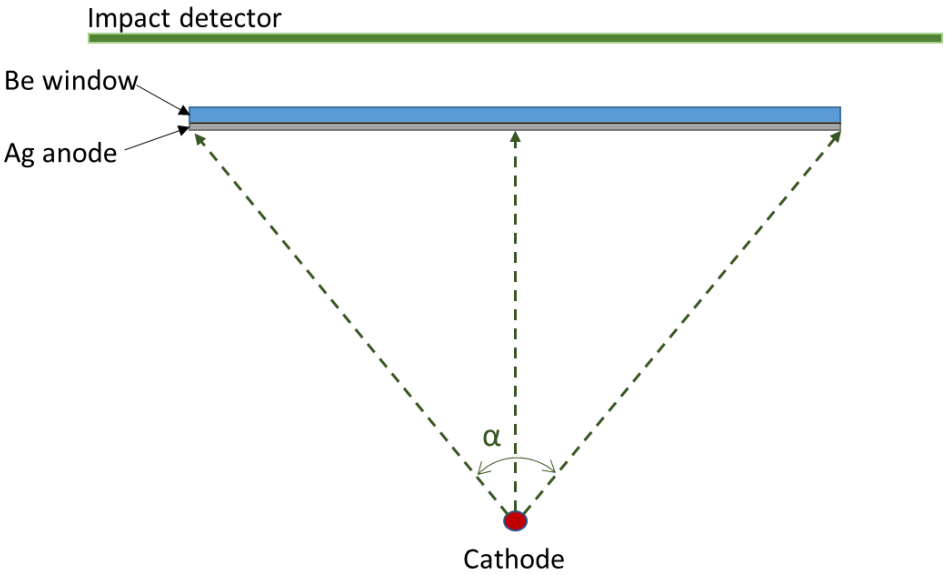

Figure 5.1. Model of the transmission anode X-ray tube designed through the subroutine package PENGEOM. Note that the target thickness is enlarged for display purposes.

In this model, mono-energetic electrons are emitted from the cathode towards the Ag anode, which is located at 3 cm. Here, the cathode is considered as a point source. The distribution of electrons is uniformly sampled within a cone of given angular aperture α (dashed lines) in order to cover only the target area. The 0.75 μm thick Ag target is deposited directly on the internal side of the 127 μm thick Be window. The X-rays produced in the Ag

anode subsequently pass through the Be window and are collected outside by the impact (virtual) detector. The latter is a fictitious body placed at a distance 1 cm after the Be window. It is defined as a part of the tube geometry and does not affect particle tracking. The tracking is stopped at the entrance of the detector body. The particle transport is performed in a vacuum, in order to avoid interaction on the tracking of X-rays on their path from the Be window to the detection surface. The energy window covered by the impact detector is defined from 1 keV to the maximum energy of the primary particles. The impact detector thus provides the energy distribution of generated X-rays [6], [7] which can subsequently be utilised as input data for the simulation of spectra for the X-ray setup.

It should be noted that due to the extremely thin anode material and small effective solid angle, the interaction probability of electrons within the target material is very low. One of the disadvantages of the Monte Carlo method is that the statistical uncertainties of the results are linked to the number of simulations; consequently, the required value (<3 %) can be reached at the cost of computation time [7], [8]. To increase the efficiency of simulations of low-probability processes and avoid time-consuming simulations, the variance-reduction technique was applied [9]. The interaction forcing method (or method of weights) allows artificial increasing of the probability of the interaction events within the target. In particular, interaction forcing was applied for inner-shell ionisation and bremsstrahlung splitting was in turn applied in combination with interaction forcing. The effective mean free path for these interactions was substituted by values less than the real ones by a forcing factor (*F=100*), thereby increasing the frequency of interactions. The application of this variance reduction technique does not influence the overall spectral shape.

The simulation result for the tube spectrum is illustrated in Figure 5.2. The Ag target was "hit" with 40 keV electrons to simulate the emission of Ag characteristic K lines. The calculated spectrum includes the bremsstrahlung, which is the result of the energy loss of electrons through inelastic collisions, and the characteristic X-rays of the target material due to the relaxation of vacancies produced in the K and L subshells. The spectrum was collected on 350 bins uniformly distributed in the energy window from 1 keV to 40 keV. The bin width used in the simulations is ~0.11 keV which enabled resolution of the Ag K-L_2 and K-L_3 lines with energies of 21.99 keV and 22.16 keV, respectively. The bremsstrahlung output intensity was low enough, due to the target thickness.

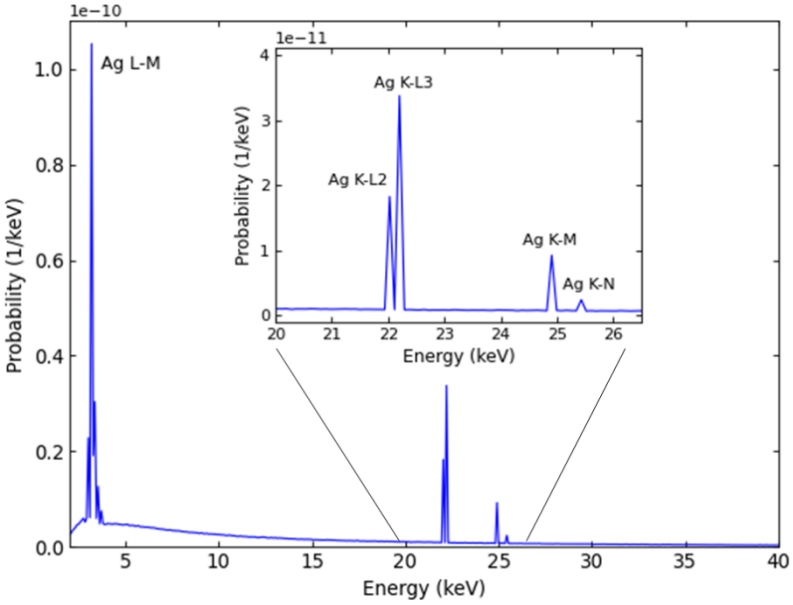

Figure 5.2. Emission spectrum of the X-ray transmission tube with Ag anode and 40-keV electrons simulated by PENELOPE. The spectrum is as collected in the virtual detector.

In another experimental arrangement of the X-ray tube, a filter was used directly above the Be window, as illustrated in Figure 5.3, and the same conditions were considered in the simulation.

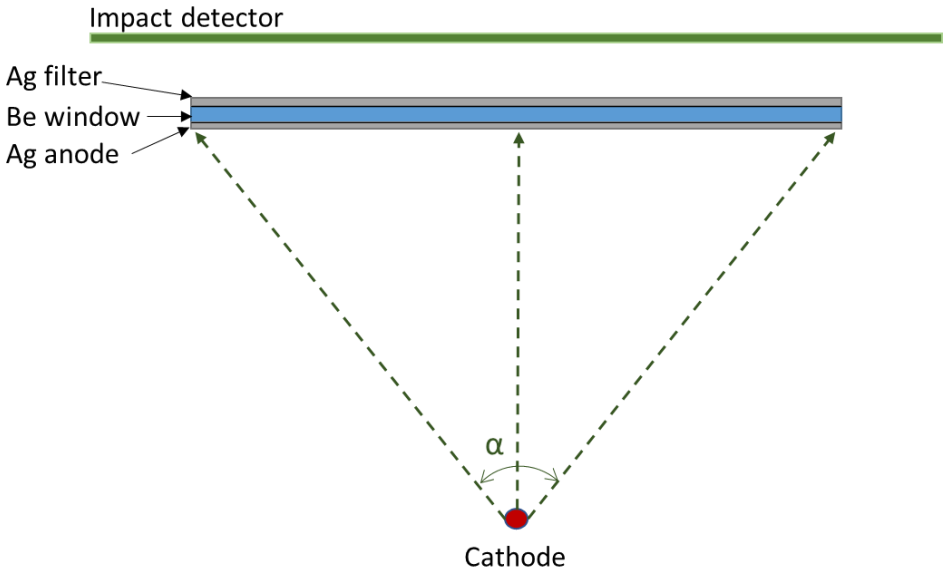

Figure 5.3. Model of the transmission X-ray tube with the 25 μm thick Ag filter built with the subroutine package PENGEOM. Note that the target and filter thicknesses have been scaled up for display purposes.

The conical source with angular aperture α corresponds to the size of the anode. The filter was a 25 μm thick Ag disc with a radius of 3 mm. Due to the absorption in the filter material,

the shape of the output spectrum was modified, as shown in Figure 5.4.
One can observe that the Ag L-M lines have been removed, and that the background is considerably reduced in the energy range from 1 keV to 15 keV. The intensities of the characteristic lines illustrated in Figure 5.2 Figure 5.4 are the same order of magnitude.

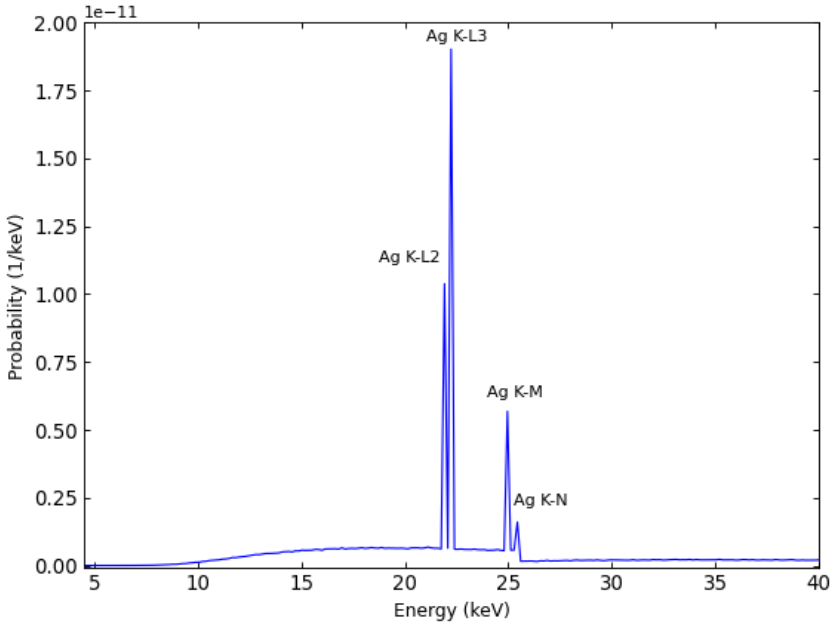

Figure 5.4. Emission spectrum of the transmission tube with Ag anode and 40-keV electrons, with 25 μm thick Ag filter simulated by PENELOPE. The spectrum is as collected in the virtual detector.

1.2. Comparison of the spectra calculated with the PENELOPE and theoretical models

There are different theoretical algorithms available for the evaluation of X-ray tube spectra [10], which are included in fundamental parameter software. It is interesting to compare the simulated X-ray tube spectrum with one calculated from a theoretical algorithm.
Here, the X-ray tube spectrum is estimated using the semi-empirical algorithm proposed by H. Ebel [11]. It is based on the corrected Kramer's formula, where the continuum spectral distribution of the number of dN X-rays in the energy range from E to $E+dE$ is expressed as:

$$\mathrm{dN} = \mathrm{const\ i\ \Omega\ Z}\left(\frac{\mathrm{E_0}}{\mathrm{E}} - 1\right)^{\mathrm{x}} \mathrm{f\ F_{Be}\ dE} \tag{5.1}$$

where $const = 1.35 \times 10^9$ (in sr^{-1} mA^{-1} keV^{-1} s^{-1}), i is the X-ray tube current (in mA), Ω is the solid angle (in sr), which the target subtends from the source, Z is the atomic number of a target, and E_0 is the incident electron energy (in keV), $x = 1.109 - 0.00435Z + 0.00175\ E_0$; F_{Be} is the Be window absorption correction term, which is defined as $F_{Be} = exp(-0.35E^{2.86}t_{Be})$ where t_{Be} is the thickness of the Be window (in μm); f is the absorption term given by:

$$f = \frac{1 - \exp(-\mu(E)\ 2\ \overline{\rho z}\ \sin\varphi/\sin\psi)}{\mu(E)\ 2\ \overline{\rho z}\ \sin\varphi/\sin\psi} \tag{5.2}$$

$\mu(E)$ is the mass attenuation coefficient for the target, $\overline{\rho z}$ is the mean range of penetration, φ is the incident angle of electrons on the target surface, ψ is the target take-off angle.
The characteristic radiation generated by primary electrons in the case of a target of one element is expressed by:

$$N_{kl} = \Omega_i Const_{kl} \frac{1}{S_k} R\ \omega_k\ p_{kl}\ f\ F_{Be} \tag{5.3}$$

where k is the ionized atomic level, l is the level from which the vacancy is filled, $Const_{kl} = 6 \times 10^{13}$, ω_k is the K fluorescence yield, p_{kl} is the transition probability, and f is the absorption term calculated from Eq. (5.2) for continuum radiation where E is replaced by the energy of characteristic line E_{kl}; $^1/_{S_k}$ is the stopping power factor and R is the backscattering factor (for more details, refer to [10], [11]).
The theoretical tube spectrum was calculated using the subroutine of the PyMCA package which is based on the Ebel algorithm. PyMCA is a widely-used toolkit for the visualisation and analysis of X-ray fluorescence data based on the fundamental parameters algorithm [12], [13]. Details on the features and applications of PyMCA will be discussed in Chapter 7.
The simulated tube spectrum, as well as the computed version, were obtained by considering the incident electron energy of 40 keV, a 0.75 μm thick target, a 25 μm thick filter, and 90° incident and take-off angles with respect to the target surface (see Figure 5.5).

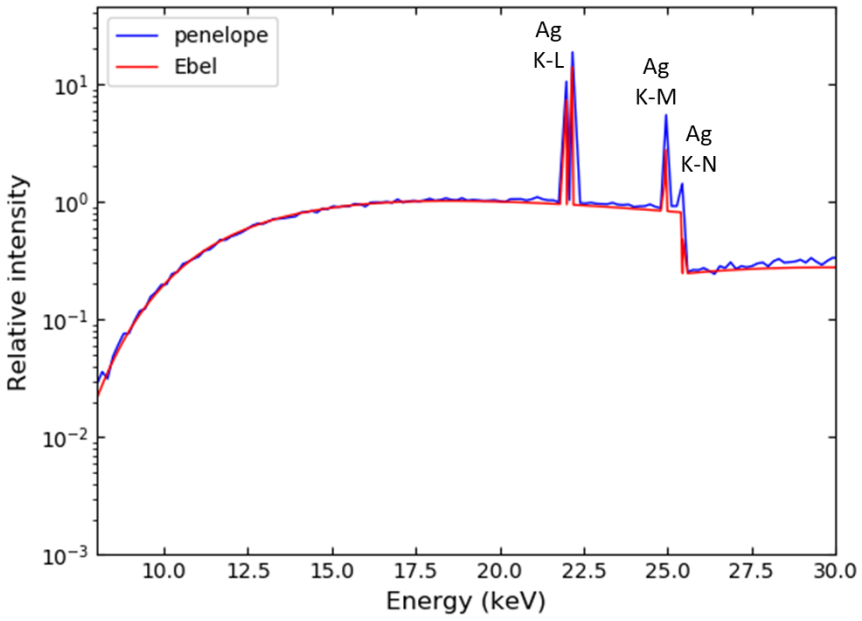

Figure 5.5. Comparison of the spectra from the transmission target X-ray tube computed with theoretical algorithm from Ebel (red line) and PENELOPE code (blue line). Both models include the Ag filter. The spectra are normalised to unity at 20 keV.

As can be observed, the models agree with each other very well. They show the same spectral shape, and the backgrounds exhibit very good matching. However, PENELOPE slightly

overestimates the intensities of the characteristic K-L lines and the difference is more significant in the case of the intensities of the K-M lines, which may be due to the forced interactions in the PENELOPE model. Additional Ag K-N lines are observed in the PENELOPE results, while their computation is omitted in the theoretical model.
The spectrum computed with the theoretical algorithm from Ebel can be used as an alternative in PENELOPE simulations.

2. Simulation of the first channel of the experimental setup

The PENELOPE code enables detailed modelling of an experimental setup, to gain a better understanding of the interactions and resulting spectra. The basic idea here was to reproduce the measured X-ray spectra, and to explore the performance and possibilities of the given system. First, the simulation model requires knowledge of the primary X-ray energy distribution and for this point, tube spectra simulated in the previous paragraph with PENELOPE could be integrated into the code as input energy spectra.
Now let us consider the system geometry developed using the PENGEOM package. The model includes a point source emitting the primary X-rays, a cup with a sample solution, and a detection surface (see Figure 5.6.); the X-ray source and the detector are in the same plane. All components of the system are represented as cylinders with corresponding dimensions.

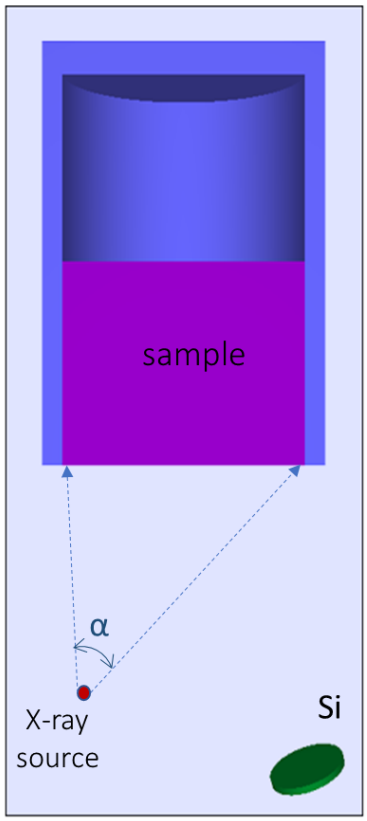

Figure 5.6. Side view of the system geometry built with the PENGEOM package. The model corresponds to the geometry of the first channel of the miniature setup.

The sample, composed of various elements in nitric acid, is placed in a polypropylene cup

with 3 mm thick walls and 15 mm radius. The sample is irradiated by a polychromatic X-ray source employing the tube spectra calculated with PENELOPE in § 1. The primary X-rays are uniformly emitted from the starting point within a cone of angular aperture α in order to expose only the sample surface and avoid irradiation of the detector. In contrast to the SDD used in the measurements, the modelled detector does not include the Be window, since it affects only the transmission of low-energy X-rays. Nor does it include the multilayer collimator, in order to avoid particle tracking through a detection system with complex geometries, which can be time-consuming. Here, the detector is represented by a 500 μm thick silicon disc with a radius of 2.33 mm, which meets the effective dimension of the SDD active region. The radius of the modelled disc is equal to that of the multilayer collimator since, as discussed in Chapter 3, the latter limits the collection of X-rays on the edges of the detector active volume where the charge collection is poor. Outgoing X-rays are detected at an angle of 23° to the sample normal, at a distance of 17.9 mm. To be closer to the experimental conditions, the space in the model was filled with air. For the simulation of the sample spectra, variance reduction techniques were not applied.
The simulated spectrum of the sample containing Sr is depicted in Figure 5.7. The characteristic peaks at Sr K-emission energies, as well as the Rayleigh and Compton peaks of the anode tube, are observed.

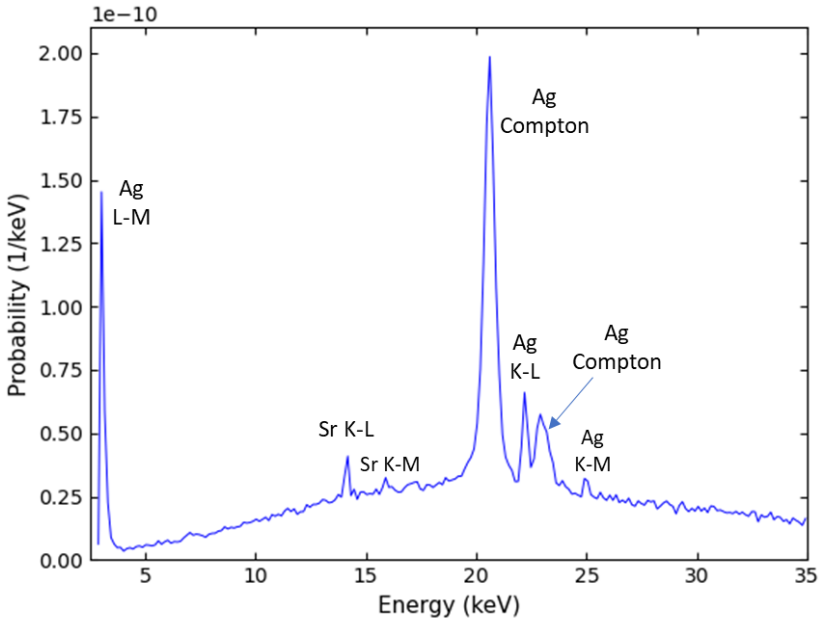

Figure 5.7. Simulated spectrum from a sample containing Sr collected with an impact detector.

Additionally, the information was simultaneously generated in the energy-deposition detector, also defined by the Si disc. The output spectrum of this kind of detector, contrary to the impact detector, is the distribution of absorbed energy in the detector body (see Chapter 4, [7]). The simulation was carried in the energy region 1 keV<E<27 keV in 300 bins, giving the bin width of ~0.09 keV for both types of detectors. The information from the simulation presents the energy deposition of X-rays in the detector volume. To validate the

modelled system, simulated results extracted from the energy-deposition detector have to be compared with experimental data.
In another way, the output spectrum of the impact detector can also be compared with measurements. It should however be pointed out that not all X-rays entering the impact detector body subsequently deposit their energies, as some X-rays can leave the body without being completely absorbed. Thus, it is necessary to multiply the simulation results by the intrinsic efficiency of the SDD. The latter presents the fraction of X-rays absorbed within the sensitive volume. For a detailed description of the intrinsic efficiency calculation for the SDD, refer to Chapter 3.
In PENELOPE, the results are given as the probability density for detecting X-rays per unit of energy. While the experimental spectrum is expressed in a number of events recorded at energy *E*, it is necessary to normalise the results in order to compare them. For the following examples, unless otherwise stated, the intensities are normalised to unity at the Sr K-L_3 line.

2.1. Comparison of X-ray fluorescence spectra with unfiltered primary radiation

Figure 5.8 compares the simulated and measured spectra for the sample solution containing Sr of 100 mg L^{-1}. In the experiment, the X-ray tube operated at 45 kV and 15 µA for 900 s, and the spectrum was collected with the SDD. The results are in very good agreement and show the same spectral shape, but a small difference can be seen in the region of the Ag Rayleigh and Compton peaks. This can be explained by the simulated primary tube spectrum, since the manufacturer did not provide detailed information about the instrument construction.
In addition, it should be noted that the data collected with energy-deposition and impact detectors multiplied by the SDD efficiency agree very closely. The difference observed is presumably due to absorption in the SDD multilayer collimator. Nevertheless, the data recorded with the energy-deposition detector, as well as the spectrum obtained with the impact detector, can be used. It should be pointed out that the energy resolution of the detector was not taken into account in the PENELOPE simulation.
In the experimental spectrum, the peaks in the energy range from 5 keV to 10 keV are due to the material of the X-ray tube, SDD housing, or setup shielding, which are not of interest for this application and therefore were not included in the modelling.

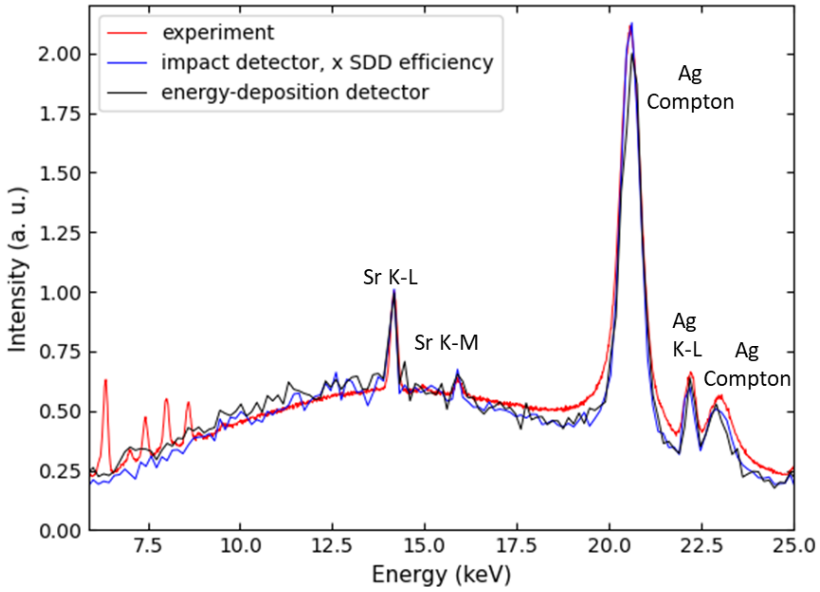

Figure 5.8. Comparison of the simulated spectra obtained with the energy-deposition detector (black line), the impact detector (blue line), and measured (red line) spectrum from the Sr-containing sample. The output spectrum from the impact detector was multiplied by the SDD efficiency.

The simulations and measurements were performed for various sample compositions and concentrations. Figure 5.9 illustrates the comparison of spectra for the sample with 100 mg L^{-1} of Se, Rb, and Sr in equal concentrations, and shows good agreement for the fluorescence peaks.

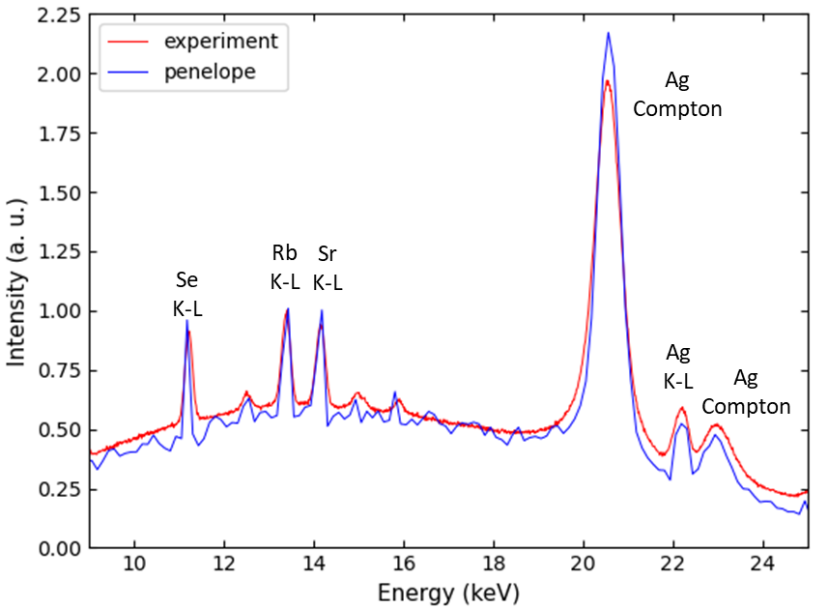

Figure 5.9. Comparison of the simulated (blue line) and measured (red line) spectra from the sample solution containing Se, Rb, Sr. Simulations and measurements were performed with the first channel of the experimental setup. Spectra are normalised to the Rb K-L line.

2.2. Comparison of X-ray fluorescence spectra with filtered primary radiation

The next simulations were performed to demonstrate the influence of the Ag filter on the X-ray energy spectra for the same set of samples and geometrical arrangement (see Figure 5.10 and Figure 5.11).

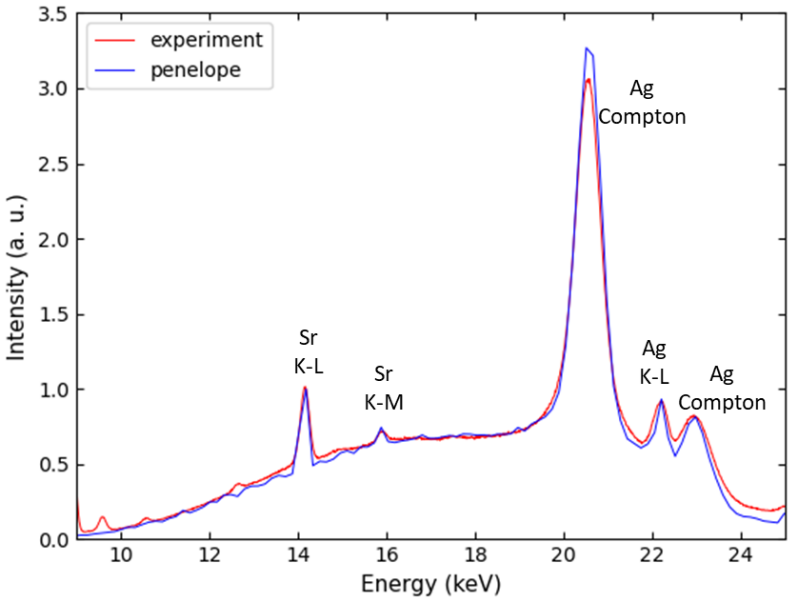

Figure 5.10. Comparison of the simulated (blue line) and measured (red line) spectra from the Sr-containing sample solution performed with the first channel of the experimental setup.

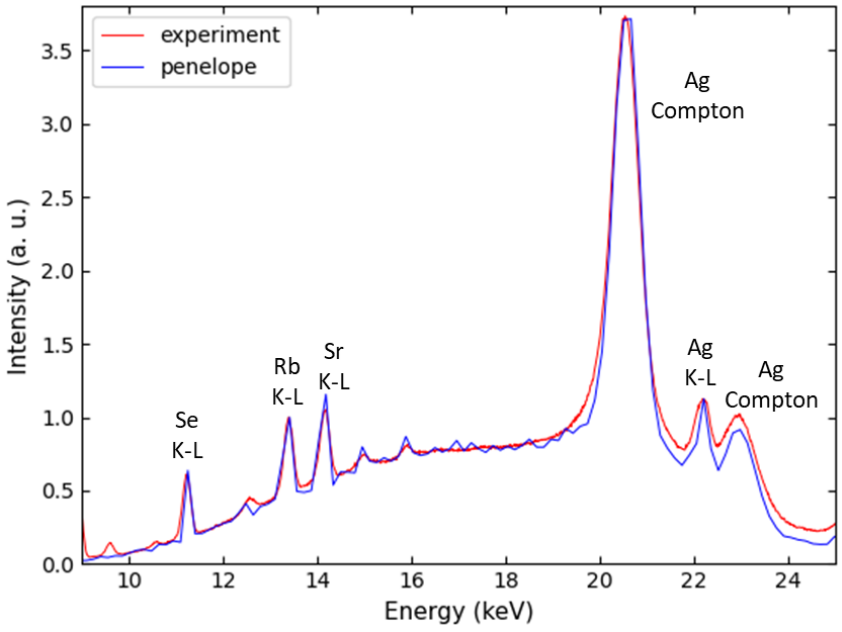

Figure 5.11. Comparison of the simulated (blue line) and measured (red line) spectra from the sample solution containing Se, Rb, and Sr. Simulations and measurements were performed with the first channel of the experimental setup. Spectra are normalised to the Rb K-L line.

The comparison with the experimental data again proves that the PENELOPE code correctly

reproduces the response of the XRF setup. The simulated spectrum presented below is smoother than that in Figure 5.9 due to longer computation times.

3. Simulation of the second channel

There is also considerable interest in modelling the second channel of the miniature setup without the HOPG monochromator. As mentioned at the beginning of this chapter, it was important to investigate the setup with PENELOPE, since it could contribute to the modelling of the X-ray reflection from the HOPG crystal, reported in Chapter 6.
The next modelled system corresponds geometrically to the second channel of the experimental setup, where the axis of the X-ray tube and the second SDD are perpendicular to each other (see Figure 5.12). The closest distance possible from the sample to the SDD is 125 mm.

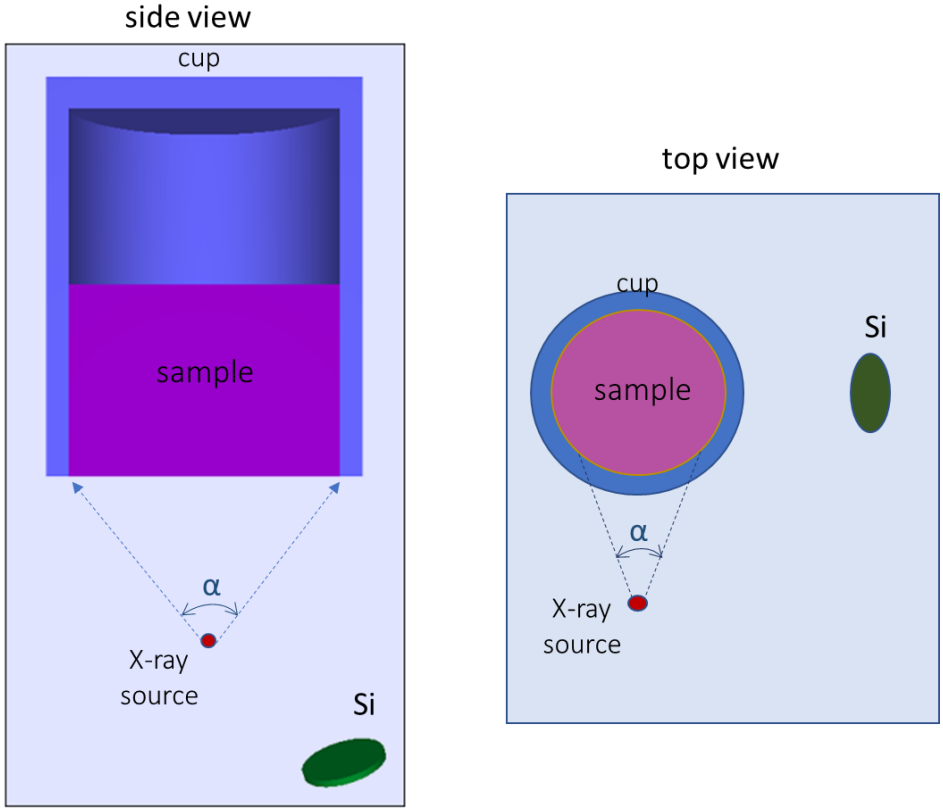

Figure 5.12. System geometry built with the PENGEOM package. The model geometrically corresponds to the second channel of the experimental setup.

The simulations and measurements were performed simultaneously for the samples with Sr (see Figure 5.13) and Se (see Figure 5.14). Note that the simulated and experimental results compared in Figure 5.10, in the case of the first channel, are significantly more intense than those in Figure 5.13 performed for the second channel, respectively. This is the consequence of different effective solid angles, which depend on the detector positions relative to the sample. Also, the absorption of X-rays along their paths to the sensitive surface influence the calculated/measured intensities.

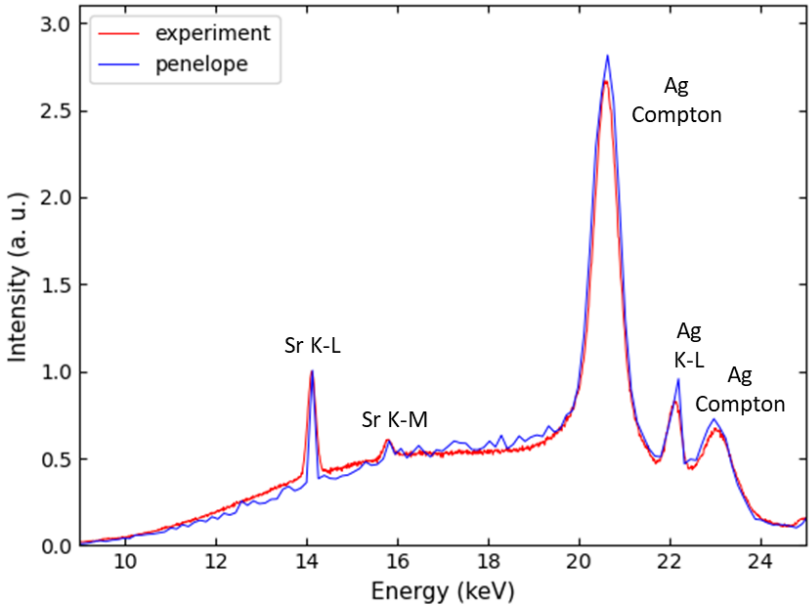

Figure 5.13. Comparison of the simulated (blue line) and measured (red line) spectra from the sample solution with Sr performed with the second channel of the miniature setup without the HOPG monochromator.

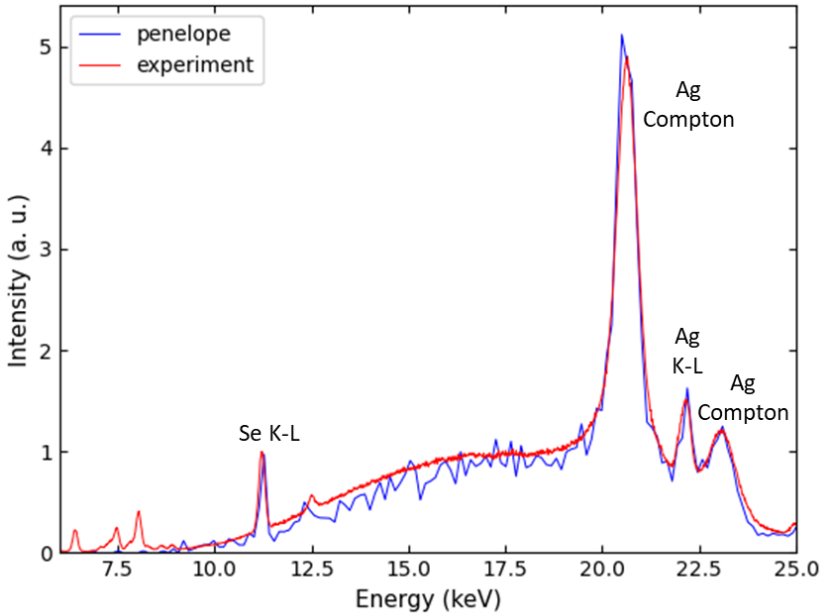

Figure 5.14. Comparison of the simulated (blue line) and measured (red line) spectra from the sample solution containing Se. Simulations and measurements were performed with the second channel of the miniature setup. Spectra are normalised to the Se K-L line.

4. Conclusions

In this chapter, the experimental setup was successfully simulated via Monte Carlo simulations using the PENELOPE code, enabling a detailed definition of the entire system. The complex model involved the calculation of the X-ray spectrum from the transmission anode X-ray tube and the interaction of X-rays through the system employing the tube spectrum as the source. The tube spectrum calculated by PENELOPE showed good agreement with that calculated from the theoretical algorithm proposed by Ebel. It can be concluded that the X-ray tube simulated by PENELOPE was described with sufficient accuracy. The computed spectra were directly inserted in the model of the experimental system, which included the point source, the sample, and the detection body. A number of simulations were performed and shown to be sufficiently consistent with the measurement results. Hence, it can be concluded that the simulation model enables us to accurately predict the response of the XRF setup. PENELOPE simulations are useful for the setup design optimisation, since the output spectra can be used for predictive simulations and efficiently contribute to the full modelling of the second channel, including the HOPG crystal, which is the subject of the next chapter.

References

[1] L. M. N. Távora, E. J. Morton, W. B. Gilboy. "Design considerations for transmission X-ray tubes operated at diagnostic energies", *J. Phys. D. Appl. Phys.*, 33, 2497–2507, 2000.

[2] J. G. Zhou, D. Lockley, A. Vella, A. M. A. Munoz, M. J. F. Healy, D. W. Lane. "A fast and reliable approach to simulating the output from an x-ray tube used for developing security backscatter imaging", *Adv. Comput. Methods X-Ray Opt. IV*, 33, 2017.

[3] M. Yücel, E. Emirhan, A. Bayrak, C. S. Ozben, E. B. Yücel. "Comparison of simulated and measured spectra from an X-ray tube for the energies between 20 and 35 keV", *Nucl. Instruments Methods Phys. Res. A*, 799, 50–53, 2015.

[4] G. J. Bootsma, H. Nordström, M. Eriksson, D. A. Jaffray. "Monte Carlo kilovoltage X-ray tube simulation: A statistical analysis and compact simulation method", *Phys. Medica*, 72, 80–87, 2020.

[5] "Mini-X2 X-Ray Tube System for XRF – Amptek – X-Ray Detectors and Electronics". (available at https://www.amptek.com/products/x-ray-sources/mini-x2-ray-tube).

[6] F. Salvat. "The penelope code system. Specific features and recent improvements", *Ann. Nucl. Energy*, 82, 98–109, 2015.

[7] F. Salvat, J. Fernández-Varea, J. Sempau. *PENELOPE-2014: A Code System for Monte Carlo Simulation of Electron and Photon Transport*. OECD/NEA Data Bank, 2014.

[8] X. Llovet, F. Salvat. "PENEPMA: A Monte Carlo programme for the simulation of X-ray emission in EPMA", *IOP Conf. Ser. Mater. Sci. Eng.*, 109, 2016.

[9] D. M. Cunha, A. Tomal, M. E. Poletti. "Monte carlo simulation of X-ray spectra in mammography and contrast-enhanced digital mammography using the code PENELOPE", *IEEE Trans. Nucl. Sci.*, 60, 495–502, 2013.

[10] R. Sitko. "Influence of X-ray tube spectral distribution on uncertainty of calculated fluorescent radiation intensity", *Spectrochim. Acta - Part B*, 62, 777–786, 2007.

[11] H. Ebel. "X-ray Tube Spectra", *X-Ray Spectrom.*, 28, 255–266, 1999.

[12] V. A. Solé, E. Papillon, M. Cotte, P. Walter, J. Susini. "A multiplatform code for the analysis of energy-dispersive X-ray fluorescence spectra", *Spectrochim. Acta - Part B*, 62, 63–68, 2007.

[13] ["PyMCA Fluorescence Toolkit". (available at http://pymca.sourceforge.net/).

Chapter 6

Modelling of the optical system with a ray-tracing method

The second detection channel of the experimental setup is of particular interest for this thesis. It is based on a von Hamos full-cylinder geometry [1] employing highly oriented pyrolytic graphite (HOPG) crystal as a dispersion filter. The energy bandwidth covered by the instrument is an important parameter, and is dependent on the sizes and relative positions of the source, the crystal, and the detector. In order to evaluate the performance of the HOPG crystal-based channel, it is necessary to consider the contribution of each parameter to the output results.

With the help of the ray tracing XRT code, the second detection channel of the miniature setup was modelled taking into account all elements of the system between the sample and the SDD. The first part of this chapter deals with the focusing properties of the cylindrical HOPG crystal. A number of simulations were performed in order to evaluate the effects of the source size on the output beam. Afterwards, the complex optical model was developed, with the sample regarded as a geometrical source. The ray tracing calculations were compared with the experimental data. The chapter concludes with the simulation of the entire experimental setup coupling Monte Carlo and ray tracing simulation results.

1. Investigation of the optical system by ray-tracing

The open-source XRT code [2] was retained in this work for the ray-tracing calculation. Written in Python, it allowed us to develop an optical system and extract useful data.
The investigations started with the simulation of the simple optical system sketched in Figure 6.1. In von Hamos full-cylinder geometry, the source is positioned on the cylinder axis (Y axis), which is the principal system axis, and the image plane is perpendicular to it.

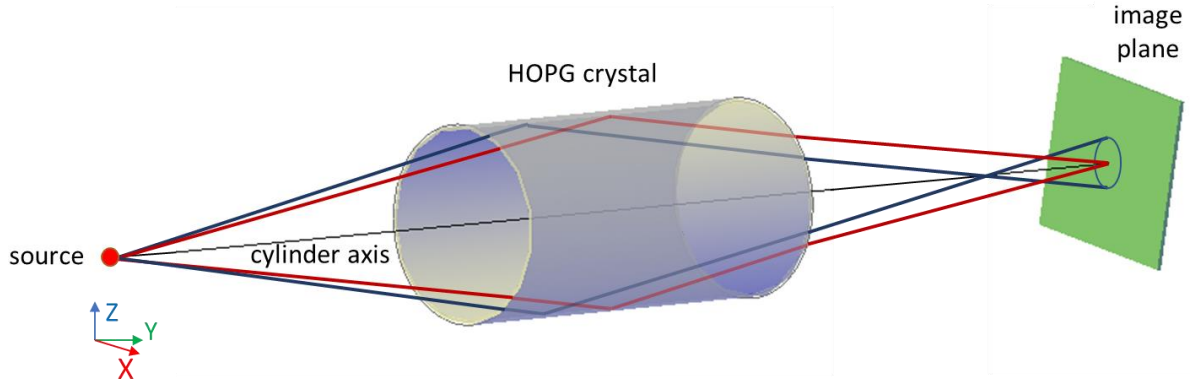

Figure 6.1. The optical system with the HOPG cylinder.

The HOPG crystal is the key element in the modelling of this optical system. The XRT package includes an optical element as a parametric surface, which is useful for representing closed surfaces such as capillaries [2]. It enabled us to define the cylindrical optical element with a 10.1 mm radius and 40 mm in length, which corresponds to the dimensions of the HOPG monochromator (see Chapter 3). The cylinder is coated with a 200 μm thickness of HOPG crystal, representing a so-called optical surface. The crystal itself is defined manually from unit-cell parameters and the atomic positions of a graphite crystal. The parameters such as atomic scattering factors and the absorption coefficients of the graphite crystal used in the simulations are tabulated in [3]. The angular distribution of the crystallites is described by a Gaussian distribution (for details, see Chapter 2) where the standard deviation is equal to the mosaic spread (here, η=0.4°). All characteristics of the crystal material mentioned above correspond to those of the HOPG crystal in the experimental setup. During the initial stage of the study of the HOPG optical element focusing properties, the beam stop within the HOPG cylinder (see Chapter 3) was not included.
Accurate definitions of the source and, more specifically the ray properties, are a very crucial step in the system modelling, since all possible emission directions of rays from the starting point to the optical surface need to be taken into account. On the other hand, our aim was to define the source in an efficient way for the computation, i.e. it is desirable to illuminate only the optical surface and not to generate rays that are not supposed to reach the crystal surface. The source is the origin of rays which are characterised by their coordinates X,Y,Z (starting point), directions, and energies (see Figure 6.2).

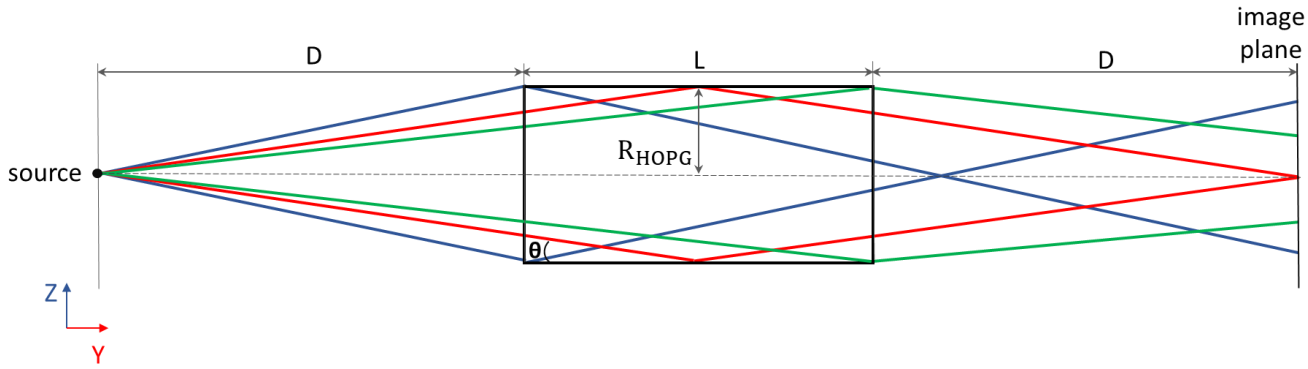

Figure 6.2. Illustration of the ray distribution from a point source in the optical system (side view). The X-rays originating from the source (starting point) reflect off the cylindrical HOPG crystal towards the image plane.

The geometrical acceptance of the crystal is determined by the source-to-crystal distance, *D,* and the crystal size. The efficient incident angles lie in the range:

$$\arctan\left(\frac{R}{D+L}\right) \leq \theta \leq \arctan\left(\frac{R}{D}\right) \tag{6.1}$$

where *R* and *L* are the radius and length of the HOPG cylinder, respectively.
In the simulation model, the rays propagate away from the source along the Y-direction in a conical ring (between the blue and green rays in Figure 6.2), thus illuminating only the crystal surface, and are sampled with a uniform (X, Z) distribution.
The angle at which an incoming ray intersects the crystal at a distance *ΔL* from the crystal entrance is derived as:

$$\theta = \arctan\left(\frac{R}{D+\Delta L}\right) \tag{6.2}$$

To maximize the focusing effect of a mosaic crystal, the distance between the source and the image plane must be twice the distance between the source and the optical element [4]. In such a geometrical arrangement, rays reflected at the crystal centre are focused in a spot within the image plane, and their maximum collection is achieved (see Figure 6.2). Throughout the manuscript, the energy of the rays reflected from the centre of the HOPG cylinder in the case of a point source is called the central energy.
The rays with a particular energy reflected on the image plane correspond geometrically to a particular angle, according to the Bragg Law:

$$E = \frac{12.398\ n}{2\ d\ \sin\theta} \tag{6.3}$$

where *n* is the order of reflection, θ is the Bragg angle. The interplanar distance of the lattice planes of HOPG in the first order reflection corresponds to *d*=0.335 nm.
To obtain reflection at a specific central energy, the corresponding Bragg angle must be adjusted by moving the crystal cylinder and the image plane along the Y axis. Thus, the

source-to-crystal (SC) and crystal-to-image plane (CP) distances have to be changed simultaneously and kept equal. The distance *D* and the energy of an incident ray are related as:

$$E = \frac{12.398\ n}{2\ d\ \sin\left(\arctan\left(\frac{R}{D + \Delta L}\right)\right)} \tag{6.4}$$

In modelling with XRT, the rays reflected from the HOPG crystal are intercepted by a plane for beam visualisation.

1.1. Reflection of a monochromatic beam from a point source

The reflectivity of a single HOPG crystal was discussed in Chapter 2. Let us consider the focusing of a monochromatic beam by a cylindrical HOPG crystal. Both the source to the centre of the cylinder and the centre of the cylinder to the image plane distances were set at 65 mm, which for this geometry corresponds to a central Bragg angle θ=8.86° or, equivalently, to a central energy of 12 keV in the first order of reflection. In order to obtain an image of the ray distribution from the source to the optical element along the principal axis of the system, two image planes were positioned at distances of 10 mm and 44.8 mm from the source, transversal to the beam direction (see Figure 6.3); the image planes do not affect the ray-tracing. Note that the second image plane is right at the entrance of the HOPG cylinder.

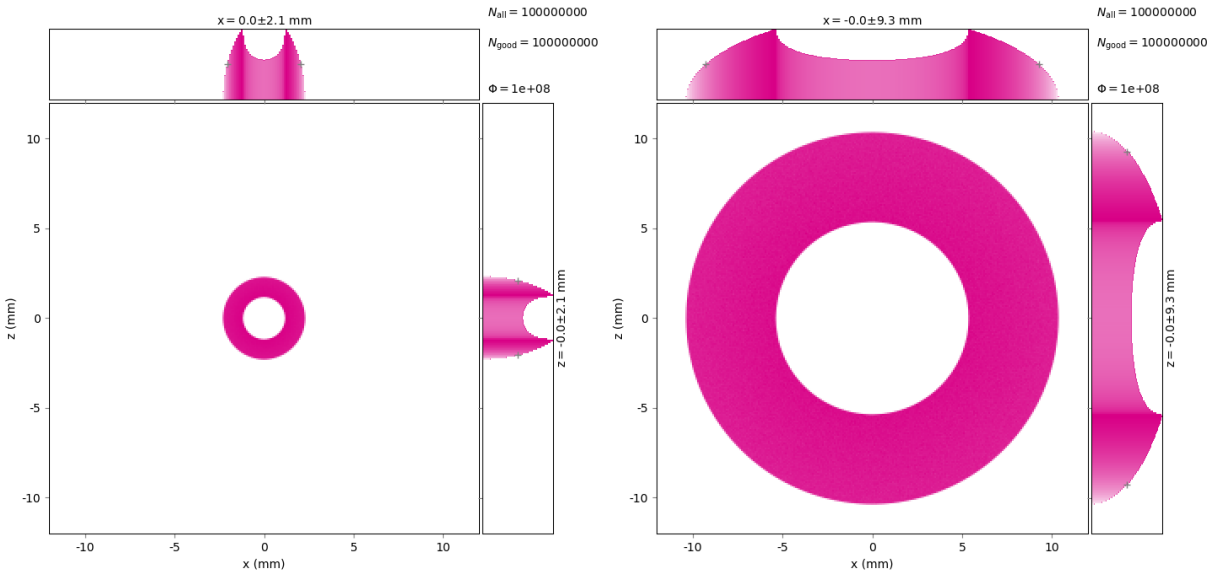

Figure 6.3. Images of the transversal distribution of rays from the 12 keV monochromatic beam on the image planes set at distances of 10 mm (left panel) and 44.8 mm (right panel) from the source.

The footprints of the diffracted rays on the crystal surface are shown in Figure 6.4. It is important to point out that only a small part of the optical surface contributes to the reflection. The asymmetry of the footprints of the rays on the crystal surface in the horizontal

axis is due to the mosaic distribution of crystallites [5].

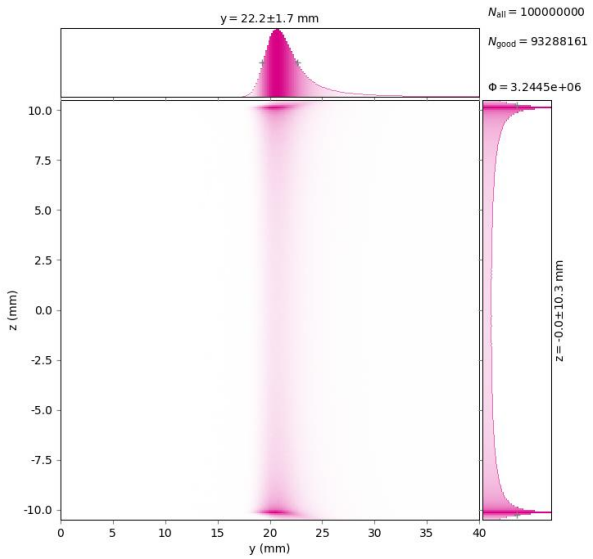

Figure 6.4. Ray-traced footprints on the cylindrical HOPG crystal with collection length L=40 mm (Y-axis) and radius R=10.1 mm (Z-axis) at the energy of 12 keV ($\theta_B = 8.86°$) in the first order of reflection.

Among all the rays (N_{all}) impinging onto the crystal, only those that are incident at the Bragg angle are reflected within the crystal surface (N_{good}), leaving footprints. About 93 % of all emitted rays are Bragg-reflected, but only those which are incident near the crystal centre focus in a dense spot onto the image plane. The transversal image of the reflected beam and its intensity distribution are shown in Figure 6.5.

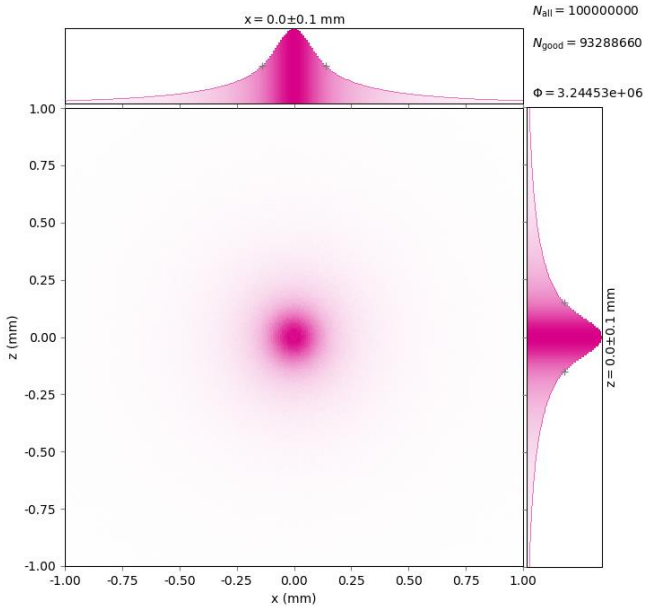

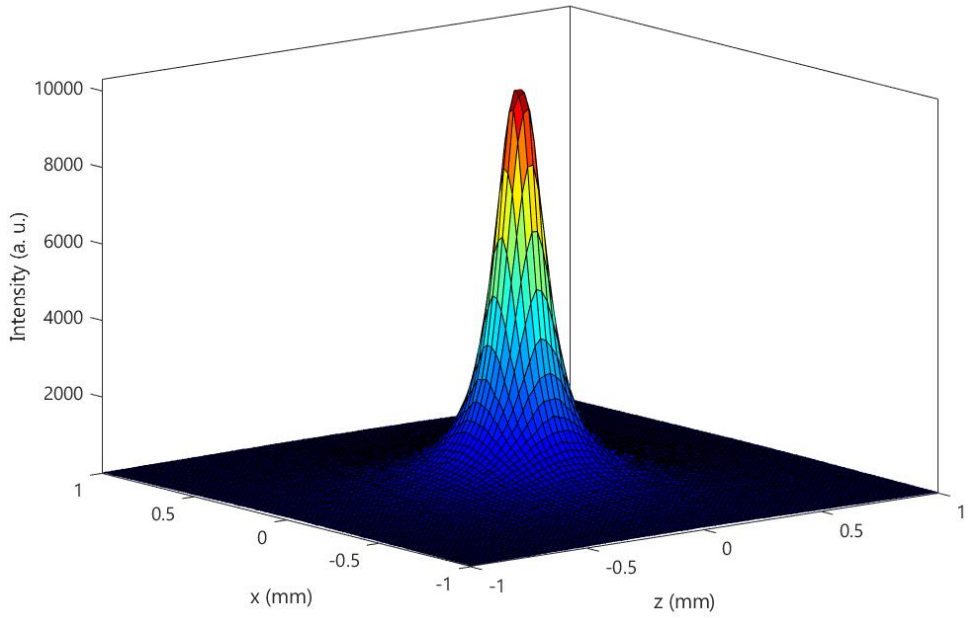

Figure 6.5. Upper panel: 12 keV ($\theta_B = 8.86°$) rays reflected at first order on the image plane positioned transversal to the ray direction. Lower panel: map of the intensity distribution of the reflected rays in the X Z plane.

1.2. Diffraction of a beam with several discrete energies

To establish a better understanding of the crystal reflectivity at different energies, a point source with three equally weighted energy lines of 10 keV, 12 keV, and 14 keV was created. It is important to underline that the distribution of the ray directions is also equally weighted. The optical system was adapted to reflect 12 keV rays in the first order of reflection, at the monochromator centre. The coloured segments on the surface of the optical element in Figure 6.6 represent reflected rays of particular energies.

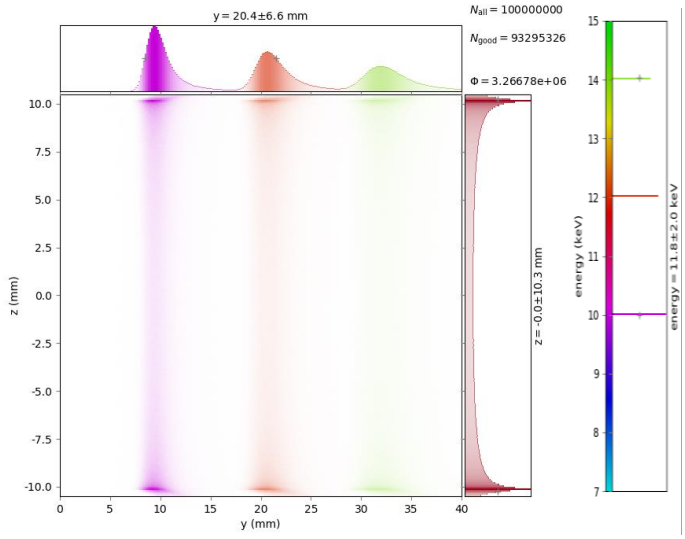

Figure 6.6. Footprint image of the three-energy line source (10 keV, 12 keV, and 14 keV) at the central energy of 12 keV ($\theta_B = 8.86°$) in the first order of reflection over the HOPG crystal surface with collection length L=40 mm (Y-axis) and radius R=10.1 mm (Z-axis). Footprint colouring is given by energy.

The values of FWHM for the positional distribution over the crystal surface for each line of the source are given in Table 6.1. FWHM of the positional distribution The distribution of the rays over the crystal surface broadens as the energy increases.

Table 6.1. FWHM of the positional distribution of the 10 keV, 12 keV, and 14 keV rays traced through the HOPG crystal.

Energy, keV	FWHM, mm
10	2.4
12	3.4
14	4.7

Figure 6.7 demonstrates the positional ray distribution (upper panel) and intensity distribution (lower panel) on the image plane.

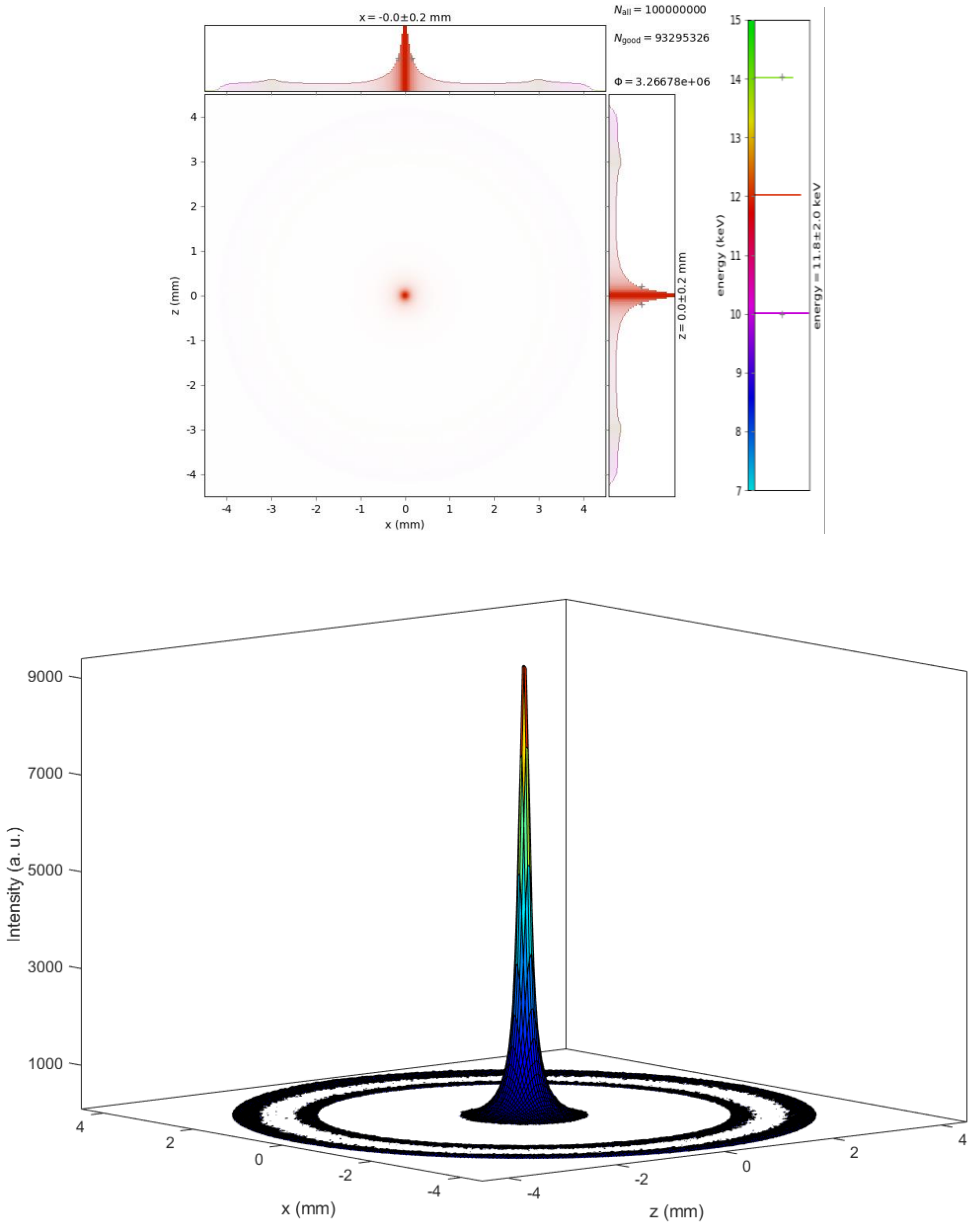

Figure 6.7. Upper panel: distribution of the reflected 12 keV rays ($\theta_B = 8.86°$) over the transversal image plane. Lower panel: map of intensity distribution of reflected rays in the X Z plane.

The rays of the central energy (12 keV) are concentrated onto a spot in the image plane. However, the latter is geometrically set out of focus for rays of 10 keV and 14 keV energies, and these rays are focused onto spots on the cylinder axis in front of and behind the plane, respectively (see Figure 6.2). Consequently, the contributions of these rays to the output are represented as scattered points whose maximum intensities are in two circles. The 10 keV rays represent the maximum intensity on the image plane and the 14 keV rays represent the minimum (see Figure 6.7, upper plane). The effect of the focused and defocused geometry will be presented in detail in § 2.

1.3. Diffraction of a polychromatic beam for a point source

In the simulation model, the number of rays generated in the source was uniformly distributed within the given energy interval with precise values for the lower and higher boundaries (limits). The energy weight of each ray was taken as unity. The ray directions were also equally distributed.

The source covers the energy domain from 5 keV to 25 keV. The crystal cylinder was moved to a distance D=50 mm from the source along the principal axis of the system to adjust the reflectivity of 13 keV rays at its centre, which corresponds to a Bragg angle of θ=8.17°. The distances SC and CP were equal. Figure 6.8 shows the positional distribution of diffracted rays over the crystal surface and onto the image plane. The intensity distribution of the collected rays was modified: only the rays with energies from 9.7 keV to 17.5 keV are observed on the image plane, with unequal probabilities.

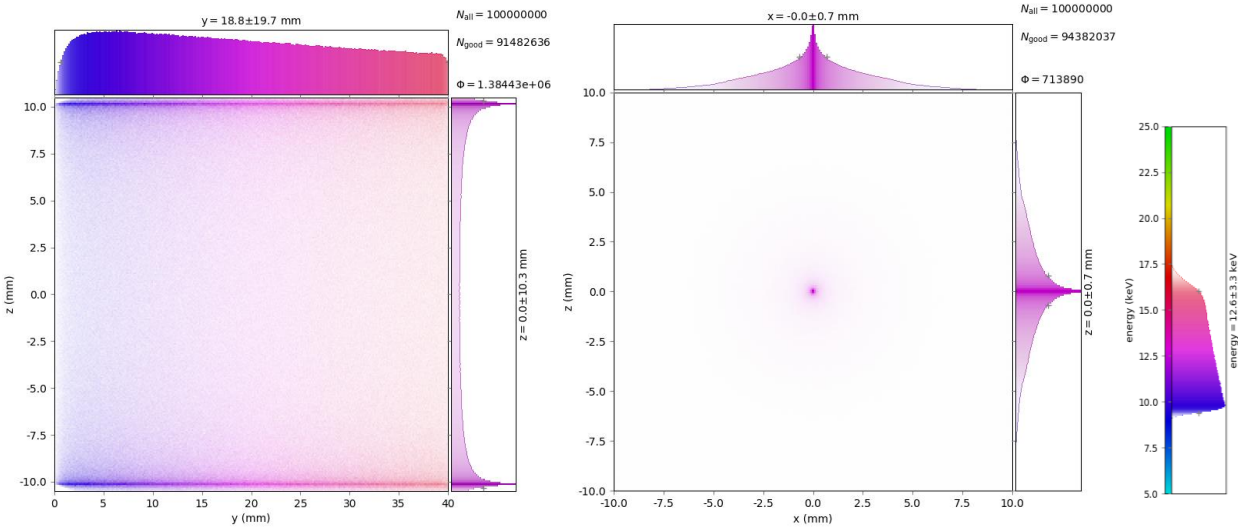

Figure 6.8. Left panel: Image of the reflected rays from the cylindrical crystal with collection length L=40 mm (Y-axis) and radius R=10.1 mm (Z-axis) in the energy range between 5 keV and 25 keV. Right panel: Image of the reflected rays intercepted by the image plane.

One of the important characteristics of the optical element is the energy bandwidth of the reflected rays at a given position of the elements. The HOPG cylinder length defines the width of the energy window, as depicted in Figure 6.9. For longer crystals, the bandwidth becomes wider.

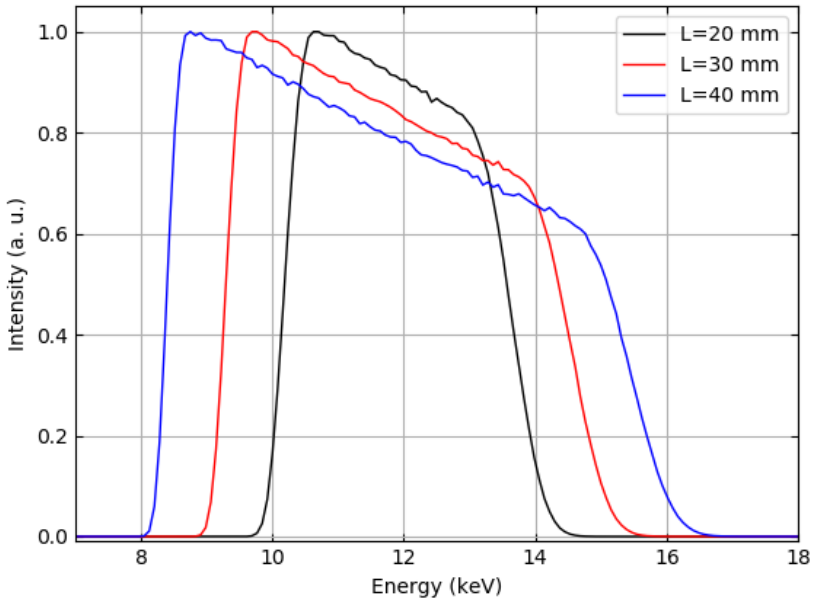

Figure 6.9. Energy band of the HOPG cylinder at a central energy of 12 keV ($\theta_B = 8.86°$) in the first order of reflection for different HOPG cylinder lengths.

The position of the energy window is dependent on the central energy, i.e. the distance SC (see Figure 6.10). Moving the crystal further from the source, higher energies meet the Bragg Law.

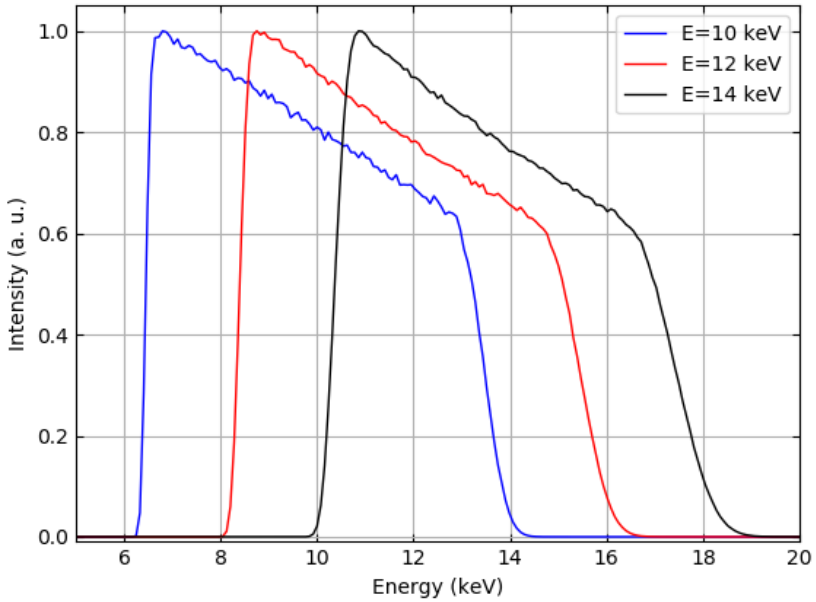

Figure 6.10. Energy band of the HOPG cylinder at 10 keV, 12 keV, and 14 keV central energies in the first order of reflection, corresponding to the distance D of 34 mm, 45 mm, and 56 mm, respectively.

2. Investigation of the optical performance of the system

As explained in Chapter 3, the second detection channel of the experimental setup presents a more complex configuration than the one described above in the simulation model. To best resemble the physical optical system, all the relevant elements and their actual dimensions were introduced step by step in the simulation model, as described in the next paragraphs.

In the experimental setup, the detector lies on the cylinder axis of the HOPG crystal which is tilted to 46° compared to the sample holder axis (for details, see Chapter 3). The sample, on being exposed to the primary X-rays, is regarded as the physical source of radiation in the ray-tracing simulation model. For the sake of simplicity, the source was modelled as a disc in the X Z plane, perpendicular to the principal axis of the optical system and parallel to the image plane (see Figure 6.11). Additionally, due to the mechanical construction of the setup, the source divergence was limited by a circular aperture with a radius of 7 mm at a distance *d* 34.5 mm from the centre of the sample.

Now let us consider the optical system with an extended source with a radius r_s and a circular collimator with a radius r_a, as illustrated in Figure 6.11.

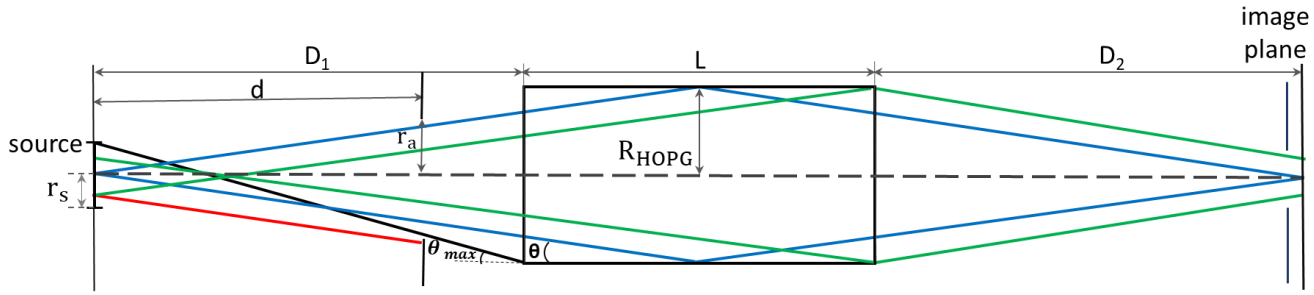

Figure 6.11. Illustration of the ray path from the extended source of radius r_s toward the cylindrical HOPG crystal through the collimator r_a.

The monoenergetic rays, emitted in a conic ring from a point source lying on the cylinder axis, are reflected from a small crystal surface, as illustrated in Figure 6.4 and Figure 6.6. If the source has an extension r_s along the X and Z axis, monoenergetic rays can be emitted from any point of the source and consequently, unlike a point source, rays with different directions impinge on the crystal surface at the same axial position. In this case, the angular acceptance of the optical surface is given by the size of the source viewed by the crystal, the size of the crystal, and its distance from the source. Thus, all effective angles need to be considered in this respect.

Rays are incident on the optical surface with an angle θ lying in the range:

$$\arctan\left(\frac{R_{HOPG}-r_s}{D_1+L}\right) \le \theta \le \arctan\left(\frac{R_{HOPG}+r_s}{D_1}\right) \qquad (6.5)$$

The effective incident angles dictated by Eq. (6.5) are further limited by the collimator aperture with a radius r_a at a distance d from the source (see Figure 6.11, red line). Thus, the condition (6.5) must satisfy the next relation:

$$\arctan\left(\frac{r_a - r_s}{d}\right) \leq \theta \leq \arctan\left(\frac{r_a + r_s}{d}\right) \tag{6.6}$$

From equation (6.5) and (6.6), the maximum θ_{max} angle can be calculated to define the angle of the truncated cone delimiting the beam source (see Figure 6.12). Thus, all possible angles on the crystal surface are taken into account.

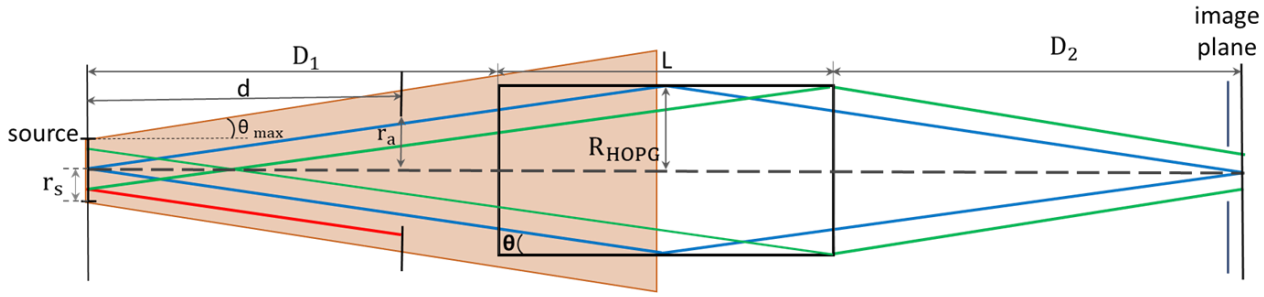

Figure 6.12. Illustration of the source emittance distribution.

As reported in Chapter 3, the HOPG monochromator is provided with a beam stop inside the cylinder (see Figure 3.22 and Figure 3.23) to prevent the rays passing directly through the cylinder to the detection surface [6], [7], [8]. Since rays from an extended source propagate in a truncated cone with a uniform distribution and with all their directions from the starting point to the optical surface, it was necessary to include beam stops. The exact shape of the beam stop is complicated to reproduce in a simulation model. It can be represented as simple obstacles in the system: two identical circular beam stops on each side of the cylinder and a larger one in the centre, as depicted in Figure 6.13. Furthermore, the energy window of the collected X-rays is dependent on the solid angle of detection subtended by the detector from the HOPG monochromator, i.e., the detector size and crystal-to-detector distance. In order to simulate the detection area of the SDD, a circular aperture with an equivalent radius of 2.33 mm was positioned just in front of the image plane. Thus, the beam collected on the image plane will be representative of the detector view. In the rest of this chapter, the *"image plane"* term means the image plane with the aperture in front (i.e., the detection area).

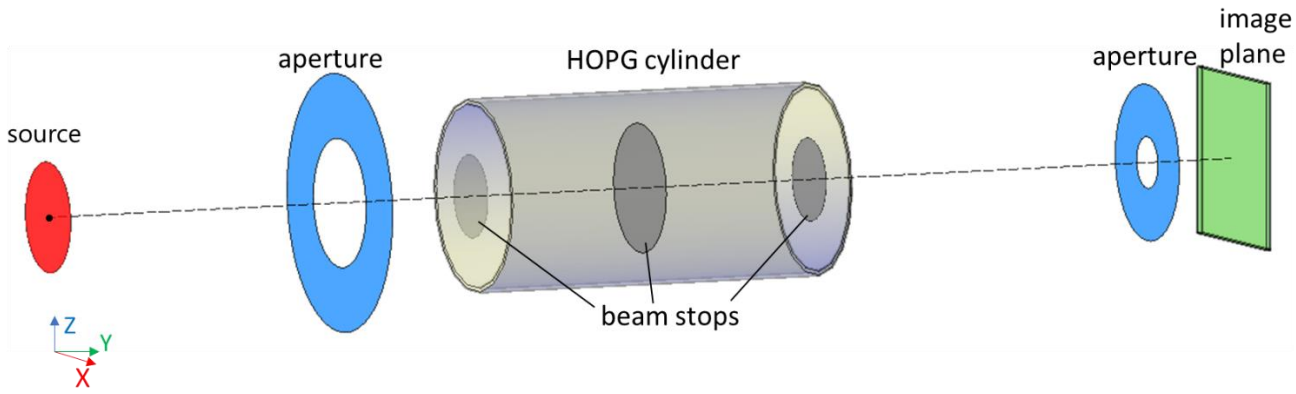

Figure 6.13. Illustration of the complex optical system for ray tracing simulation, including all principal components. Three beam stops are placed inside the HOPG cylinder to avoid rays passing directly through the optical element. A second aperture positioned just in front of the image plane represents the dimension of the SDD area in the experimental setup.

The complex optical system was designed to investigate its performance for various configurations. Some calculations had to be performed to study the dependence of the energy bandwidth and the intensity of the reflected beam at a given central energy depending on the source size, and source to crystal and crystal to image plane positions.

2.1. Influence of the source size on the reflection profile

As illustrated in Figure 6.11 for an extended source, rays of the same energy coming from various points of the source-disk travel different distances in different directions to the optical surface, and consequently are focused onto the image plane at different positions [9]. Therefore, the incoming rays of the same energy are reflected from a larger optical surface. A series of simulations were carried out to examine the effects of the extended source on the energy bandpass and the intensity of the reflected rays.
In Figure 6.14, the ray tracing simulations of the optical system (illustrated in Figure 6.13) for sources with a radius of 0.5 mm (upper panels) and 3 mm (lower panels) and at the central energy of 13 keV are presented. The crystal segments contributing to the beam image at different source sizes are shown in the left panels. The beam footprint on the crystal becomes larger and more blurred with a wider source.

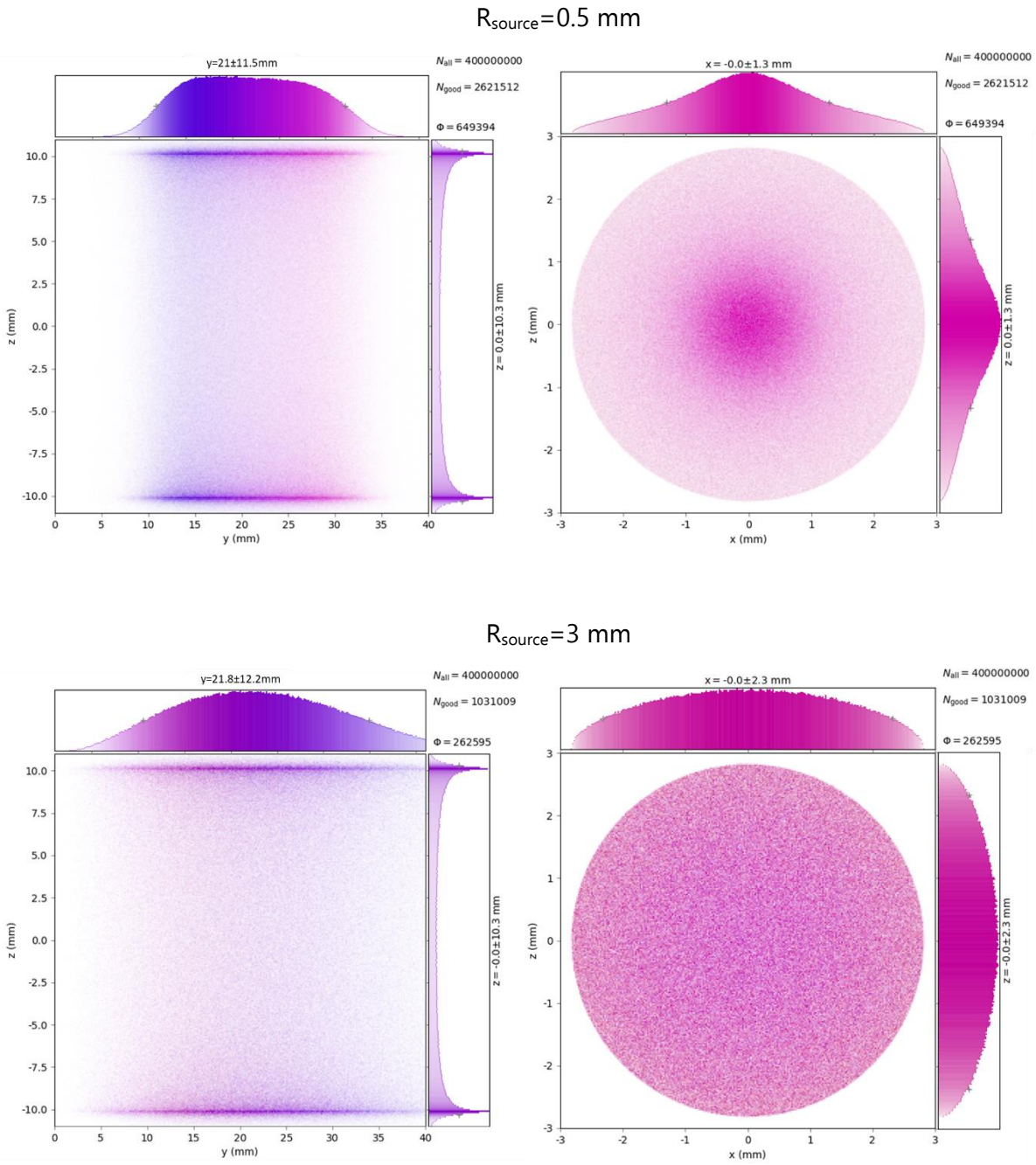

Figure 6.14. Ray footprint of a polychromatic beam on the cylindrical HOPG crystal (left panels) with collection length L=40 mm (Y-axis) and radius R=10.1 mm (Z-axis), and image of the reflected rays intercepted by the image plane (right panels). The radius of the source is 0.5 mm (upper panels) and 3 mm (lower panels). The distances D_1 and D_2 are equal to 50 mm for the central energy of 13 keV ($\theta_B = 8.17°$).

The images of the output beams on the image plane at the corresponding source sizes are shown on the right side. It should be noted that the resulting images appear as circles with a fixed radius, due to the aperture in front of the plane. For very small source radii ($R_{source} \to 0$), the positional distribution of rays over the image plane is Gaussian-shaped, while with an increased source size, the distribution becomes more uniform.

Figure 6.15 illustrates the FWHM broadening for various source radii at one position of the optical system elements, and for different central energies (12, 13, 14, and 15 keV). It is worth

noting that increasing the central energy, i.e. moving the crystal and the image plane farther from the source, also widens the profile for the same source size.

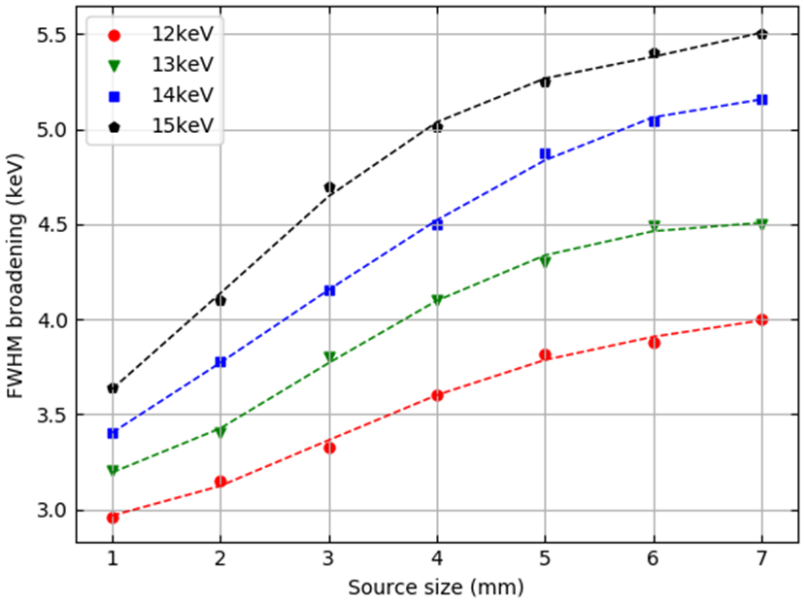

Figure 6.15. Energy band broadening as a function of the source size and the central energy

The broadening also depends on the size of the aperture in front of the image plane (which models the detector area), as illustrated in Figure 6.16.

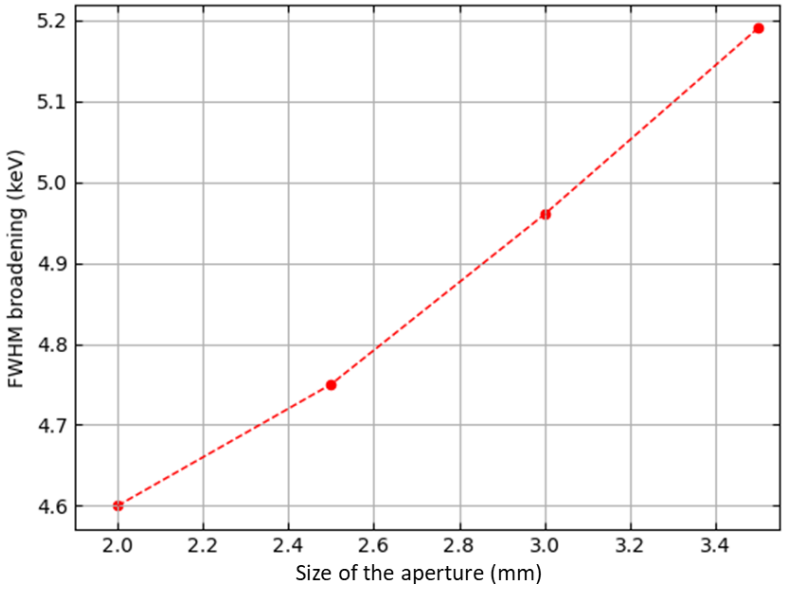

Figure 6.16. FWHM of the system response depending on the size of the aperture in front of the image plane. Calculations were performed for a source size $r_s = 1\ mm$.

2.2. Influence of the focused and defocused geometry on the reflection profile

Previously, all simulations were carried out for equal source to optical element and optical

element to image plane distances, to maximize the collection in the desired energy range. The distance from the source to the crystal D_1 determines the central Bragg angle and thereby the energy range reflected by the crystal. The crystal-to-plane distance D_2 is responsible for the position of rays of a certain energy on the image plane, which is limited by the aperture [1]. It is worth considering the evaluation of the beam image on the plane for various distances D_2 in the cases of point and extended sources.

A series of simulations were performed at a fixed position of the crystal at D_1=56 mm, corresponding to the energy window from 10.5 keV to 17.5 keV and a central energy of 14 keV in the first order of reflection. If the image plane is moved closer to the crystal along the principal axis, i.e., D_1>D_2, the left part of the cylinder mostly contributes to the reflection, as displayed in the left panels of Figure 6.17 for point and extended sources, respectively. Otherwise, if D_1<D_2, the right part of the cylinder mostly contributes to the reflection, and the effective reflecting surface is larger, as illustrated in the right panels. As was outlined above, rays are distributed uniformly along the HOPG cylinder however, and the colouring in the figures shows only rays that contribute to the beam image onto the image plane.

Point source

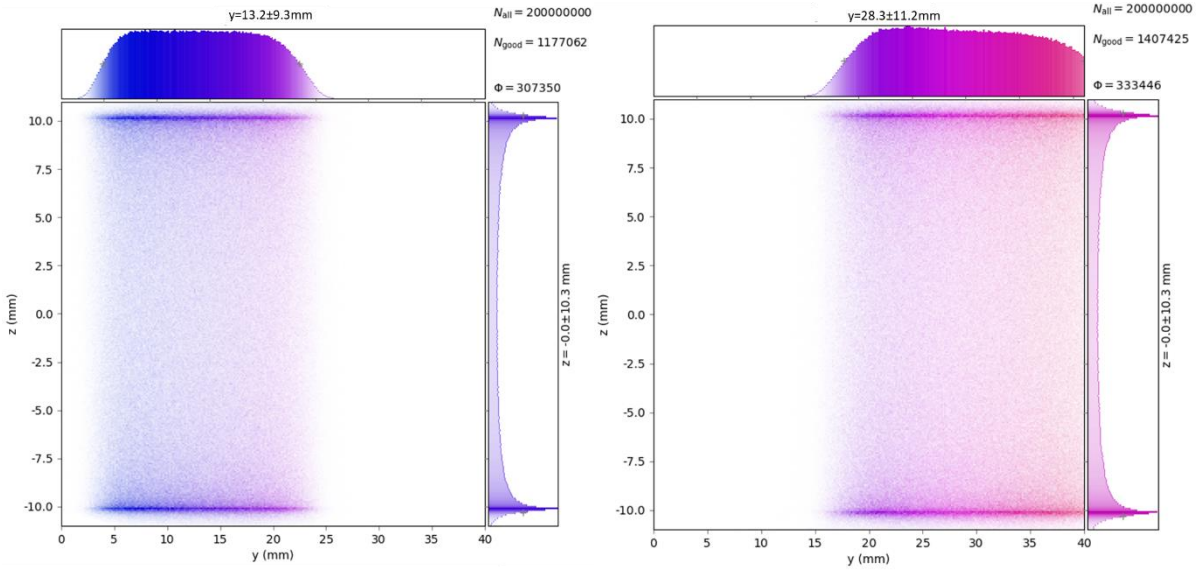

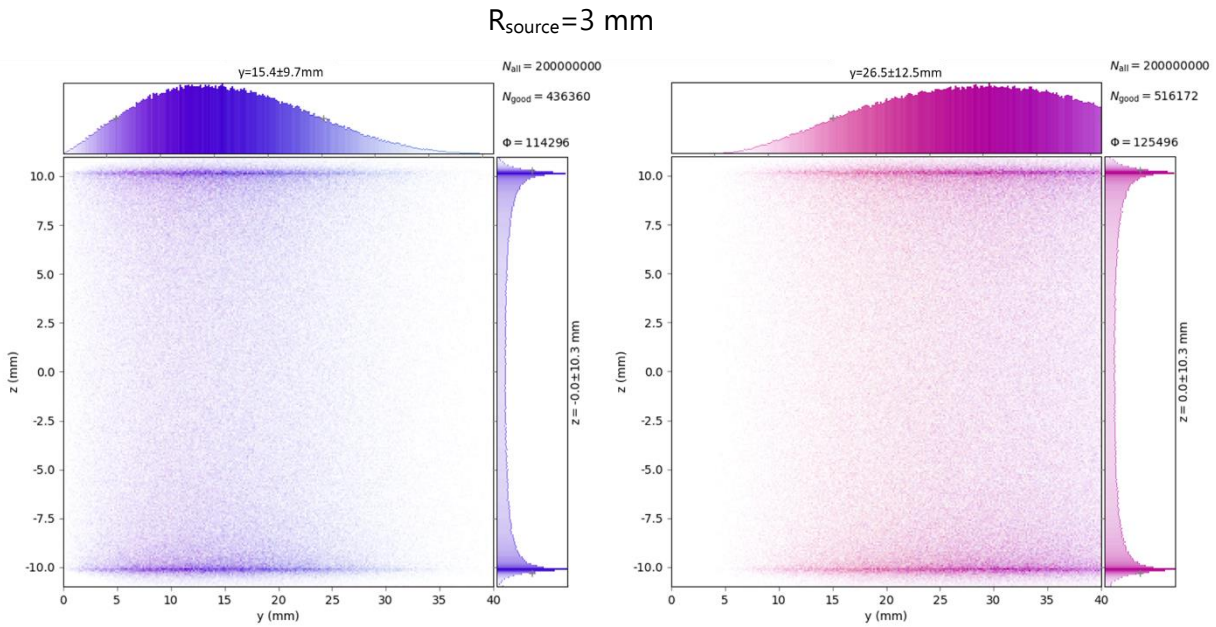

Figure 6.17. Footprints of the polychromatic rays on the HOPG crystal for D_1=56 mm, D_2=40 mm (left panels) and D_2=70 mm (right panels). The colouring indicates only the rays that reached the effective area of the image plane.

The distance D_2 also plays an important role in the definition of the energy window within the image plane. Moving the latter component farther from or closer to the crystal simultaneously moves the effective segment on the optical surface . The evaluation of the output beam profile is presented in Figure 6.18.

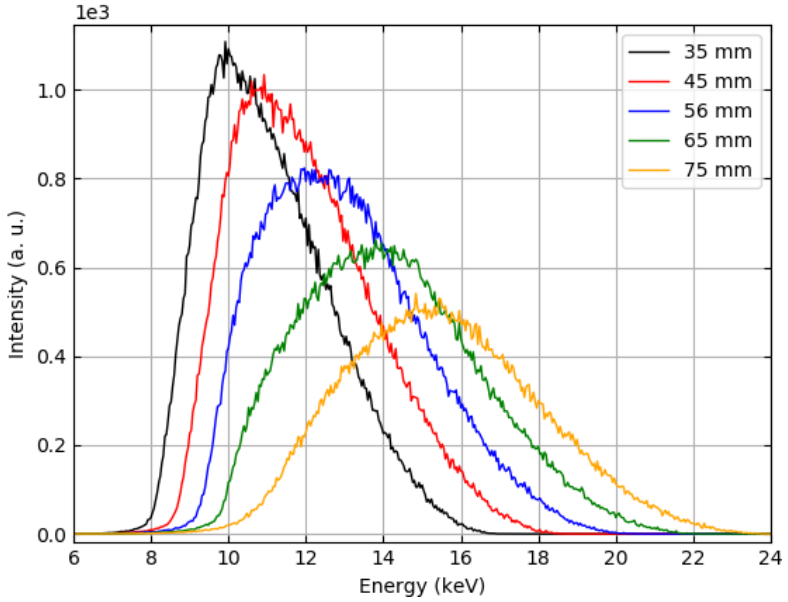

Figure 6.18. Intensity distribution as a function of the distance D_2; D_1=56 mm.

Figure 6.19 provides information on the broadening of the energy window as a function of the distance D_2. With an asymmetry $D_1 > D_2$, a narrower and more intensive bandwidth can be observed compared to that seen when $D_1 < D_2$.

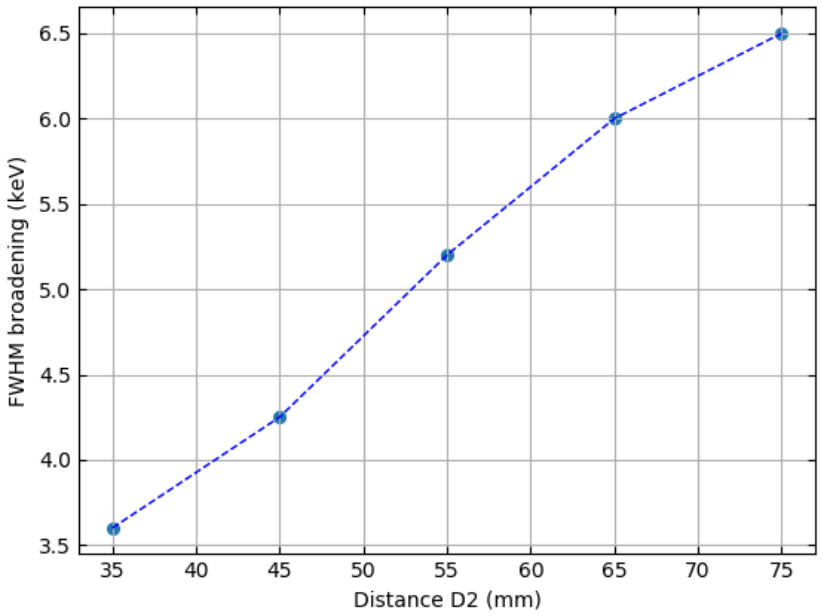

Figure 6.19. Bandwidth broadening at various distances D_2. The distance D_1=56 mm for the central energy of 14 keV for all calculations.

Furthermore, the energy corresponding to the maximum transmission is moved when D_2 varies. This energy displacement is illustrated in Figure 6.20.

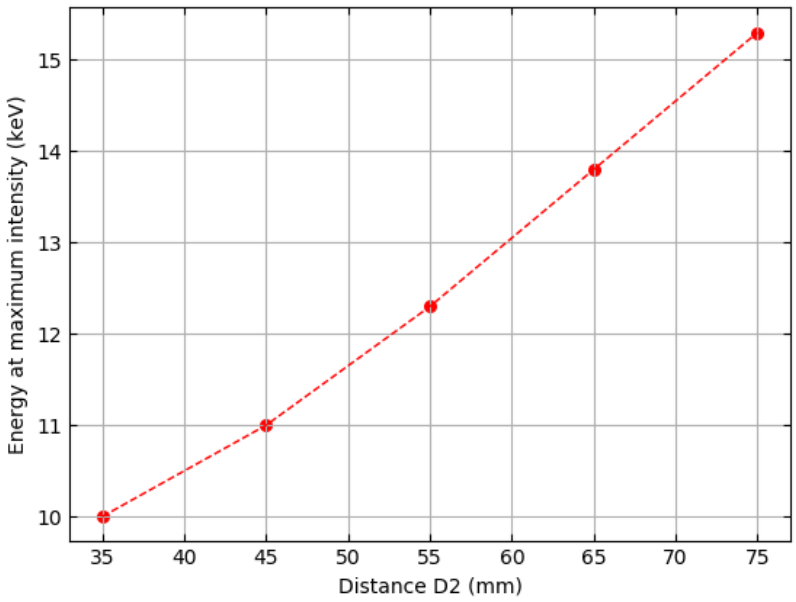

Figure 6.20. Displacement of the energy at maximum transmission as a function of the distance D_2.

2.3. Calculation of the second order reflection of the HOPG crystal

In the geometrical configuration for equal D_1 and D_2 distances, the reflectivity from the first and second order reflections can be calculated. To reflect the rays of 13 keV in the first order

of reflection (see Eq. (6.4), with the reflection order n=1), the distances D_1 and D_2 were set at 50 mm. For the same position of the elements, the rays of twice the central energy are reflected in the second order (n=2). The rays with higher energies can be reflected from deeper crystal planes, contributing to the output results. Since the experimental measurements were performed at up to over 30 keV, both the first and second orders of reflection had to be taken into account in the simulations (see Figure 6.21).

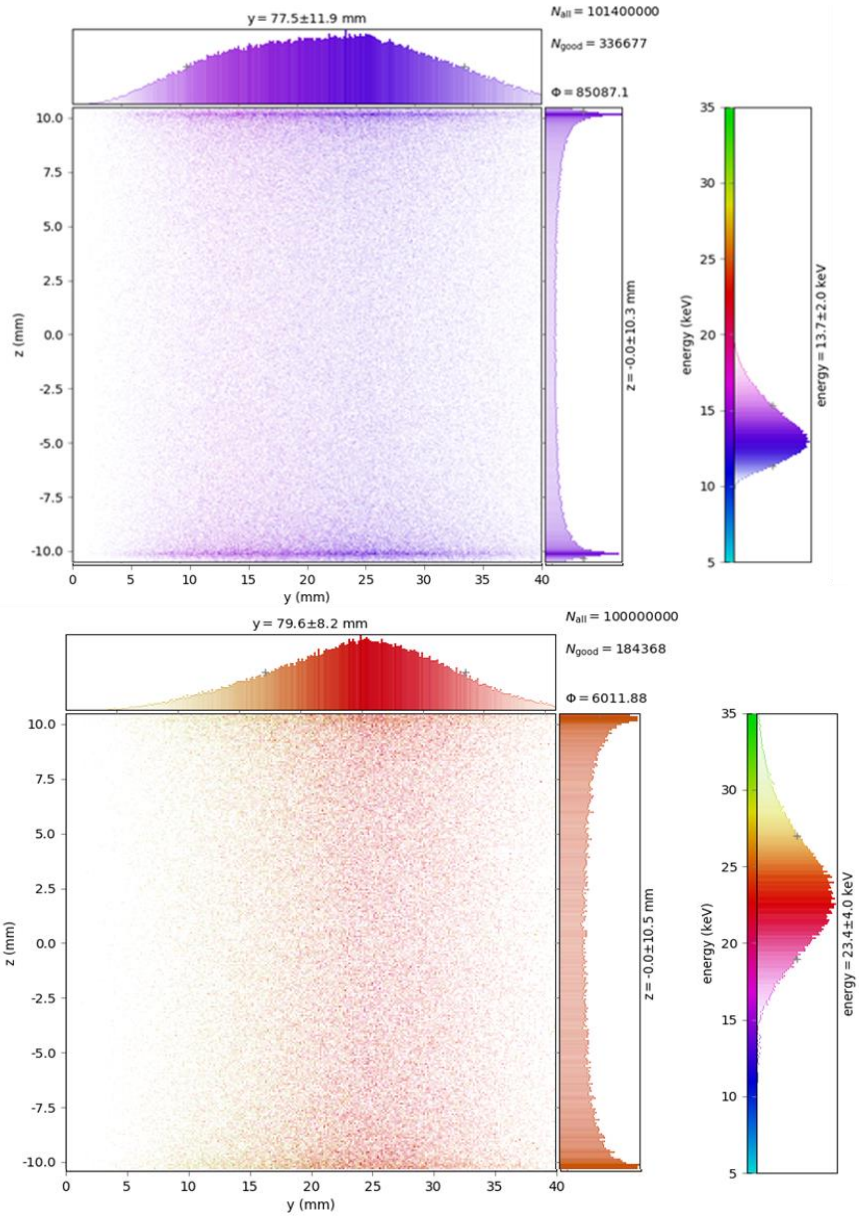

Figure 6.21. Simulation of the reflectivity for the polychromatic beam in the energy range 5 keV<E<35 keV in the first (upper panel) and second (lower panel) orders of reflection. Both simulations were performed for the SC and CP for the central energy of 13 keV in the first order of reflection.

From Figure 6.22, it can be seen that rays reflected in the first order of reflection are collected in the energy range from 10 keV to 17 keV, while the rays of energies from 15 keV to 33 keV correspond to the second order of reflection. It is important to point out that almost all the optical surface contributes to the first order of reflection, whereas a narrower part of the

crystal reflects the rays in the second order. The FWHM of profiles are 4 keV and 8 keV in the first and second order of reflections, respectively.
The intensities of the reflected rays in the second order are much lower, however, and they appear in the energy range of the Compton and Rayleigh scattering lines of the Ag anode tube (19 keV<E<24 keV). The calculations were performed separately for the same number of rays, and since the X-rays in the experimental setup were unpolarised, they allow both results to be summarized.

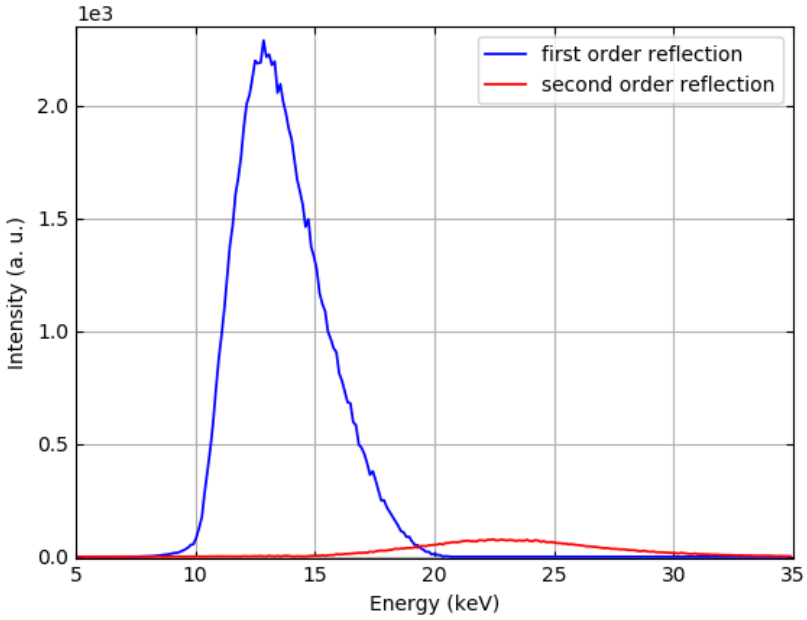

Figure 6.22. Simulation of the first and second order of reflection of the HOPG crystal for the polychromatic beam in the energy range from 5 keV to 35 keV.

3. Simulations using the experimental spectrum as input data

The simulation results presented in Figure 6.22 illustrate the energy spectrum of rays (with uniform initial intensity) passed through the HOPG crystal, i.e. the transfer function of the given optical element [10]. Before using this function in a spectrum processing model, it was necessary to check the agreement of the XRT simulation with experimental results.
For this task, an X-ray spectrum of a sample recorded with the SDD without monochromator was used as an input source spectrum to carry out ray tracing simulations for the HOPG crystal. The results of these calculations were compared with the measurements performed in presence of the HOPG monochromator.
First of all, let us consider the experimental spectra that can be used for ray tracing calculations. The miniature XRF setup can be operated with two channels. The second channel, in turn, can be employed in two different modes: with and without the HOPG monochromator. However, classical XRF spectra recorded with each channel (without monochromator) do not coincide with each other, due to the different scattering angles and distances of the SDDs with respect to the sample holder (see Figure 6.23).

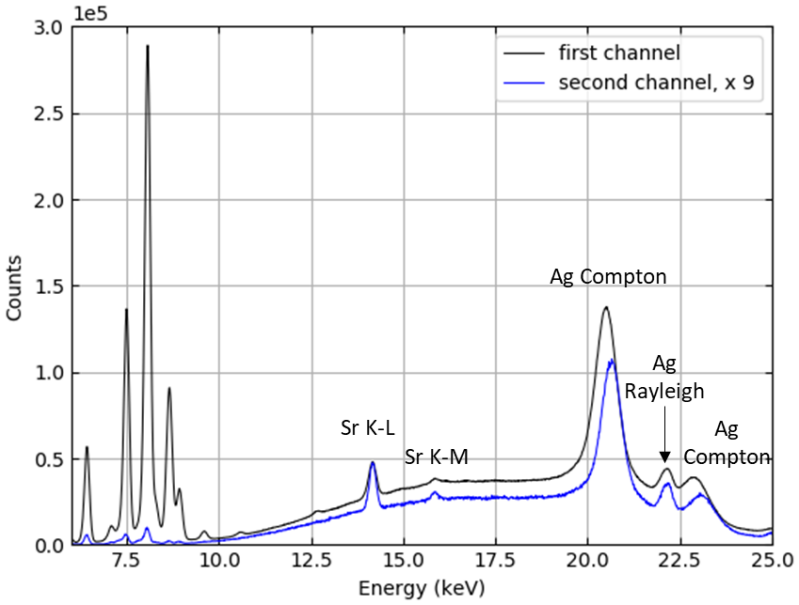

Figure 6.23. Spectra of the Sr solution at a concentration of 100 mg L^{-1} in HNO_3 0.5M measured with the first channel (black line) and second channel (blue line).

Measurements were performed at a nominal voltage of 40 kV and at a tube current of 50 μA in both cases. SDD-1 was placed at a distance of 17.9 mm from the sample holder, while SDD-2 was placed at 125 mm, which is the closest distance possible. The spectrum obtained with the second channel was multiplied by a factor of 9.

Using a spectrum measured in the second channel, without monochromator, as input data for the ray tracing simulations enabled interpretation of the experimental results obtained in the presence of the HOPG monochromator. Figure 6.24 shows the comparison of spectra for a sample solution containing Sr at the concentration of 100 mg L^{-1} measured with and without HOPG crystal. For both experiments, the X-ray tube was operated at 40 kV voltage and 99 μA current during 900 s and the SDD was positioned at a distance of 145 mm from the sample. In the case with the crystal, the source-crystal and crystal-SDD distances were set at D=56 mm, corresponding to the central energy of 14 keV, to maximize the collection of the Sr K-L line.

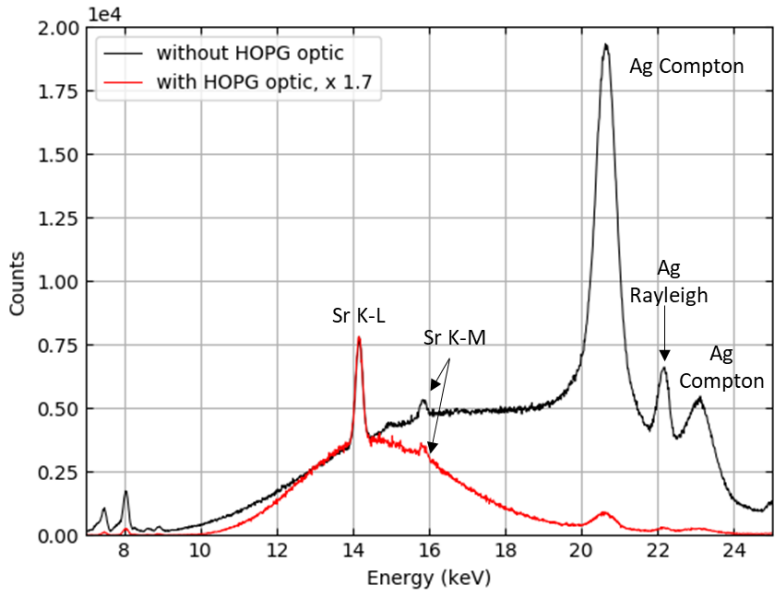

Figure 6.24. Measured spectra of a sample containing Sr at the concentration of 100 mg L^{-1} in HNO_3 0.5M with the second channel, without (blue line) and with (red line) the HOPG monochromator. The HOPG monochromator position was adjusted to the central energy of 14 keV in the first order of reflection.

In order to insert the experimental spectrum into the XRT code, each energy line of the experimental spectrum had to be specified with its relative weight. Figure 6.25 shows the weighted input source spectrum (upper panel) and ray tracing simulation results (lower panel); all simulation parameters are the same as those presented in the previous paragraph. The simulations were carried out for the first and second orders of reflection for the same position of elements, and results were summed. In an effort to imitate the experimental result, the number of bins in accumulated histograms [11], [12] was equal to the gain (eV/channel) in the measurements for all results presented.

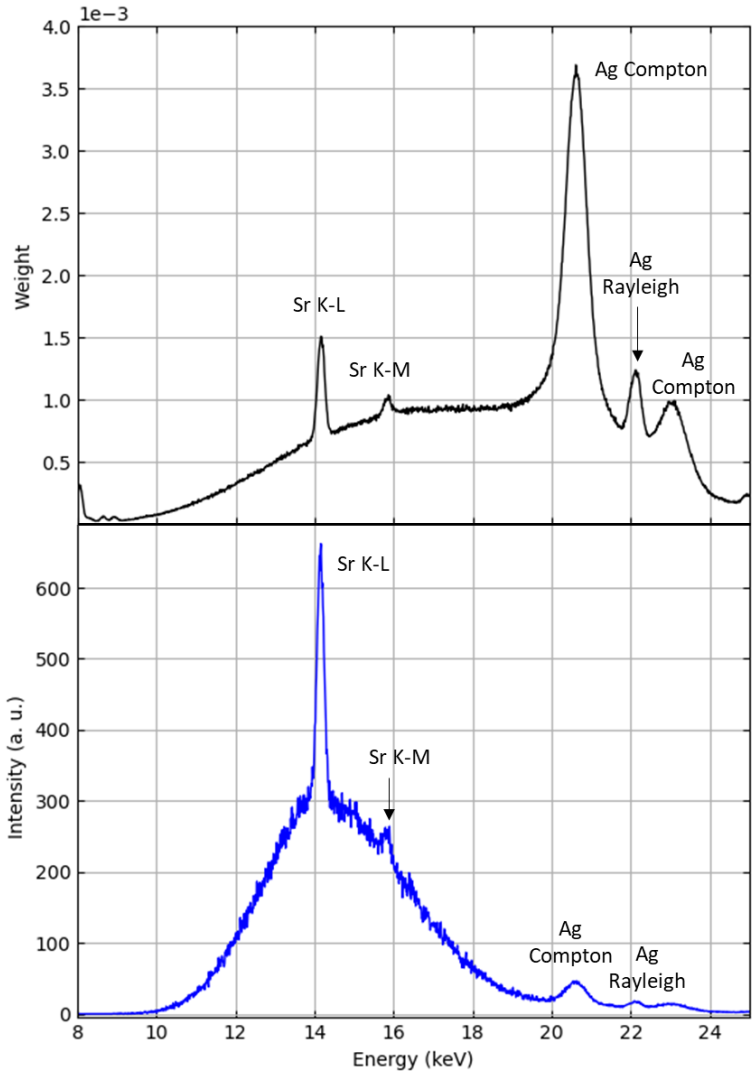

Figure 6.25. Upper panel: experimental spectrum of a sample containing Sr at the concentration of 100 mg L^{-1} in HNO_3 0.5M measured with the second channel. To use this spectrum for ray tracing calculation as an input source spectrum, each energy line was weighted. Lower panel: ray tracing simulation for a complete optical system with HOPG crystal adjusted to the central energy of 14 keV in the first order of reflection. Both first and second order reflections were calculated with the elements in the same positions.

The ray tracing calculations using the experimental spectrum and experiments performed in the presence of the HOPG monochromator were compared for two selected central energies in Figure 6.26. The spectra were normalised to unity at the Sr K-L line.

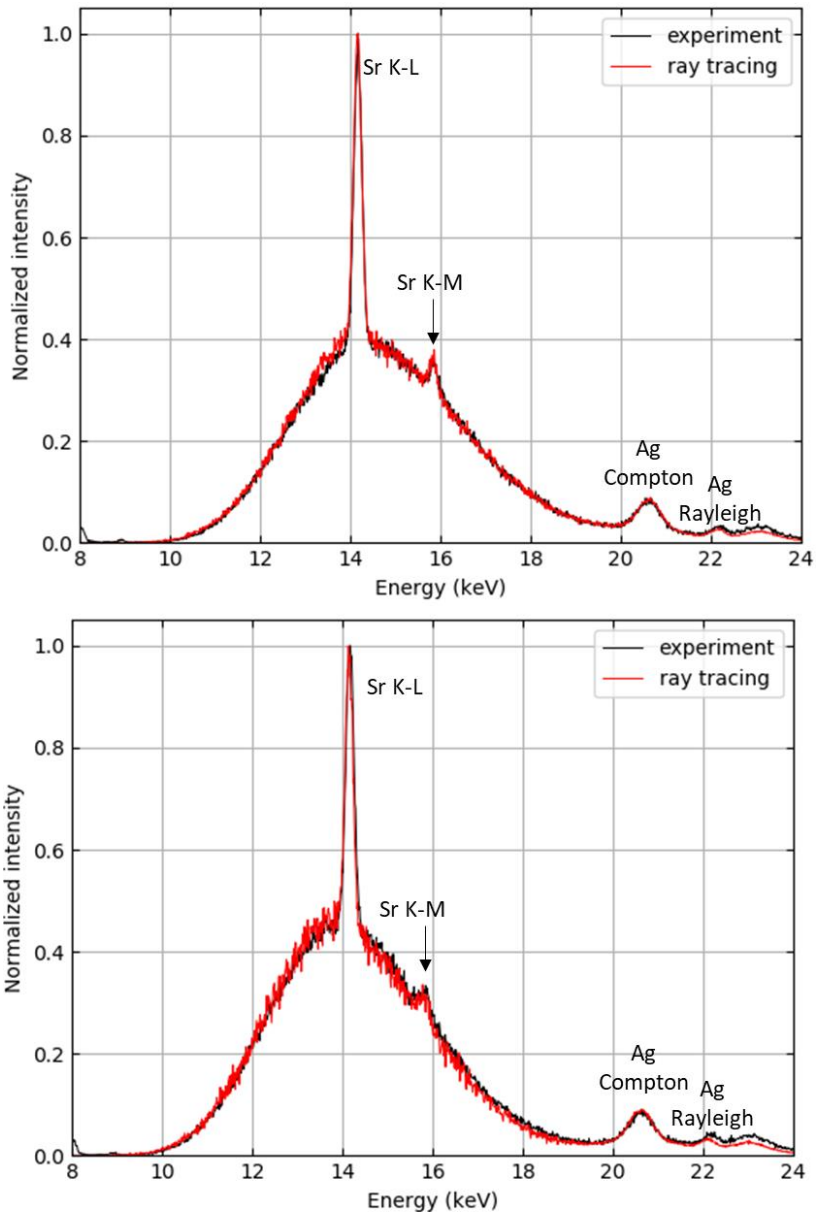

Figure 6.26. Experimental and simulation results for equal distances D=54.5 mm for central energy of 13.75 keV (upper panel) and D=57 mm for E=14.2 keV (lower panel).

However, in order to verify the accuracy and the applicability of the ray tracing model, various experiments and ray tracing simulations with corresponding parameters were carried out simultaneously. Figure 6.27 shows the results obtained in the defocused geometry: the HOPG monochromator was at a distance of 62 mm from the geometrical source (sample) and 60 mm from the SDD.

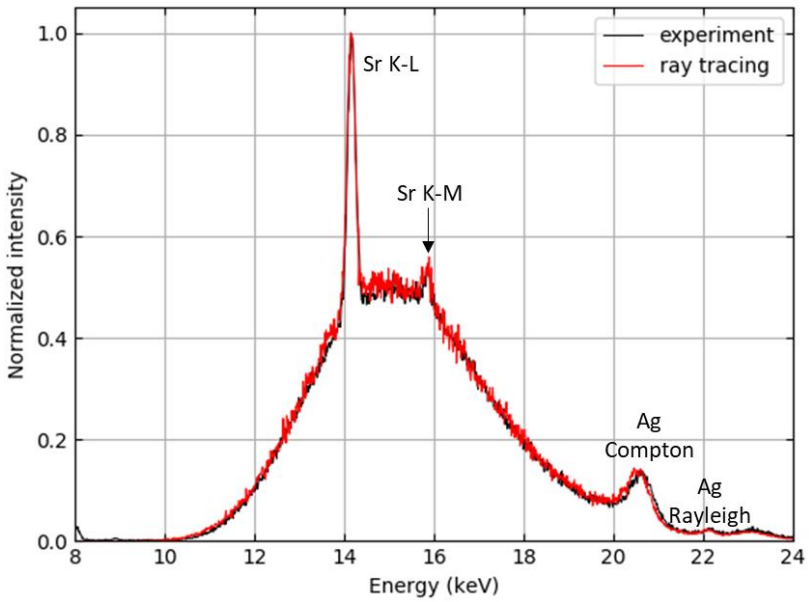

Figure 6.27. Experimental (black line) and simulation (red line) results for source to crystal distance 62 mm and crystal to SDD distance 60 mm (defocused geometry).

For the next comparison, a sample solution containing Se at a concentration of 100 mg L^{-1} was used (see Figure 6.28). The optical system was adjusted for the central energy of 12.5 keV corresponding to D=48 mm, and peaks of Se appear on the shoulder of the curve where the reflectivity is reduced.

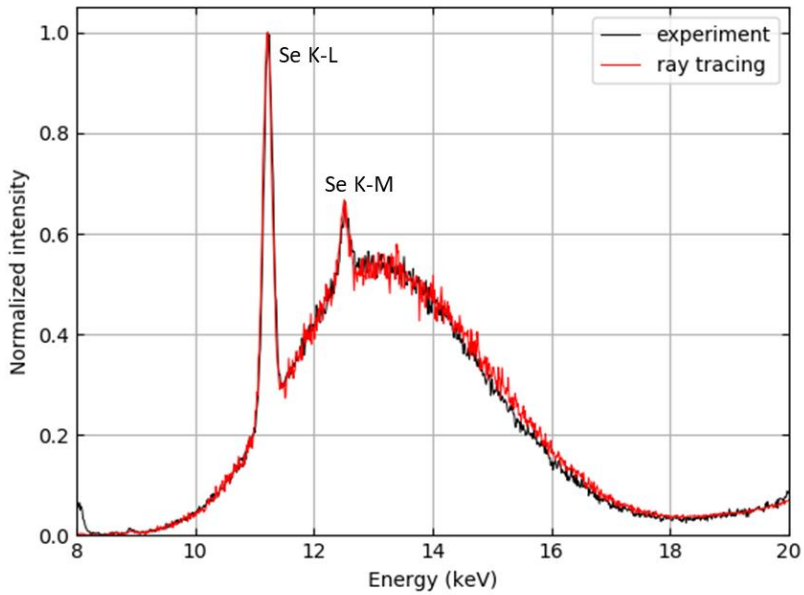

Figure 6.28. Experimental (black line) and simulation (red line) results for a sample at a concentration of 100 mg L^{-1} of Se in HNO_3 0.5M for equal distances D=48 mm.

Afterwards, a sample was prepared containing Rb and Y at a concentration of 100 mg L^{-1} for each element in nitric acid. The comparison of the experimental (in black) and ray tracing (in red) curves for a focused geometry of D=63 mm is presented in Figure 6.29. The agreement

between the results was also reached at higher central energies.

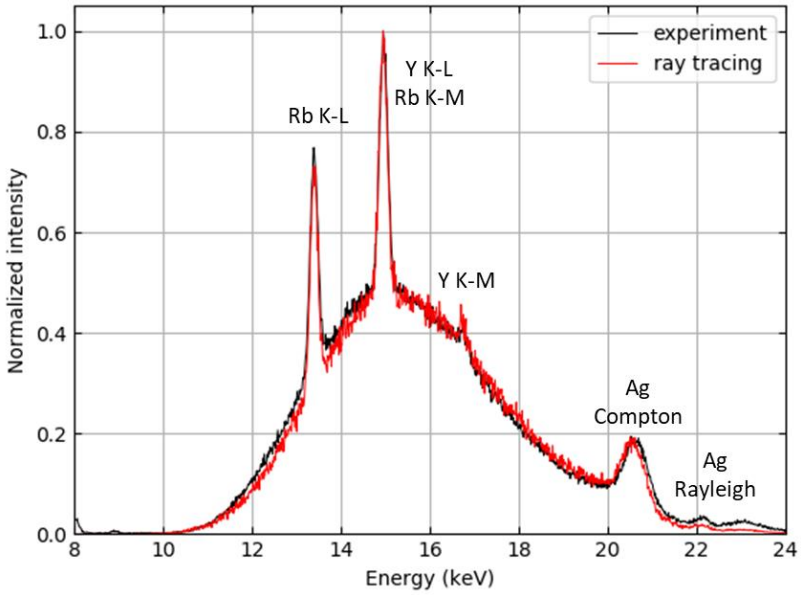

Figure 6.29. Experimental (black line) and simulation (red line) results for the sample containing Rb and Y at a concentration of 100 mg L^{-1} of each element for a focused geometry of D=63 mm, corresponding to the central energy of 15 keV.

4. Ray-tracing simulations with PENELOPE results as input data

There was high interest in mimicking the miniature setup and accurately reproducing the experimental results obtained. Thereby, the design of the whole system could be optimised through modelling and, notably, the performance of the second channel could be improved. As reported in Chapter 5, the PENELOPE code allows simulation of the fluorescence spectra of the sample at both experimental channels without HOPG optics. Consequently, these simulation results could be used as input data to calculate the reflection by the HOPG crystal. Let us therefore consider the combination of the PENELOPE and ray tracing simulations.
For the ray tracing calculations, each energy line of the PENELOPE spectrum collected with the impact detector was weighted in the same way as the experimental spectra in § 3. Next, the spectrum calculated with XRT was multiplied by the efficiency of the SDD calculated in Chapter 3, and compared with the experimental data (see Figure 6.30).

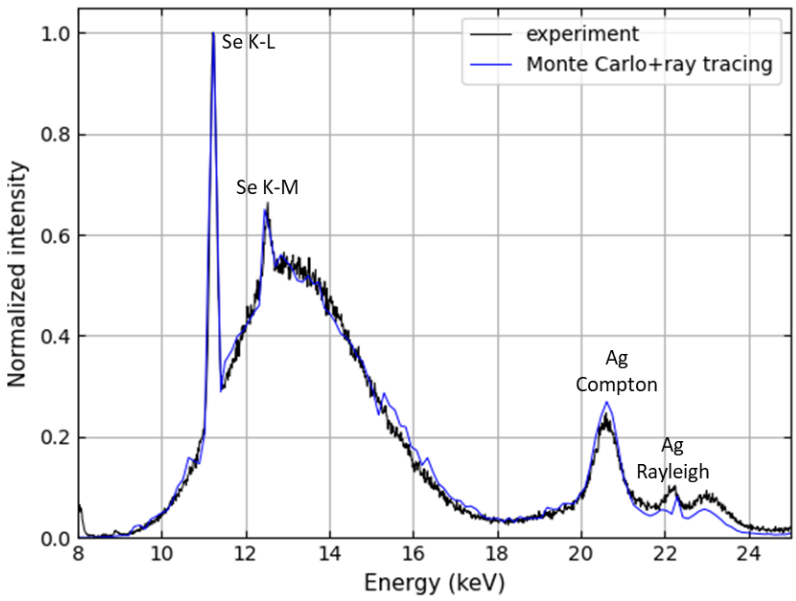

Figure 6.30. Comparison between the experimental data (black line) and combined PENELOPE and ray tracing simulations (blue line) for the sample solution with Se at a concentration of 100 mg L^{-1}.

The full accord between the results allowed us to modify the system geometry in the PENELOPE model, and by means of the XRT to predict the output spectrum after its reflection by the monochromator.

5. Conclusions

The investigations of the HOPG crystal properties and the performances of the optical system were conducted by means of the XRT package. Thanks to the simulations, it was possible to study the influence of the source size and the geometrical arrangement of components on the output results. This enabled us to examine the system applicability and understand the complete instrument response. It was shown that the distance D_1 defined the central energy, while D_2 was responsible for the intensity, displacement, and broadening of the transmission energy window within the image plane. In addition, the width of the energy window increased with the length of the HOPG cylinder. The simulation model developed here allows prediction of the performance of the setup, and of adjustments for different experiments.

To estimate the accuracy of the simulation model, the experimental results were used as input data in the XRT model. The combination showed good agreement, and enabled us to define the transfer function of the optical element. It was also shown that the entire miniature setup could be simulated using the PENELOPE and the XRT ray-tracing code.

References

[1] L. Anklamm, C. Schlesiger, W. Malzer, D. Grötzsch, M. Neitzel, B. Kanngießer. "A novel von Hamos spectrometer for efficient X-ray emission spectroscopy in the laboratory", *Rev. Sci. Instrum.*, 85, 2014.

[2] "XRT - XRayTracer". (available at https://xrt.readthedocs.io/).

[3] C. T. Chantler. "Theoretical Form Factor, Attenuation and Scattering Tabulation for Z=1-92 from E=1-10 eV to E=0.4-1.0 MeV", *J. Phys. Chem.*, 24, 71, 1995.

[4] M. Sanchez del Rio, M. Gambaccini, G. Pareschi, A. Taibi, A. Tuffanelli, A. K. Freund. "Focusing properties of mosaic crystals", *Proc. SPIE 3448*, 246–255, 1998.

[5] W. Malzer, D. Grötzsch, R. Gnewkow, C. Schlesiger, F. Kowalewski, B. Van Kuiken, S. Debeer, B. Kanngießer. "A laboratory spectrometer for high throughput X-ray emission spectroscopy in catalysis research", *Rev. Sci. Instrum.*, 89, 113111, 2018.

[6] A. A. Antonov, V. B. Baryshev, I. G. Grigoryeva, G. N. Kulipanov, Y. V Terekhov, N. N. Shipkov. "First results on application of short-focus monochromators from formed pyrolytic graphite for x-ray fluorescent analysis using synchrotron radiation", *Rev. Sci. Instrum.*, 60, 2462, 1989.

[7] A. A. Antonov, V. B. Baryshev, I. G. Grigoryeva, G. N. Kulipanov, N. N. Shchipkov. "Focusing shaped pyrographite monochromators in synchrotron radiation experiments", *Nucl. Inst. Methods Phys. Res. A*, 442–446, 1991.

[8] "Optigraph". (available at http://www.optigraph.eu/).

[9] L. V Knight, A. P. Shevelko, Y. S. Kasyanov, O. F. Yakushev, L. V Knight. "Compact focusing von Hamos spectrometer for quantitative x-ray spectroscopy", *Rev. Sci. Instrum.*, 73, 3458–3463, 2002.

[10] J. Als-Nielsen, D. McMorrow. *Elements of modern X-ray physics Second Edition*. Wiley, 2011.

[11] "Histograms and kernel density estimation KDE 2 | Biophysics and Beer". (available at https://mglerner.github.io/posts/histograms-and-kernel-density-estimation-kde-2.html?p=28).

[12] K. Klementiev, R. Chernikov. in Powerful scriptable ray tracing package xrt. *Proc. of SPIE* Vol. 9209 92090A-1, 2014.

Chapter 7

Implementation of the transfer function into the fundamental parameters algorithm

In this chapter, the analysis of the XRF spectra obtained by X-ray tube excitation and filtered by the HOPG monochromator will be discussed. The purpose of spectrum analysis is to obtain useful information from measured data. Peak location in a fluorescence spectrum corresponds to a measurement of the X-ray energy and allows identification of the elements in the sample, whereas the net area of fluorescence peaks is representative of the concentration of the elements in the given sample. Because of the matrix effects (absorption and enhancement), the relationship between concentration and peak intensity is not so simple. For quantitative analysis of a material, reliable software must be used. Some of them are based on the fundamental parameters method, which was presented in Chapter 1. It allows the concentration and intensity to be related using fundamental equations, if the experimental conditions and the setup geometry are well known. Throughout this thesis, the PyMCA dedicated software was used for spectrum processing. PyMCA was developed by the Software Group of the ESRF [1], [2]. It is based on the fundamental parameters algorithm, and enables the determination of the elemental composition, the estimation of the thickness of different layers, and is also used for the imaging of XRF data. It is widely employed for the quantification of XRF spectra [3] in a wide range of applications, including data obtained from cultural heritage and archaeological samples [4], analysis of multilayered samples [5], [6], etc.

The mathematical procedures used to derive quantitative information from X-ray spectra are presented in the first section of this chapter. By means of the PyMCA package, X-ray spectra obtained with both measurement channels of the miniature setup without the HOPG

monochromator could be directly analysed. The results of the processing of spectra from different samples are presented here. However, the spectra measured with the second channel in the presence of the HOPG monochromator could not be processed in the same manner, because the HOPG optics modify the spectral distribution of fluorescence radiation. The transmission functions of the HOPG monochromator computed in Chapter 6 were implemented in PyMCA, enabling it to process the spectra accurately. The capabilities of the algorithm are demonstrated in the second section of this chapter.

1. Spectrum processing

The first step in quantitative analysis consists in processing the acquired spectra. In the region of the fluorescence peaks, the spectrum can be described by functions representing background and peaks. The goal of spectrum evaluation is to remove unwanted background and noise, in order to obtain the net peak areas of the characteristic lines of an analyte. This can be undertaken with mathematical techniques that comprise the next steps:

I. Spectrum smoothing
II. Background modelling
III. Description of the full-energy peaks

This spectrum processing also assumes removal of the escape and sum peaks, and peak overlap corrections. A more detailed description of the spectrum evaluation procedures, their principles, and practical applications were extensively introduced by Van Espen and Janssens [7]. In the following paragraph, the spectrum processing methods implemented in PyMCA software are reported, with emphasis on the mathematical algorithms applied in this thesis.

I. Smoothing

During XRF spectrum acquisition statistical fluctuations occur on each channel content, affecting the appearance of the spectrum. Such distortions, or so-called noise, can interfere with a low-intensity characteristic peak and subsequently, impede its identification. They can also occur on the slope of a peak, preventing a valid peak description. The first step in the spectrum evaluation procedure is digital filtering or spectrum smoothing, in order to reduce the noise without distortions of the useful data. For noise minimization, various signal-smoothing algorithms such as signal averaging, Savitsky-Golay polynomial filters, low statistics digital filters, etc., can be employed [7], [8].
In this thesis, the noise fluctuations in the XRF spectra were handled with a Savitsky-Golay polynomial filter, which is a classical smoothing technique. It is based on the modelling of part of the experimental spectrum using a polynomial of a given order. Besides the filtering function, a Savitsky-Golay smoothing operation requires the specification of the number of points in the smoothing interval and the number of fit iterations to apply the filter to the data [8], [9]. Smoothing of the experimental data with the Savitsky-Golay filter is illustrated in Figure 7.1.

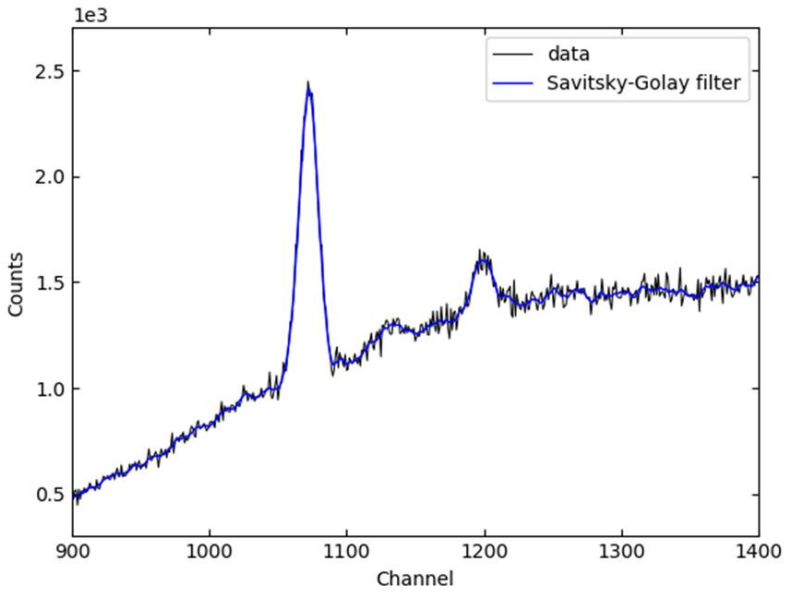

Figure 7.1. Savitsky-Golay smoothing filter with a smoothing width of 13 and a polynomial degree of 4.

II. Background modelling

The relevant analytical information can be obtained from the net peak area of a characteristic line corrected for the continuum background. The description of the continuum is a crucial part of spectrum processing, because its underestimation or overestimation can cause errors in quantitative analysis. Furthermore, the continuum estimation algorithm must be able to distinguish small isolated peaks on a continuum.

There are three ways in which the continuum can be handled: 1) it can be eliminated by applying a filter, 2) it can be calculated independently and removed from the original spectrum before the description of fluorescence lines, or 3) it can be calculated considering other features in the spectrum. There are a number of analytical functions used to describe the spectral background.

In the smoothed spectrum presented in the previous section, the continuum background was calculated with the SNIP (statistical nonlinear iterative peak clipping) algorithm (see Figure 7.2). This method combines a low statistics digital filter with a peak stripping method. The latter is an iterative procedure that involves parameters such as strip background width g and number of iterations. The model compares the count y_i of a given channel i, at a distance g from the surrounding channels y_{i-g} and y_{i+g}. If y_i exceeds the average *of* y_{i-g} and y_{i+g}, it is substituted by the average [7], [10].

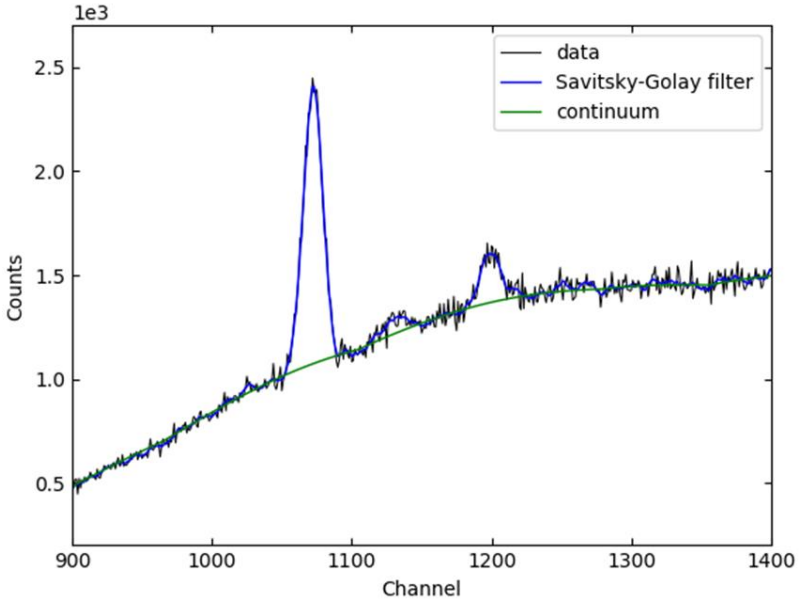

Figure 7.2. Continuum background modelling using the SNIP algorithm. The strip background width is 18 channels.

III. Description of the full-energy peak

Since the response functions of most solid-state detectors are mainly represented by a Gaussian function, a full-energy peak (peak) can be represented by this function [11]. Thus, the profile of a single peak can be described by:

$$G(x_i) = \frac{A}{s\sqrt{2\pi}} \exp\left[-\frac{(x_i - x_0)^2}{2s^2}\right] \tag{7.1}$$

The distribution is defined by three parameters: the position of the peak maximum x_0, the standard deviation s which is a measurement of the width of the Gaussian, and the peak area A. Here, the peak amplitude is expressed in terms of its area because it is directly related to the number of X-rays collected. The Gaussian standard deviation and its FWHM are related by FWHM=2.35 s. These parameters will be clarifed throughout the paragraph.
Generally, the position and width of each observed peak should be optimised independently. However, a peak corresponds to a specific element in a sample and since the knowledge of the energies of the fluorescence lines enables the identification of this element, other characteristic peaks can be linked to the first one. Each peak in a measured spectrum can be fitted with a Gaussian, and consequently, in the case of a multielement specimen, the fitting function will involve the optimization of many parameters. In order to facilitate the task, Van Espen and Janssens [7] proposed a procedure described below.
The expression of the energy (peak position) *E(i)* as a function of the channel number *i* (energy calibration) is given by:

$$E(i) = ZERO + (GAIN)\, i \tag{7.2}$$

Since the zero channel is not exactly at zero energy, there is a *ZERO* offset in the spectrum; *GAIN* is expressed in eV/channel.
Thus, referring to Eq. (7.1) and Eq. (7.2), the Gaussian profile can be defined as follows:

$$\mathrm{G(i, E_j)} = \frac{\mathrm{GAIN}}{\mathrm{s}\sqrt{2\pi}} \exp\left[-\frac{\left(\mathrm{E_j} - \mathrm{E(i)}\right)^2}{2\,\mathrm{s}^2}\right] \tag{7.3}$$

where E_j is the energy of a X-ray line and *s* is the peak broadening, expressed as:

$$\mathrm{s} = \sqrt{\left(\frac{\mathrm{NOISE}}{2.3548}\right)^2 + \varepsilon_{\mathrm{Si}}\,\mathrm{F_{Fano}}\,\mathrm{E_j}} \tag{7.4}$$

NOISE is the electronic noise contribution to the peak width which is from 80 eV to 100 eV. F_{Fano} is the Fano factor, and is approximately 0.114 for Si. $\varepsilon_{Si} = 3.6\ eV$ is the mean energy necessary to create an electron-hole pair in Si.
The modelling of an entire element permits a reduction in the number of fitting parameters. In fact, the fluorescence lines of an element can be grouped (e.g. K_α, K_β groups, or the entire family of lines (K, L, M etc.) of a given element), and characterised by the total number of counts of all lines, *A*, in a relevant group. The spectrum of an element is thus expressed by:

$$\mathrm{y_p(i)} = \mathrm{A}\sum_{\mathrm{j=1}}^{\mathrm{N_p}} \mathrm{R_j G(i, E_j)} \tag{7.5}$$

where *G* is the Gaussian function for a line of energy E_j with relative intensity R_j. N_p represents all the lines in a respective group.
The transition probabilities of the fluorescence lines between (sub)shells are constant. However, their apparent intensities depend on the absorption in the sample and on absorbers between the sample surface and the active area of the detector. Thus, X-ray attenuation must be considered in Eq. (7.5) to define the correct fitting function. In such a case, the apparent intensities are multiplied by the transition probabilities with an absorption correction term, as presented in [2]:

$$\mathrm{R'_j} = \frac{\mathrm{R_j T_A(E_j)}\left[1 - \mathrm{T_D(E_j)}\right]}{\sum_{\mathrm{j}} \mathrm{R_j T_A(E_j)}\left[1 - \mathrm{T_D(E_j)}\right]} \tag{7.6}$$

where the absorption correction term $T_A(E_j)$ considers all attenuators between the sample and the active area of the detector. The second absorption correction term $\left[1 - T_D(E_j)\right]$ represents the absorption of the detector for X-rays.
In the case of a polychromatic excitation (e.g. the X-ray tube excitation), the approach considers an incident beam of X-rays of energies E_{0k} with relative rates w_k. Thus, the relative

intensity ratios are defined as:

$$R'_j = \sum_k \frac{w_k T_A(E_{0k}) \omega_j P_j(E_{0k}) R_j T_A(E_j)[1 - T_D(E_j)]}{\mu_T(E_{0k}) + \mu_T(E_j)\frac{\sin\varphi_1}{\sin\varphi_2}} \times \left[1 - \exp\left\{\left[\frac{\mu_T(E_{0k})}{\sin\varphi_1}\right] + \left[\frac{\mu_T(E_j)}{\sin\varphi_2}\right]\rho d\right\}\right] \quad (7.7)$$

where ω_j is the fluorescence yield of the given shell, P_j considers the possibility of leaving a vacancy in the j shell, μ_T is the total mass attenuation coefficient of the sample, φ_1 and φ_2 are the incoming and outgoing angles of the beam with respect to the sample surface, ρ is the sample density, and d is the sample thickness. The total mass attenuation coefficient μ_T of the sample takes into account the attenuation of the primary radiation E_{0k} and of the fluorescence radiation E_j. In relationship (7.5), this apparent transition has to be taken into account with $R''_j = R'_j / \sum_j R'_j$.

The total count rate A in an X-ray group of an element is determined by the incident beam intensity I_0, the mass fraction C of this element in the sample, and the geometrical efficiency of the detector. The count rate for the group of an element is expressed as:

$$A = I_0 C \frac{\Omega}{4\pi} \sum_j R'_j \quad (7.8)$$

where Ω is the solid angle of detection, which is determined by the sample-to-detector distance and the sensitive area of the detector.

In Eq. (7.8), the total count rate A is a measured value, while the X-ray tube flux and the geometrical efficiency of the detector are generally unknown.

A simple representation of the peak profile is not sufficient when it comprises additional components in the tailing region on the low-energy side. The latter arise from effects such as charge collection losses and the escape of Auger electrons and photoelectrons from the active area of the detector. Thus, its shape can be described by the main Gaussian component plus an additional term that represents the tailing component. In the overwhelming majority of cases, peak tailing is described by an exponential or by a second Gaussian [7], [11], [12].

The peak shape must be examined more accurately in order to fit it with a suitable function. The natural fluorescence line shape can be approximated by a Lorentzian function. This must be taken into account if the natural width of the emitted X-ray line is not negligible (e.g. the K-lines of high-Z elements) compared to the width of the profile delivered by the detector. The Lorentzian function comes from the width of the subshell level, leading to the width of the corresponding X-ray line. In this case, the peak profile can be fitted with a Voigt function, which is the convolution of the natural line shape (Lorentzian) and the detector response function (Gaussian) [11].

The fitting procedure consists in determining the best parameters to minimize the difference

between the mathematical function(s) used to represent the peaks and the experimental data, thus allowing determination of the net peak area and derivation of the elemental concentrations as long as the experimental conditions have been correctly entered.

2. Spectrum processing with FP-based package

Throughout this thesis, the spectra were acquired with the Amptek application software DPPMCA [13]. It displays the live spectrum, allows the hardware features to be controlled (number of channels, gain, peaking time, acquisition time, etc.) and, additionally, enables the analysis in a region of interest to be carried out. The XRF data is saved as an MCA file that includes information on hardware configuration parameters and the raw data for each channel (histogram). The data recorded with the DPPMCA software can be directly read by the PyMCA spectrum processing software. The package includes the algorithm for the spectrum processing and peak area evaluation described in § 1. It is used to identify elements in the sample manually, if necessary, in order to resolve the overlapping peaks and calculate the elemental concentrations. To extract accurate quantitative information from the acquired spectra, it is necessary to supply the software with all the experimental conditions and the geometrical arrangement of the instrument.

2.1. XRF analysis with PyMCA

The quantitative analysis procedure using the PyMCA package will be demonstrated below. Firstly, the feasibility of processing the spectra acquired with both measurement channels without HOPG optics will be presented and discussed. In the second section of this paragraph, the spectra measured in the presence of the HOPG monochromator will be quantified using first the basic quantification model, and then with the model that includes the transmission function of the monochromator.

An X-ray spectrum acquired from a sample containing 100 mg L^{-1} of Sr in HNO_3 0.5 M with the first detection channel is illustrated in Figure 7.3. The X-ray tube was operated at a nominal voltage of 50 kV with a 20 µA tube current, using a 25 µm Ag primary filter to reduce the background continuum. The distance between the sample holder and the detector was 17.9 mm. The acquisition live time was 900 s, as well as for all the following spectra.

The spectrum contains the scattering peaks of the tube target, Sr K-L and K-M fluorescence peaks, and other X-ray lines (Cr, Ni, Fe, Cu, Zn) on the low-energy side of the spectrum that are produced by the elements of the X-ray tube and of the SDD housing and shielding [14].

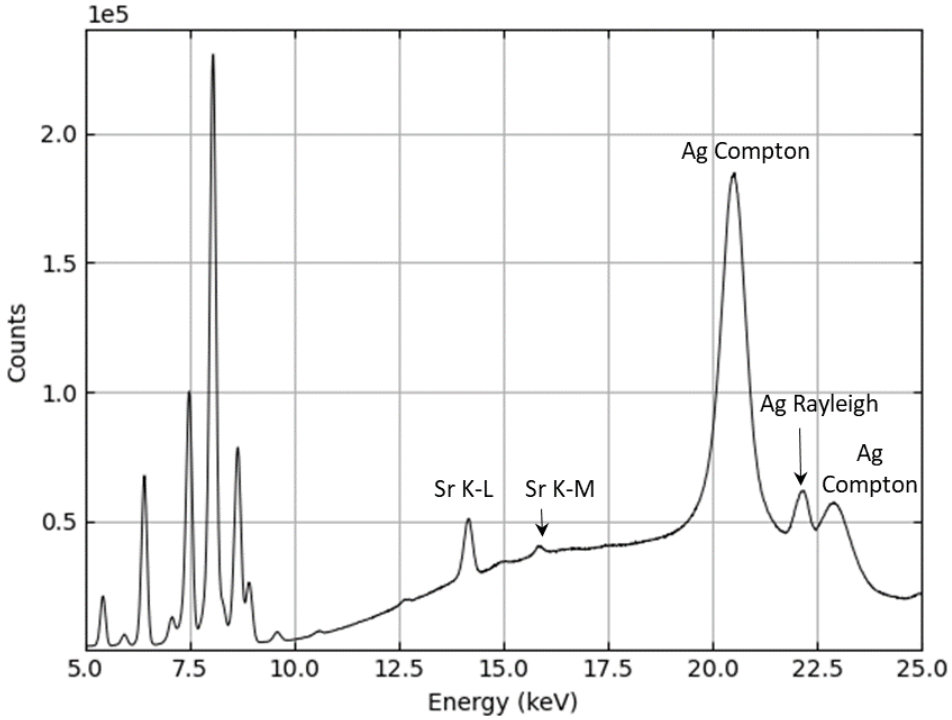

Figure 7.3. XRF spectrum of a solution of Sr at a concentration of 100 mg L^{-1} in HNO_3 0.5 M, measured with the first channel.

Thereafter, the measurements were performed with the second channel without the HOPG monochromator (see Figure 7.4). The measurement settings for spectrum acquisition were the same as in the previously discussed experiment; however, the SDD was positioned at a distance of 125 mm from the sample holder. In Figure 7.4 it can be clearly seen that the total intensity of the spectrum is considerably reduced compared to that of the first channel, and the peak intensities in the low-energy region below 10 keV are significantly lower. The difference can be explained by the fact that the solid angle of collection is larger for the first channel, as the SDD is closer to the sample. Additionally, the intensity of the emitted X-rays along their path from the sample to the SDD is reduced according to the Lambert-Beer law. The Sr K-L peak at 14.17 keV has a peak amplitude of 20 000 in the spectrum measured with the first channel, whereas for the second channel the value is reduced by a factor of 13. More experimental results with different sample and measurement settings can be found in Appendix A.

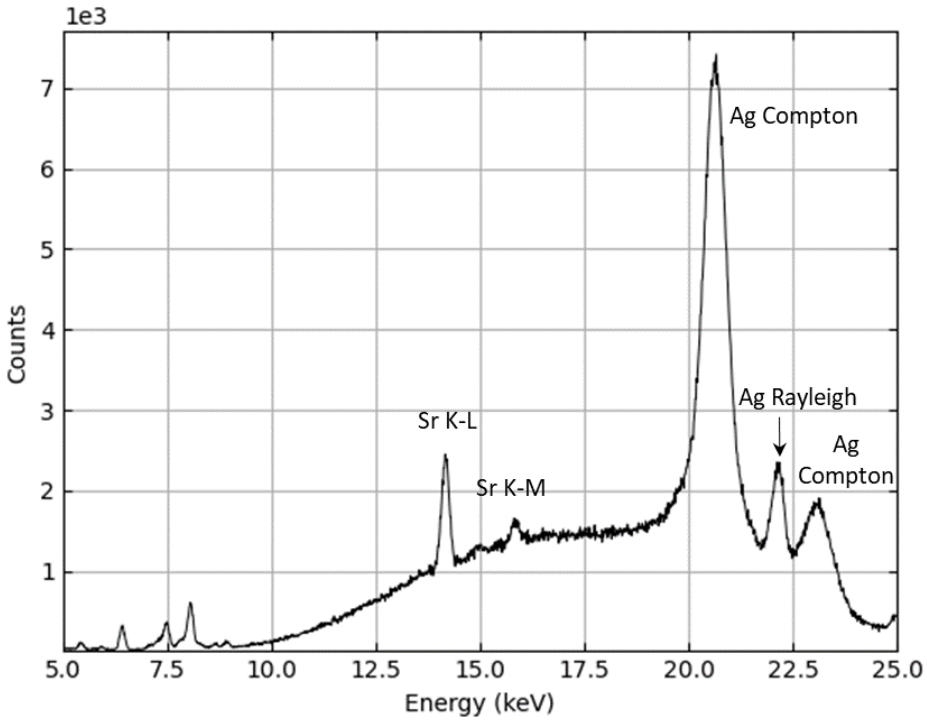

Figure 7.4. XRF spectrum of a solution of Sr at a concentration of 100 mg L^{-1} in HNO_3 0.5 M measured with the second channel, in the absence of the HOPG monochromator.

The spectra presented above were processed using the PyMCA software. Firstly, the energy scale was calibrated, and the elements of interest and their X-ray groups selected. Parameters such as the thickness of the Be window, the primary beam filter, the sample matrix, and the parameters of the active area of the detector were entered. PyMCA includes the approach proposed by Ebel [15] to calculate the X-ray tube emission profile. The software also enables representation of the continuum spectrum in the case of the transmission-anode X-ray tube. For a detailed description of this approach, refer to Chapter 5. All materials that attenuated the X-ray radiation in the path from the sample surface to the active area of the SDD were taken into account. It is important to specify the composition, density, and thickness of each medium that the fluorescence X-rays travel through before being detected, as well as the incoming and take-off angles.

To calculate the concentration of an analyte, a set of experimental parameters such as the acquisition time, the solid angle, and the tube flux must be entered in the software. The latter is the only unknown parameter. Since we did not have an internal standard, a reference solution containing 100 mg L^{-1} (9.79×10^{-5} mass fraction) of Sr was prepared from a certified standard (1 000 mg L^{-1} in 2% HNO_3, manufactured by SPEX SertiPrep (USA) [16]) in HNO_3 0.5 M. This reference solution enabled the tube flux value used in the PyMCA algorithm to be adjusted.

Figure 7.5 illustrates the fitted spectrum from the reference sample measured with the first channel. The known composition of the sample was entered in the program as the matrix composition, as recommended by the developers [10]. The tube flux parameter was adjusted

until the expected concentration of the analyte was reached.
Together with the experimental data and the fit, the residuals are also displayed in the lower panel to demonstrate the quality of the fit. The relative residuals are expressed as a percentage and calculated as [17]:

$$r_i = \frac{y_i - y(i)}{{\sigma_i}^2} \times 100 = \frac{y_i - y(i)}{y_i} \times 100 \qquad (7.9)$$

where y_i is the measured value, and $y(i)$ the fitted model; σ_i is the standard deviation of the experimental data, which can be estimated by $\sqrt{y_i}$ (the counting process obeyed a Poisson distribution). The large differences denote poorly fitted spectrum regions.

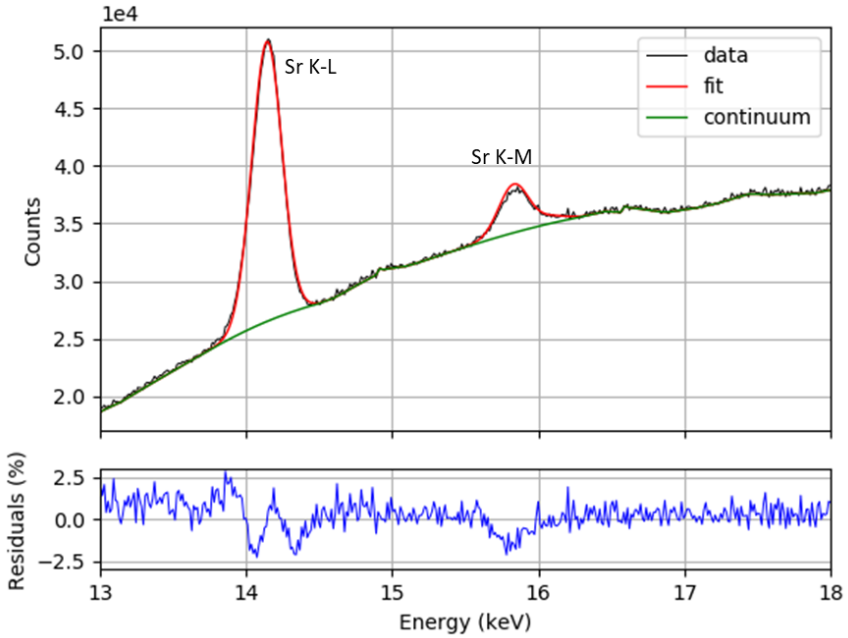

Figure 7.5. Processing of the spectrum of the sample with 100 mg L^{-1} of Sr in HNO_3 0.5 M, collected with the first channel.

Afterwards, the spectra measured with the second channel, without the HOPG crystal, were processed (see Figure 7.6 and Figure 7.7). The geometrical parameters of the corresponding channel, such as the source to SDD distance and the incident and take-off angles, were adjusted in the model to match those of the experiment. The second channel was also calibrated prior to the spectrum analysis using the same reference solution as before.

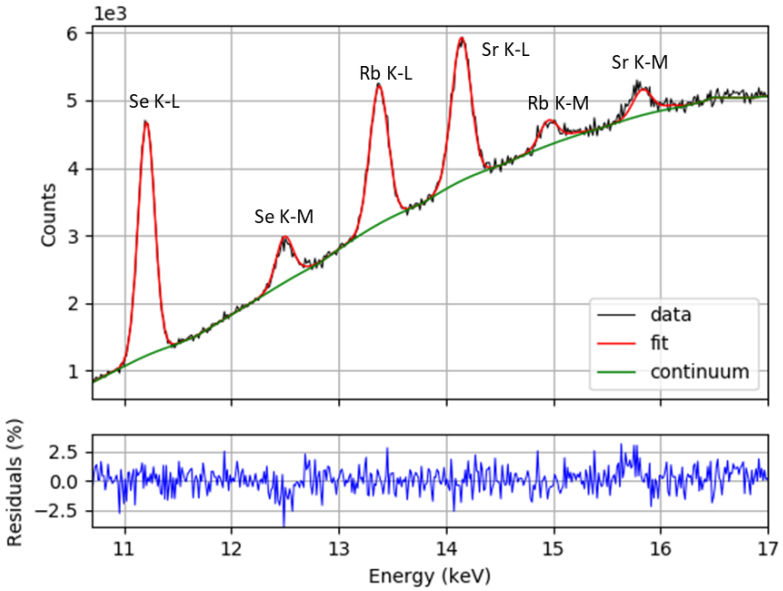

Figure 7.6. Processing of the spectrum of the sample with 100, 50, and 50 mg L^{-1} of Se, Rb, and Sr, respectively, in HNO_3 0.5 M. The spectrum was obtained with the second channel, without the HOPG monochromator.

The estimated mass fractions of each analyte in the latter sample are reported in Table 7.1 and are compared to the prepared values. The latter were carried out by volume dilution and their associated uncertainties were estimated at around 2 %. The relative uncertainty associated to PyMCA calculation depends on the uncertainty of each input parameter and is estimated at about 5 %.

Table 7.1. Comparison of prepared and estimated mass fractions with PyMCA. The data was obtained from the spectrum in Figure 7.6.

Element	Prepared mass fraction	Estimated mass fraction	Relative difference, %
Se	9.79×10^{-5}	10.10×10^{-5}	+3 %
Rb	4.89×10^{-5}	4.84×10^{-5}	-1 %
Sr	4.89×10^{-5}	4.87×10^{-5}	-0.4 %

In the following step, a sample with Rb and Y at a concentration of 100 mg L^{-1} each in HNO_3 0.5 M was analysed. The software successfully resolved the overlapping of the Y K-L and Rb K-M lines (see Figure 7.7). The calculated mass fractions of the corresponding elements are reported in Table 7.2.

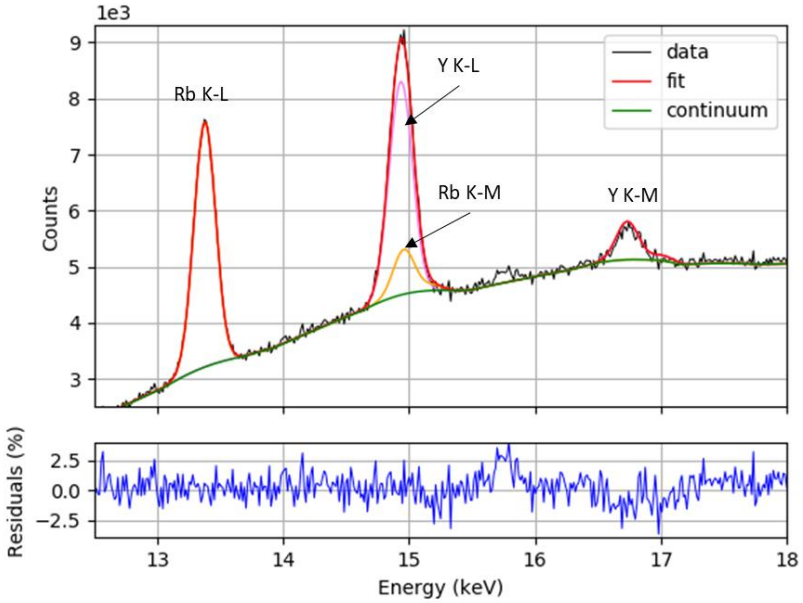

Figure 7.7. Processing of the spectrum of the sample containing Rb and Y at a concentration of 100 mg L^{-1} in HNO_3 0.5 M obtained with the second channel, without the HOPG crystal.

Table 7.2. Comparison of prepared and estimated mass fractions with PyMCA. The data was obtained from the spectrum in Figure 7.7.

Element	Prepared mass fraction	Estimated mass fraction	Relative difference, %
Rb	9.79×10^{-5}	10.40×10^{-5}	+6 %
Y	9.79×10^{-5}	9.27×10^{-5}	-5 %

The calculated and measured spectra are in good agreement, which means that the software is able to correctly process the different spectra recorded with the miniature setup (without the HOPG optics), and to calculate the concentration of an analyte with sufficient accuracy.
The key component of the miniature setup is the HOPG monochromator. As was discussed previously, this optical element significantly modifies the spectral distribution of the fluorescence radiation. Now let us consider the processing spectra acquired with the second channel in the presence of the optical element.
The operating conditions of the X-ray tube were 40 kV and 99 μA for all measurements (i.e. the maximum power of the X-ray tube), with the 25-μm thick Ag filter. The monochromator was positioned at a distance of 50 mm from the sample surface, which corresponds to the central energy of 13 keV. The value was estimated taking into account the geometry of the optical element and its position between the sample and the SDD (see Chapter 6). The spectrum measured is illustrated in Figure 7.8.

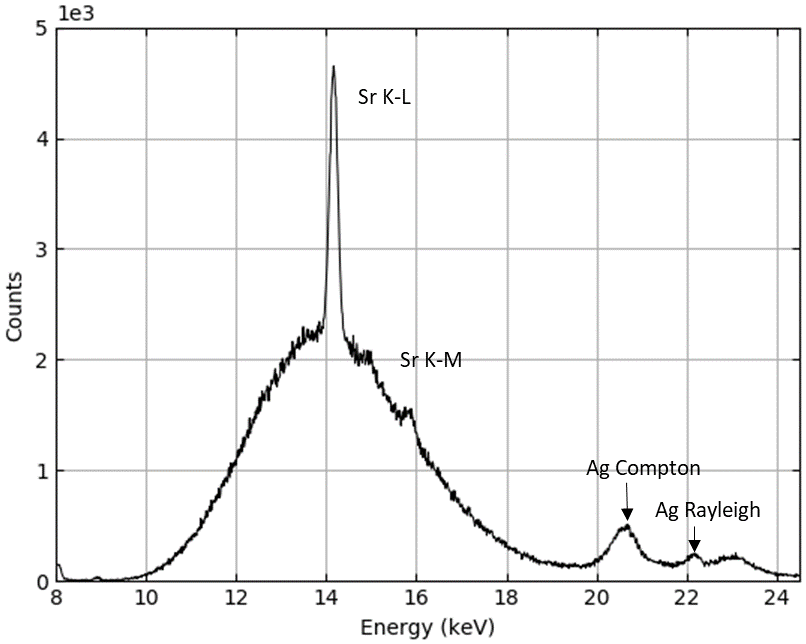

Figure 7.8. Spectrum of a sample with 100 mg L^{-1} Sr in HNO_3 0.5 M, measured using the second channel with the HOPG monochromator. The sample to crystal and crystal to SDD distances are equal to 50 mm.

By comparing the measurement in Figure 7.8 to that made without the HOPG crystal, at the same position of the SDD and with the same acquisition time, it was deduced that the amplitude of the Sr K-L line is reduced by about 40 %, while that of the Sr K-M line is reduced by approximately 70 %.

Now we can examine the feasibility of PyMCA software analysis of the spectra measured with the optical element. In Figure 7.9, it can be seen that the Sr peaks are fitted inaccurately, especially the Sr K-M peak which is largely overestimated by the software. The latter peak is located on the shoulder of the hump of the spectrum, where the reflectivity is reduced.

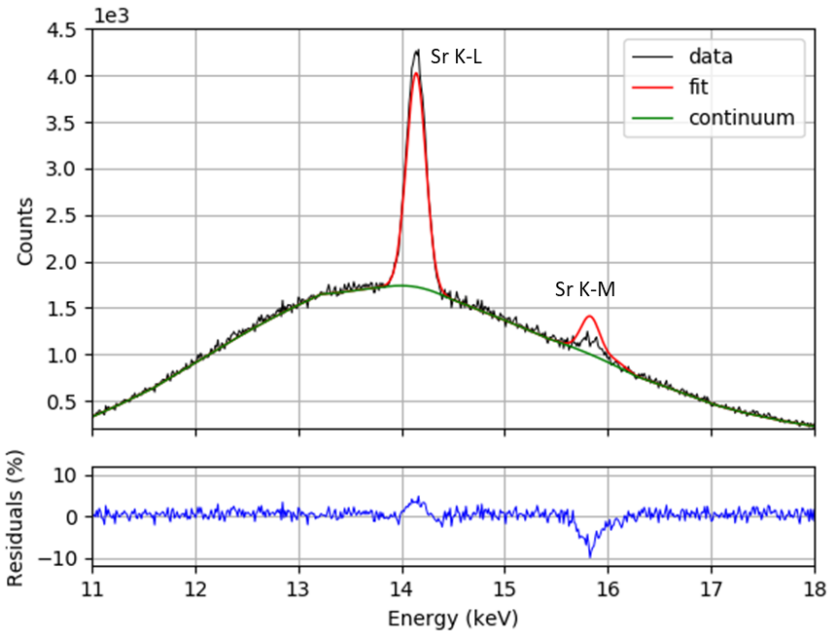

Figure 7.9. Processing of the spectrum from the sample containing Sr at a concentration of 100 mg. L^{-1} in HNO_3 0.5 M. Measurement was performed on the second channel with the HOPG optics. The spectrum analysis model does not take into account the modification of spectral distribution by the HOPG monochromator.

The multi-element spectrum depicted in Figure 7.10 was also processed inaccurately. The K-L peaks of most elements closely fit the measured data, whereas the Se K-M peak is underestimated and Sr K-M is overestimated.

To obtain quantitative information, the second detection channel was calibrated using the same reference solution (containing 100 mg L^{-1} (9.79×10^{-5} mass fraction) of Sr in HNO_3 0.5 M), for a given sample to detector distance as described in § 2.1. The tube flux was adjusted to obtain the expected value of the Sr mass fraction, and then entered in the model to process the spectrum illustrated in Figure 7.10. The calculated values of mass fractions are in complete disagreement with the reality reported in Table 7.3.

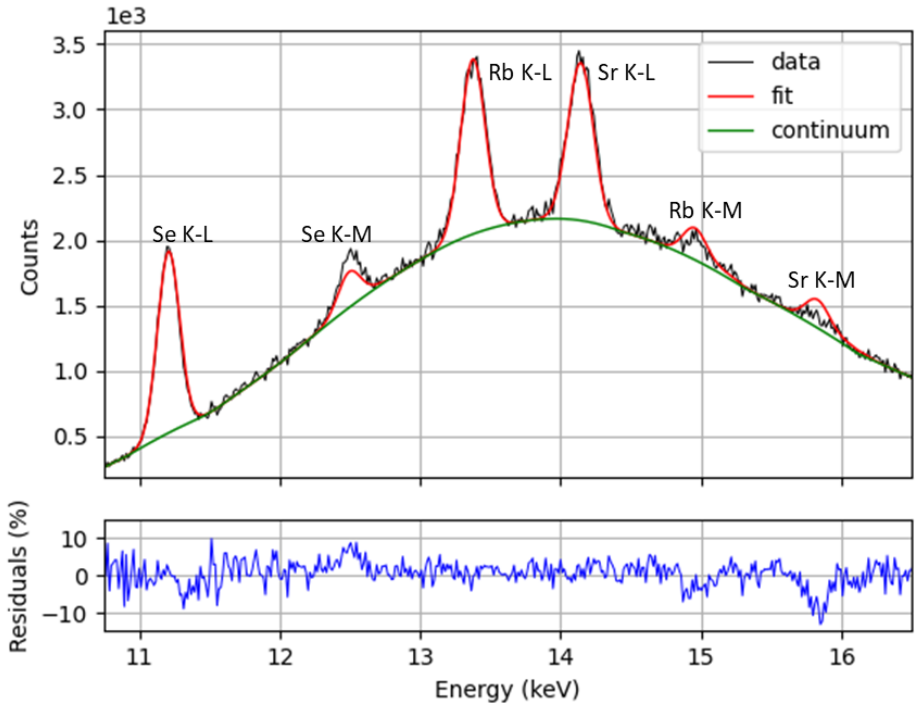

Figure 7.10. Processing of the spectrum from the sample containing Se, Rb, Sr in concentrations of 100, 50, 50 mg L^{-1}, respectively, in HNO_3 0.5 M. Measurement was performed on the second channel with the HOPG optics. The spectrum analysis model does not take into account the modification of spectral distribution by the HOPG monochromator.

Table 7.3. Comparison of prepared and estimated mass fractions with PyMCA. The data was obtained from the spectrum in Figure 7.10.

Element	Prepared mass fraction	Estimated mass fraction	Relative difference, %
Se	9.79×10^{-5}	7.70×10^{-5}	-21 %
Rb	4.89×10^{-5}	5.41×10^{-5}	+ 10%
Sr	4.89×10^{-5}	4.85×10^{-5}	-0.6 %

It is obvious that the elemental concentrations could not be calculated correctly. The degree to which the calculated spectrum deviates from the acquired data is dependent on the accuracy of the model description. The latter takes into account all experimental conditions, but does not consider the presence of the optical element. For correct spectrum processing, it is necessary for the spectrum analysis model to include the function that describes the transmission of the HOPG crystal.

2.2. Definition of the transfer function

In Chapter 6, we studied the reflection properties of the HOPG crystal. By means of the XRT ray tracing code, the reflection profile of this optical element with the source sampled with a uniform ray distribution was calculated. At this point, it is necessary to represent the output

of ray distribution after the crystal mathematically, in order to integrate it into the PyMCA model. However, since the broadening of the reflection profile varies with the monochromator position, the crystal output must be calculated for each desirable central energy. The energy bandwidth as a function of the sample to HOPG crystal distance was reported in Chapter 6.

The reflection profiles of the HOPG crystal in the first and second orders of reflection are asymmetric. The complex profile could be fitted with several Gaussian functions [18], but this would involve a large number of parameters. To simplify the monochromator output fitting and perform it independently of the crystal position, a spline function was used [18], [19]. This estimates a spline representation of the curve and can be evaluated for a desired set of points. Figure 7.11 illustrates the fitting of the complex reflection profile calculated with XRT (blue line) by the splines (red line).

In this ray tracing model, D_1 and D_2 were 50 mm, corresponding to the central energy of 13 keV (see Chapter 6).

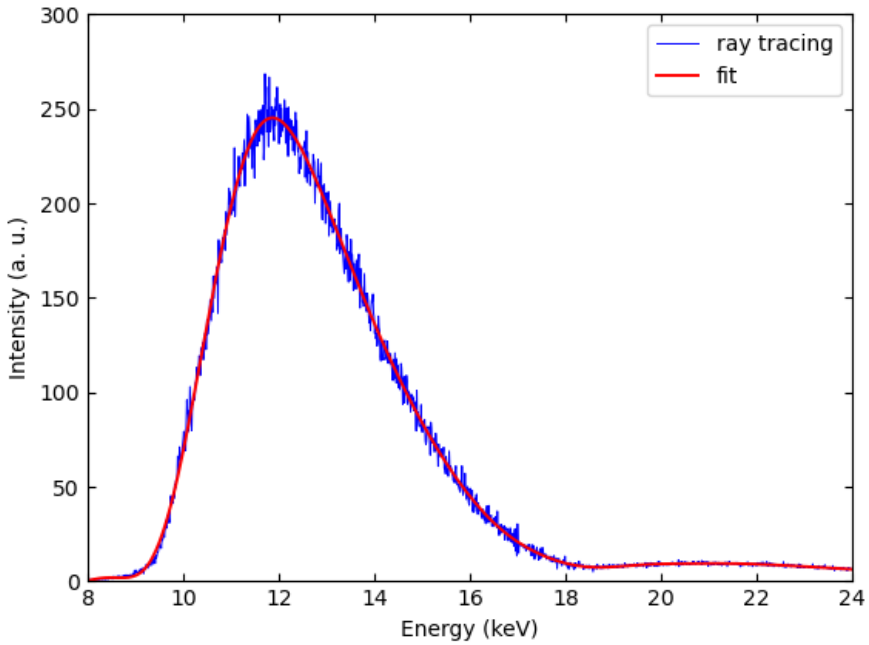

Figure 7.11. Fit of the reflection profile of the HOPG monochromator calculated with the source sampled with the uniform ray distribution by means of the ray tracing method. Calculations were performed in the first and second orders of reflection.

In fact, the model can consider the presence of the monochromator as a new attenuator between the sample and the detector. To take this into account in Eq. (7.7), each relative intensity R'_j of the line of energy E_j is multiplied by a new attenuator term, T_{Mj}, which is the relevant transfer function estimated for given positions of the HOPG monochromator and the SDD.

Thus, the apparent intensities become:

$$R_j^* = \left[R'_j * T_{M_j}\right] \tag{7.10}$$

This modification was implemented in the PyMCA code.
In order to validate the new spectrum analysis model, several experiments were performed for different samples and at various sample to crystal distances. A number of transfer functions for the central energies in the range from 12.8 keV to 15 keV were calculated beforehand, to be applied in the model.
Figure 7.12 shows the spectrum acquired for the solution containing 100 mg L^{-1} of Se in HNO_3 0.5 M (black line) and the result of the fit (red line). The comparisons of the prepared and estimated mass fractions are reported in Table 7.4. In the presence of the monochromator, estimating the solid angle is not an easy task. The term $I_0 \frac{\Omega}{4\pi}$ was therefore adjusted for each desired position of the monochromator, and entered in the corresponding model.

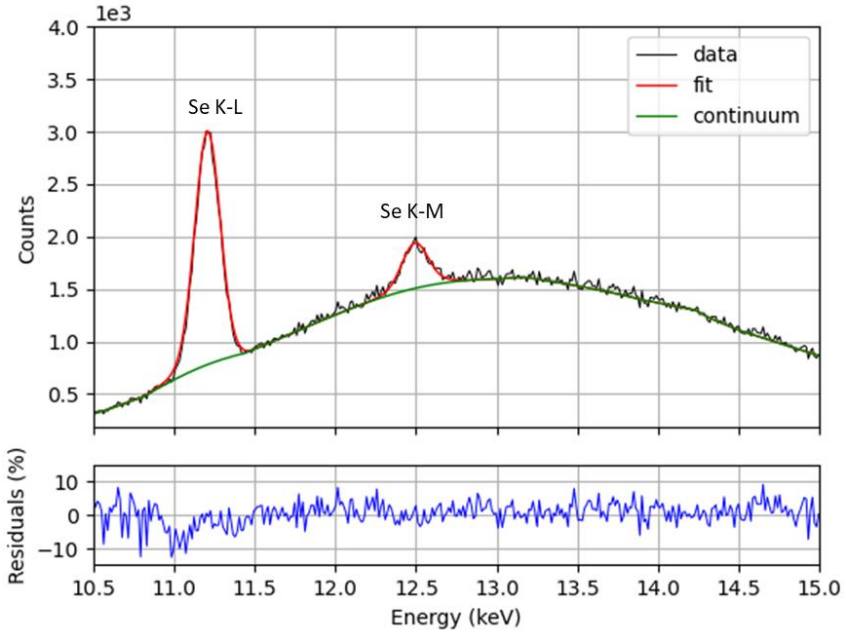

Figure 7.12. Processing of the spectrum from the sample containing Se at 100 mg. L^{-1} in HNO_3 0.5 M. Measurement was performed on the second channel with the HOPG optics. The transfer function was implemented in the analysis model.

Table 7.4. Comparison of prepared and estimated mass fractions with PyMCA, taking into account the transfer function of the HOPG monochromator. The data was obtained from the spectrum in Figure 7.12.

Element	Prepared mass fraction	Estimated mass fraction	Relative difference, %
Se	9.79×10^{-5}	10.25×10^{-5}	+5 %

Another example of a fit procedure is depicted in Figure 7.13. For this experiment, Rb and Y at a concentration of 100 mg L^{-1} of each element in HNO_3 0.5 M were used. The monochromator was positioned at the furthest possible distance from the sample surface allowed by the setup to reach the central energy of 15 keV. It can be seen that the fitting of

the spectrum has been performed accurately, and that the Y K-L and Rb K-M peaks are resolved. Thus, only small deviations of the computed concentrations from the prepared values are observed (see Table 7.5).

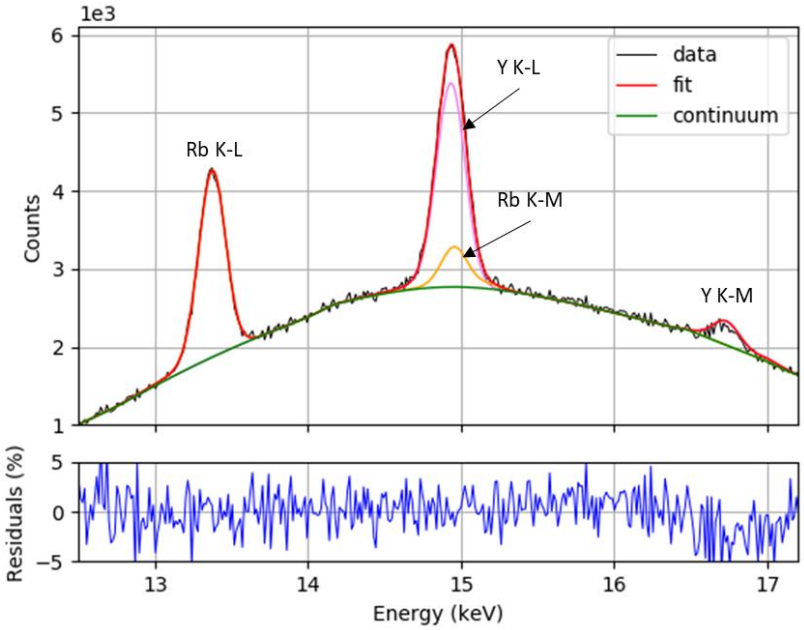

Figure 7.13. Processing of the spectrum from the sample containing Rb and Y at concentrations of 100 mg. L^{-1} in HNO_3 0.5 M. Measurement was performed on the second channel with the HOPG optics. The transfer function was implemented in the analysis model.

Table 7.5. Comparison of prepared and estimated mass fractions with PyMCA, taking into account the transfer function of the HOPG monochromator. The data was obtained from the spectrum in Figure 7.13.

Element	Prepared mass fraction	Estimated mass fraction	Relative difference, %
Rb	9.79×10^{-5}	10.22×10^{-5}	+4 %
Y	9.79×10^{-5}	9.24×10^{-5}	-5 %

To go further in the analyses, the spectrum from a sample with three elements at different concentrations was processed (see Figure 7.14). It can be seen that the lines on the shoulders of the hump fit perfectly. The concentrations of all elements in the sample could be accurately calculated, despite intensities reduced by the monochromator (see Table 7.6).

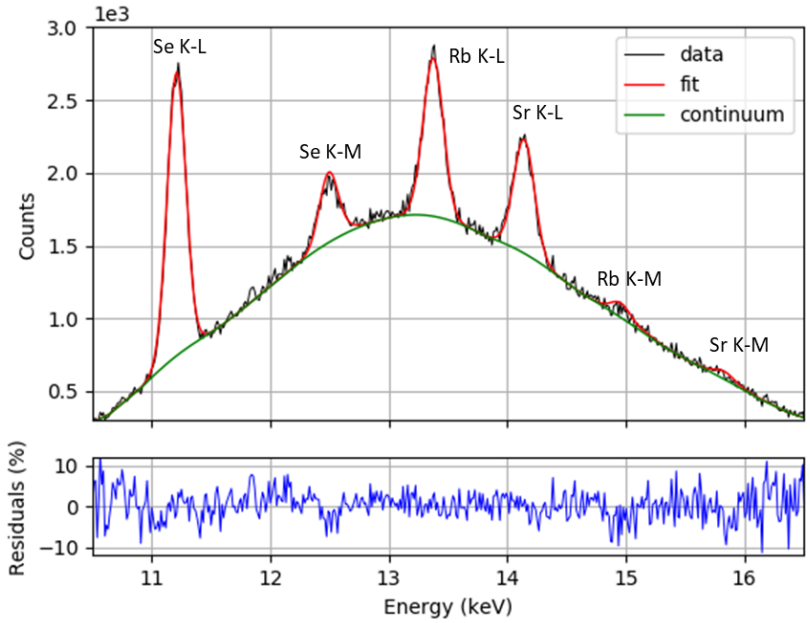

Figure 7.14. Processing of the spectrum from a sample containing Se, Rb, and Sr in concentrations of 100, 50, and 50 mg. L^{-1}, respectively, in HNO_3 0.5 M. Measurement was performed on the second channel with the HOPG optics. The transfer function was implemented in the analysis model.

Table 7.6. Comparison of prepared and estimated mass fractions with PyMCA, taking into account the transfer function of the HOPG monochromator. The data was obtained from the spectrum in Figure 7.14.

Element	Prepared mass fraction	Estimated mass fraction	Relative difference, %
Se	9.79×10^{-5}	9.58×10^{-5}	-2 %
Rb	4.89×10^{-5}	4.80×10^{-5}	-2 %
Sr	4.89×10^{-5}	4.92×10^{-5}	+0.6 %

For the measurements of a much lower concentration (about 10 mg L^{-1}), the primary X-ray beam was filtered with a 25 µm thick W filter (see Figure 7.15). The acquisition live time of this spectrum was 9×10^3 s, in order to obtain good counting statistics.

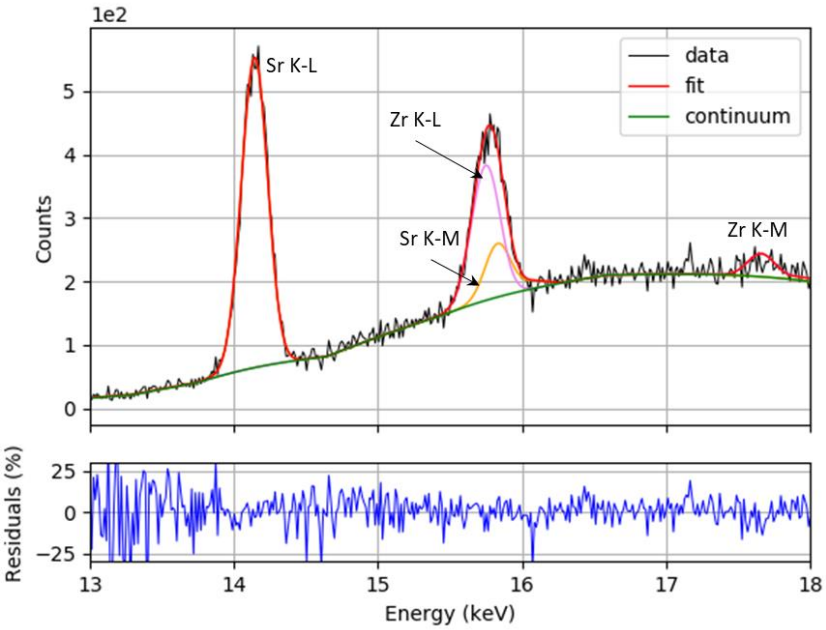

Figure 7.15. Processing of the spectrum from the sample containing Sr, Zr in concentrations of 10 mg. L^{-1}, in HNO_3 0.5 M. Measurement was performed on the second channel with the HOPG optics. The transfer function was implemented in the analysis model.

Table 7.7. Comparison of prepared and estimated mass fractions with PyMCA, taking into account the transfer function of the HOPG monochromator. The data was obtained from the spectrum in Figure 7.15.

Element	Prepared mass fraction	Estimated mass fraction	Relative difference, %
Sr	9.79×10^{-6}	9.69×10^{-6}	-1 %
Zr	9.79×10^{-6}	9.51×10^{-6}	-3 %

3. Conclusions

The possibilities of using PyMCA for the XRF spectra analysis of data obtained from both channels without the optical element were demonstrated. The software enabled us to process spectra without the optical element. However, as was emphasized above, the data collected in the presence of the monochromator could not be processed correctly. The investigations of the HOPG monochromator features reported in Chapter 6 enabled the transfer function of this optical element to be computed for each system configuration. To obtain an accurate elemental quantification, the HOPG monochromator was considered as a new attenuator, and the corresponding transfer function was implemented in the PyMCA code. Spectra obtained from various system configurations were processed. The implementation of the transfer function does not induce significant uncertainty, and the relative differences are similar to those obtained for a system without a monochromator.

References

[1] "PyMCA Fluorescence Toolkit". (available at http://pymca.sourceforge.net/).

[2] V. A. Solé, E. Papillon, M. Cotte, P. Walter, J. Susini. "A multiplatform code for the analysis of energy-dispersive X-ray fluorescence spectra", *Spectrochim. Acta - Part B*, 62, 63–68, 2007.

[3] D. E. B. Fleming, S. L. Crook, C. T. Evans. "Assessing zinc from a nail clipping using mono-energetic portable X-ray fluorescence", *Appl. Radiat. Isot.*, 145, 170–175, 2019.

[4] J. Hormes, A. Roy, G. L. Bovenkamp, K. Simon, C. Y. Kim, N. Börste, S. Gai. "Medieval glass from the Cathedral in Paderborn: A comparative study using X-ray absorption spectroscopy, X-ray fluorescence, and inductively coupled laser ablation mass spectrometry", *Appl. Phys. A Mater. Sci. Process.*, 111, 91–97, 2013.

[5] M. Ferretti, C. Polese, C. Roldán García. "X-ray fluorescence investigation of gilded and enamelled silver: The case study of four medieval processional crosses from central Italy", *Spectrochim. Acta - Part B*, 83–84, 21–27, 2013.

[6] L. De Viguerie, V. A. Sole, P. Walter. "Multilayers quantitative X-ray fluorescence analysis applied to easel paintings", *Anal. Bioanal. Chem.*, 395, 2015–2020, 2009.

[7] R. E. Van Grieken, A. A. Markowicz. *Handbook of X-ray Spectrometry Second edition*. Marcel Dekker, Inc., 2001.

[8] Mike J. Adams. *Chemometrics in analytical spectroscopy Second Edition*. The Royal Society of Chemistry, 2004.

[9] R. Gullayanon. *A calibration methodology for energy dispersive X-ra fluorescence measurements based upon synthetically generated reference spectra,* PhD Dissertation. Georgia Institute of Technology, 2011.

[10] "PyMCA documentation". (available at http://www.silx.org/doc/PyMCA/dev/tutorials.html).

[11] K. Debertin, R. G. Helmer. *Gamma and X-ray spectrometry with semicondactor detectors*. North-Holland, 1988.

[12] L. A. McNelles, J. L. Campbell. "Analytic approximations to peak shapes produced by Ge(Li) and Si(Li) spectrometers", *Nucl. Instruments Methods*, 127, 73–81, 1975.

[13] "DPPMCA Display & Acquisition Software – Amptek". (available at https://www.amptek.com/software/dpp-mca-display-acquisition-software).

[14] "Amptek". (available at https://www.amptek.com/).

[15] H. Ebel. "X-ray Tube Spectra", *X-Ray Spectrom.*, 28, 255–266, 1999.

[16] "SPEX CertiPrep Certified Reference Materials - Inorganic and Organic Standards". (available at https://www.spexcertiprep.com/).

[17] M.-C. Lépy. "*Presentation of the COLEGRAM software*," Laboratoire National Henri Becquerel (2004).

[18] A. Matthew Newville, Till Stensitzki. *Non-Linear Least-Squares Minimization and Curve-Fitting for Python*. Release Notes, 2018.

[19] "SciPy Reference Guide". (available at https://docs.scipy.org/doc/scipy/reference/generated/scipy.interpolate.LSQUnivariateSpline.html).

Conclusions & recommendations for future work

Conclusions

This PhD project demonstrated the possibility of analysing spectra obtained with a classical EDXRF setup equipped with HOPG optics, using a quantification algorithm based on the fundamental parameters. The task was complex, and had the following objectives: 1) probing the performances of a miniature XRF setup designed for the analysis of medium-Z (Se, Rb, Sr, Y, etc.) and high-Z (mainly U, Np, Pu, Am, and Cm) elements by their K and L X-ray lines, respectively; 2) investigating the entire experimental setup by computational methods; 3) studying the reflection properties of the HOPG optics and the influences of different parameters on its output; 3) defining the transmission function of the HOPG optics; 4) refining the classical standardless algorithm for the quantitative XRF analysis of the data measured with the special experimental setup.

The miniature setup was designed with an Ag anode X-ray tube and two detection channels with different geometrical arrangements. Representing a conventional EDXRF setup, the first channel has allowed the recording of wide XRF spectrum energy ranges. The energy domain in the scope of this work was 3 keV<E<30 keV. The second detection channel was constructed in combination with the HOPG optics located between the sample and the SDD. This channel had a miniaturised copy of the nuclearized setup utilised in the hot cell of the LAAT analysis laboratory. The HOPG optics device was used as a broadband filter. This favoured the collection of the fluorescence radiation emitted in the desired energy ranges, and the suppression of the low energy peaks and of scattering radiation from the anode material. Thus, the detector dead time was reduced and its count rate capability was improved. The HOPG optics and the SDD in the miniature setup could be moved along the detection line, thereby displacing the filtered energy window. The energy range selected extended from 10 keV to 18 keV, which corresponds to the energy domain of actinide L X-ray lines. The minimum central energy allowed by the setup was 12.5 keV and the maximum value reached 15 keV. During the thesis work, the miniature setup was tested in a non-nuclear laboratory by analysing medium-Z elements (Rb, Sr, Y, Zr) whose K X-ray emission lines are in the energy range of the L X-ray lines of actinides. The elements could be determined down to concentrations of 5 mg L^{-1} (see Appendix A). As presented above, the

second channel could be operated with or without the optical element. The experiments showed that in the presence of the HOPG monochromator, the intensities of the X-ray lines of interest were reduced by a factor of 1.7, while coherently and incoherently scattered tube radiation was strongly suppressed.

The entire miniature XRF setup was modelled using the PENELOPE Monte Carlo code for radiation transport and the XRT ray tracing package. The simulation model developed with PENELOPE comprised two parts: 1) calculation of the spectrum of the transmission X-ray tube; 2) calculation of the XRF spectra obtained with both detection channels without HOPG optics. The X-ray tube spectrum was calculated applying the variance reduction technique (forcing interaction), in order to reduce the computation times. The simulated spectrum and that calculated from the theoretical approach proposed by Ebel showed good agreement. In the second step, the XRF spectra were simulated, employing the X-ray tube spectrum as input data. The simulation results were validated by means of comparisons with the experimental spectra.

One of the objectives for the ray tracing modelling was to gain a better understanding of the reflection properties of the cylindrical HOPG optics, and to investigate the performances of the optical system. The XRT package enabled us to model the cylindrically bent mosaic crystal and to represent the entire response of the second detection channel step by step. The dependences of the energy window characteristics (width and central energy) as a function of the length of the crystal and its position in the optical system, respectively, were demonstrated in the case of a polychromatic point source. The influences of source size and ray distribution on the output results were studied. It was shown that with larger sources, a larger optical surface contributes to the reflection and the positional distribution of rays over the image plane becomes more uniform. For larger sources, the effective optical surface of the crystal became larger and, consequently, the output profile broadened. Furthermore, increasing the central energy broadened the energy window. For example, in the case of the source r_s=7 mm, the FWHM of the energy window at the central energy of 12 keV was 4 keV, whereas at the central energy of 15 keV this value reached 5.5 keV. Additionally, the width of the energy window was dependent on the effective size of the detection surface. The work pointed out that the rays of energies higher than the central energy could be reflected from the deeper crystal layers when the optical system was arranged for the first order of reflection. From this arose the necessity to calculate the reflection on the second order. The summed contributions from the first and second orders of reflection represented the complete transmission function of the HOPG optics.

The source to crystal distance D_1 was responsible for the central Bragg angle, while the crystal to image plane distance D_2 determined the positional distribution of the rays of a certain energy over the image plane. The beam images for the defocusing geometries were evaluated. The simulation demonstrated that by going from $D_1<D_2$ to $D_1>D_2$, the area of the optical surface that contributed to the effective reflection was displaced from left to right. The energy at the maximum intensity of the exit beam increased, and the energy bandwidth broadened. For D_1=56 mm and 35 mm$<D_2<$75 mm, the FWHM broadening rose 3.5 keV$<$FWHM$<$6.5 keV, respectively.

It was necessary to approve the validity of the estimated transfer function for further

applications. To do so, the optical system was simulated considering the experimental spectrum recorded without the HOPG optics as an input source spectrum. The simulation results were directly compared with the experimental data acquired under the same geometrical conditions, and were found to be in very good agreement. In addition, the models developed with two different numerical tools enabled representation of the output of the whole miniature setup. The fluorescence spectrum for the geometry corresponding to the second detection channel calculated by the PENELOPE code was introduced as the input data in the ray tracing model. The results were consistent with the experiment. This provided the opportunity to predict the spectral responses of the miniature setup under tube different geometrical conditions.

The measurements obtained from both channels without the HOPG crystal were processed using the PyMCA FP based analysis tool. A set of experimental parameters, such as the acquisition time, flux from the X-ray tube, and the incident and take-off angles, were required for the quantification procedure. The flux of the X-ray beam as the only unknown parameter was determined before the quantitative analysis, using the reference solution prepared from a certified standard. The estimated mass fractions deviated from the prepared values by less than 6%.

However, as expected, the situation for the spectra recorded in the presence of the HOPG crystal was unsatisfactory. The same spectrum-processing software was not able to evaluate the X-ray fluorescence spectra modified by the HOPG optics adequately. Consequently, large deviations (of about 21%) between the prepared and calculated mass fractions were obtained. As well as all the factors influencing an analyte intensity already provided, the transmission function of the HOPG optics was required. The functions obtained with the ray-tracing model were implemented in the PyMCA code in such a way that each intensity of each measured line of given energy was multiplied by the relevant transition efficiency. A term corresponding to the X-ray beam flux times the solid angle had to be adjusted once for each HOPG optic configuration, using the reference solution. The model was supplied with the transmission function for corresponding sets of working distances D_1 and D_2. When the processing algorithm was applied to spectra acquired under different conditions, the results showed the same order of deviation from the prepared mass fractions as without the HOPG crystal. It can be noted that these results are compatible given the mentioned uncertainties. However, more detailed studies on the influence of the input parameters uncertainties could be performed in a future work.

Recommendations for future work

Additional investigations of the miniature setup were needed for its optimisation and the improvement of performances in the energy domain of interest, to reach those comparable with the full-size nuclearized device.

A comparison of the spectrum measured with the nuclearized device and that obtained with the miniature setup shows that the latter is characterised by a large background hump. The first system was operated using an Rh 200 µm thick primary filter, which significantly reduced the background. Unfortunately, thick filters are not available for such low power X-ray tube,

but the model developed with PENELOPE for the simulation of the X-ray tube spectrum can be employed.

Comparing the calculations for tube spectra filtered through Ag filters 25 μm and 75 μm thick (illustrated in Figure 1), it can be noted that when the thick filter is used the bremsstrahlung is reduced below the Ag K-L lines (notably in the energy domain of interest), which in turn are more intense. The number of simulated primary particles was the same for both models.

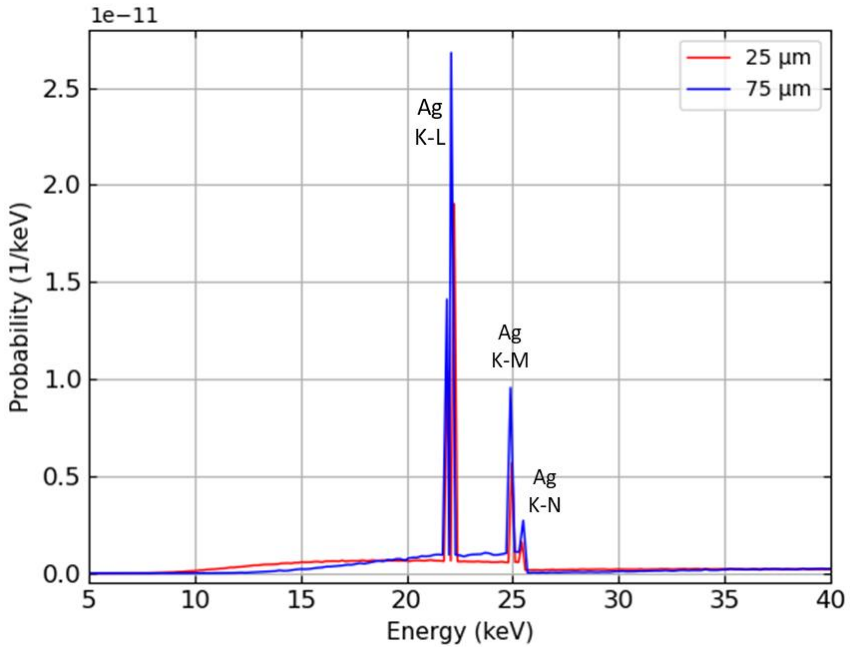

Figure 1. Emission spectrum of the transmission tube with Ag anode and 40-keV electrons, and with Ag filters 25 μm or 75 μm thick simulated by PENELOPE.

The tube spectrum filtered by 75 μm of Ag was added to the model of the second channel in the manner described in Chapter 5. The simulated fluorescence spectrum is illustrated in Figure 2. The strongly filtered excitation spectrum provides a higher peak to background ratio for the Sr K-L line than that with the thinner filter.

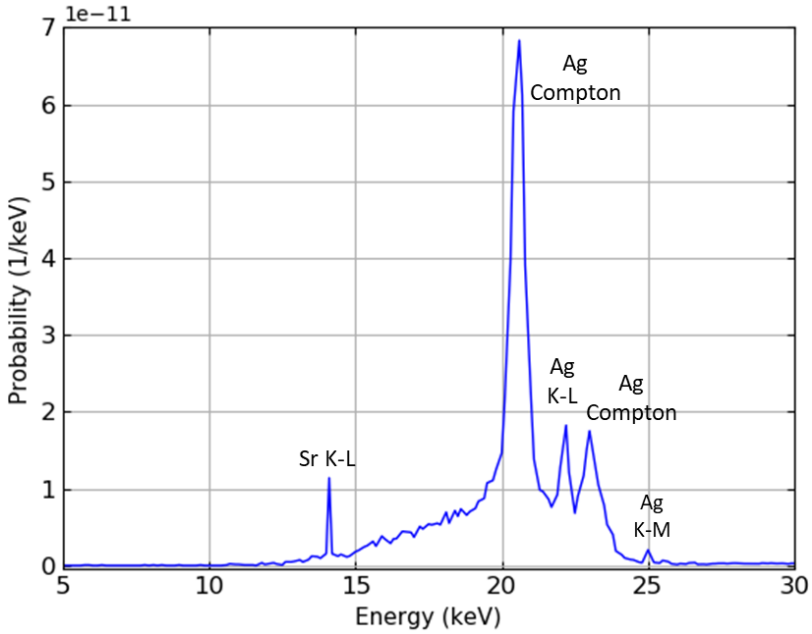

Figure 2. Simulated spectrum from the sample solution with Sr performed with the second channel of the miniature setup without the HOPG monochromator. The spectrum was previously corrected for the detector efficiency.

In Chapter 6, the simulations demonstrated that a narrow energy window could be obtained with a small source (close to a point source). Given the mechanical constructions of the experimental setup, the size of the circular aperture in front of the HOPG crystal (for details see Figure 6.13) can be reduced to the optimal values with a radius of 1 or 2 mm. In this case, the aperture, instead of the sample, will be regarded geometrically as a source of X-rays. Therefore, the HOPG crystal as well the SDD have to move farther along the cylinder axis from the new source, in order to keep a point-to-point geometry and cover the desirable energy region.

The spectrum calculated by PENELOPE was implemented in the ray tracing model as input data, as presented in Chapter 6. The geometrical source had a 1 mm radius, and the aperture in front of the HOPG cylinder was not introduced. The distances D_1 and D_2 were set at 57 mm to take advantage of the reflection of Sr K X-rays. Due to the small size of the source, a small segment in the optical surface reflected the beam (see Figure 3).

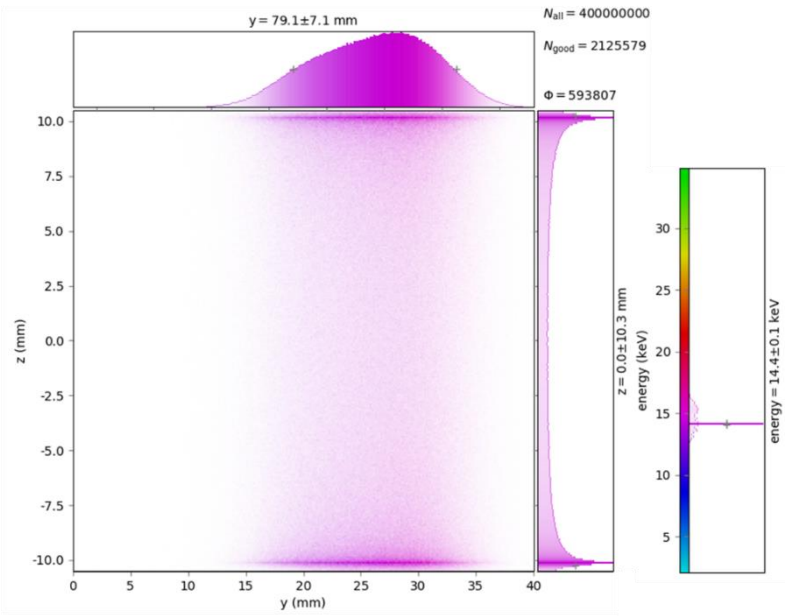

Figure 3. Footprint image of the beam pre-calculated by PENELOPE in the first order of reflection over the HOPG crystal surface with collection length L=40 mm (Y-axis) and radius R=10.1 mm (Z-axis).

The calculated results were compared with the experimental spectrum recorded for the same working distances, where the sample was considered as a ray starting point (see Figure 4). The scattered background under the characteristic lines is significantly reduced, and the energy window is much narrower. It should be noted that there is only a small contribution of rays reflected from the second order.

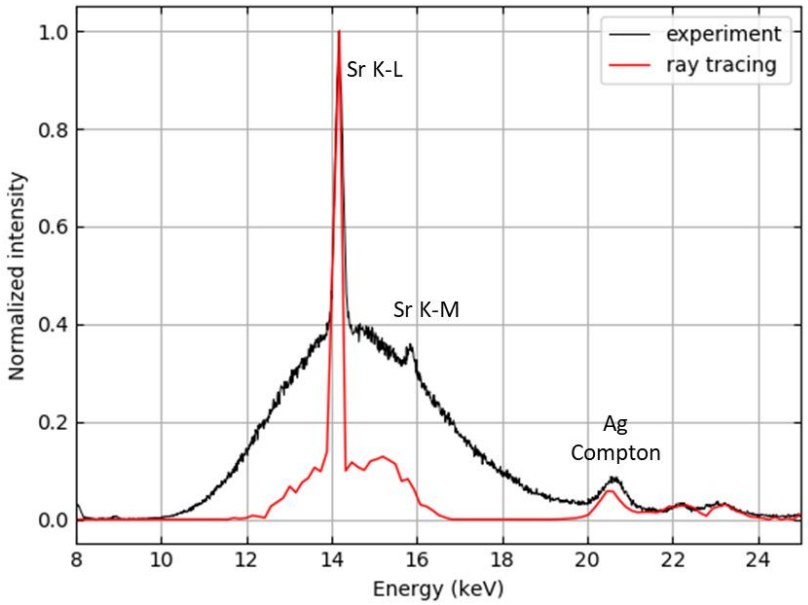

Figure 4. Comparison of the experimental (black line) and simulated (red line) spectra with optimized parameters from the Sr sample solution performed with the second channel of the miniature setup. The spectra were normalised to unity at the Sr K-L line.

Summing up all the proposed modifications, better performances could be achieved for the second detection channel. Although such a setup may provide the opportunity to detect lower analyte concentrations (<5 mg L^{-1}), the proposed modifications will be paid for by the loss of intensity while X-rays pass through the thicker filter and the very small aperture. In this case, it would be advantageous to employ a more powerful source of primary radiation. In the experimental setup with a conventional EDXRF arrangement, both fluorescence and scattered radiation contribute to the total amount of counts detected. For the XRF analysis of elements at very low concentrations, high intensities of excitation radiation are needed. However, this produces a high detector dead time, which does not allow the required count rate of characteristic radiation to be recorded. The utilization of the HOPG optics in the detection line permits collection of the fluorescence radiation in a particular energy range, and a considerable reduction in the participation of the tube-scattered radiation in the total count rate. Thus, a sufficient input count rate in the energy domain of interest is achievable. Today, the capabilities of the miniature setup are limited due to the low excitation intensity, and performances equal to those of the nuclearized device cannot be attained. Primarily, this study has helped to understand the properties of the HOPG optics, enabled the transmission function of the crystal to be determined, and its inclusion in the standardless algorithm. In the future, the knowledge acquired and the simulation models developed during this PhD project can contribute to further detection limit improvements for the miniature setup, or even to the modelling of the nuclearized setup in the hot cell.

Résumé en Français

ATALANTE (ATelier Alpha et Laboratoires pour ANalyses, Transuraniens et Études de retraitement) est l'installation nucléaire la plus importante au monde, dédiée à la recherche et au développent sur le cycle du combustible nucléaire. Située au Commissariat à l'énergie atomique et aux énergies alternatives (CEA) de Marcoule, ses installations permettent d'effectuer des expériences fondamentales, de la recherche sur la chimie du traitement-recyclage des combustibles nucléaires irradiés et la gestion des déchets radioactifs de haute activité et à vie longue.

Le Laboratoire d'analyses d'ATALANTE (LAAT) est particulièrement axé sur l'analyse des actinides. Les expériences sont réalisées en boîtes à gants sur des échantillons de moyenne activité et en chaîne blindée pour ceux de haute activité. Différentes méthodes analytiques peuvent être utilisées pour l'analyse quantitative et qualitative des actinides telles que: la spectrométrie à plasma à couplage inductif (ICP), la spectrométrie de masse, les spectrométries alpha et gamma et la spectroscopie des rayons X (fluorescence et absorption).

La fluorescence X est une méthode bien établie et largement exploitée pour obtenir des informations qualitatives et quantitatives sur la composition élémentaire de nombreux types de matériaux. Elle se base sur le principe de l'irradiation d'un échantillon par un faisceau primaire de rayons X d'énergie suffisante afin d'ioniser les atomes de l'analyte d'intérêt. Ces atomes vont alors émettre des rayonnements de fluorescence X, qui leurs sont propres, lors de leur retour à l'état stable. Le spectre énergétique des rayons X est donc caractéristique de la composition de l'échantillon. Cette technique d'analyse est rapide, non destructive ; elle convient à l'analyse d'une large gamme d'éléments (Na jusqu'à U), peut être utilisée pour différents matériaux sous forme solide, liquide ou de poudre et ne nécessite pas de préparation spéciale des échantillons.

L'objectif de l'analyse quantitative par fluorescence X est d'établir la relation entre la concentration de l'analyte et l'intensité mesurée de ses raies de fluorescence. Cette relation n'est pas directement proportionnelle. En effet, les intensités mesurées dépendent aussi du flux et de la distribution énergétique des rayons X primaires, de la fraction massique de l'analyte dans l'échantillon, de la composition de la matrice, de la géométrie du système expérimental, du rendement de détection, etc. Pour établir la corrélation entre la fluorescence et la concentration d'un élément, des approches théoriques et empiriques ont été développées.

Au LAAT, il existe un équipement de fluorescence X, implanté en zone arrière d'une chaîne blindée. Ce dispositif a été spécifiquement conçu pour l'analyse des actinides par leurs raies XL dans le domaine d'énergie de 12 keV à 17 keV. Afin d'assurer la radioprotection et sécurité, le dispositif a été blindé avec du plomb. Les échantillons sont transportés de l'enceinte blindée à la gare de mesure par un dispositif de transfert pneumatique. Le spectromètre est composé d'un tube à rayons X à anode de rhodium (Rh), d'un filtre cylindrique inséré entre l'échantillon et le détecteur dont la surface interne est recouverte de graphite pyrolytique

hautement orienté (HOPG en anglais), et d'un détecteur au germanium de haute pureté (HPGe).

Le HOPG constitue un filtre passe-bande pour privilégier les énergies d'intérêt : c'est un cristal mosaïque constitué par un grand nombre de petits cristaux parfaits (cristallites) légèrement inclinés les uns par rapport aux autres. Il se caractérise par la répartition angulaire des cristallites (mosaïcité) qui varie entre 0,2° et 1,2° en fonction de l'épaisseur du cristal. Chaque rayon incident sur un cristal mosaïque tente de trouver une cristallite pour laquelle la relation de Bragg est satisfaite ; celle-ci relie l'énergie de la radiation E et l'angle d'incidence θ :

$$\mathrm{E} = \frac{12.398\ \mathrm{n}}{2\ \mathrm{d}\ \sin\theta}$$

où d représente la distance inter-réticulaire et n est un entier appelé ordre de diffraction.

Du fait de la répartition angulaire des cristallites, les rayons sont réfléchis dans une large bande d'énergie et la réflectivité intégrée est plus importante que celle d'un cristal parfait.

Afin d'analyser les analytes de plus faibles concentrations (quelques mg L^{-1}), il est nécessaire d'augmenter le courant de tube. Dans ces conditions, l'augmentation du taux de comptage global, principalement dû à la diffusion du spectre du tube à rayon X, risque de saturer le détecteur. Le HOPG placé entre l'échantillon et le détecteur permet de sélectionner une bande passante d'environ 4 keV. La détection des rayons X dans la gamme d'énergie d'intérêt est préservée tout en réduisant le taux de comptage dû aux rayonnements des diffusions cohérentes et incohérentes du tube qui se situent dans la gamme d'énergie comprise entre 19 keV et 22 keV. La bande passante sélectionnée par l'optique HOPG dépend de la mosaïcité, de la taille du HOPG, de la surface active du détecteur et des distances échantillon-HOPG et HOPG-détecteur. Le filtre HOPG du dispositif expérimental couvre le domaine d'énergie de 12 keV à 17 keV permettant ainsi d'analyser les éléments de Z moyen (Se, Rb, Sr, Y, etc.) et les actinides (U, Np, Pu, Am et Cm) par leurs raies K et L respectivement. Ce dispositif « nucléarisé » permet de détecter les concentrations des actinides jusqu'à 0,5 mg L^{-1}.

Les spectres XRF mesurés par ce dispositif nucléarisé sont traités avec une approche semi-empirique spécialement développée au laboratoire. En particulier, le processus d'étalonnage s'appuie sur l'utilisation d'une bibliothèque composée de nombreux spectres étalons. Ce processus est très long. De plus, les solutions étalons de certains actinides sont difficiles à obtenir. Il serait donc souhaitable d'éviter ces procédures d'étalonnage. Les spectres mesurés avec un spectromètre conventionnel peuvent être traités avec succès en utilisant une méthode théorique basée sur les équations mathématiques descriptives des intensités de fluorescence X sans nécessiter d'étalon. Il s'agit de la méthode dite des paramètres fondamentaux (PF). Cependant, pour traiter avec précision les spectres mesurés avec la présente configuration, il est nécessaire de définir la fonction de transmission du filtre HOPG afin de l'implémenter dans l'algorithme de PF.

Pour atteindre ces objectifs, un nouveau dispositif « miniaturisé » a été conçu au laboratoire. Celui comprend deux voies de mesure : la première constitue un spectromètre conventionnel à dispersion en énergie tandis que la deuxième voie a été conçue comme la copie du dispositif nucléarisé. Cette nouvelle installation est équipée d'un tube à anode d'argent (Ag),

d'un filtre HOPG et d'un détecteur au silicium à dérive (Silicon Drift Detector - SDD) (voir Figure 16).

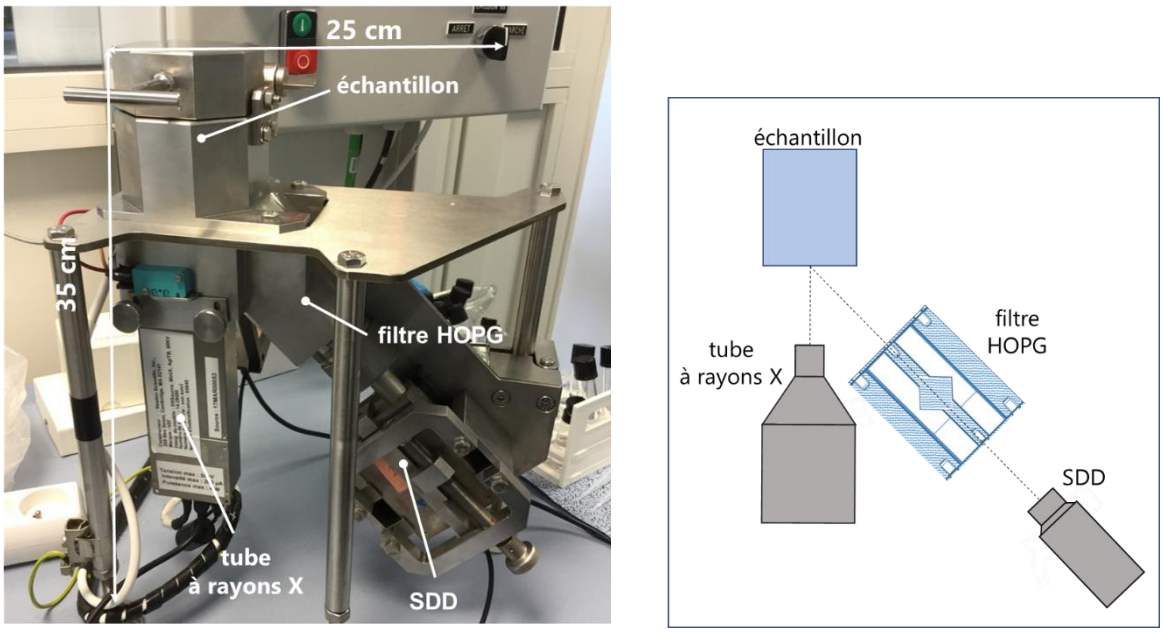

Figure 16. Photographie du dispositif miniaturisé (à gauche) et son schéma (à droite).

Dans ce cas, le filtre HOPG est un cylindre dont la surface intérieure est couverte d'une épaisseur de graphite pyrolytique hautement orienté de 200 µm avec une mosaïcité de 0,4°. Au cours de ce travail, le dispositif miniaturisé a été utilisé dans un laboratoire conventionnel, non réglementé pour l'usage de matériaux radioactifs. Des échantillons contenant des éléments de Z moyen (Se, Rb, Sr, Y, Zr) dont les raies XK sont dans la gamme d'énergie des raies XL des actinides, ont été utilisés.

Le traitement des spectres acquis sur la voie de mesure équipée du filtre HOPG nécessite la connaissance exacte des effets sur le spectre de chaque élément du système, en particulier celui du filtre. Pour répondre à ces besoins, le dispositif expérimental a été modélisé en couplant deux approches différentes qui ont permis de simuler le comportement des différentes parties du système.

La première étape a consisté en la modélisation de la distribution spectrale du tube à rayons X. Le code de simulation de Monte Carlo PENELOPE (PENetration and ENergy LOss of Positrons and Electrons), développé par l'Université de Barcelone, a été utilisé. Cet outil est dédié au transport des électrons, photons et positrons dans la matière et est particulièrement bien adapté à la simulation des interactions des particules de basse énergie.

La seconde étape a permis de simuler, avec le même outil, le spectre de fluorescence X émis par un échantillon représentant la solution avec les éléments étudiés. Pour cette simulation, le profil du tube calculé à la première étape a été utilisé comme source de rayons X. Les résultats de simulation obtenus ont été corrigés par le rendement du détecteur SDD utilisé avant d'être comparés aux mesures expérimentales. Cette courbe de rendement a été établie expérimentalement à l'aide d'étalons radioactifs certifiés au Laboratoire National Henri Becquerel (LNHB). La Figure 17 présente la comparaison entre une expérience et un résultat obtenu par la simulation avec PENELOPE pour une solution d'un mélange de Se, Rb et Sr à

100 mg L^{-1} de chaque élément dans une matrice HNO_3 0,5 M.

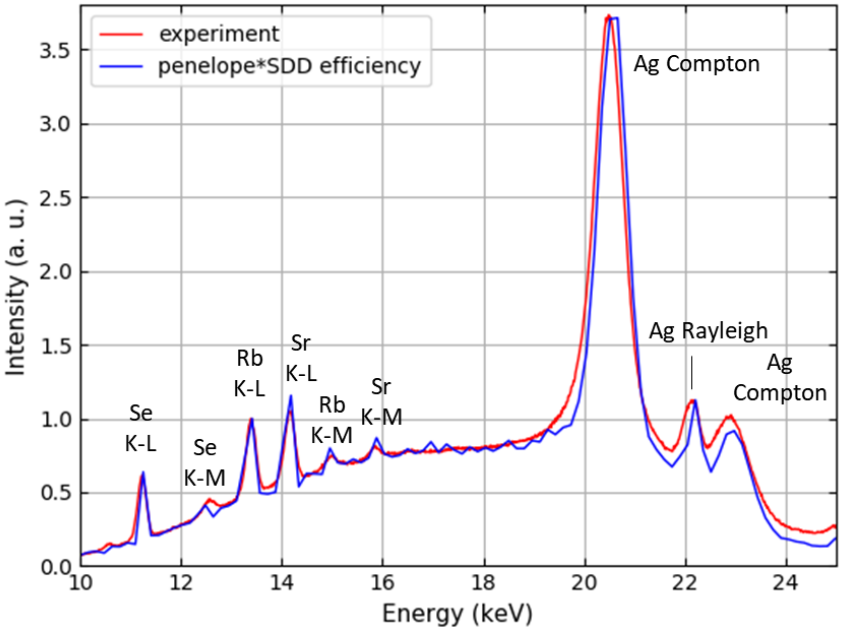

Figure 17. Comparaison des spectres obtenus expérimentalement et avec PENELOPE corrigé par le rendement du SDD.

La troisième étape a été dédiée à l'étude détaillée des propriétés optiques du HOPG cylindrique. Celle-ci s'appuie sur l'utilisation du code python XRT (XRayTracer) permettant le suivi des rayons et la propagation des ondes dans le domaine d'énergie des rayons X. Pour mieux comprendre les caractéristiques de l'optique HOPG, les simulations de la réflexion sur sa surface ont été effectuées successivement pour des faisceaux monochromatiques, puis polychromatiques. Les études numériques ont permis d'examiner la variation de la largeur à mi-hauteur (FWHM en anglais) de la bande passante en fonction de la taille du cylindre HOPG et de la distance entre la source et le HOPG.

La modélisation qui nous intéresse concerne la partie du mini-système située entre l'échantillon et le SDD (partie optique). Tous les éléments qui ont une influence sur les intensités des rayons X émis ont été pris en compte. D'abord, dans le modèle simulé, l'échantillon a été considéré comme la source physique (i.e. le point de départ des raies X). Etant donné que la source réelle n'est pas ponctuelle mais étendue, une attention particulière a été portée sur la définition de ses paramètres caractéristiques. Ainsi, la réponse du système optique complexe a été étudiée en fonction de la taille de la source. Il a été démontré que, dans le cas d'une source plus large, une surface optique plus importante contribue à la réflexion et, par conséquent, cela rend la bande passante plus large. Dans le modèle optique, les dimensions de tous les éléments correspondent à celles du dispositif miniaturisé.

Ensuite, les simulations ont été réalisées en utilisant des spectres expérimentaux enregistrés sans le filtre HOPG comme spectres de la source. Les simulations du modèle optique décrit sous XRT ont été validées par comparaison avec des mesures expérimentales pour différents échantillons liquides contenant des éléments de Z moyen, et des concentrations de quelques dizaines de mg L^{-1}. Cette étape a permis de déterminer la fonction de transmission du filtre

HOPG, qui sera utilisée pour la partie quantification de l'étude. La Figure 18 présente la comparaison du spectre simulé par XRT et de celui mesuré expérimentalement pour une solution d'un mélange de Se, Rb et Sr à 100 mg L^{-1} de chaque élément dans une matrice HNO_3 0,5 M.

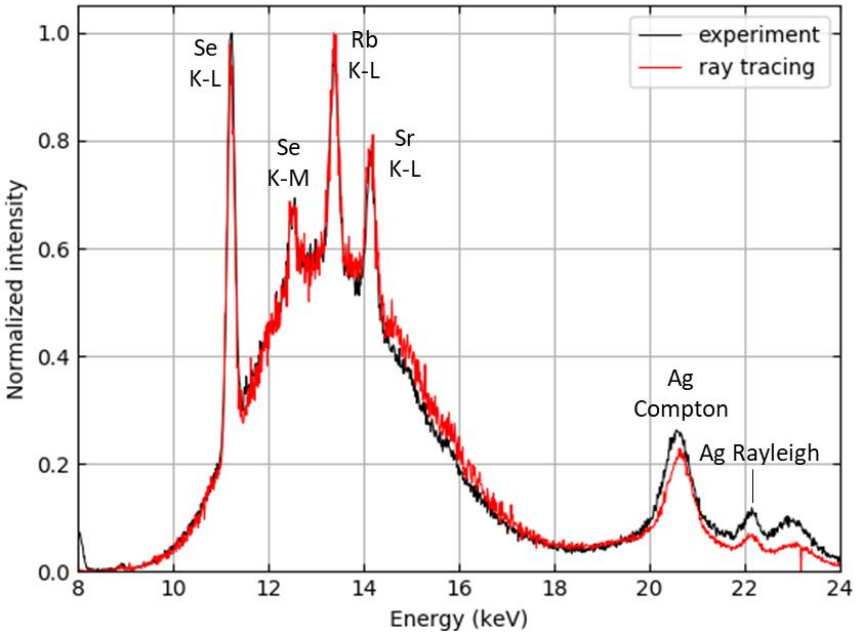

Figure 18. Comparaison des spectres calculé par XRT et mesuré expérimentalement.

Ensuite, le spectre de fluorescence X calculé précédemment par PENELOPE a été introduit dans le modèle optique de même manière que celui mesuré l'avait été dans l'étape précédente. Le couplage des modélisations avec deux méthodes différentes a donné ainsi la possibilité de reproduire le système miniaturisé dans sa globalité.

La quatrième étape de ce travail a été d'adapter l'algorithme classique de quantification basé sur les paramètres fondamentaux en tenant compte des modifications spectrales apportées par le filtre HOPG. Pour le traitement des spectres mesurés, le logiciel PyMCA a été retenu. Ce code est développé par une équipe de l'ESRF et est largement utilisé pour le traitement des spectres de fluorescence, pour la visualisation des résultats et la caractérisation des épaisseurs de couches de matériaux.

Dans le modèle de quantification de PyMCA, qui nécessite de tenir compte de toutes les interactions entre la source de rayonnement X et détecteur (atténuation du rayonnement incident et émis, photoabsorption, rendement de fluorescence, etc.), le HOPG a été considéré comme un nouvel atténuateur. Les intensité apparentes relatives des raies d'un analyte ont donc été pondérées par la fonction de transmission calculée précédemment à l'aide de XRT. Il convient de rappeler que cette fonction dépend de la position du HOPG et doit donc être recalculée pour chaque nouvelle position du filtre HOPG. Le traitement avec PyMCA du spectre d'une solution de Rb et Y à 100 mg L^{-1} de chaque élément dans une matrice HNO_3 0,5 M est présenté dans Figure 19 et les écarts relatifs obtenus par rapport aux valeurs attendues sont présentés dans le Tableau 1.

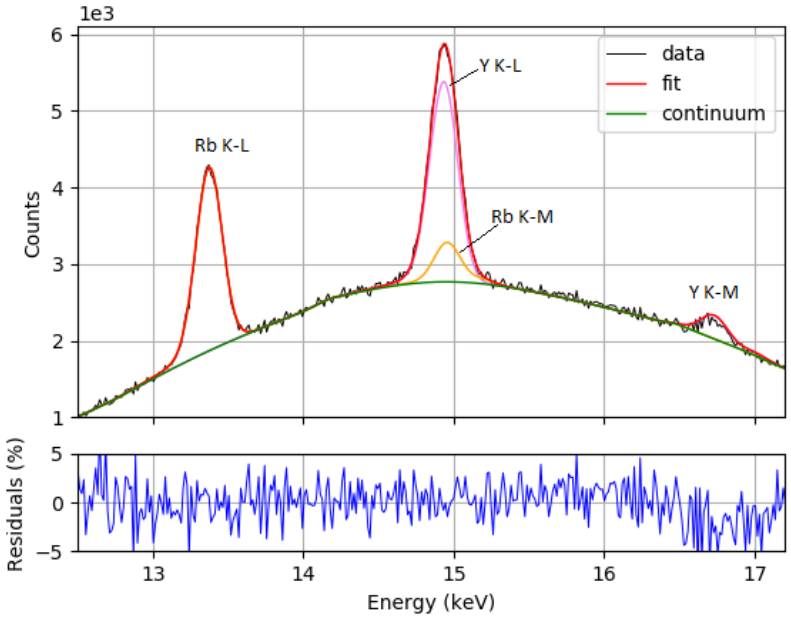

Figure 19. Traitement du spectre avec le logiciel PyMCA prenant en compte la fonction de transmission du filtre HOPG.

Tableau 1. Fractions massiques préparées et estimées avec PyMCA en tenant compte des modifications du spectre par le filtre HOPG.

Elément	Fraction massique préparée	Fraction massique estimée	Ecart relatif, %
Rb	$9{,}79 \times 10^{-5}$	$10{,}22 \times 10^{-5}$	+4 %
Y	$9{,}79 \times 10^{-5}$	$9{,}24 \times 10^{-5}$	-5 %

Pour conclure, le système miniaturisé a été entièrement modélisé grâce au couplage des résultats issus deux méthodes différentes : la première concernant le transport de particule (ici électrons et photons) dans la matière et la seconde la propagation optique de rayons X. La fonction de transmission calculée par XRT a été introduite dans le logiciel PyMCA dont l'algorithme est basé sur les paramètres fondamentaux. Cette étude a démontré que la quantification était réalisable sans étalon et avec un bon niveau de confiance. Quant au modèle global, les réponses spectrales de l'instrumentation miniature pour différentes conditions géométriques ont montré un très bon accord avec les spectres expérimentaux. Cet outil prédictif pourra être mis à profit pour améliorer le dispositif actuel et/ou à en définir une version optimisée.

Appendices

A. Experimental data

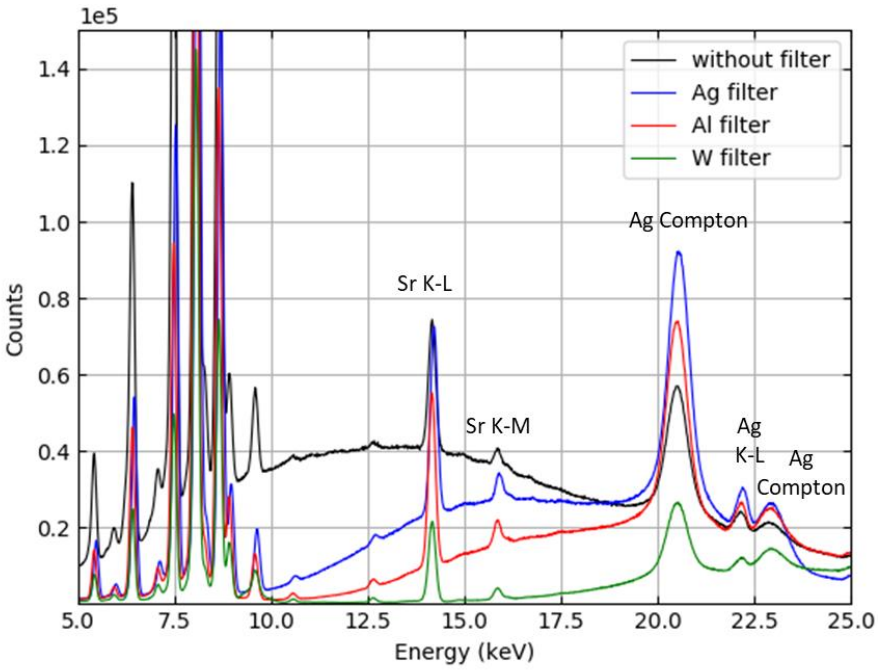

Figure A 1. Spectra of the solution containing Sr at a concentration of 10 mg L^{-1} in HNO_3 0.5M measured with the first channel. The X-ray tube was operated at a nominal voltage of 40 kV without primary filter and using Ag, Al and W filters. Acquisition time was 900 s in all measurements.

Solution containing Sr and Zr at a concentration of 10 mg L^{-1} in HNO_3 0.5 M

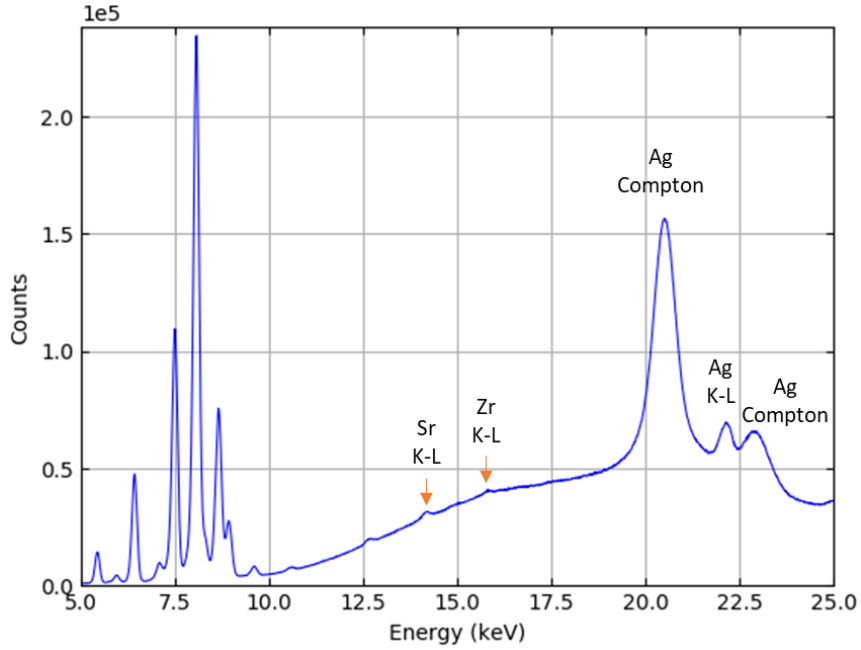

Figure A 2. Spectra measured with the first channel. The X-ray tube was operated at a nominal voltage of 40 kV with a 50 µA tube current, using a 25 µm Ag primary filter. Acquisition time was 900 s.

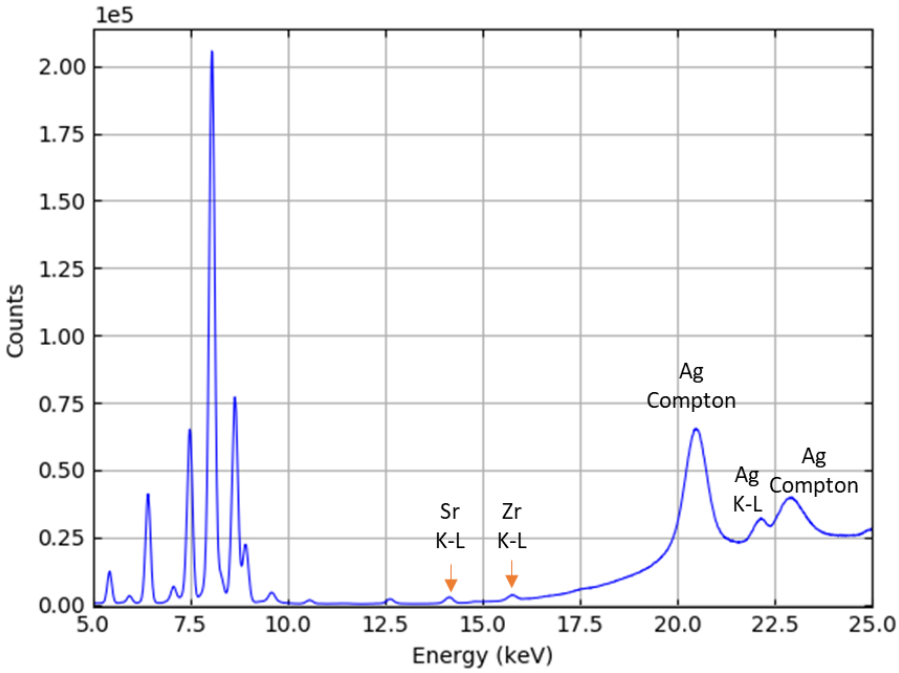

Figure A 3. Spectra acquired with the first channel. The X-ray tube voltage was set to 40 kV and tube current to 99 µA tube current. Primary radiation was filtered using a 25 µm W filter. Acquisition time was 900 s.

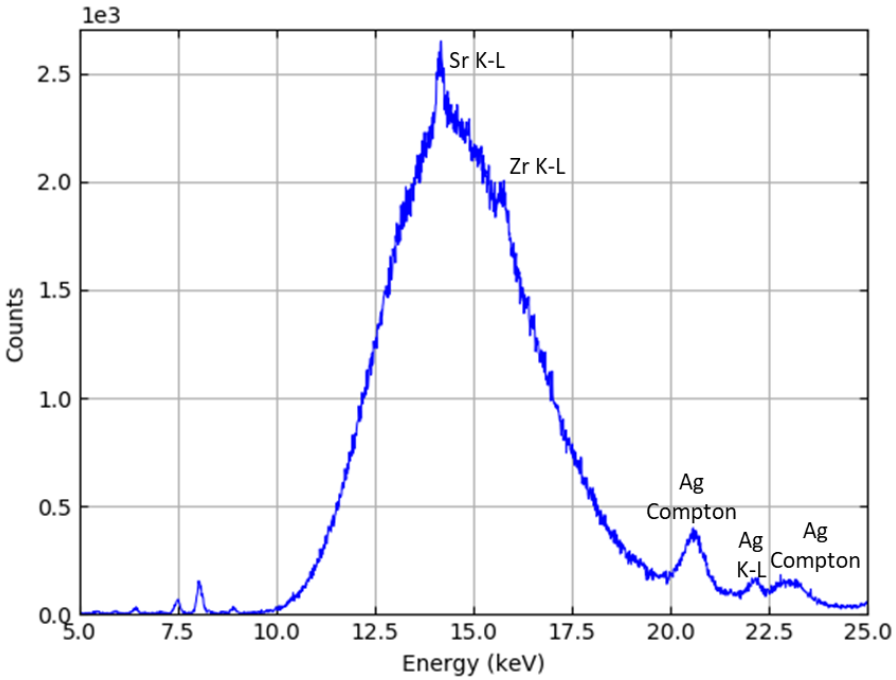

Figure A 4. Spectra acquired with the second channel in the presence of the HOPG crystal. The X-ray tube was operated at a nominal voltage of 40 kV with a 99 µA tube current, using a 25 µm Ag primary filter. Acquisition time was 900 s.

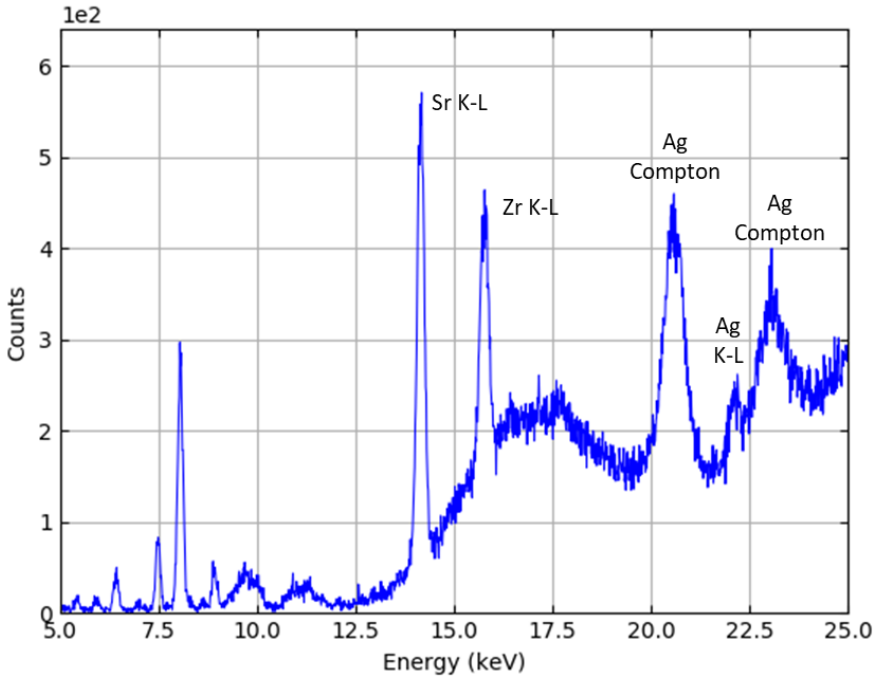

Figure A 5. Spectra measured with the second channel in the presence of the HOPG crystal. The X-ray tube was operated at a nominal voltage of 40 kV with a 99 µA tube current, using a 25 µm W primary filter. Acquisition time was 9×10^3 s.

Solution containing Zr at a concentration of 5 mg L^{-1} in HNO_3 0.5 M

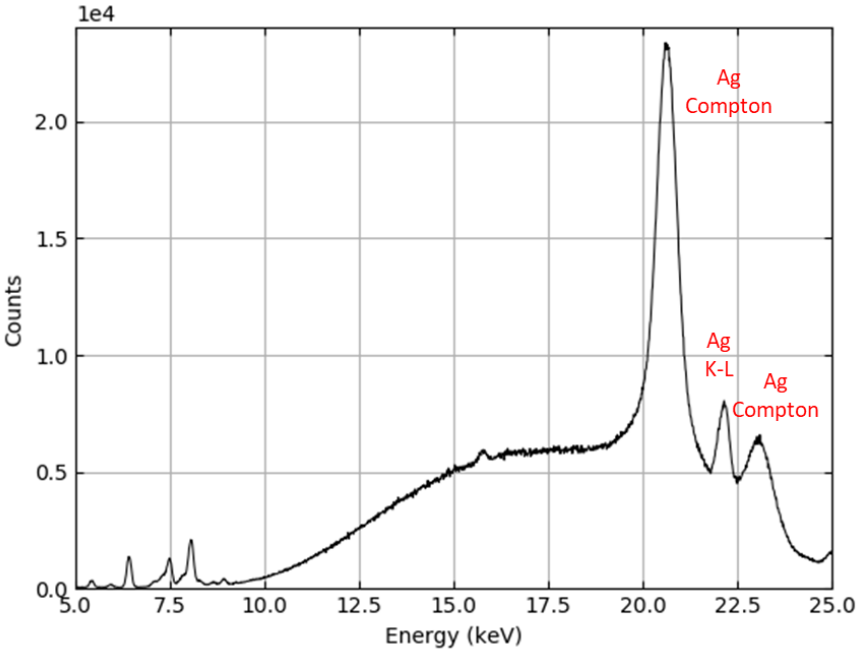

Figure A 6. Spectra acquired with the second channel with the HOPG crystal removed. The X-ray tube voltage was set to 40 kV and tube current to 99 µA tube current. Primary radiation was filtered using a 25 µm Ag filter. Acquisition time was 900 s.

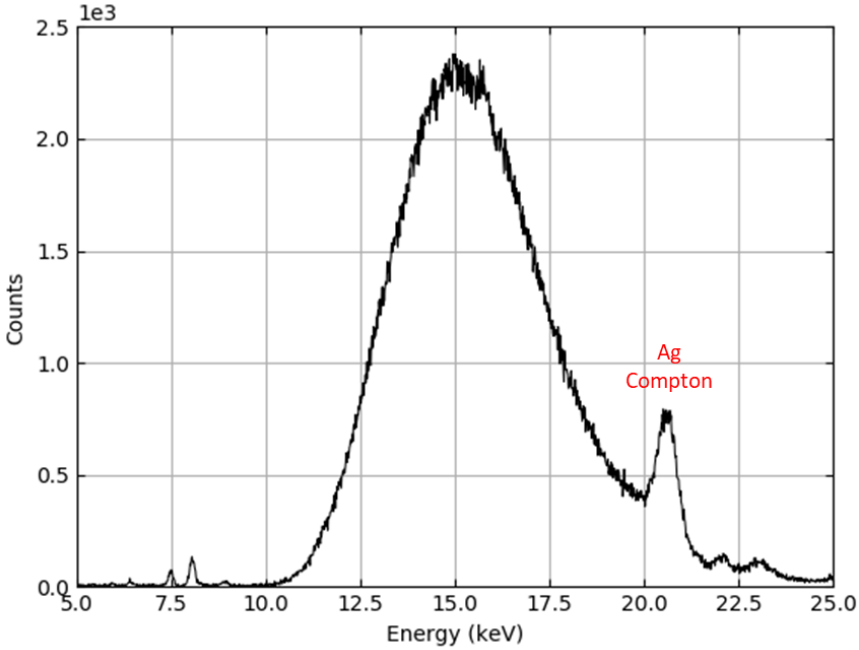

Figure A 7. Spectra measured with the second channel with the HOPG crystal. The X-ray tube was operated at a nominal voltage of 40 kV with a 99 µA tube current, using a 25 µm Ag primary filter. Acquisition time was 900 s.

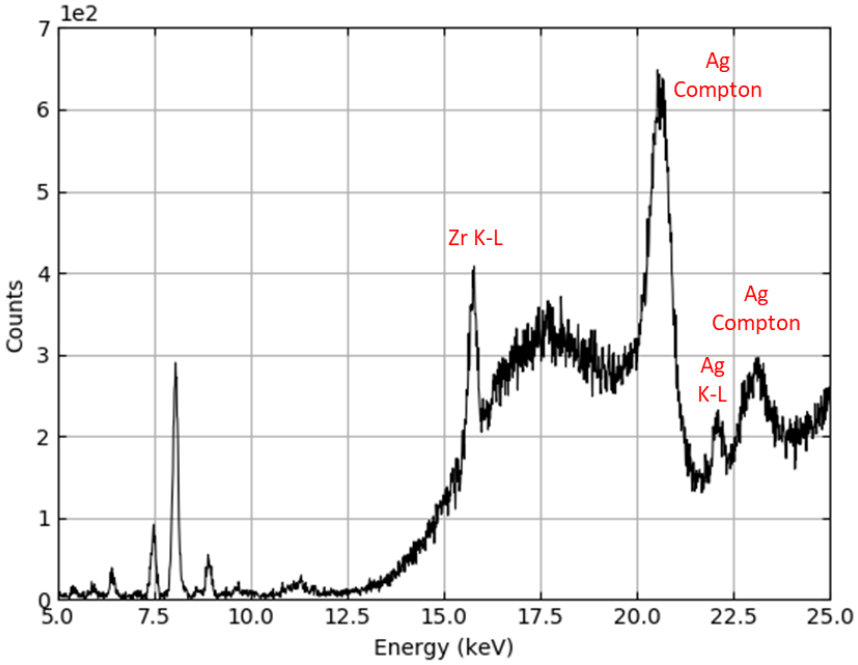

Figure A 8. Spectra measured with the second channel with the HOPG crystal. The X-ray tube was operated at a nominal voltage of 40 kV with a 99 µA tube current, using a 25 µm W primary filter. Acquisition time was 9×10^3 s.

B. PENELOPE simulations of the miniature XRF setup

1. Simulation of the X-ray tube spectrum with Ag filter (for Chapter 5, § 1)

I. Geometry of the model

```
SURFACE      ( 1)
  INDICES    ( 0, 0, 0, 1, 0)
  Z-SHIFT    ( 3.000, 0)
SURFACE      ( 2)
  INDICES    ( 0, 0, 0, 1, 0)
  Z-SHIFT    ( 3.000075, 0)
SURFACE      ( 3)
  INDICES    ( 1, 1, 0, 0,-1)
  X-SCALE    ( 5.000000000000000E-01,   0)
  Y-SCALE    ( 5.000000000000000E-01,   0)
MODULE       ( M1) (Ag Anode)
  MATERIAL   ( 1)
  SURFACE    ( 1), SIDE POINTER=( 1)
  SURFACE    ( 2), SIDE POINTER=(-1)
  SURFACE    ( 3), SIDE POINTER=(-1)
SURFACE      ( 4)
  INDICES    ( 0, 0, 0, 1, 0)
  Z-SHIFT    ( 3.012775,   0)
MODULE       ( M2)  (Be window)
  MATERIAL   ( 2)
  SURFACE    ( 2), SIDE POINTER=( 1)
  SURFACE    ( 3), SIDE POINTER=(-1)
  SURFACE    ( 4), SIDE POINTER=(-1)
SURFACE      ( 5)
  INDICES    ( 0, 0, 0, 1, 0)
  Z-SHIFT    ( 3.015275,   0)
MODULE       ( M3) (Ag filter)
  MATERIAL   ( 1)
  SURFACE    ( 3), SIDE POINTER=(-1)
  SURFACE    ( 4), SIDE POINTER=( 1)
  SURFACE    ( 5), SIDE POINTER=(-1)
SURFACE      ( 7)
  INDICES    ( 0, 0, 0, 1, 0)
  Z-SHIFT    ( 4.012775,   0)
SURFACE      ( 8)
```

INDICES (1, 1, 0, 0,-1)
X-SCALE (1, 0)
Y-SCALE (1, 0)
SURFACE (9)
INDICES (0, 0, 0, 1, 0)
Z-SHIFT (4.0200, 0)
MODULE (M4) *(Air det)*
MATERIAL (3)
SURFACE (7), SIDE POINTER=(1)
SURFACE (8), SIDE POINTER=(-1)
SURFACE (9), SIDE POINTER=(-1)

II. Definition of the model

- Source definition

SKPAR 1.....[Primary particles: 1=electron, 2=photon, 3=positron]
SENERG 4E4.....[Initial energy (monoenergetic sources only)]
SPOSIT0 0 0.....[Coordinates of the source]
SCONE0 0 1.23.....[Conical beam; angles in deg]

- Material data and simulation parameters

MFNAME Ag.mat.....[Material file, up to 20 chars]
MSIMPA 2E3 1E3 2E3 0.05 0.05 1E3 1E3...[EABS(1:3),C1,C2,WCC,WCR]
MFNAME Be.mat.....[Material file, up to 20 chars]
MSIMPA 2E3 1E3 2E3 0.05 0.05 1E3 1E3...[EABS(1:3),C1,C2,WCC,WCR]
MFNAME Air.mat.....[Material file, up to 20 chars]
MSIMPA 2E3 1E3 2E3 0.05 0.05 1E3 1E3...[EABS(1:3),C1,C2,WCC,WCR]

- Geometry and local simulation parameters

GEOMFN Tube_geometry.geo.....[Geometry file, up to 20 chars]

- Interaction forcing

IFORCE 1 1 4 100 0.1 2.....[KB,KPAR,ICOL,FORCER,WLOW,WHIG]
IFORCE 1 1 5 100 0.1 2.....[KB,KPAR,ICOL,FORCER,WLOW,WHIG]
IFORCE 2 1 4 100 0.1 2.....[KB,KPAR,ICOL,FORCER,WLOW,WHIG]
IFORCE 2 1 5 100 0.1 2.....[KB,KPAR,ICOL,FORCER,WLOW,WHIG]

- Emerging particles. Energy and angular distributions

NBE 1E3 4E4 350.....[Energy window and no. of bins]
NBANGL 45 18.....[No. of bins for the angles THETA and PHI]

- Impact detectors (up to 25 different detectors)

IMPDET 1E3 4E4 350 1 1.....[E-window, no. of bins, IPSF, IDCUT]
IDBODY 4.....[Active body]

- Job properties

RESUME dump1.dat.....[Resume from this dump file, 20 chars]
DUMPTO dump1.dat.....[Generate this dump file, 20 chars]
DUMPP 60.....[Dumping period, in sec]
LTRACK 25.....[Generate shower files for visualisation]
RSEED -10 1.....[Seeds of the random-number generator]

NSIMSH 2E9.....[Desired number of simulated showers]
TIME 2E9.....[Allotted simulation time, in sec]
END.....[Ends the reading of input data]

2. Simulation of the fluorescence spectrum (for Chapter 6, § 4)

I. Geometry of the model

SURFACE (1)
INDICES (0, 0, 0, 1, 0)
Z-SHIFT (2.5, 0)
SURFACE (2)
INDICES (0, 0, 0, 1, 0)
Z-SHIFT (4.0, 0)
SURFACE (3)
INDICES (1, 1, 0, 0,-1)
X-SCALE (0.75, 0)
Y-SCALE (0.75, 0)
MODULE (M1) *(Sample)*
MATERIAL (1)
SURFACE (1), SIDE POINTER=(1)
SURFACE (2), SIDE POINTER=(-1)
SURFACE (3), SIDE POINTER=(-1)
SURFACE (4)
INDICES (1, 1, 0, 0,-1)
X-SCALE (0.75, 0)
Y-SCALE (0.75, 0)
SURFACE (5)
INDICES (0, 0, 0, 1, 0)
Z-SHIFT (5.0, 0)
SURFACE (6)
INDICES (1, 1, 0, 0,-1)
X-SCALE (1.05, 0)
Y-SCALE (1.05, 0)
MODULE (M2) *(Sample cup)*
MATERIAL (2)
SURFACE (1), SIDE POINTER=(1)
SURFACE (4), SIDE POINTER=(1)
SURFACE (5), SIDE POINTER=(-1)
SURFACE (6), SIDE POINTER=(-1)
SURFACE (7)
INDICES (0, 0, 0, 1, 0)
Z-SHIFT (0, 0)
SURFACE (8)
INDICES (0, 0, 0, 1, 0)
Z-SHIFT (0.05, 0)
SURFACE (9)

```
  INDICES     ( 1, 1, 0, 0,-1)
  X-SCALE     ( 0.233, 0)
  Y-SCALE     ( 0.233, 0)
MODULE        (  M3) (Detector)
  MATERIAL    ( 3)
  SURFACE     ( 7), SIDE POINTER=( 1)
  SURFACE     ( 8), SIDE POINTER=(-1)
  SURFACE     ( 9), SIDE POINTER=(-1)
  THETA       (-46,   0) DEG
  X-SHIFT     ( 2.4,   0)
SURFACE       ( 10)
  INDICES     ( 0, 0, 0, 1, 0)
  Z-SHIFT     ( -0.5, 0)
SURFACE       ( 11)
  INDICES     ( 1, 1, 0, 0,-1)
  X-SCALE     ( 3, 0)
  Y-SCALE     ( 3, 0)
SURFACE       ( 12)
  INDICES     ( 0, 0, 0, 1, 0)
  Z-SHIFT     ( 5.1, 0)
BODY          ( M4) (Air)
  MATERIAL    ( 4)
  SURFACE     ( 10), SIDE POINTER=( 1)
  SURFACE     ( 11), SIDE POINTER=(-1)
  SURFACE     ( 12), SIDE POINTER=(-1)
  MODULE      ( M1)
  MODULE      ( M2)
  MODULE      ( M3)
```

II. Definition of the model

- Source definition

```
SKPAR     2.....[Primary particles: 1=electron, 2=photon, 3=positron]
SPECTR    2.08E3  3.5941E-12
SPECTR    2.24E3  5.03174E-12
SPECTR    2.40E3  4.07331E-12
    ...
    ...
    ...
SPECTR    4.96E3  2.1325E-11
SPECTR    4.97E3  1.55744E-11
SPECTR    4.99E3  8.14663E-12
SPECTR    5.00E3  -1.....[E bin: lower end and probability]
SPOSIT    0  0.6  1.....[Coordinates of the source]
SCONE0  0  27.....[Conical beam; angles in deg]
```

- Material data and simulation parameters

```
MFNAME    Sample.mat.....[Material file, up to 20 chars]
MSIMPA    3E3  1E3  3E3  0.1  0.1  3E3  1E3.....[EABS(1:3),C1,C2,WCC,WCR]
```

MFNAME Air.mat.....[Material file, up to 20 chars]
MSIMPA 3E3 1E3 3E3 0.1 0.1 3E3 1E3.....[EABS(1:3),C1,C2,WCC,WCR]
MFNAME Sample_Cup.mat.....[Material file, up to 20 chars]
MSIMPA 3E3 1E3 3E3 0.1 0.1 3E3 1E3.....[EABS(1:3),C1,C2,WCC,WCR]
MFNAME Si.mat.....[Material file, up to 20 chars]
MSIMPA 3E3 1E3 3E3 0.1 0.1 3E3 1E3.....[EABS(1:3),C1,C2,WCC,WCR]

- Geometry and local simulation parameters

GEOMFN Setup.geo.....[Geometry file, up to 20 chars]

- Emerging particles. Energy and angular distributions

NBE 3.0E3 3.0E4 300.....[Energy window and no. of bins]

- Impact detectors

IMPDET 3.0E3 3.0E4 300 0 2.....[E-window, no. of bins, IPSF, IDCUT]
IDBODY 5.....[Active body]

- Energy-deposition detectors

ENDETC 3.0E3 3.0E4 300.....[Energy window and no. of bins]
EDBODY 5.....[Active body]

- Job properties

RESUME dump.dmp.....[Resume from this dump file, 20 chars]
DUMPTO dump.dmp.....[Generate this dump file, 20 chars]
DUMPP 60.....[Dumping period, in sec]
NSIMSH 2E9.....[Desired number of simulated showers]
TIME 2E9.....[Allotted simulation time, in sec]
END.....[Ends the reading of input data]

C. Ray-tracing simulations

```
import numpy as np
import xrt.backends.raycing.sources as rsources
import xrt.backends.raycing.screens as rscreens
import xrt.backends.raycing.materials as rmats
import xrt.backends.raycing.oes as roes
import xrt.backends.raycing.apertures as rapts
import xrt.backends.raycing.run as rrun
import xrt.backends.raycing as raycing
import xrt.plotter as xrtplot
import xrt.runner as xrtrun
#Definition of a mosaic crystal
mosaicityFWHMdeg = 0.4
mosaicityFWHM = np.deg2rad(mosaicityFWHMdeg)
mosaicity=mosaicityFWHM/2.355
Crystal1 = rmats.CrystalFromCell(name='graphite', hkl=(0, 0, 2), a=2.456, b=a, c=6.7080,
        alpha=90, beta=90, gamma=120, atoms=[6]*4, atomsXYZ=[[0., 0., 0.], [0., 0., 0.5],
        [1./3, 2./3, 0.], [2./3, 1./3, 0.5]], t=0.2, geom='Bragg reflected', table='Chantler', mo-
        saicity=mosaicity)
Crystal2 = Crystal1(hkl=(0, 0, 4))
#Definition of a cylindrical optical element
class Cylinder(roes.SurfaceOfRevolution):
        def __init__(self, *args, **kwargs):
                self.r = kwargs.pop('Rm')
                roes.SurfaceOfRevolution.__init__(self, *args, **kwargs)
        def local_r(self, s, phi):
                return self.r
        def local_n(self, s, phi):
                a = -np.sin(phi)
                b = np.zeros_like(s)
                c = -np.cos(phi)
                return a, b, c

Rm=10.1 #cylinder radius
L=40 #cylinder length
D1=62 #source-to-crystal distance
D2=56 # crystal-to-image plane distance
rs=2.25 # beam stop radius
rc=7 # aperture radius
```

```
rdet=2.33# radius of the detection surface
lc=34.5 # source-to-circular aperture distance
rbeam=1# source radius

# Distances of the emitting points from the source
d1=np.sqrt(x0**2+z0**2) # radius vector from the source center to the emitting point
d2=np.abs(d1+rbeam)
d3=np.abs(d1-rbeam)
d4=min(d2,d3) # the closest point to the source center
d5=max(d2,d3) # the farthest point from the source center
# Angular acceptance of the HOPG cylinder
a1=(Rm+d5)/D1
a2=(Rm+d5)/(D1+L)
a3=np.abs(Rm-d5)/D1
a4=np.abs(Rm-d5)/(D1+L)
a5=(Rm+d4)/D1
a6=(Rm+d4)/(D1+L)
a7=np.abs(Rm-d4)/D1
a8=np.abs(Rm-d4)/(D1+L)
amono_min=min(a1,a2,a3,a4,a5,a6,a7,a8)
amono_max=max(a1,a2,a3,a4,a5,a6,a7,a8)
# Angular acceptance of the circular aperture
a9=(rc+d5)/lc
a10=np.abs(rc-d5)/lc
a11=(rc+d4)/lc
a12=np.abs(rc-d4)/lc
acoll_min=min(a9,a10,a11,a12)
acoll_max=max(a9,a10,a11,a12)

def build_beamline(nrays=1e7):
        beamLine.geometricSource01 = rsources.GeometricSource(bl=beamLine,
                center=[x0, 0, z0],
                dx=(0, rbeam),
                dz=(0, 2 * np.pi),
                distx=r"annulus", # uniform (X, Z) distribution
                distz=r"annulus",
                dxprime=(amin, amax),
                dzprime=(0, 2 * np.pi),
                distxprime=r"annulus",
                polarization=None,
                distE=r"flat",
                energies=[5000, 45000])
```

```
        beamLine.roundAperture01 = rapts.RoundAperture(bl=beamLine, center=[0, 34.5,
0], r=rc)
        beamLine.roundBeamStop01 = rapts.RoundBeamStop(bl=beamLine, center=[0, D,
0], r=rs)
        beamLine.screen01 = rscreens.Screen(bl=beamLine, center=[0, D, 0])
        beamLine.cylinder1 = Cylinder(bl=beamLine, center=[0, D, 0], Rm=Rm, limPhysY=[0,
L],             material=Crystal)
        beamLine.cylinder2 = Cylinder(bl=beamLine, center=[0, D, 0], Rm=Rm, limPhysY=[0,
L],     material=Crystal2)
        beamLine.roundBeamStop02 = rapts.RoundBeamStop(bl=beamLine, center=[0,
(D+L/2), 0], r=7)
        beamLine.roundBeamStop03 = rapts.RoundBeamStop(bl=beamLine, center=[0,
(L+D), 0], r=rs)
        beamLine.roundAperture02 = rapts.RoundAperture(bl=beamLine, center=[0, (L+2D),
0],r=rdet)
        beamLine.screen02 = rscreens.Screen(bl=beamLine, center=[0, (L+2D), 0])
        return beamLine

def run_process(beamLine): #
        geometricSource01beamGlobal01 = beamLine.sources[0].shine()
        roundAperture01 = beamLine.roundAperture01.propagate(geomet-
ricSource01beamGlobal01)
        roundBeamStop01 = beamLine.roundBeamStop01.propagate(geomet-
ricSource01beamGlobal01)
        screen01 = beamLine.screen01.expose(geometricSource01beamGlobal01)
        beamOrder1global, beamOrder1local = beamLine.cylinder1.reflect(
                        geometricSource01beamGlobal01)
        beamOrder2global, beamOrder2local = beamLine.cylinder2.reflect(
                                geometricSource01beamGlobal01)
        beamOrder2global.Jss += beamOrder1global.Jss
        beamOrder2global.Jpp += beamOrder1global.Jpp
        beamOrder2local.Jss += beamOrder1local.Jss
        beamOrder2local.Jpp += beamOrder1local.Jpp
        roundBeamStop02 = beamLine.roundBeamStop02.propagate(geomet-
ricSource01beamGlobal01)
        roundBeamStop03 = beamLine.roundBeamStop03.propagate(geomet-
ricSource01beamGlobal01)
        roundAperture102 = beamLine.roundAperture02.propagate(beamOrder1global)
        screen102 = beamLine.screen02.expose(beamOrder1global)
        roundAperture202 = beamLine.roundAperture02.propagate(beamOrder2global)
        screen202 = beamLine.screen02.expose(beamOrder2global)
        outDict = {
                'geometricSource01beamGlobal01': geometricSource01beamGlobal01,
```

```
                'roundAperture01': roundAperture01,
                'roundBeamStop01': roundBeamStop01,
                'screen01': screen01,
                'beamOrder1global': beamOrder1global,
                'beamOrder1local': beamOrder1local,
                'beamOrder2global': beamOrder2global,
                'beamOrder2local': beamOrder2local,
                'roundBeamStop02': roundBeamStop02,
                'roundBeamStop03': roundBeamStop03,
                'roundAperture102': roundAperture102,
                'screen102': screen102,
                'roundAperture202': roundAperture202,
                'screen202': screen202}
        return outDict
rrun.run_process = run_process
def define_plots():
        plots = []
        plot = xrtplot.XYCPlot(
                beam=r"screen01",
                xaxis=xrtplot.XYCAxis(
                        label=r"x",
                        limits=[-15, 15],
                        bins=256),
                yaxis=xrtplot.XYCAxis(
                        label=r"z",
                        limits=[-15, 15],
                        bins=256),
                caxis=xrtplot.XYCAxis(
                        label=r"energy",
                        limits=[5, 45],
                        unit=r"keV",
                        bins=256),
                title=r"plot01")
        plot.baseName = 'source_spectrum'
        plots.append(plot)

        plot02 = xrtplot.XYCPlot(
                beam=r"beamOrder1local",
                xaxis=xrtplot.XYCAxis(
                        label=r"y",
                        data=raycing.get_y,
                        limits=[0, L],
                        bins=256),
```

```
        yaxis=xrtplot.XYCAxis(
                label=r"z",
                data=raycing.get_z,
                limits=[-10.5, 10.5],
                bins=256),
        caxis=xrtplot.XYCAxis(
                label=r"energy",
                limits=[5, 35],
                unit=r"keV",
                bins=450),
        title=r"cylinder",
        aspect="auto",
        negative=True)
plot02.baseName = 'crystal_local_002'
plots.append(plot02)

plot03 = xrtplot.XYCPlot(
        beam=r"beamOrder2local",
        xaxis=xrtplot.XYCAxis(
                label=r"y",
                data=raycing.get_y,
                limits=[0, L],
                bins=256),
        yaxis=xrtplot.XYCAxis(
                label=r"z",
                data=raycing.get_z,
                limits=[-10.5, 10.5],
                bins=256),
        caxis=xrtplot.XYCAxis(
                label=r"energy",
                limits=[5, 35],
                unit=r"keV",
                bins=450),
        title=r"plot03",
        aspect="auto",
        negative=True)
plot03.baseName = ''crystal_local_004'
plots.append(plot03)

plot04 = xrtplot.XYCPlot(
        beam=r"screen102",
        xaxis=xrtplot.XYCAxis(
                label=r"x",
```

```
                data=raycing.get_x,
                limits=[-3.1, 3.1],
                bins=256),
        yaxis=xrtplot.XYCAxis(
                label=r"z",
                data=raycing.get_z,
                limits=[-3.1, 3.1],
                bins=256),
        caxis=xrtplot.XYCAxis(
                label=r"energy",
                limits=[5, 35],
                unit=r"keV",
                bins=450),
        title=r"plot04",
        aspect="auto",
        negative=True)
plot04.baseName = 'image_plane_002'
plots.append(plot04)

plot05 = xrtplot.XYCPlot(
        beam=r"screen202",
        xaxis=xrtplot.XYCAxis(
                label=r"x",
                data=raycing.get_x,
                limits=[-3.1, 3.1],
                bins=256),
        yaxis=xrtplot.XYCAxis(
                label=r"z",
                data=raycing.get_z,
                limits=[-3.1, 3.1],
                bins=256),
        caxis=xrtplot.XYCAxis(
                label=r"energy",
                limits=[5, 35],
                unit=r"keV",
                bins=450),
        title=r"plot05",
        aspect="auto",
        negative=True)
plot05.baseName = 'image_plane_004'
plots.append(plot05)

for plot in plots:
```

```
            plot.saveName = plot.baseName + '.png'
            plot.persistentName = plot.baseName + '.mat'
    return plots

def main():
    beamLine = build_beamline()
    plots = define_plots()
    xrtrun.run_ray_tracing(
            plots=plots,
            repeats=500,
            backend=r"raycing",
            beamLine=beamLine)

if __name__ == '__main__':
    main()
```

Titre : Développement d'un système XRF miniaturisé standardless pour l'analyse des actinides : couplage modélisation MC et paramètres fondamentaux

Mots clés : Fluorescence des rayons X, analyse quantitative, paramètres fondamentaux, monochromateur HOPG, simulations Monte Carlo, calculs ray-tracing

Résumé : La fluorescence des rayons X (XRF) est un outil analytique qualitatif et quantitatif pour la caractérisation élémentaire de nombreux types de matériaux ; elle est non destructive, rapide et convient à l'analyse d'une large gamme d'éléments. La méthode est basée sur l'excitation d'un analyte par un faisceau primaire de rayons X qui induit l'émission de la fluorescence X de l'échantillon. L'objectif de l'analyse quantitative par fluorescence X est d'établir la relation entre la concentration des éléments avec les intensités de fluorescence mesurées. Cependant, cette tâche n'est pas simple puisque les intensités de fluorescence apparentes dépendent de la fraction pondérale de l'élément dans l'analyte, de la composition de la matrice, de la géométrie du dispositif expérimental, des paramètres de la source de rayons X primaires et du système de détection, etc. Les informations quantitatives peuvent être obtenues en appliquant des approches théoriques ou empiriques.
Un des objectifs de cette thèse est d'étudier les performances d'une installation miniaturisée de fluorescence X destinée à l'analyse des actinides par leurs raies XL (12 keV < E < 17 keV), implantée dans le laboratoire d'analyses de l'installation ATALANTE (CEA Marcoule). Le dispositif expérimental comprend un tube à rayons X à anode d'argent (Ag) qui irradie un échantillon, un détecteur au silicium à dérive (SDD) et un monochromateur HOPG cylindrique. Ce dernier élément est placé entre l'échantillon et le système de détection et agit comme un filtre passe-bande en modifiant la distribution spectrale du rayonnement de fluorescence. De cette manière, les spectres peuvent être enregistrés dans la gamme d'énergie d'intérêt, tout en réduisant le taux de comptage dû aux rayonnements parasites. Le monochromateur HOPG du dispositif expérimental couvre la gamme d'énergie d'intérêt qui permet d'analyser les éléments de Z moyen (Se, Rb, Sr, Y, etc.) et les actinides (U, Np, Pu, Am et Cm) par leurs raies K et L, respectivement.
Le second objectif de ce travail est d'affiner l'algorithme classique de quantification basé sur les paramètres fondamentaux en tenant compte des modifications de la distribution spectrale par le cristal HOPG. En effet, les spectres mesurés avec un système de fluorescence classique peuvent être traités avec succès en utilisant une méthode théorique basée sur des équations mathématiques sans nécessiter d'étalons. Il s'agit de la méthode dite des paramètres fondamentaux (PF). Cependant, pour traiter avec précision les spectres mesurés avec la présente configuration, il est nécessaire de connaître la fonction de transmission du cristal HOPG.
L'étude détaillée de l'instrumentation miniature et des phénomènes physiques mis en jeu a été réalisée en utilisant la méthode de Monte Carlo pour le transport des rayonnements, avec le code PENELOPE. Ensuite, pour mieux comprendre les propriétés de réflexion du cristal de HOPG, des simulations d'optique des rayons X ont été réalisées à l'aide du logiciel XRT afin de modéliser la réponse du cristal cylindrique de HOPG et représenter pas à pas l'ensemble de détection. La réponse du système optique développé a été simulée en utilisant des spectres expérimentaux enregistrés sans le monochromateur HOPG comme données d'entrée. Le modèle de simulation a été validé par la comparaison avec des données expérimentales pour différents échantillons liquides contenant des éléments de Z moyens (quelques dizaines de mg.L-1), ce qui a permis de caractériser la fonction de transfert du cristal HOPG. Ensuite, celle-ci a pu être importée avec succès dans le logiciel PyMCA, basé sur les paramètres fondamentaux, afin de fournir des résultats quantitatifs.
Pour conclure, il est démontré que le couplage du code Monte Carlo PENELOPE et des simulations XRT peut être utilisé pour prédire les réponses spectrales de l'instrumentation de fluorescence miniature pour différentes conditions géométriques dans le but de contribuer à l'améliorer.

Title : Development of a standardless miniature XRF setup for the analysis of actinides : coupling MC methods with fundamental parameters

Keywords : X-ray fluorescence, quantitative analysis, fundamental parameters, HOPG monochromator, Monte Carlo simulations, ray-tracing calculations

Abstract : X-ray fluorescence (XRF) is qualitative and quantitative analytical tool for elemental analysis of many types of materials; it is non-destructive, fast and is suitable for the analysis of the wide range of elements. The method is based on the excitation of an analyte by a beam of primary X-rays to induce the emission of X-ray fluorescence from the sample. The goal of the quantitative XRF analysis is to relate the elemental concentrations to the measured fluorescence intensities. However, this task is not straightforward since the apparent fluorescence intensities are dependent on the weight fraction of an analyte, matrix composition, geometry of the experimental setup, parameters of the primary X-ray source and detection system, etc.. The quantitative information can be obtained applying theoretical or empirical approaches.

One of the aims of this thesis is to investigate the performances of the miniaturised XRF setup intended to the analysis of actinides by their L X-ray lines (12 keV < E < 17 keV) installed in the analysis laboratory within ATALANTE facility (CEA Marcoule). The experimental setup includes a silver anode (Ag) X-ray tube which irradiates a sample, a silicon drift detector (SDD) and a cylindrical highly oriented pyrolytic graphite (HOPG) monochromator. The latter element is positioned between the sample and the detection system and in such a geometry, it acts as a bandpass filter modifying the spectral distribution of the fluorescence radiation. In this manner, the spectra can be recorded in the energy range of interest reducing the burden on the detection system from an unwanted radiation. The HOPG monochromator of the experimental setup cover the energy range of interest and permits to analyse the medium-Z elements (Se, Rb, Sr, Y, etc.) and actinides (U, Np, Pu, Am, and Cm) by their K and L X-ray lines, respectively. The second goal of this work is to refine the classical quantification algorithm based on the fundamental parameters taking into account the modifications of the spectral distribution by the HOPG crystal. Indeed, spectra measured with a classical XRF system can be successfully processed using a theoretical method based on mathematical equations without standards. Such method is called the fundamental parameters (FP) method. However, in order to process accurately the spectra measured with the present setup, it arises the necessity to know the transmission function of the HOPG filter.

The detailed investigation of the miniature setup and of the physical phenomena involved was performed utilizing the Monte Carlo method for the radiation transport with the code PENELOPE. In addition, to establish a better understanding of the reflection properties of the HOPG crystal, ray-tracing simulations were performed using the dedicated the ray-tracing package XRT (XRayTracer) to model the cylindrical HOPG crystal and represent step by step the entire detection channel. The response of the developed optical system was simulated applying the experimental spectra recorded without the HOPG monochromator as an input data. The validity of the simulation model has been approved through the comparison with experimental data for different liquid samples containing medium-Z elements (a few tens of mg L^{-1}), that allowed to define the HOPG transfer function. Next, the estimated transfer function could be successfully applied in the FP-based software PyMCA to provide quantitative results.

To conclude, it is demonstrated that the coupling of the PENELOPE and XRT simulations can be used to predict the spectral responses of the miniature setup under different geometrical conditions in order to help to improve it.